FZR-407

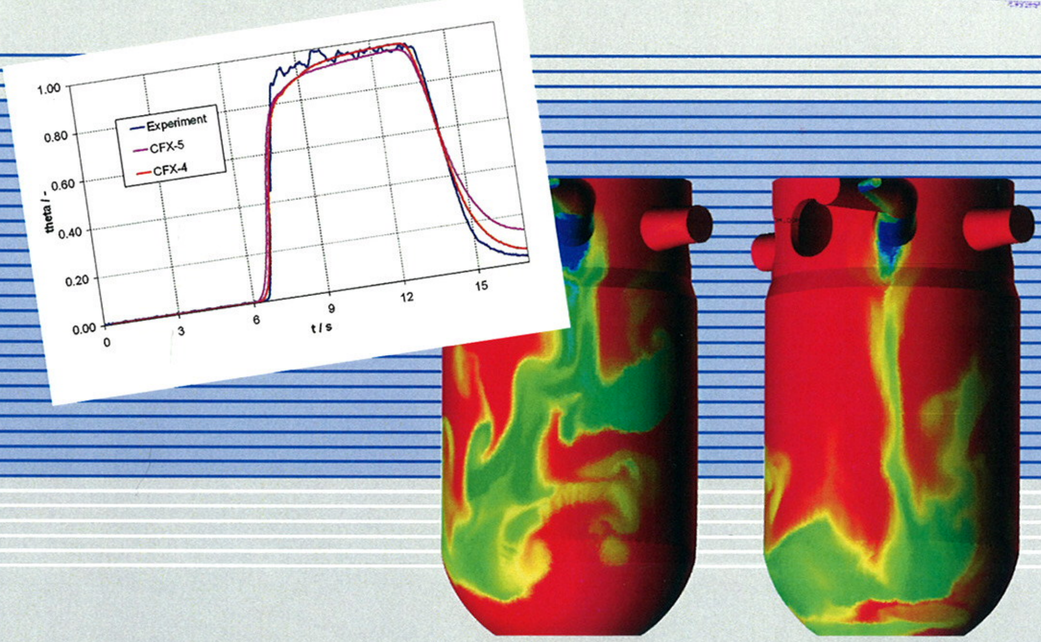

Wissenschaftlich-Technische Berichte
FZR-407 2004 · ISSN 1437-322X

Annual Report 2003

Institute of Safety Research

**Forschungszentrum
Rossendorf**

Wissenschaftlich-Technische Berichte
FZR-407
2004

Annual Report 2003

Institute of Safety Research

Editors:
Prof. Dr. Frank-Peter Weiß
Prof. Dr. Udo Rindelhardt

Forschungszentrum
Rossendorf

Cover figure:

The figure shows results of Computational Fluid Dynamics (CFD) simulations of the coolant mixing in the pressure vessel of a pressurised water nuclear reactor. A slug of water with different temperature and boron content might be injected from a primary circuit coolant loop into the reactor in accidental situations (see contribution pages 7ff).

The 3D visualisation demonstrates the mixing of colder water of higher density with the ambient coolant on the way from the coolant loop to the reactor core. The advanced technique of Large Eddy Simulation was applied for the simulation. Corresponding experiments have been performed at the Rossendorf coolant mixing facility ROCOM for the validation of the CFD models.

Forschungszentrum Rossendorf e.V.
Institut für Sicherheitsforschung

Postfach 51 01 19
D-01314 Dresden
Bundesrepublik Deutschland

Direktor Prof. Frank-Peter Weiß
Telefon + 49 (3 51) 2 60 34 80
Telefax + 49 (3 51) 2 60 34 40
E-Mail f.p.weiss@fz-rossendorf.de

WWW http://www.fz-rossendorf.de/FWS

CONTENTS

Preface

Selected Reports

Preface

The Institute of Safety Research (ISR) is part of Forschungszentrum Rossendorf e.V. (FZR e.V.) which is a member institution of the Wissenschaftsgemeinschaft Gottfried Wilhelm Leibniz (Leibniz Association).
ISR is the main contributor to the FZR research programme „Safety and Environment“. There, the institute is responsible for all scientific projects of the sub-programmes “Plant and Reactor Safety” and “Thermal Fluid Dynamics”, respectively.
The work of the institute is directed to the assessment and enhancement of the safety of technical plants and to the increase of the efficiency and environmental sustainability of those facilities. Subjects of investigation are equally nuclear plants and installations of process industries.
To achieve the goals mentioned, the institute is mainly engaged in the scientific fields of thermal fluid dynamics including magneto-hydrodynamics (MHD) and materials sciences.
In 2003, the ISR worked on the following main scientific projects.

Sub-programme	Project
Plant and Reactor Safety	accident analysis of nuclear reactors
	safety of materials and components
	particle and radiation transport
	safety and efficiency of chemical processes
Thermal Fluid Dynamics	magneto-hydrodynamics
	thermal fluid dynamics of multiphase systems

The work on these projects is based on shared financing through the basic funding of FZR and through external funding by research grants and scientific contracts with the industry. In 2003, 37 % (2.500 k€) of the total budget came from such external funding sources with 17 % from research grants of the Federal Government and the Free State of Saxony, 9 % of the funding originated from Deutsche Forschungsgemeinschaft, 7 % from the EU and 4 % from research contracts mainly with the industry (see fig.1) The deployment of the total budget on the different projects can be seen in fig.2.

During the reporting period, the ISR performed 5 meetings and workshops with international participation. In particular, one should mention the Topical Meeting of the German Kerntechnische Gesellschaft on “Reactor Operation and Core Monitoring”, the 13th Symposium of the Atomic Energy Research Association on the safety of VVER reactors, and the Workshop on Multiphase Flows in Industrial Applications that was commonly organised by ISR and ANSYS/CFX.

The institute is involved in many international projects, especially in projects of the 5th EU Research Framework Programme (EU FP). The participation in new projects and networks of EU FP6 like in PERFECT, SARNET, and NURESIM could successfully be prepared.

One of the most important running EU projects is the FLOWMIX-R project dealing with mixing phenomena during boron dilution transients in PWRs. The project is coordinated by ISR. The course and the consequences of such boron dilution transients in PWRs is a topical theme of international reactor safety research. ISR contributed internationally well recognized results to the clarification of boron dilution transients by mixing studies at the Rossendorf ROCOM test facility including CFD calculations and by reactor dynamic calculations using the code package DYN3D. The experiments related to restarting natural circulation with deborated coolant slugs in the cold legs have shown that the degree of mixing of these slugs with the ambient water in the pressure vessel and consequently the reactivity insertion sensitively depend on the density differences of those slugs with the ambient coolant.

The results of the work are also used in the nuclear oversight process. The concerned researchers of ISR were invited for guest stays abroad, articles in international journals and lectures at the Otto Hahn – Frederic Joliot Summer School.

Considerable progress could also be achieved in the CFD simulation of two-phase flows. New approaches for the forces acting on steam bubbles in a water flow could be developed and implemented into the CFX code in close cooperation with the CFX developer ANSYS/CFX. The qualified models allow to simulate the evolution of bubble size specific radial void distribution profiles along the flow path. These theoretical studies and the related experiments at the Rossendorf TOPFLOW test facility represent an important part of the German CFD network that aims at the improvement of thermal hydraulic calculation methods in reactor safety.

The development of sophisticated measuring technologies is an essential part of all our research in fluid dynamics. Especially for opaque liquid metals and semiconductor melts, there is a strong need for measuring techniques that provide information about the velocity field with good resolution in space and time. Therefore, an inverse non-invasive technique was developed that derives a 3-dimensional reconstruction of the liquid velocity field from the measurement of the deformation of an externally applied magnetic field.

This kind of magnetic tomography could successfully be demonstrated in an experiment. The technique worked stable and was capable of reconstructing the flow structure and its evolution over time.

Together with the Dresden Technical University and with the Zittau University of Applied Sciences, the ISR represents the East German Center of Competence in Nuclear Technology being a member of the National Nuclear Competence Alliance (Kompetenzverbund Kerntechnik). As such the ISR also takes care for the conservation and promotion of expertise in nuclear engineering. In this context we are proud that our colleague H.-G. Willschütz was awarded the Siempelkamp Nuclear Competence Award 2003 for his work on the behaviour of the reactor pressure vessel during a severe accident with core melt in the lower plenum.

I would like to thank H.-G. Willschütz and all the other fellow employees of ISR for their excellent work in 2003.

F.-P. Weiß

Fig. 1: Funding sources 2003

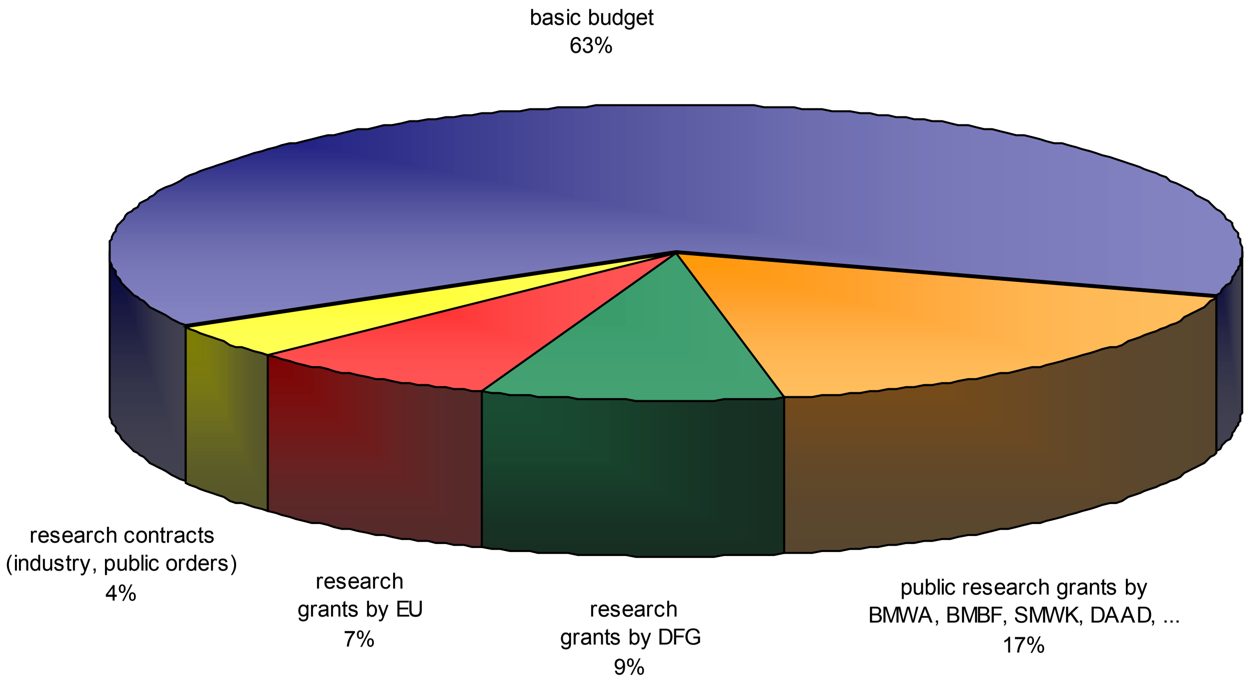

Fig 2: Deployment of funding on the tasks/projects 2003

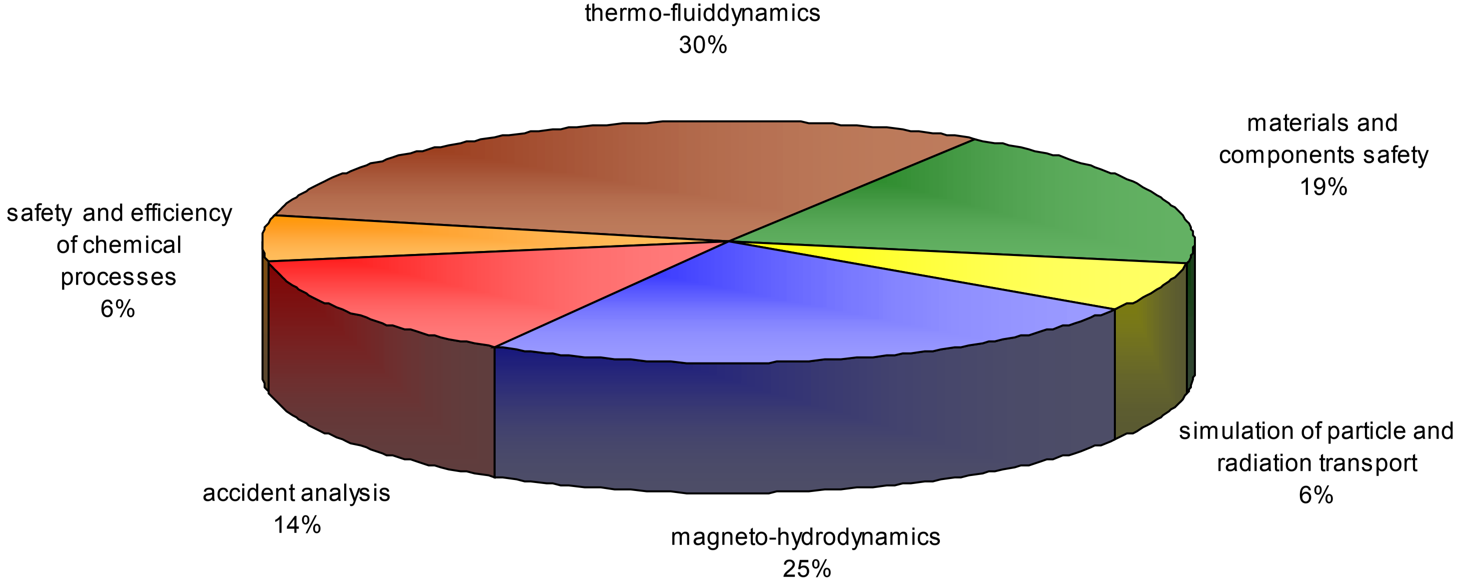

MODELLING OF NON-DRAG FORCES FOR BUBBLY FLOWS

Dirk Lucas, Jun-Mei Shi, and Eckhard Krepper

1. Introduction

Interfacial force closure is one of the central topics in Eulerian multiphase flow modelling. In vertical bubbly flow, the non-drag forces, namely the lift, wall, turbulent dispersion and added mass force, play the most important role in calculating the gas concentration distribution. These forces have a complex nature. Generally their magnitudes depend on the bubble size. Moreover, it is found that the lift force changes its sign with increasing bubble diameter [1,2]. For this reason, a wall gas peak is observed for small bubbles in comparison with a central peak for larger bubbles in vertical co-current upflows [3,4]. In an air-water system at ambient conditions, the change of the direction of the lift force in the shear field occurred at a bubble diameter of 5.8 mm. Therefore, one has to consider an inhomogeneous multi-size class model in order to correctly predict the gas distribution in a poly disperse flow [5,6].

Non-drag force models were implemented in CFX-5.6 and validated using the experimental database for air-water flow in a vertical pipe (inner diameter 51.2 mm), established at FZR using wire-mesh sensor technology. Bubble size distributions as well as radial profiles of the gas volume fraction, represented by bubbles of different size were measured. A simplified model [4] was also used to test a number of these models in an extended range of parameters.

2. Non-drag bubble forces

The non-drag forces discussed here are: lift force, wall force and turbulent dispersion force. The **lift force** considers the interaction of the bubble with the shear field of the liquid. Related on the unit volume it can be calculated as:

$$\vec{F}_L = -C_L \rho_l (\vec{w}_g - \vec{w}_l) \times rot(\vec{w}_l) \tag{1}$$

The classical lift force, which has a positive coefficient C_L , acts in the direction of decreasing liquid velocity, i.e. in case of co-current upwards pipe flow in the direction towards the pipe wall. Numerical [1] and experimental [2] investigations showed, that the direction of the lift force changes its sign, if a substantial deformation of the bubble occur. Tomiyama et al. [2] conducted investigations on single bubbles and derived a correlation for the coefficient of the lift force C_L from these experiments. This coefficient depends on the Eötvös number, which is proportional to the square of the bubble diameter. For the water-air system at normal conditions C_L changes its sign at an bubble diameter of d_b = 5.8 mm. Bubble diameter in this paper always means the equivalent bubble diameter regarding the volume of a sphere.

The **wall lubrication force**, which pushes the bubbles away from the wall, was first introduced by Antal [7]. A modified formulation was introduced by Tomiyama et al. [2]:

$$\vec{F}_W = -C_W \frac{d_{bubb}}{2} \left(\frac{1}{y^2} - \frac{1}{(D-y)^2} \right) \rho_l w_{rel}^2 \vec{n}_r \tag{2}$$

They also proposed a correlation for the coefficient, which again depends on the Eötvös number [2]. Later a modified correlation for this coefficient was published [8]. It was used in our investigations together with a bubble deformation force, introduced in [9].

The **turbulent dispersion force** is the result of the turbulent fluctuations of liquid velocity. Lahey et al. [10] derived an equation for the force per unit volume as

$$\vec{F}_{TD} = -C_{TD}\rho_l k_l \,\mathrm{grad}\,\alpha\text{, with } \mathrm{C_{TD}} = 0.1. \tag{3}$$

Burns [11] derived an equation from the fluctuations of the drag force by Favre averaging procedure (FAD model):

$$\vec{F}_{TD} = -\frac{3C_D \nu_{t,l}}{4d_b \,\mathrm{Pr}}\frac{\rho_l w_{rel}}{1-\alpha}\mathrm{grad}\,\alpha \qquad = -C_{TD}^{FAD}\rho_l k_l \,\mathrm{grad}\,\alpha, with \qquad C_{TD}^{FAD} = \frac{3C_D \nu_{t,l}}{4d_b k_l \,\mathrm{Pr}}\frac{w_{rel}}{1-\alpha} \tag{4}$$

The turbulent Prandtl number (or Schmidt number) has an order of magnitude of 1. Similar expressions were derived earlier by a number of authors, e.g. by Gosman et al. [12].

3. Validation of non-drag force models using the simplified model

The simplified model for vertical pipe flow introduced in [4] was used to test and to validate the different models for the non-drag forces. It considers a large number of bubble classes. The model bases on the assumption of an equilibrium of the non-drag forces. This assumption is valid as good approximation at the upper end of the investigated pipe. The model solves the radial profiles of liquid and gas velocities, bubble-size class resolved gas fraction profiles as well as turbulence parameters on basis of a given bubble size distribution. The Sato model [13] is used to calculate the radial profile of the liquid velocity and the turbulent viscosity required as an input for the models for the forces (see eq. (1),(4)). Because of the strong interaction between the radial profiles of the liquid velocity and the gas volume fraction, an iteration procedure is used. The model was extended to consider the dimension of the bubbles [9]. The lateral extension of the bubble is especially important for large bubbles. All equations describing the forces acting on bubbles are derived for parameters present at the position of the centre of mass of the bubble. The bubble itself is an object with a considerable extension in space, i.e. the distributions found for an equilibrium of the forces have to be transformed into gas fraction distributions by convoluting them with a geometry function characteristic for the lateral gas fraction distribution of a bubble.

Fig. 1 compares measured and calculated radial gas volume fraction profiles for selected combinations of superficial velocities. The profiles were calculated using lift and wall forces according to eq. (1) and (2) with correlations for the coefficients from Tomiyama et al. and different dispersion forces. The red curves accord to the model introduced in [4]. Here for the turbulent dispersion force eq. (3) was used. In addition an Eötvös number dependend dispersion force was introduced. It increases with the Eötvös number without any limitation, what provokes the flat profiles for large bubbles and slugs, which occur in the case of low liquid and high gas superficial velocities. Using the dispersion FAD model, eq. (4) for these points radial gas fraction profiles with pronounced peaks in the pipe centre and at wall occur (green curves). This is due to the non-considered effect of the extension of the large bubbles and slugs. By consideration of the bubble dimensions, these deviations from the measured profiles vanish (blue curves). In general the agreement between calculated and measured profiles is satisfactory despite for liquid superficial velocity of 4 m/s. Because of the strong gradient of the liquid velocity the lift force causes a pronounced wall peak in the calculation, while the measurements show an intermediate peak of the radial gas volume fraction. Investigations on bubble forces were also done for other variations of the dispersion force as well as for different wall force models.

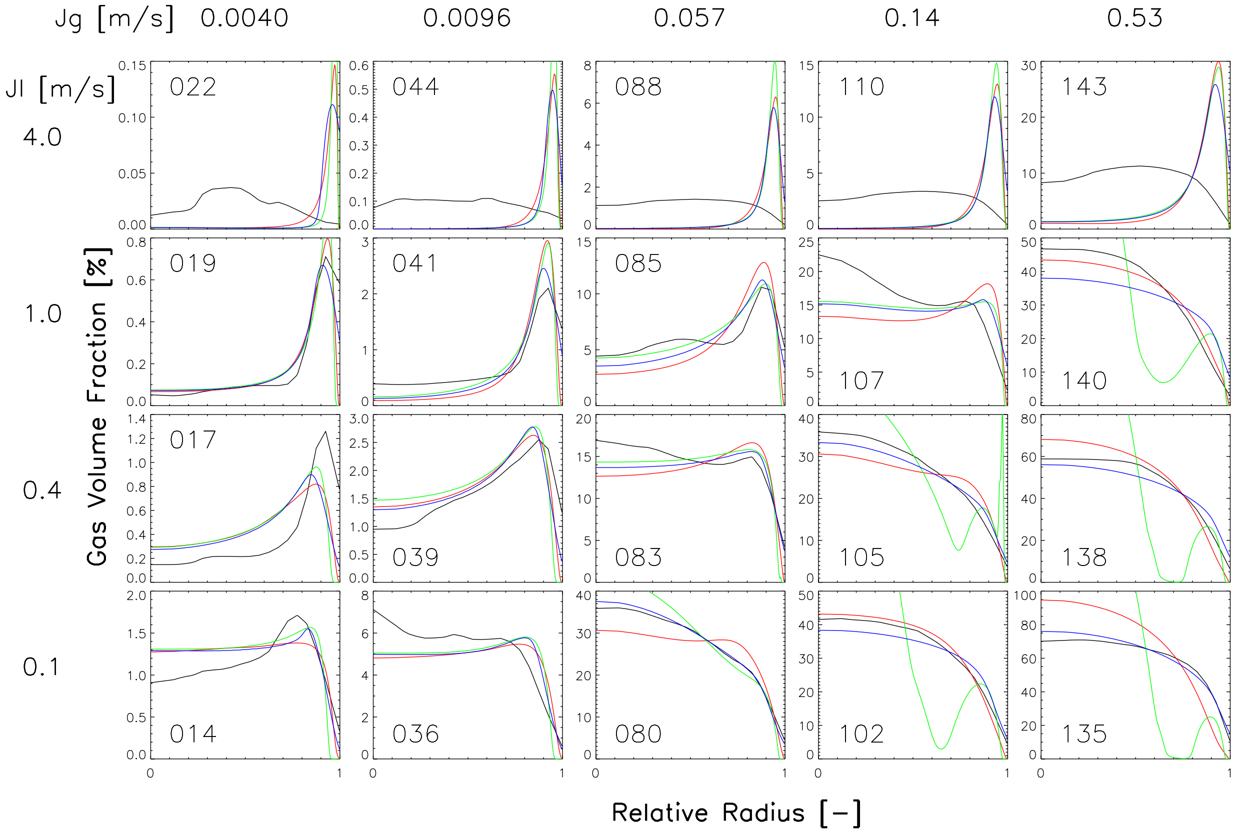

Fig. 1: Effect of different dispersion force models: ▬ *Experiment,* ▬ *model in [4],* ▬ *Eq. (4)* ▬ *Eq. (4) and consideration of bubble dimension.*

4. Implementation and validation of non-drag force models in CFX-5.6

A number of non-drag force models available in literature were implemented via CFX USER ROUTINE and CFX command language in collaboration with ANSYS CFX Germany. Moreover, detailed validations were carried out for these models using the experimental database. Based on the present work, several non-drag force models are now available in CFX-5.7. Especially, the FAD model, eq. (4) has been implemented as the default turbulent dispersion force model in CFX-5.7 Eulerian multiphase flow package [11]. Details of the work were reported in Shi et al. [14], Frank et al. [15] and Burns et al. [11]. In addition, inspired by the success of the FAD model, an alternative model derivation was provided, which bridges the Eulerian and Lagrangian approach. Concepts were also proposed to improve the turbulent dispersion force model, eq. (3) by taking into account the bubble induced turbulence.

For the validation, a number of test cases in the bubbly flow regime were defined. A computational domain consisting of a 3 degree sector of the pipe with the symmetry condition on both sector faces was applied in the simulation. The numerical simulation was based on the CFX-5.6 two-fluid model. Both fluids were assumed to be incompressible and one constant bubble diameter was assumed within the total computational domain. The Shear Stress Transport (SST) turbulence model [16] was applied to the continuous phase. Bubble induced turbulence was accounted for following the enhanced eddy viscosity model of Sato [13]. The dispersed phase turbulence was treated assuming a simple algebraic relationship between the dispersed phase and continuous phase kinematic eddy viscosities. The interfacial forces are considered by the Grace model for the drag force, the Tomiyama correlations for the lift and wall lubrication force [2], and either the FAD model or eq. (3) with C_{TD} = 0.35 for the turbulence dispersion force. The added mass force was neglected for the stationary flow considered here. Details on the convergence error, grid dependence of the results and the inlet condition effect are reported in Shi et al. [14]. Numerical results for the normalized air volume fraction profiles, defined by

$$\alpha_g^* = \frac{\alpha_g}{\alpha_{g,0}}, \text{ with } \quad \alpha_{g,0} = 2\int_0^1 \alpha_g(r^*) r^* dr^* \tag{5}$$

were compared against the wire-mesh measurement data at L/D = 59.2 (Fig. 2). It can be observed that all numerical results based on the FAD model agree fairly well with the experimental data. It is observed from Fig. 2 that the gas volume fraction obtained using eq. 3 is consistently lower in the core region than those based on the FAD model (eq. 4). This indicates a stronger turbulence dispersion force given by the latter. The FAD model leads to much better agreements with the experimental data in certain cases, such as FZR-074, though the core gas concentration is still underpredicted. This deviation can be reduced by using two fluids for the gas phase, namely separating the larger bubbles (negative lift force) from the small ones. This will be the subject of future investigation.

Fig. 3 shows the the corresponding turbulence dispersion force coefficient of the FAD model C_{TD}^{FAD} (see eq. 4). The results clearly show that the turbulent dispersion force given by eq. 3 is much too weak, except in the near-wall region. Moreover, Fig. 3 also shows that a constant coefficient C_{TD} as assumed in eq. 3 is not realistic. In addition, it is interesting to note that C_{TD} decreases with increasing superficial velocity of the continuous phase. This is because the bubble response time τ_d is similar for all test cases due to their similar d_p, whereas the turbulence time scale τ_t decreases with increasing flow Reynolds numbers.

Table 1: Test cases used for the validation

No.	J_L [m/s]	J_G [m/s]	d_b [mm]	No.	J_L [m/s]	J_G [m/s]	d_b [mm]
017	0,405	0,0040	4,8	040	0,641	0,0096	4,6
019	1,017	0,0040	4,8	041	1,017	0,0096	4,5
038	0,255	0,0096	4,3	042	1,611	0,0096	3,6
039	0,405	0,0096	4,5	074	1.017	0,0368	4.5

5. Conclusions

A number of non-drag force models were implemented in CFX-5.6. Careful validations were carried out based on FZR MTLOOP experimental data base. The FAD Model has been shown to lead to better agreements with the measurement data for most of the test cases and to be numerically more robust than the model given by eq. (3). Consequently, it has been implemented as the default model of choice for turbulence dispersion in CFX-5.7.

Acknowledgements

This work is the result of a strong collaboration between Forschungszentrum Rossendorf and ANSYS-CFX Germany. Financial support is gratefully acknowledged from the Ministry of Economy and Labour (BMWA) of Germany in the project “TOPFLOW – Transient two phase flow test facility for generic investigation of two-phase flows and further development and validation of CFD codes”.

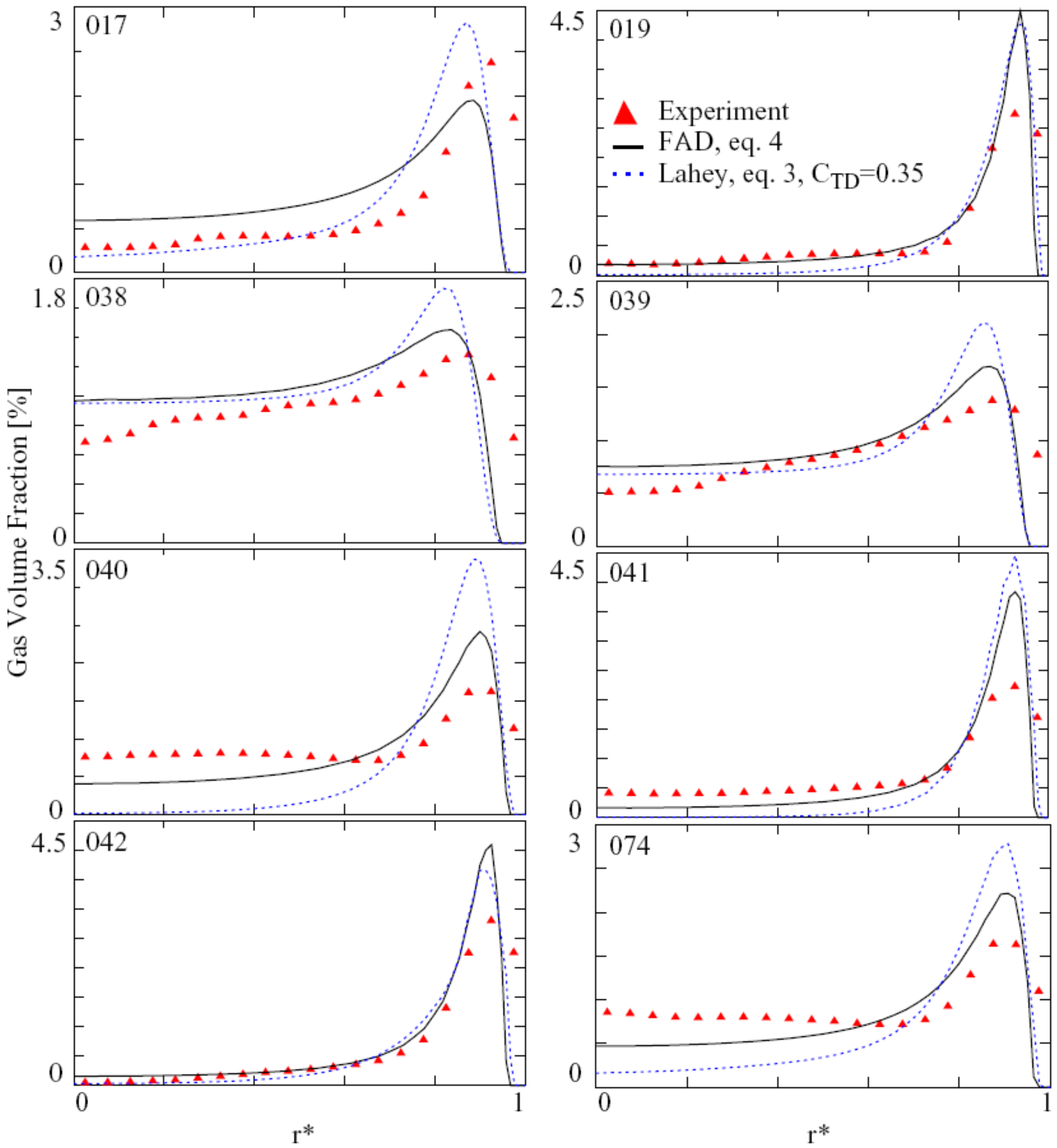

Fig. 2: Comparisons between FAD model (eq.4) and eq. 3 for the test cases defined in Tab. 1.

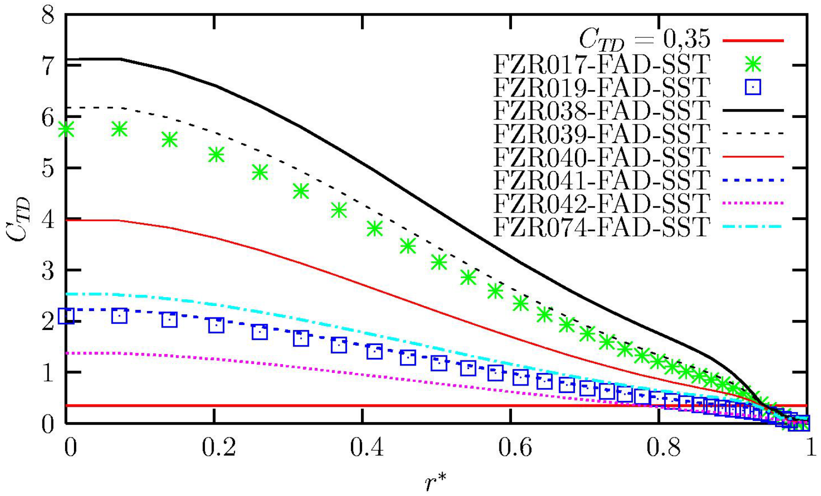

Fig. 3: Equivalent C_{TD} coefficient of FAD model in comparison with constant coefficient eq. 3.

References

[1] E.A. Ervin, G. Tryggvason, The rise of bubbles in a vertical shear flow, Journal of Fluids Engineering, vol. 119, pp. 443-449, 1997.

[2] A. Tomiyama, A. Sou, I. Zun, N. Kanami, T. Sakaguchi, Effects of Eötvös number and dimensionless liquid volumetric flux on lateral motion of a bubble in a laminar duct flow, Advances in Multiphase Flow, pp. 3-15, 1995.

[3] H.-M. Prasser, E. Krepper, D. Lucas, Evolution of the two-phase flow in a vertical tube - decomposition of gas fraction profiles according to bubble size classes using wire-mesh sensors, Int. J. of Thermal Sciences, vol. 41, pp. 17-28 (2002).

[4] D. Lucas, E. Krepper, H.-M. Prasser, Prediction of radial gas profiles in vertical pipe flow on basis of the bubble size distribution, International *J. of Thermal Sciences*, vol. 40, pp. 217-225, 2001.

[5] D. Lucas, E. Krepper, H.-M. Prasser, Modelling of bubble flow in vertical pipes, The 10th Int. Topical Meeting on Nuclear Reactor Thermal Hydraulics (NURETH-10), Seoul, Korea, paper A00301, 2003.

[6] J.-M. Shi, E. Krepper, D. Lucas, U. Rohde, Some concepts for improving the MUSIG model. Internal note Forschungszentrum Rossendorf, March 2003

[7] S.P. Antal, R.T. Lahey, J.E. Flaherty, Analysis of phase distribution in fully developed laminar bubbly two-phase flow, *Int. J.l of Multiphase Flow*, vol. 7, pp. 635-652, 1991.

[8] S. Hosokawa, A. Tomiyama, S. Misaki, T. Hamada, Lateral migration of single bubbles due to the presence of wall, *Proceedings of ASME Fluids Engineering Division Summer Meeting*, Montreal, Ouebec, Canada, 2002.

[9] D. Lucas, J.-M. Shi, E. Krepper, H.-M. Prasser, Models for the forces acting on bubbles in comparison with experimental data for vertical pipe flow, 3rd International Symposium on Two-Phase Flow Modelling and Experimentation, Pisa, Italy, September 22-24, 2004

[10] R.T. Lahey, M. Lopez de Bertodano, O.C. Jones, Phase distribution in complex geometry conduits, Nuclear Engineering and Design, vol. 141, pp. 177-201, 1993.

[11] A.D. Burns, T. Frank, I. Hamill, J.-M. Shi, The favre averaged drag model for turbulence dispersion in Eulerian multi-phase flows, *5th Int. Conf. on Multiphase Flow,* Paper No. 392, *ICMF'2004*, Yokohama, Japan, 2004.

[12] A.D. Gosman, C. Lekakou, S. Politis, R.I. Issa, M.K. Looney, Multidimensional modeling of turbulent two-phase flow in stirred vessels, AIChE Journal, vol. 38, pp. 1946-1956, 1992.

[13] Y. Sato, M. Sadatomi, K. Sekoguchi, Momentum and heat transfer in two-phase bubble flow-I, *Int. J. of Multiphase Flow*, vol. 7, pp. 167-177, 1981.

[14] J.-M. Shi, Th. Frank, E.Krepper, D. Lucas, U. Rohde, H.-M. Prasser, Implementation and validation of non-drag interfacial forces in CFX-5.6, *5th Int. Conf. on Multiphase Flow,* Paper No. 400, *ICMF'2004*, Yokohama, Japan, 2004.

[15] Th. Frank, J.-M. Shi, A. Burns, Validation of Eulerian multiphase flow models for nuclear safety applications, 3rd Int. Symposium on Two-Phase Flow Modeling and Experimentation, Pisa, Italy, September 22-24, 2004.

[16] F.R. Menter, Two-equation eddy-viscosity turbulence models for engineering applications, *AIAA-Journal*, Vol. 32, No. 8., 1994.

CFD SIMULATION OF BUOYANCY DRIVEN MIXING BY USING THE CODE TRIO_U WITH LARGE EDDY SIMULATION

Thomas Höhne and Ulrich Bieder[1]

1. Introduction

During emergency core cooling the higher density of the Emergency Core Cooling (ECC) water forms a plum of cold water flowing downwards the downcomer. This can cause thermal loads on the reactor pressure vessel (RPV). Additionally, in the case of inadvertent injection of low borated ECC water, a boron dilution transient would be initiated.

To make realistic predictions about the consequences it is necessary to study the coolant mixing, which is a complicated three-dimensional fluid dynamic problem. Modern CFD codes running on powerful computers became available to model the coolant flow in the complex geometry of a PWR a couple of years ago. Due to the high safety relevance of the coolant mixing phenomenon it is necessary to validate computer codes and to verify computational results using experimental data.

In order to study coolant mixing under these conditions inside the RPV of a German type PWR the test facility ROCOM (**Ro**ssendorf **Co**olant **M**ixing Model) was used. Within a co-operation with CEA Grenoble the TRIO_U code was applied for a Large Eddy Simulation (LES) of density driven flow and mixing phenomena.

2. The ROCOM Test Facility

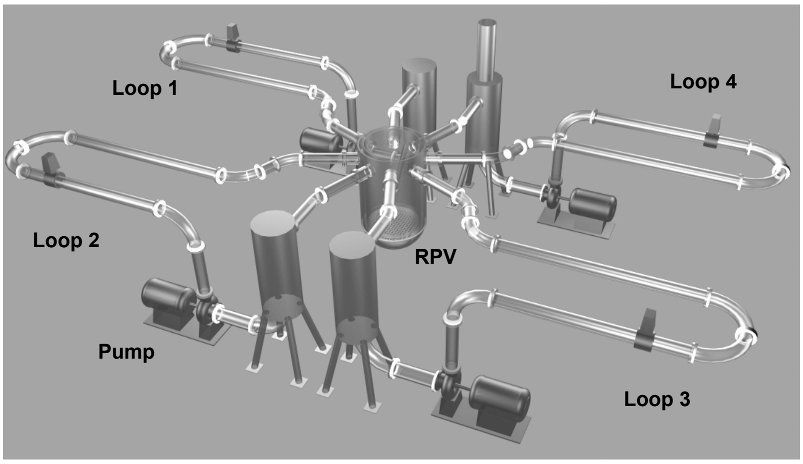

Fig. 1: Coolant Mixing Test Facility ROCOM

ROCOM is a 1:5 scaled 4-loop model of a German Konvoi pressurized water reactor. There are controllable pumps (Fig. 1) in each of the loops so that flow regimes can be simulated from natural coolant circulation to nominal flow conditions [1]. Beginning from the bends in the cold legs, which are close to the reactor inlet, the geometrical similarity between model and original reactor is respected until the core inlet. The RPV model is manufactured from Plexiglas$^{©}$. In case of the experiments on ECC injection, an injection nozzle was used, which was geometrically similar to the original Konvoi reactor. The higher density of the cold ECC water was simulated by adding sugar (glucose), since density gradients cannot be created by temperature differences, because the facility cannot be heated up. Fortunately, the viscosity of glucose solution becomes large only at concentrations, where the relative density increase is well above the 10 % necessary for the experiments. A sugar solu-

---

[1] CEA Grenoble, France

tion with the corresponding density of 1100 kg/m^3 has a viscosity, which is still just by factor of about 3 higher than that of pure water. The tracer can therefore still be envisaged as a low-viscous fluid.

The test facility is equipped with advanced instrumentation [2], which delivers high-resolution information characterizing either temperature or boron concentration fields in the investigated pressurized water reactor.

3. The Buoyancy Driven Experiment

The goal of the experiment was the generic investigation of the influence of density differences between the primary loop inventory and the ECC water on the mixing in the downcomer. To separate the density effects from the influence of other parameters, a constant flow in the loop with the ECC injection nozzle was assumed in this study. The volume flow rate of the ECC injection system was kept constant at 1.0 l/s. For the comparison with Trio_U an experiment with constant flow rate of 5% of nominal flow in one loop (magnitude of natural circulation) and 10% density difference between ECC and loop water was taken (Table 2). According to the classification of mixing provided in [1] based on the Froude number, it was identified as density dominated mixing .

Table 1: Experiment chosen for code validation

$\dot{V}$ (ECCS) / [m^3/h]	$\dot{V}$ (Cold Leg) / [m^3/h]	Density difference Loop Inventory / ECC water [kg/m^3]/[kg/m^3]	Fr (Downcomer) [-]
3.6	9.25	1:1.1	1.62

4. The Trio_U Code

Within the Trio_U project, a thermal hydraulic code for strongly unsteady low Mach number, single phase turbulent flows is under development at the CEA-Grenoble, which is especially designed for industrial LES on structured and non-structured grids of several tens of millions of nodes [3]. The platform independent code is based on an object oriented, intrinsically parallel approach and is coded in C++. The flexible code structure allows the user to choose a suitable discretization method and to combine various appropriate physical models. Several convection and time marching schemes as well as a wide range of boundary conditions are available. This flexibility is implemented without a reduction of the overall performance of the code.

For unstructured grids, the hybrid « Finite Volume based Finite Element » method (VEF) is applied. This method consists in determining for a continuous problem a discrete solution in the space of the finite element by maintaining the balance notation of finite volumes. The space discretization is performed with triangles in 2-dimensional case and with tetrahedral cells in 3-dimensional case. In Trio_U, the main unknowns velocity and temperature are located in the center of the faces of an element (triangle or tetrahedron) whereas the pressure is discretized in the center and in the vertices of the element (staggered mesh) in order to improve the velocity/pressure coupling for LES applications.

5. Grid Generation and Boundary Conditions

This meshing has been generated from the CAD model using the mesh generator ICEM-CFD TETRA. For this study, a LES approach was used for mesh sizes between 1–2 million control volumes.

Solid walls bound the fluid domain, an outlet boundary was put at the position above the core support plate. The cold leg CL1 (see Fig. 2) including the ECC injection line was modeled. Inlet boundary conditions were put at the ECC line and at the area after the bend of the cold leg CL1. At the outlet, a free outflow condition with a constant pressure was used. For the solid walls, standard wall functions were applied for both momentum and temperature transport equation. The velocities in the idle loops were defined as zero. The ECC injection lasts 10 s. A uniform velocity profile was defined at the injection line during this period. The tracer injection was simulated by the help of a scalar field, which was defined to be unity in the cold leg CL 1 and zero at the ECC injection line.

The Boussinesq approximation (1) was used to model the effect of density differences.

$$\frac{\rho}{\rho_0} = 1 - \beta\left(T - T_0\right) \tag{1}$$

6. Results

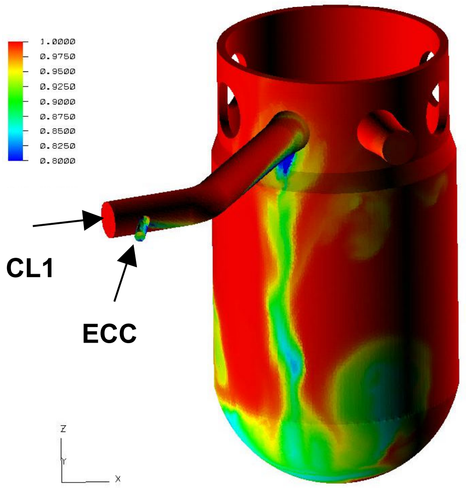

Fig. 2: Mixing in the downcomer (23s)

Both, the experiment and the Trio_U calculation show qualitatively the same flow and mixing behavior.

In the cold leg the ECC water only partly mixes with the loop inventory. A clear stratified flow is developing during the injection. At the upper downcomer sensor position, the ECC water appears directly below the inlet nozzle.

At the beginning, the covered area in the downcomer is bigger, because the momentum driven flow field of CL1 (mass flow rate of 5% of nominal flow rate) is still present. After this, the density difference partly suppresses the propagation of the ECC water in circumferential direction. The ECC water falls down in an almost straight streamline (Fig. 2) and reaches the lower downcomer sensor directly below the affected inlet nozzle (Fig. 3). The well mixed ECC water in the lower plenum is directed upwards towards the core by the impact of the perforated drum. As a result, the well mixed ECC water at the core inlet arrives also in the sector below the inlet nozzle CL1 (Fig. 4).

Only later, coolant containing ECC water appears at the opposite side of the lower downcomer area and occurs also at the opposite part of the core inlet.

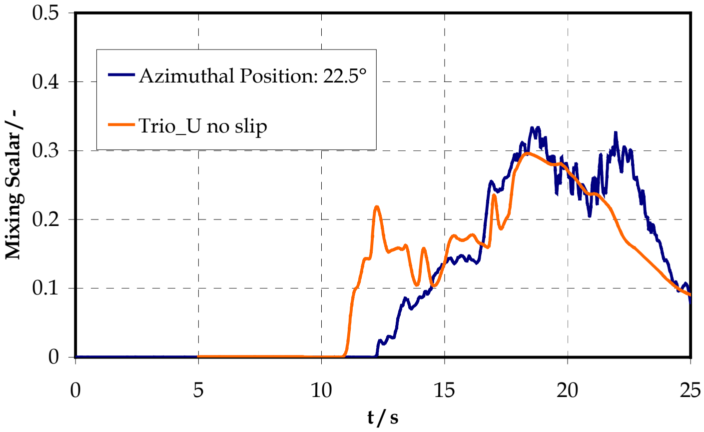

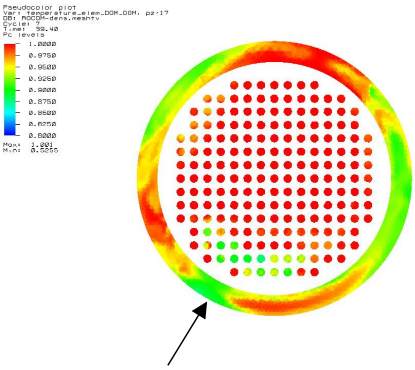

Fig. 3: Time dependent ECC water distribution in the upper downcomer below the loop CL1

Fig. 4: ECC water distribution at the core inlet (27s)

7. Conclusion

A generic investigation of the influence of density differences between the primary loop inventory and the ECC water on the mixing in the downcomer was made at the ROCOM Mixing Test Facility at Forschungszentrum Rossendorf (FZR). For the validation of the Trio_U code an experiment with 5% constant flow rate in one loop (magnitude of natural circulation) and 10% density difference between ECC and loop inventory was taken. The study showed, that density effects play an important role during natural convection with ECC injection in pressurized water reactors. Furthermore it was important to point out, that Trio_U is able to cope the main flow and mixing phenomena.

References

[1] H.-M. Prasser, G. Grunwald, T. Höhne, S. Kliem, U. Rohde, F.-P. Weiss, Coolant mixing in a Pressurized Water Reactor: Deboration Transients, Steam-Line Breaks, and Emergency Core Cooling Injection, Nuclear Technology 143 (1), p.37, 2003.

[2] H.-M. Prasser, J. Zschau, D. Peters, G. Pietzsch, W. Taubert, M. Trepte: Fast wire-mesh sensors for gas-liquid flows - visualisation with up to 10 000 frames per second, International Congress on Advanced Nuclear Power Plants (ICAPP), June 9-13, 2002 - Hollywood Florida, USA, paper 1055.

[3] Bieder U., Ch. Calvin, H. Mutelle : Detailed Thermal Hydraulic Analysis of Induced Break Severe Accidents Using the Massively Parallel CFD Code Trio_U/PRICELES . Supercomputing in Nuclear Applications, Paris 2003

SCALING EFFECTS OF THE TWO-PHASE FLOW IN VERTICAL PIPES - NEW RESULTS OF TOPFLOW

Horst-Michael Prasser, Matthias Beyer, Helmar Carl, and Peter Schütz

Introduction

In autumn 2002 the Institute of Safety Research of Forschungszentrum Rossendorf e.V. has commissioned the new thermal-fluiddynamic test facility TOPFLOW. The first tests carried out in a vertical pipe of 194.1 mm diameter have shown that a region of well-organized slug flow is no more observed in pipes of such large diameters [1]. This confirms the findings of Ohnuki [2], who reported, that slug flow which is established in small pipes, is not found in larger pipes. In the meanwhile, more experiments were carried out at the TOPFLOW facility. Special attention was paid to the influence of the gas injection. The primary bubble size has a deciding influence on the appearance of the wall peak in the radial void fraction profiles. The present paper gives an overview on experiments which were dedicated to this phenomenon.

Test section DN 200

The test pipe has an inner diameter of 194.1 mm and a total height of 9 m. Close to the lower end a gas injector is located (Fig. 1). A tube is bend into the main flow direction, forming a coaxial segment. A gas injection head is screwed on top of this tube. In order to study the influence of the primary bubble size, two different gas injection heads were used in the experiments described here. Gas injection head A (Fig. 2) has a perforation consisting of three rings, each with 20 orifices of 6 mm diameter. Above the perforated region there is a conical part in order to reduce the formation of vortices due to flow separation effects.

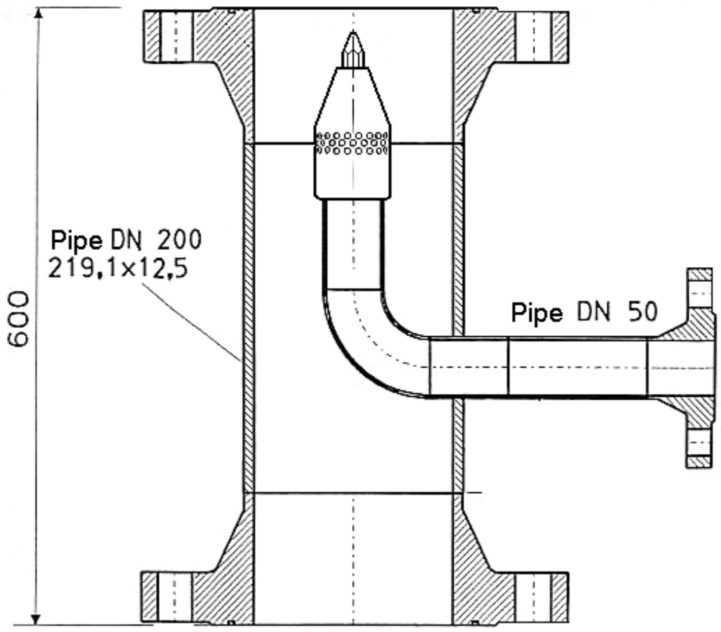

Fig. 1: Gas injection device in the DN200 test pipe

The second injection head B is shown in Fig. 3. Instead of the large orifices directly drilled into the wall of the head, 16 small steel tubes with gas injection orifices of 0.8 mm diameter are radially welded to the gas injection head. The total number of orifices is 152. Each second radial tube has 12 orifices, the other half of the tubes has 7 orifices each.

Two wire-mesh sensors were used for the measurements, each comprising a matrix of 64x64 measuring points that are scanned at 2500 Hz (Fig. 4). The large number of electrode wires allows to achieve a resolution of 3 mm in the entire cross section. The sensor is mounted into a flange connection 1000 mm below the upper end of the test section. The distance between gas injection and the measuring plane of the wire-mesh sensor was L_{wms} = 7660 mm.

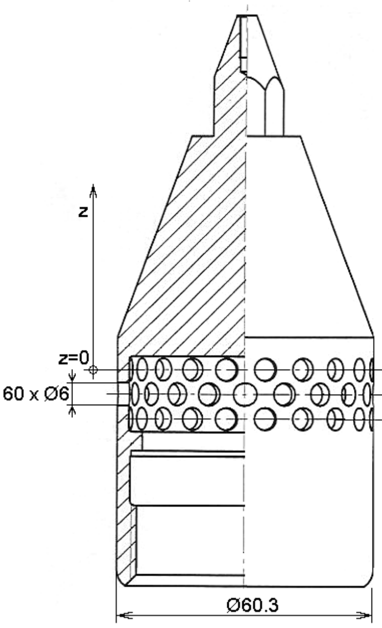

Fig. 2: Gas injection head type A

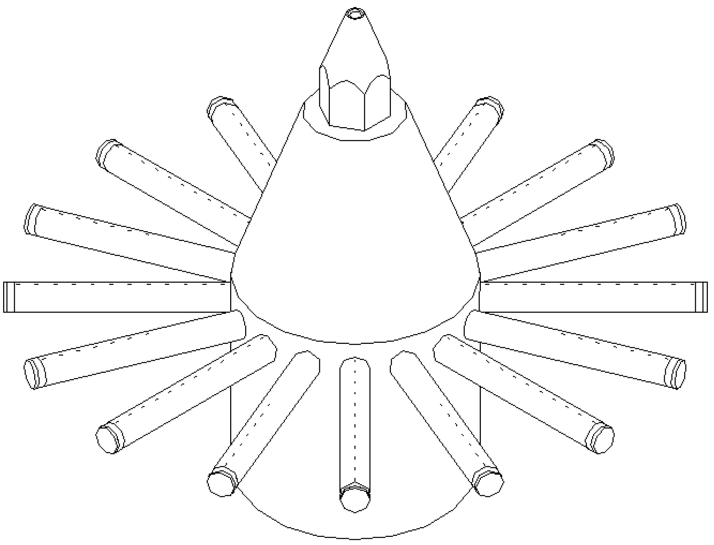

Fig. 3: Gas injection head type B

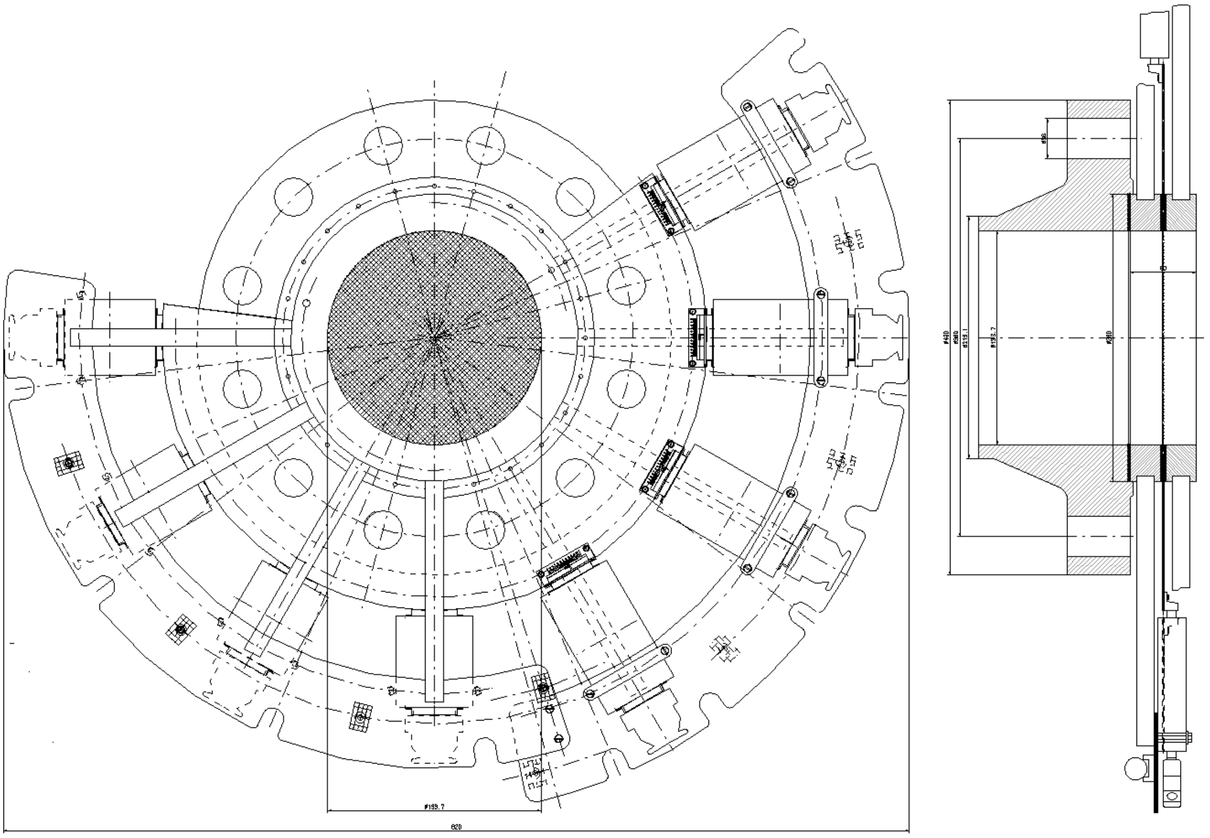

Fig. 4: Wire-mesh sensor for the DN200 test pipe with a measuring matrix of 64x64 points

Appearance of a wall peak in the gas fraction profiles

Gas fraction profiles were obtained from the high-resolution wire-mesh data by averaging over a measuring period of 10 s and over the circumference at different radial positions. Profiles measured for different superficial gas velocities at a constant liquid flow rate are shown in Fig. 5. In case of gas injection through the orifices of 6 mm, all distributions show a central peak. This was found for the entire studied range of superficial velocities ($0.0025 \leq J_G \leq 4.98$ m/s, $0.102 \leq J_L \leq 1.61$ m/s). The profiles show some distortions close to the centre of the pipe, which are still reflecting the rather complicated geometry of the gas injection device. They are probably caused by the wake generated by the gas injection head. In the large pipe a wall peak appeared only in tests with the gas injection geometry B (Fig. 5, right side). It vanishes when a certain superficial air velocity is exceeded.

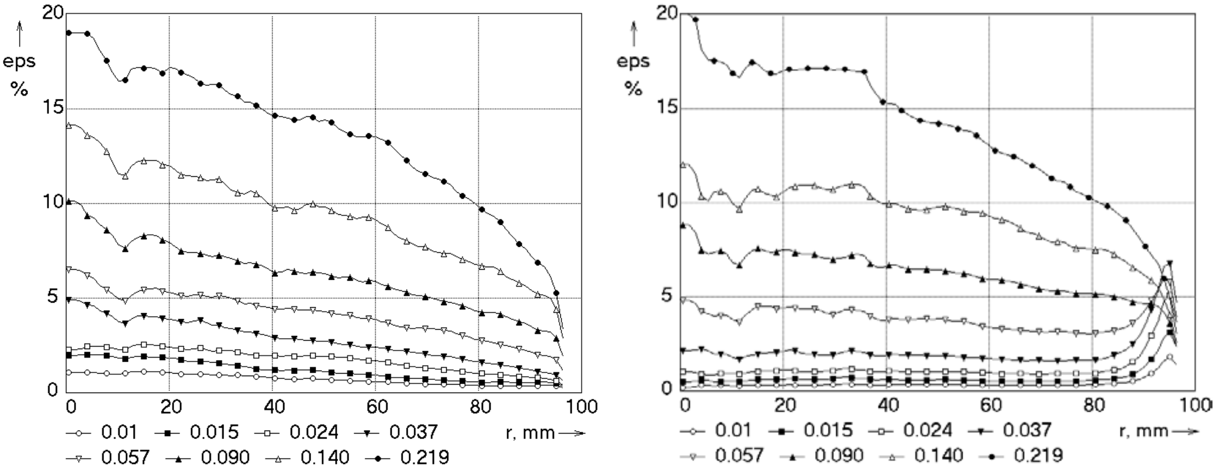

Injection geometry A (60 orifices, ∅ 6 mm)

Injection geometry B (152 orifices, ∅ 0.8 mm)

Fig. 5: Radial gas fraction profiles in the 194.1 mm pipe $J_L = 1,02$ m/s, varied parameter: J_G, m/s, L/D = 39.2

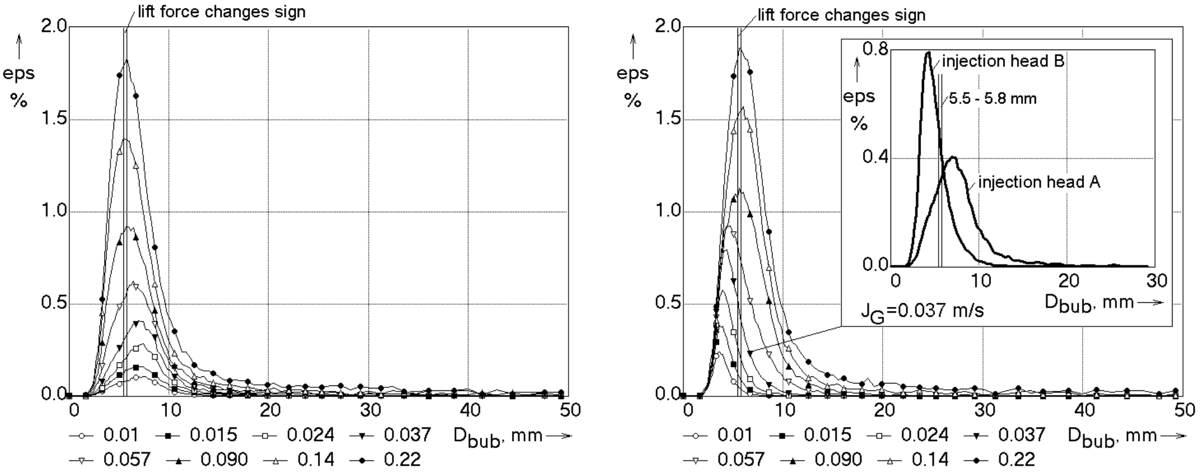

Injection geometry A (60 orifices, ∅ 6 mm)

Injection geometry B (152 orifices, ∅ 0.8 mm)

Fig. 6: Bubble size distributions (part of gas fraction represented by a given bubble size class) in the 194.1 mm pipe, $J_L = 1,02$ m/s, varied parameter: J_G, m/s, L/D = 39.2

The measured bubble size distributions (for details see [3]) explain the reason for the wall peak appearance (Fig. 6): in this case most of the gas fraction is still found in bubbles with an equivalent diameter less than 5.5 - 5.8 mm, which is the characteristic diameter for the change of the sign of the lift force according to Tomiyama [4]. For bubbles smaller than this diameter, the lift force points towards the wall and is therefore responsible for the appearance of the wall peak.

As it can be seen from Fig. 6, the vanishing of the wall peak with growing superficial gas velocity corresponds with a shift of the peak in the bubble size distribution towards larger bubble diameters. In case of the gas injection head A, most of the bubbles is bigger than 5.5 - 5.8 mm, consequently a wall peak is not observed.

The wall peak disappears also with decreasing liquid velocity, as shown in Fig. 7. This is mainly due to the fact that the liquid velocity gradient decreases with decreasing liquid flow rate. As a consequence the lift force decreases, since it is proportional to the local gradient of the liquid velocity. At a certain point, the lift force is no more sufficient to create the wall peak. A second tendency is again connected with the bubble size. Since the gas fraction grows with decreasing superficial liquid velocity (at a constant air injection rate), the bubble size increases and more bubbles exceed the critical diameter for the lift force inverse.

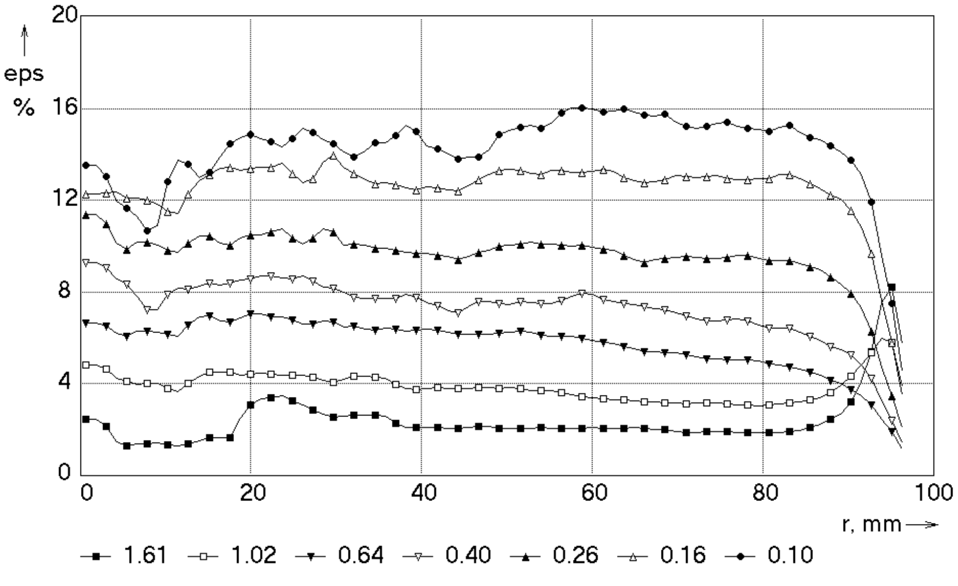

Fig. 7: Radial gas fraction profiles in the 194.1 mm pipe, $J_G = 0.057$ m/s varied parameter: J_L, m/s, injection geometry B (152 orifices, ∅0.8 mm)

The global situation is shown in Fig. 8, where the occurrence of the wall peak is mapped as a function of both gas and liquid superficial velocities. The wall peak is observed in a region that is bordered towards high superficial gas velocities and low superficial liquid velocities. This behaviour is well-known from studies of two-phase flow in small pipes. In earlier studies of our own [5] performed in a pipe of 51.2 mm at the test facility MTLoop, we found a wall peak, too, when the air was injected through 19 capillaries of 0.8 mm inner diameter (see also Fig. 8). However, the wall-peak region was significantly extended towards lower superficial liquid velocities. We believe that this is mainly explained by the fact that the liquid velocity gradient is greater in a small pipe compared to a large pipe with the same superficial liquid velocity.

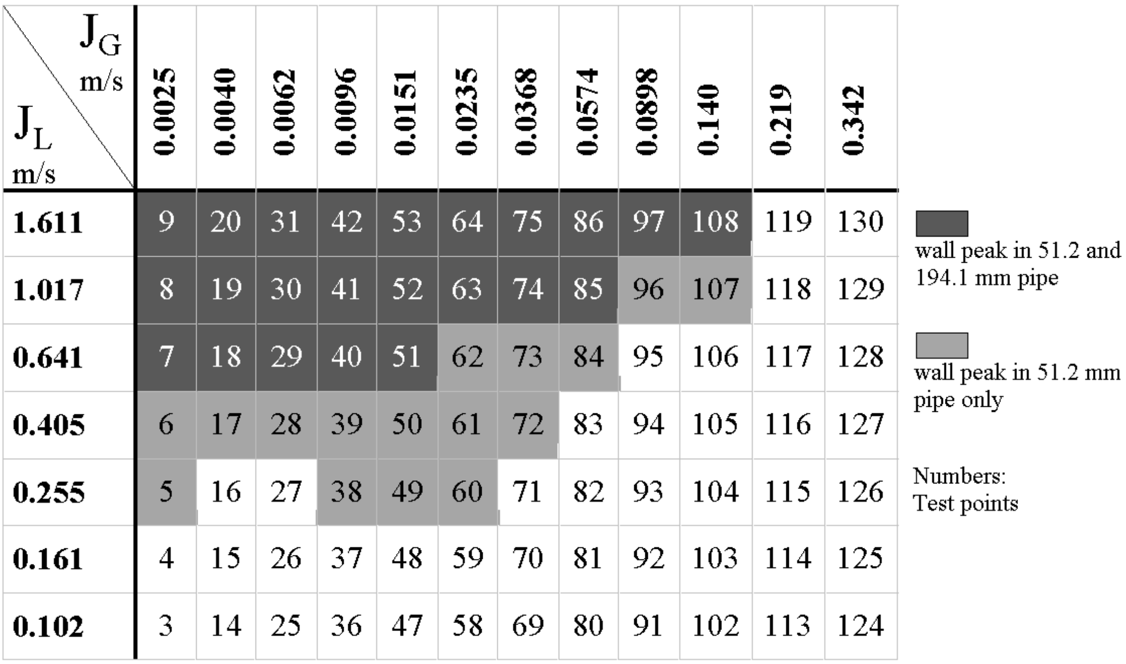

J_G m/s \ J_L m/s	**0.0025**	**0.0040**	**0.0062**	**0.0096**	**0.0151**	**0.0235**	**0.0368**	**0.0574**	**0.0898**	**0.140**	**0.219**	**0.342**
1.611	9	20	31	42	53	64	75	86	97	108	119	130
1.017	8	19	30	41	52	63	74	85	96	107	118	129
0.641	7	18	29	40	51	62	73	84	95	106	117	128
0.405	6	17	28	39	50	61	72	83	94	105	116	127
0.255	5	16	27	38	49	60	71	82	93	104	115	126
0.161	4	15	26	37	48	59	70	81	92	103	114	125
0.102	3	14	25	36	47	58	69	80	91	102	113	124

■ wall peak in 51.2 and 194.1 mm pipe

▨ wall peak in 51.2 mm pipe only

Numbers:
Test points

Fig. 8: Flow map indicating the appearance of a wall peak in the radial gas fraction profiles for pipes of 51.2 mm and 194.1 mm diameter (gas injection orifices: ∅0.8 mm)

The data recorded by the wire-mesh sensors allow to obtain gas fraction profiles, which are decomposed according to bubble-size classes [6]. In Fig. 9 the result of such an analysis is given for a test point which is characterized by a wall peak when the injection head B was used (see Fig. 5). It is clearly visible that the wall peak is caused by the bubbles of an equivalent diameter below 5.5 mm (Fig. 9, right side). Bubbles bigger than 12.5 mm were hardly found in this test. At the same superficial velocities, injection head A produces a central gas fraction peak. Nevertheless, bubbles of an equivalent diameter of less than 5.5 mm still form a wall peak (Fig. 9, left side).

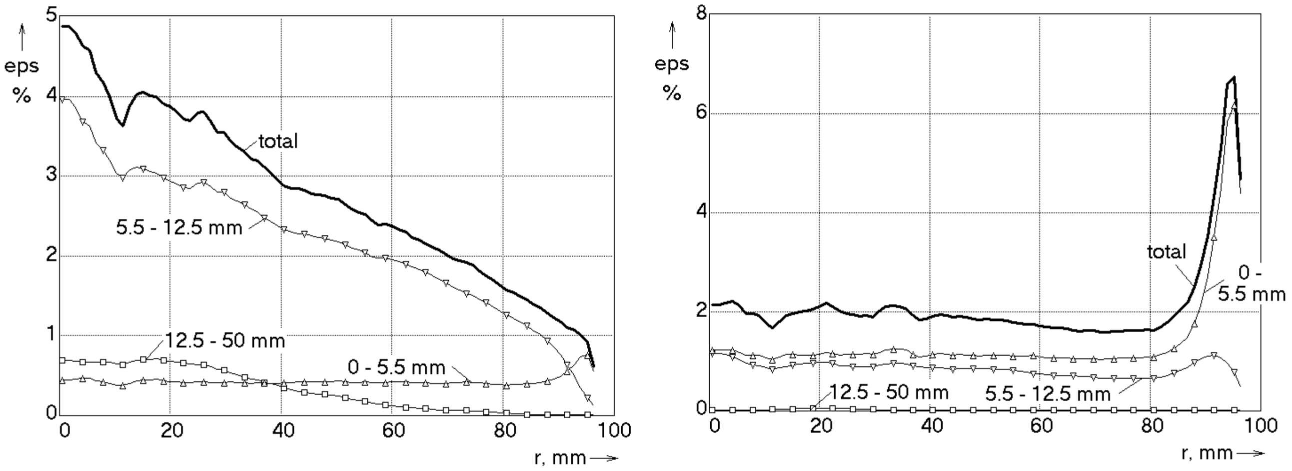

Injection geometry A (60 orifices, ∅ 6 mm) Injection geometry B (152 orifices, ∅ 0.8 mm)

Fig. 9: Radial gas fraction profiles decomposed according to bubble-size classes D_{pipe} = 194.1 mm, pipe, J_L = 1.02 m/s, J_G = 0.037 m/s, L/D = 39.2, parameter: range of equivalent bubble diameters

Conclusions

Scaling effects were found in an upwards gas-liquid flow concerning the appearance of a wall peak in the radial gas fraction profiles. It was shown that the appearance of wall peaked gas fraction profiles depends on the primary bubble size, which is determined by the geometry of the gas injection device. Nevertheless, the region in which a wall peak is observed is shifted towards higher liquid velocities for large diameter pipes. The technique of obtaining bubble-size class resolved radial gas fraction profiles allowed to demonstrate, that there is a wall peak of small bubbles even in case of a missing wall peak in the total gas fraction profile.

Nomenclature

Sign	Unit	Denomination
D	m	diameter
eps	%	void fraction
J	m/s	superficial velocity
L	m	length
r	m	radius

Subscripts and abbreviations	
bub	bubble
G	gas (air)
DN	nominal diameter
L	liquid (water)
wms	wire-mesh sensor

References

[1] H.-M. Prasser, M. Beyer, A. Böttger, H. Carl, D. Lucas, A. Schaffrath, P. Schütz, F.-P. Weiss, J. Zschau, Influence of the pipe diameter on the structure of the gas-liquid interface in a vertical two-phase pipe flow, NURETH-10, Seoul, October 5-9, 2003, paper A00308.

[2] A. Ohnuki, H. Akimoto, Experimental study on transition of flow pattern and phase distribution in upward air-water two-phase flow along a large vertical pipe, International Journal of Multiphase Flow, 26(2000)367-386.

[3] H.-M. Prasser, D. Scholz, C. Zippe, Bubble size measurement using wire-mesh sensors, Flow Measurement and Instrumentation, 12/4, pp.299-312, 2001.

[4] Tomiyama, A., Struggle with computational bubble dynamics, in: Proceedings of Third International Conference on Multiphase Flow, ICMF 98, Lyon, France, June 8-12, 1998.

[5] A.-K. Krüssenberg, H.-M. Prasser, A. Schaffrath, A new criterion for bubble slug transition in vertical tubes, Kerntechnik, 65/1(2000), pp. 7-13.

[6] H.-M. Prasser, E. Krepper, D. Lucas, Evolution of the two-phase flow in a vertical tube - decomposition of gas fraction profiles according to bubble size classes using wire-mesh sensors, International Journal of Thermal Sciences, 41 (2002) 17-28.

Acknowledgement

The work is carried out in the frame of a current research project funded by the German Federal Ministry of Economics and Labour, project number 150 1265.

The authors expresses special gratitude to the technical team of the TOPFLOW facility, by name Klaus Lindner, Heiko Pietruske, Heiko Rußig, Marko Tamme und Steffen Weichelt.

Electronic equipment for wire-mesh sensors was developed in a close co-operation with TELETRONIC GmbH in Rossendorf (www.tz-rotech.de/teletronic/).

NEW CONCEPTS FOR GAMMA-TOMOGRAPHY DETECTORS

André Bieberle, Eckhard Schleicher, and Uwe Hampel

1. Introduction

In the past years a gamma tomography measurement system has been developed at the Institute of Safety Research and applied within three projects to the visualization and analysis of stationary two-phase flow structures in hydrodynamic systems. In 2000 the tomography setup was installed at a pump test facility at Dresden University of Technology to investigate the mechanisms of two-phase flows in an impeller of an axial pump [1]. In a subsequent industrial project the same system was used to visualize fluid distributions in a hydrodynamic test coupling under operating conditions [2]. Recently, the tomograph has been used for a principle study of the void distribution measurement in nuclear fuel element bundles in a pressure vessel. The tomograph operates with an isotopic radiation source (Cs-137, 180 GBq) and a 64 element detector arc with BGO crystals and photomultiplier tubes for scintillation light detection. The system further comprises a rotational stage to move source and detector about the object of investigation and a pulse counting and energy discriminating electronics that is controlled by a measurement PC. The detector arc with elements of 1 cm x 1 cm active area is sufficiently dimensioned for the problems that have so far been investigated, yet it turned out that many potential applications would definitely require a higher spatial resolution as well as a higher robustness in harsh environments. Thus, the photomultiplier tubes are at the moment the limiting factor, since they are bulky, expensive, fragile, and susceptible to strong magnetic fields. Therefore we investigated new detector concepts for an improved gamma tomography detector arc based on the application of semiconductor photodiodes in combination with fast and high optical gain scintillator crystals made of lutetium orthosilicate (Lu_2SiO_5) [3]. In an experimental study we investigated different types of photodiodes, crystals, optical couplings and electronic processing circuits. As a result of the study we propose a new modular detector type with LYSO scintillators, avalanche photodiode and an analog signal processing unit based on an integrated circuit (IC).

2. Scintillation Detectors with Photodiodes

Fig. 1 shows the principal design of a scintillation detector with photoelectric conversion by a photodiode. First, a crystal with high scintillation light output and a good spectral fit to the photodiode's characteristic is required. By interacting with the atoms of the crystal lattice a γ-quant generates a number of optical photons depending on its energy. These photons are subsequently converted to electrons by the photodiode. Photodiodes, other than cathodes of photomultiplier tubes, typically have their spectral response maximum in the near infrared range, thus a crystal with low optical photon energy is required. Other important parameters of the crystal are its absorption lengths, the timing characteristics (fast response, low afterglow), the self-absorption and self-activity, and its hygroscopicity. Table 1 shows a selection of crystals available for scintillation detectors. Concerning the optical time response a gamma detector would greatly benefit from pulse durations below 1 µs, since longer pulses increase the dead time of the detector and thus decrease the dynamic range of pulse counting. The table shows that CsJ(TI) and LSO/LYSO crystals do best fit the requirements, however, LSO/LYSO is superior to CsJ(TI) due to its much shorter decay time. As can be seen in table 1, the properties of LSO and LYSO are nearly the same. A new gamma detector arc should thus be realized with LYSO because of its lower costs. Further, it should be mentioned that LSO/LYSO is today frequently used in modern PET systems.

For an effective discrimination between scattered and unscattered γ-quanta the detector must well resolve the energy of the γ-quanta being absorbed by the scintillation crystal. This quality is inferred from the pulse height spectrum measured for radiation of a reference isotope. As an example Fig. 2 shows the spectrum of a Cs-137 source measured with a CsI(Tl) scintillation detector and the multichannel analyser Mini MCA 166 (GBS Elektronik GmbH). The energy resolution R_E of the detector is defined as the ratio

$$R_E = \Delta E / E_C \tag{1}$$

of the energy spread ΔE (*FWHM* value) and the center energy E_C of the photo peak.

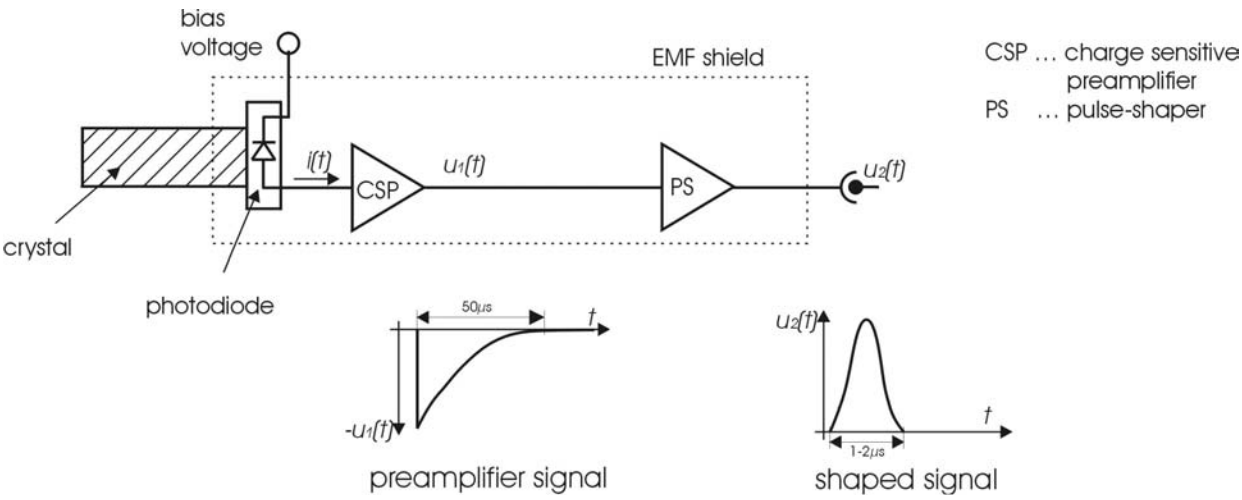

Fig. 1: Principal setup for a scintillation detector with photodiode.

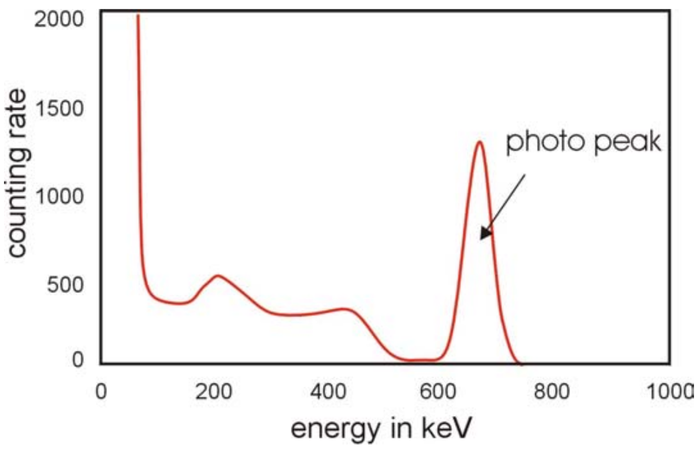

Fig. 2: Typical Cs-137 spectrum measured with a CsI(TI) scintillation detector.

Table 1: Characteristics of different scintillation crystals.

scintillator	light yield (photons/keV)	1/e Decay time (ns)	maximum of wavelength of emitted photons (nm)	thickness to stop 50% of 662 keV photons (cm)	density (g/cm^3)	hygroscopic
BGO	8 – 10	300	480	1	7,13	No
CsI(TI)	54	1005	550	2	4,51	Slightly
NaI(TI)	38	250	415	2.5	3,67	Yes
LSO	27	40	420	1.2	7,4	No
LYSO	32	48	435	1.2	7,1	No

As photodiodes we can either use a PIN type or an avalanche type (APD) photodiode. The PIN photodiode is a semiconductor device that converts the light into an equivalent electron current with no internal electron amplification (gain = 1). PIN photodiodes are inexpensive and readily available in flat epoxy covered ceramic packages, which is essential for a direct coupling onto a scintillation crystal. In the experiments we used the PIN photodiode S3590-08 (Hamamatsu GmbH) shown in Fig. 3 (left). It has an active area of 1 cm x 1 cm, a low noise equivalent power of $NEP = 3{,}8 \cdot 10^{-14}$ and a cut-off frequency of $f_c = 40$ MHz. Avalanche photodiodes have an internal gain mechanism. By supplying a reverse voltage each photoelectron is accelerated and can generate secondary electrons within the Si-lattice. The number of generated electrons (internal gain) increases with the reverse voltage. In our experimental study we used the Hamamatsu APD array S8550 (Fig. 3, right) which consists of 32 photodiodes arranged in a 4 x 8 matrix. Each APD has an active area of 1.6 mm x 1.6 mm and can be biased up to 360 V giving a gain of up to 50.

Fig. 3: PIN photodiode S3590 (left) and avalanche photodiode array S8850 (right).

3. Electronics Design

The available charge has to be amplified by a charge sensitive preamplifier (CSP). The structure of such a circuit is shown in Fig. 4. It is important to connect the CSP as close as possible to the scintillation light detector to reduce noise and the interaction with spurious signals. The key element of a CSP is the feedback capacity. An ideal circuit converts the charge into a voltage signal according to

$$U_{out} = -\frac{Q}{C_f}. \tag{2}$$

Typical values for C_f are 2 pF or less. For discharging C_f a large feedback resistor $R_f > 10$ MΩ is commonly used. A typical preamplifier signal has a fall time in the range of $20\ \mu s < t_r < 100\ \mu s$. For realizing the CSP we used the FET operational amplifier OPA656, an

IC that is excellently suited for our application. To reduce the noise and to discriminate the energy from the absorbed γ-quant the preamplifier signal is subsequently shaped by a CR-RC filter. In this way the bandwidth of the signal is limited and the signal is shaped into a Gaussian curve. The shaping time of our system is 0.5 µs giving a dead time of 1 µs for the whole detector circuit. Eventually, a buffer amplifier is placed after the CR-RC filter to adapt the signal to the required voltage range.

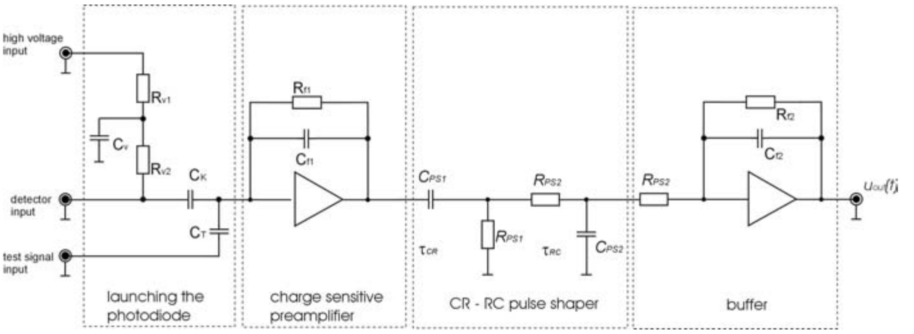

Fig. 4: Structure of a scintillation detector circuit.

4. Other design considerations

To optimize photon yield all crystal's facets were polished and coated with an optically reflective paint (TiO_2), except for the coupling facet. The photodiode is coupled to that facet by means of an optical coupling gel to avoid backreflection of scintillation light.

Beside a direct coupling of crystal and photodiode we also tried a coupling via a so called multi-clad optical fiber. Such optical fibers are made of PMMA (polymethyl methacrylate) and have multiple claddings to increase numerical aperture and thus light input at the frontal face. The fiber is very flexible which gives the opportunity to couple a set of linearly arranged crystals (as required in our detector) to a two-dimensional matrix of APDs.

Because of the high sensitivity of the CSP and the photosensitive device it is necessary to shield both. To keep electromagnetic disturbances away from the detector circuit we enclosed it in a metal frame. The printed circuit board (PCB) layout was carried out very thoroughly. Thus, a ground guard was placed around the input pin of the CSP and the photodiode's signal pin to keep it safe of leakage current. Further, all circuit paths were kept as short as possible and the ground plane was extended on the bottom layer of the PCB in such a way, that all ground connections could be realized by conducting through-holes giving a high shielding effect and very low parasitic capacitances. In fact, shielding and designing of the new detector's electronic was one of the most important parts of the detector's development. The performance of the analog electronics has been tested electronically where we achieved a signal-to-noise ratio of SNR = 30.5 after the preamplifier and SNR = 44.5 after the pulse shaping circuit

5. Results

A first detector was built with the PIN photodiode S3590-08 in combination with a 1 cm x 1 cm x 3 cm CsI(TI) crystal. The connected CSP was operated with $R_f = 1\ G\Omega$ in the feedback loop. For C_f we used the parasitic capacity of R_f ($C_f = 0.2$ pF). A typical signal of this detector is shown in Fig. 5a. With a signal-to-noise ratio of $SNR \approx 11$ a spectrum could not be measured. As a second detector we directly coupled one of the APD elements of the S8550 array to a 2 mm x 2 mm x 15 mm LSO and CsI(TI) crystal. For this arrangement with higher electron yield we set $R_f = 30$ MΩ. The shaped signal ($\tau = 0.5$ µs) is shown in Fig. 5b and a typical spectrum in Fig. 5c. The signal-to-noise ratio of the LSO scintillation detector is $SNR \approx 44.5$ and the energy resolution is $R_E = 15.3\%$. Fig. 6 shows, that the rise time of the preamplifier's signal of the CsI(TI) based detector is much larger than 1 µs and that of the LSO based detector is much smaller than 1 µs. After these results we decided to discard the CsI(TI) detector.

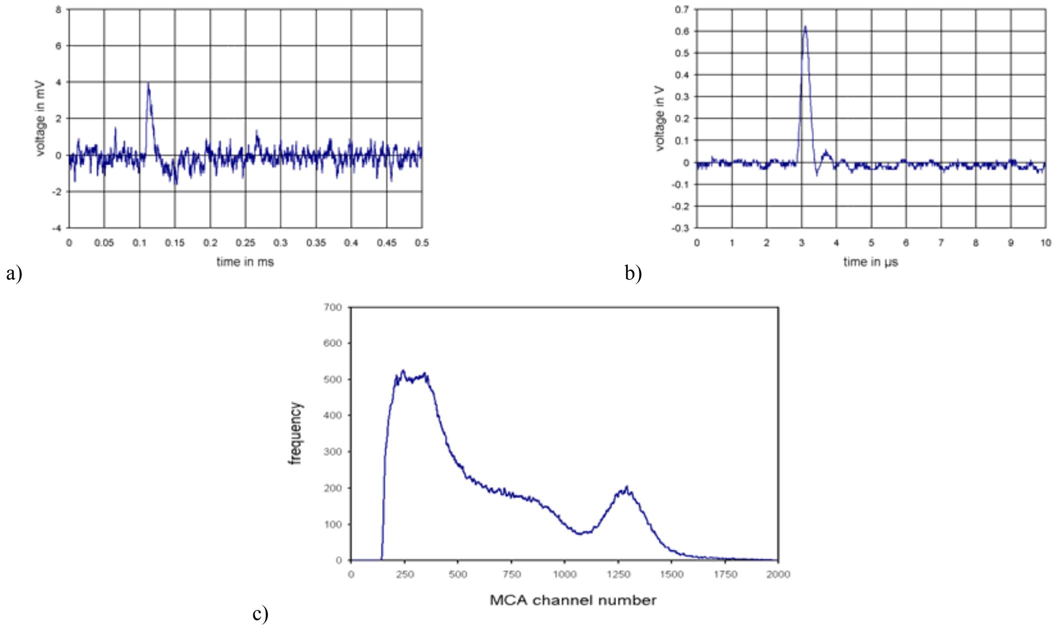

a) b) c)

Fig. 5: Signal from the PIN photodiode S3590-08 coupled to a CsI(TI) crystal (a), signal from an element of the APD array S8550 coupled to a LSO crystal (b,) and spectrum from a APD-LSO scintillation detector measured with the Mini MCA-166.

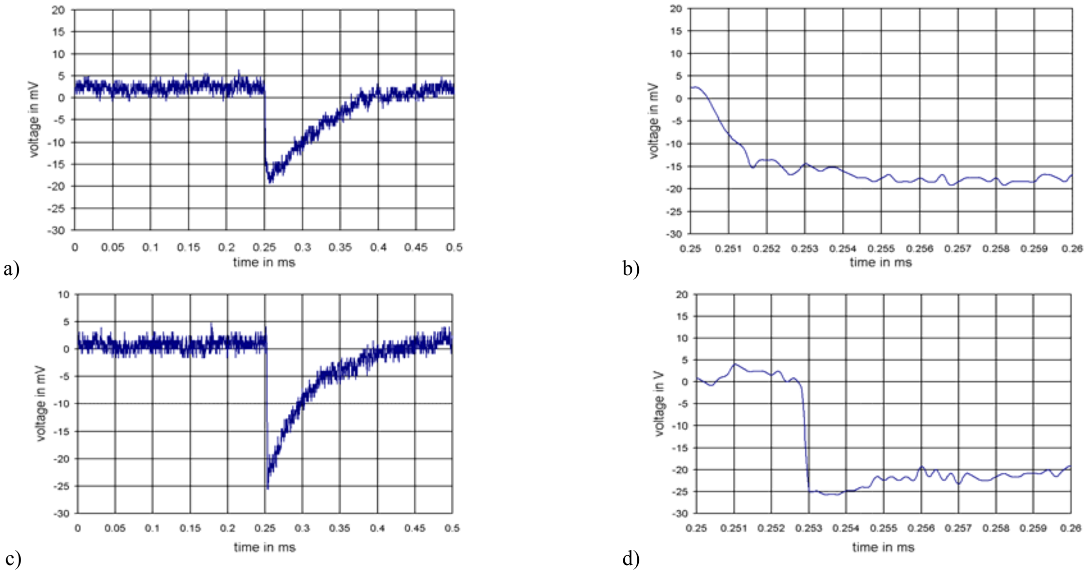

a) b) c) d)

Fig. 6: a) Preamplifier signal from a CsI(TI) scintillation detector (rising edge detailed in b), and c) preamplifier signal from a LSO scintillation detector (rising edge detailed in d) .

Further experiments were carried out with multi-clad optical fiber couplings. Therefore we used a fiber of 2 mm diameter and 30 mm length to couple the APD to the scintillation crystal. In spite of a considerable optical loss we could still measure a spectrum with an energy resolution of 22.4% (Fig. 7).

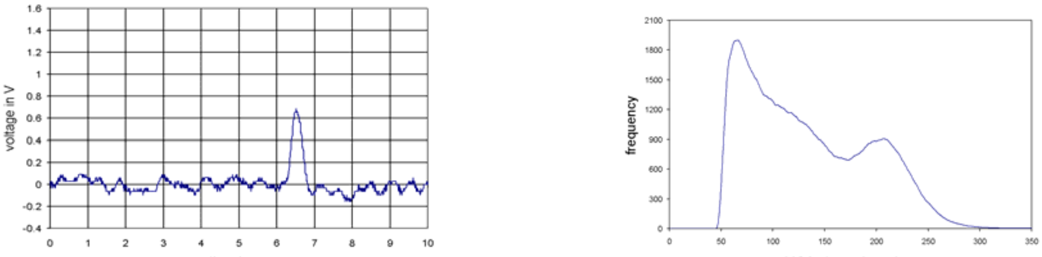

a) b)

Fig. 7: Signal (a) and spectrum (b) of the gamma ray detector with LSO crystal, APD and multi-clad optical fiber coupling.

6. Discussion and Conclusions

Building a new gamma tomography detector with spatial resolution of approximately 2 mm that is insusceptible to magnetic fields requires the application of photodiode based scintillator detectors. In our study on possible scintillator types we have selected and investigated a combination of LSO/LYSO crystals with either a PIN photodiode or APD. Additionally, we developed a special amplifier and pulse shaper electronics which is based on a commercially available fast and low-noise operational amplifier IC that can be miniaturized which is important for the assembly of a large detector array. The whole design of the circuit has been optimized concerning electrical and electromagnetic shielding such that the electronics could be immediately used in a new detector development.

In an extensive experimental study we compared detector versions with PIN photodiodes and APD, with different crystal geometries, as well as with direct and fiber optical coupling of crystal and photodiode. Thus, we found, that all detectors based on PIN photodiodes do not achieve the required energy resolution and were excluded from further considerations. APD based detectors are a good choice for a future gamma tomography device. We found, however, that when building a linear detector with the commercially available 4 x 8 diode array it is not possible to couple crystals larger than 2 mm x 2 mm x 15 mm to the APDs by means of a multi-clad optical fiber due to the overall light loss in the crystal and at the fiber ends. Thus, for the development of a new gamma tomography detector some more design considerations are necessary.

References

[1] H.-M. Prasser, D. Baldauf, J. Fietz, U. Hampel, D. Hoppe, C. Zippe, J. Zschau, M. Christen, and G. Will (2003), Time resolving gamma-tomography for periodically changing gas fraction fields and its application to an axial pump, Flow Meas. and Instrument., 14, 119.

[2] D. Hoppe, J. Fietz, U. Hampel, H.-M. Prasser, C. Zippe, K.-H. Diele, and R. Kernchen (2003), Gamma tomographic visualization of the fluid distribution in a hydrodynamic coupling, in F. P. Weiss, U. Rindelhardt (Eds.): Institute of Safety Research, Annual Report 2002, FZR-380.

[3] R. Nutt, C. L. Melcher, Current and future developments with LSO, a scintillator with excellent characteristics for PET, Revue de l’ACOMEN 5, 1999.

MEASUREMENT OF MICRO-BUBBLES USING AN ENDOSCOPIC OPTICAL SENSOR

Uwe Hampel and Eckhard Schleicher

1. Introduction

The measurement of the size distribution for small particles in gas or fluid as well as of gas bubbles in a flow has importance in many industrial and scientific problems. Gas bubble distributions, for instance, give important information on the course of fluiddynamic processes such as boiling, gas dissolution in fluids, electrolysis, and fermentation. Measurement of size distribution, local volume fraction and velocity for small particles and micro-bubbles is a typical domain of particle detectors based on laser light scattering [1]. However, commercial particle detectors and phase-Doppler particle anemometer devices are bulky and expensive and require multiple optical access to the examined fluid volume. Such devices have been developed for a broader range of particle measurement problems, comprising particles of different shapes, materials, and in various flows. Examples of that are spray analysis, environmental and clean room monitoring, and flow cytometry, only to mention a few [2], [3]. For some problems, such as the measurement of micro-bubbles in water, a conceptionally simpler measurement approach based on an optical transillumination scheme is applicable. For this purpose we developed a special endoscopic sensor that is a versatile optical instrument to obtain microscopic images from a fast fluid or gas flow. The sensor acquires digital images from the flow by means of an electronic camera system in combination with a short-time optical pulse transillumination circuit. A special software has been developed in order to control the sensor, obtain images at required rates and time intervals and to automatically analyze the images. The image analysis comprises several image processing steps, such as background subtraction, binarisation, and segmentation, together with two different algorithms to identify single bubbles, measure their volumes and diameters, and to compute bubble size distribution histograms from the image sequences.

2. The optical sensor

The principle design of the optical sensor is shown in fig. 1. The whole measurement system comprises two main components – the sensor itself and a measurement PC with a framegrabber board. The sensor consists of an aluminum housing containing the camera and the exposure control electronics and a 150 mm long tubular shaft enclosing the endoscopic optics. At the tip of the tubular shaft there is a slit of 1.5 mm width in which the flow is optically observed. A green high-power LED light source at the distal end of the shaft produces the light that transilluminates the slit. On the other side of the slit an endoscopic relay lens system transfers the image of the 2,85 mm x 2,15 mm wide field of view to the camera which resides in the sensor housing. The camera (JAI 11 monochrome progressive scan camera) can generate 30 images per second with an electronic shutter exposure down to 10 µs. However, for imaging of small particles and bubbles at flow velocities larger than 1 m/s shorter exposure times are required. Therefore the LED is flashed by means of an electric pulse current generator circuit for a user selectable pulse duration between 1 µs and 5 µs time triggered by the electronic exposure signal of the camera. For a 2 µs exposure we achieve an SNR of approximately 10 in the digital images. The camera of the sensor is connected to the PCI framegrabber board in the PC which provides the 12 V DC power supply and digitizes the video signal from the camera. A digital image in the PC has a dimension of 640 x 480 pixels and a depth of 8 bit.

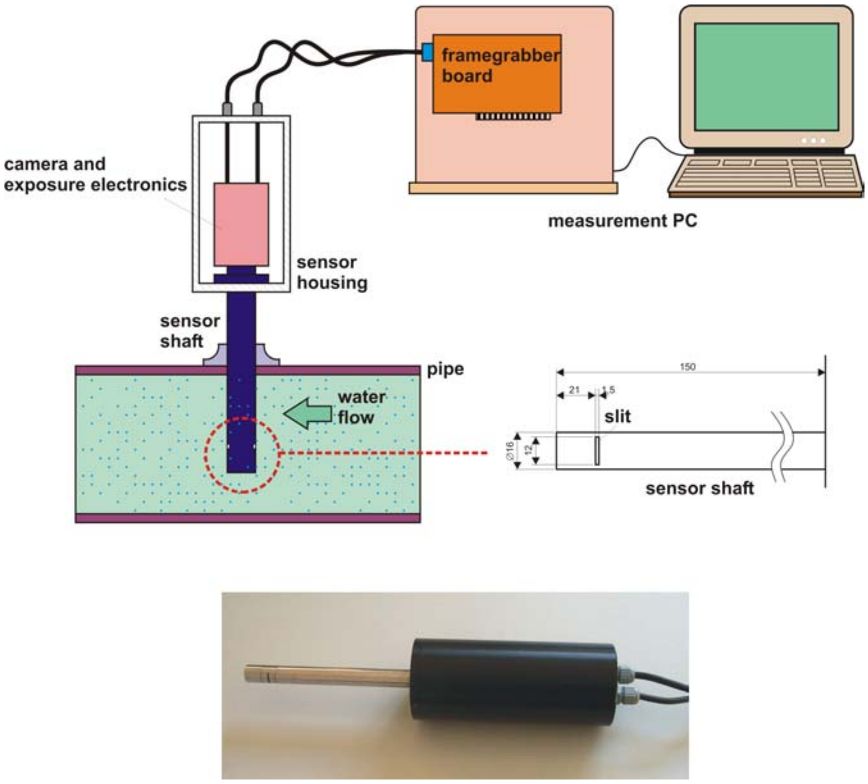

Fig 1: Design (top) and photography (bottom) of the optical gas bubble sensor.

3. Measurement principle and image processing

3.1 Operation of the sensor

The optical sensor is controlled by a special sensor software. With this software it is possible to acquire series of images as shown in fig. 2. Each series itself is a sequence of subseries with a user-defined number of images. The images of each subseries are acquired with the highest possible frame rate of 30 images per second at equidistant time points separated by a user defined time interval ΔT. Bubbles identified in the i-th subseries are then associated to the time interval $<T_i, T_i + \Delta T>$. In this way it is possible to investigate long term changes in bubble size distribution or gas fraction even if there are only few or no bubbles in a single image.

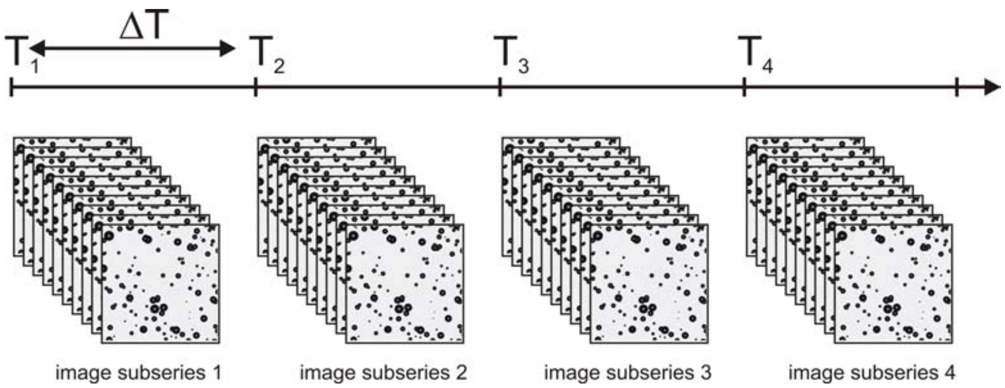

Fig 2: Structure of the image series acquired for gas bubble distribution analysis.

3.2 Basic image processing

Preparing the images for bubble identification is an algorithmic procedure with the steps shown in fig. 3. First the image contrast is optimized by scaling the raw image between a previously recorded dark image and a previously recorded bright background image according to

$$p(i,j) = \frac{p(i,j) - p_{dark}(i,j)}{p_{bg}(i,j) - p_{dark}(i,j)}, \tag{1}$$

where p, p_{dark}, and p_{bg} are the values of the pixel (i, j) for the given image (p), the dark image (p_{dark}), the background image (p_{bg}). Thus, in this step we subtract the average dark noise of the CCD sensor for the given integration time and correct for inhomogeneous background illumination and the transfer function of the optics and the camera. An image with gas bubbles then looks as indicated in fig. 4 - the gas phase has gray values close to zero (black) whereas the background has gray values close to one (white). In a second step this image is binarised by a user definable threshold TH: $0 \leq TH \leq 1$, i. e. to each pixel a value of

$$p(i,j) = \begin{cases} 1 & \text{if } p(i,j) < TH \\ 0 & \text{else} \end{cases} \tag{2}$$

is assigned. In the next step we compile coherent pixel of equal values to regions which are labeled by labels of either L = 0 or L = 1 according to their pixel values. Since the central area of a bubble is always to some degree transparent, there are regions of L = 0 which physically belong to bubbles and not to the image background. Thus, the fourth step of image processing consists in the elimination of these white spots. That is, for all regions with L = 0 it is decided, whether they are white spots or not. If so, the region is fused with its surrounding region and the values of its pixels are changed to 1. As a decision criterion we demand, that the number of coherent pixels in a region of L = 0 must be larger than 100 (an area of 10^{-3} mm²) to belong to the background. This value has been empirically determined as the largest expected white spot area. The last step is the extraction of bubble clusters, that is, regions with L = 1. The notion of cluster is used, because at this stage it is not clear, how many bubbles are present in the regions of L = 1. Thus, a cluster may be the shadow of a single or of multiple bubbles that overlap in the ray path.

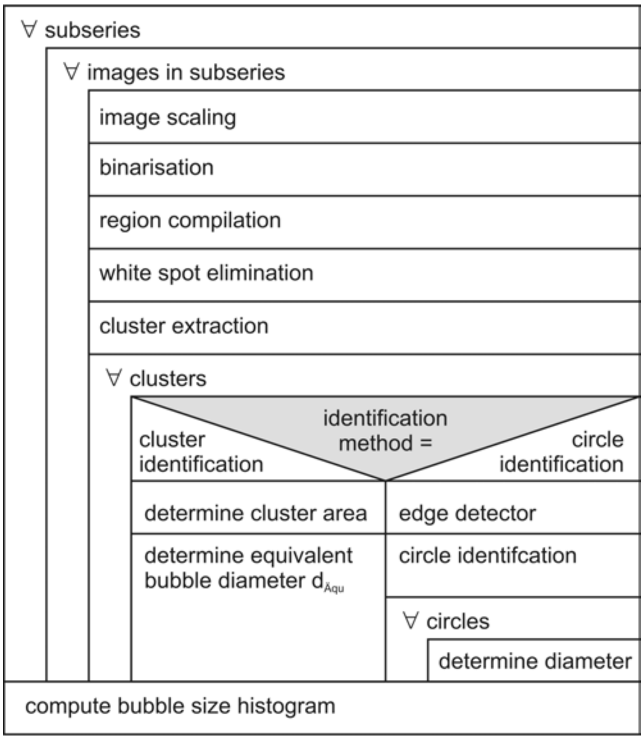

Fig 3: Structogram of the image processing and analysis steps.

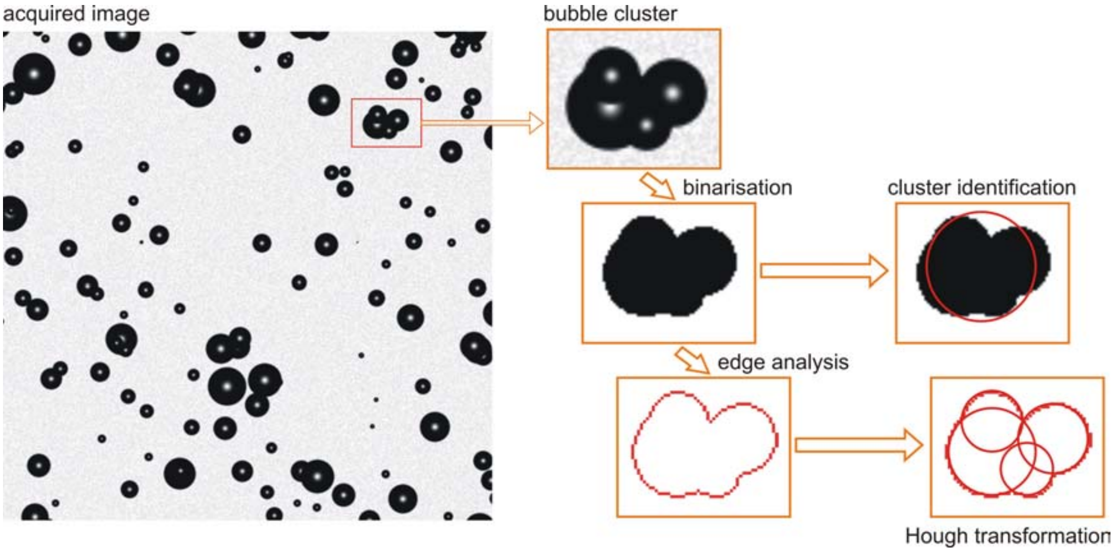

Fig 4: Principle steps of the bubble identification algorithms.

3.3 Bubble identification and measurement

There are two algorithms for bubble identification and measurement – the cluster identification algorithm and the circle identification algorithm based on the Hough transformation. The cluster identification does not account for overlapping bubbles and can be applied, when the bubbles are larger and no longer spherical and when the bubble number per image is low such that overlapping bubbles do not significantly influence the overall accuracy of the bubble size computation. The cluster identification algorithm starts from an already identified bubble cluster, i. e. the list of pixels that belong to one coherent black region with L = 1 in the image. The cluster is considered as the binary projection of a single bubble and from the number of pixels in the cluster N_C and the pixel area $A_{pix} = 20\ \mu m^2$ an equivalent bubble diameter is computed according to the formula

$$d_{\text{Äqu}} = \sqrt{\frac{A_{pix} N_C}{\pi / 4}} \,. \tag{3}$$

Thus, $d_{\text{Äqu}}$ is the diameter of a sphere with a cross-sectional area of $A_{pix} N_C$.

The second algorithm for bubble identification is the circle identification algorithm, which accounts for overlapping bubbles. This algorithm is based on the assumption, that each bubble that contributes to the cluster shape is spherical and has a partial circular cord segment within the boundary edge of the cluster. Thus, we first apply a morphological edge detector to the binary cluster image P_{clust} by the operation

$$P_{edge} = P_{clust} - E\{P_{clust}\}, \tag{4}$$

where $E\{\}$ denotes a one-step erosion operation. The resulting image P_{edge} now contains only the boundary pixels of the cluster (fig. 4) and can be analyzed by the Hough-Transform algorithm for circles (see [4], [5] for details). Attractive features of the Hough transform are, that the order of the edge pixels is of no importance for the identification process and the identification process is comparatively immune to image noise. The three-dimensional discrete Hough transform for circle primitives is defined as

$$\mathrm{h}(m,n,p)=\sum_{i=0}^{N_r}\sum_{i=0}^{N_x}\sum_{j=0}^{N_y}\mathrm{C}(r_p,m-i,n-j)\mathrm{p}(i,j)\,, \tag{5}$$

where p(i, j) is the value of the pixel with indices i and j (i – index for x direction, j – index for y direction) in the binary edge image, h(m, n, p) is the voxel value in three dimensional discrete Hough space (m – index for x direction, n – index for y direction, p – index for radius value), and C(r, k, l) is the binary image of a circle with radius r_p centered about pixel (k, l) and with values

$$\mathrm{C}(r,k,l)=\begin{cases}1 & \mathit{if\ pixel}(k,l)\ \mathit{belongs\ to\ circle\ boundary}\\ 0 & \mathit{else}\end{cases}. \tag{6}$$

Each circular edge segment associated with a circle of radius r_p gives an accumulation point (local maximum) at the voxel (m_c, n_c, p,) in Hough space, where m_c and n_c are the indices of the center pixel of the corresponding circle and the value of h(m_c, n_c, p,) is equal to the pixel number and thus to the length of the arc segment. The identification of circles then essentially consists in the determination of all relevant accumulation points. The relevance of an accumulation point, i. e. the decision whether the corresponding circle segment is sufficiently large to be associated with a single bubble, however, must be derived from some rules in order to avoid overidentification. Further, the sampling density and the range of the discrete r values also needs to be optimized to avoid prohibitive long computation times. Therefore, in our software we let the user put limits on the range of r and sample the diameter at steps of one pixel edge length l_{pix} = 4,47 µm. Thus, there are three rules to steer the identification algorithm:

1. the discrete range of r is bounded at both ends by user-defined values r_{min} and r_{max},
2. we put a lower limit on the number of cluster edge pixels, in order to prevent very small clusters or clusters which are only partly in the image being analyzed,
3. the center pixel of an identified circle must have a label of L = 1, i. e., it must not lie in the background region.

To increase accuracy we perform the identification procedure iteratively, i. e., after each Hough transformation we seek for the global maximum that indicates the longest arc segment that is present in the edge structure, we check, whether the above rules hold for the identified circle, then we save the parameters (center coordinates and diameter) of the identified circle, and eventually we erase all pixels in the binary edge image that are associated with the identified circle. The last step is in principle not necessary, since one Hough transformation finds all local maxima that correspond to circle segments at once. However, it proved to give a major improvement in identification accuracy to proceed in the described way and to redo the Hough transformation after the identification of a single circle. In fact, we also use the edge pixel erasing step not only to eliminate pixels that are exactly on the circle's boundary but also pixels in the direct vicinity of that boundary, which prevents overidentification in case of boundaries that diverge from ideal circular shape, either due to bubble deformation or due to noisy pixels.

The Hough transformation algorithm is very effective and powerful, however, it prolongs the computation time especially in cases, where large bubbles or many bubble clusters are present. A typical processing time for one image is between 0.5 and 3 seconds depending on the number and sizes of bubble clusters. As an example fig. 5 shows one of 100 processed images with identified gas bubbles and the corresponding bubble size histogram for residual CO_2 gas in a water flow at 1 m/s. The analysis of the whole sequence with an overall number of 1388 bubbles took approximately 120 seconds for the circle identification and 56 seconds with the cluster identification algorithm.

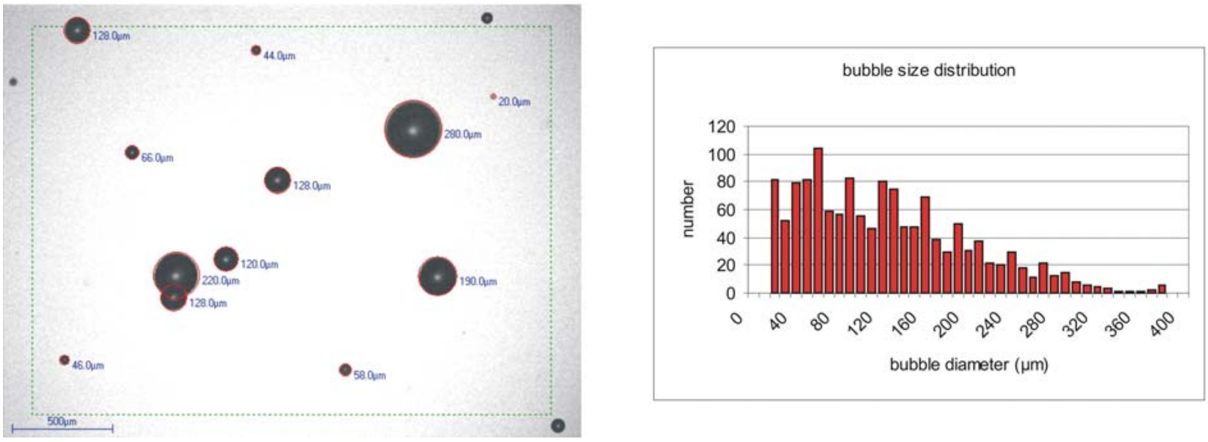

Fig. 5: Identified gas bubbles (left) and gas bubble size distribution (right) for a series of images acquired in a water flow with a residual CO_2 gas fraction.

4. Discussion and Conclusions

We have devised an endoscopic optical sensor that can be used to visualize and measure small gas bubbles or particles in flows with velocities up to 5 m/s. A special software has been developed to control the image acquisition of the sensor and to perform image processing as well as bubble identification. For bubble identification there is a choice of a simpler cluster identification algorithm or a more complex Hough transformation based circle identification algorithm. The sensor has been developed for the specific problem of gas bubble size distribution measurement in water, however, other applications in fluid-particle or gas-particle flows are conceivable, just as particle velocity measurement by double-pulse exposure or imaging of arbitrary microstructures in fast moving multi-phase flows.

References

[1] P. A. Baron, K. Willeke Ed. (2001), Aerosol Measurement: Principles, Techniques, and Applications, 2nd Edition, Wiley

[2] T. Kawaguchi, Y. Akasaka, M. Maeda (2002), Size measurements of droplets and bubbles by advanced interferometric laser imaging technique, Meas. Sci. Technol., 13, 308

[3] G. Vesey, J. Narai, N. Ashbolt, K. Williams, D. Veal (1994), Detection of specific microorganisms in environmental samples using flow cytometry, Methods In Cell Biology, 42, 489

[4] P. V. C. Hough (1962), Method and means for recognizing complex patterns, U. S. Patent 3.069.654

[5] D. H. Ballard (1981), Generalizing the Hough transform to detect arbitrary shapes. Pattern Recognition, 13, 111

HIGH-SPEED X-RAY COMPUTERIZED TOMOGRAPHY WITH A SCANNED ELECTRON BEAM SOURCE

Uwe Hampel, Jürgen Fietz, Dietrich Hoppe, Horst-Michael Prasser, Eckhard Schleicher, Martina Speck, Cornelius Zippe, Dieter Koch[1], and Hans-J. Menz[1]

1. Introduction

Today there exist only a few tomographic devices which are able to produce fast sequences of cross-sectional images from an object. In medical diagnostics the electron beam tomograph (EBT) first introduced by Boyd et. al [1], is one example of such devices that use a scanned electron beam to produce X-ray computed tomography images with up to 50 frames per second - an image acquisition rate that is sufficient to investigate cardiovascular processes in human beings and animals. However, although the EBT has brought completely new perspectives to medical diagnostics, it is too slow for the investigation of other transient phenomena and processes in physics, biology, and technical sciences. Especially the investigation of two-phase flows requires frame rates of at least 1000 per second in order to visualize the transient behavior of relevant flow structures.

One device that has recently been built for studies on two-phase flows is the X-ray computed tomography apparatus introduced by Hori et al. [2]. It uses a circular arrangement of 60 pulsed X-ray tubes in combination with an annular X-ray detector slightly above the plane defined by the focal spots of the X-ray sources. High-speed tomographic data acquisition is realised by repeated sequential flashing of all sources giving a frame rate of up to 2000 images per second. Beside the complexity and costs of this system there is also a compromise in axial resolution since the 360° tomography inevitably requires that the source and detector plane have an axial offset. This in turn might cause problems to resolve small moving objects, such as particles or bubbles in a flow.

We devised and tested a novel computed tomography approach that utilises a scanned electron beam X-ray source to produce fast sequences of tomographic images. Contrary to classical electron beam tomography a linear deflection pattern for the electron beam is used and a non-annular detector arc records transmission data of an object from different projection angles. This approach gives the highest achievable axial resolution and is comparatively moderate in effort and costs. For the inverse problem we applied iterative image reconstruction techniques to reconstruct the density distribution from a limited data set. The method has been experimentally tested on static and dynamic phantoms with a frame rate of 1000 images per second and a spatial resolution of approximately 1 mm in-plane and axial.

2. Tomography System

Fig. 1 shows the principal design of the computed tomography system with a scanned electron beam source. For the generation of the electron beam a conventional high power electron gun with up to 150 kV acceleration voltage and 600 mA continuous electron current has been used. The beam is vertically directed onto a cylindrical tungsten target whose axis is orientated perpendicular to the beam axis. The beam steering system comprises focusing and deflection coils together with high power, high speed coil current drivers. All components of this system have been especially designed and optimized for this tomography application.

---

[1] Stuttgart University, Institute of Nuclear Engineering

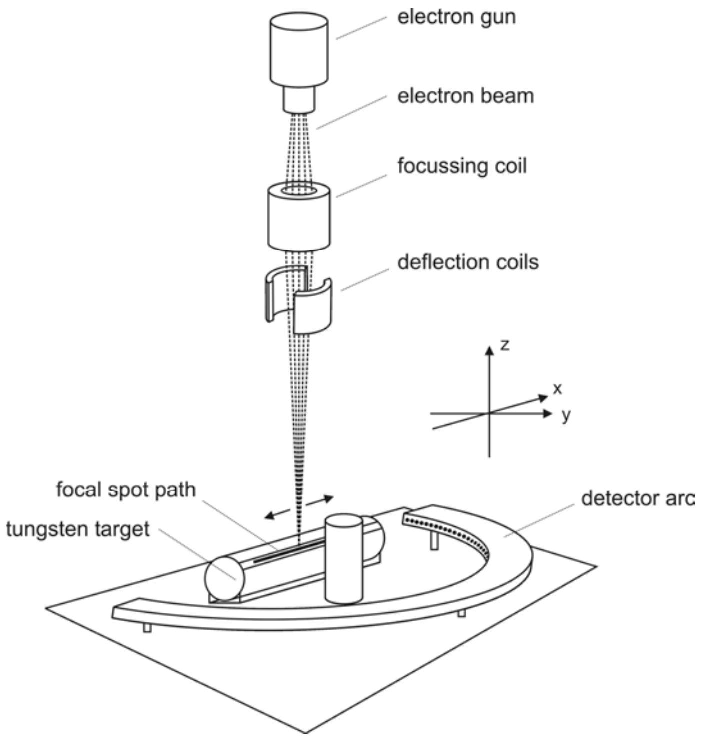

Fig. 1: Setup for a fast X-ray CT with a scanned electron beam source.

During a tomographic scan the electron beam is linearly deflected from its axial direction by applying a saw-tooth coil current pattern of 500 Hz frequency, thus producing a focal X-ray spot that moves forth and back between two turning points on a line segment on the surface of the tungsten target.

The optimal X-ray detector geometry for tomography is the one sketched in Fig 1. It is an arc of contiguous sensor elements that surrounds the object up to the prolonged axis of the target. In that way all the detector pixels are exactly aligned in one plane with the focal spot path. For the initial experiments, however, we used a smaller detector with 64 elements which we subsequently placed into different positions, simulating a larger detector in this way. The detector elements are CdZnTe semiconductor pixels of 1.5 mm x 1.5 mm active area, 1 mm depth and 1.6 mm pitch. The detector electronics, which is physically separated from the pixel array, comprises 64 two-stage transimpedance amplifiers with 1 MΩ transimpedance gain and 50 kHz bandwidth, followed by 12-bit analog-to-digital converters which sample the signals at 100 kHz in parallel and in synchronization with the beam deflection signal. The digital data is temporarily stored in a RAM array during the measurement and can be transferred to the PC after recording. The memory size allows a data acquisition for 0.8 seconds. The detector noise at no radiation exposure has been determined to be less than 2 LSB for all detectors.

The experiments were carried out in a vacuum box. Therefore, we mounted the source target, the detector and the phantom on an aluminum base plate which in turn was fixed at the bottom of the box (fig. 2). In addition to the primary components (target, detector, object) the setup comprised a 0.5 mm thick thermal shield of aluminum erected between target and object in order to prevent thermal radiation to damage sensible parts of the setup, and further a slit collimator that was placed in front of the detector array to filter out off-plane scattered radiation. The 64 coaxial signal cables connecting the detector elements with the data acquisition electronics together with detector high voltage supply and a few other signal lines have been passed through the wall of the vacuum chamber by means of a multi-pin vacuum-tight electrical connector. The electron gun and the beam deflection unit are on top of the vacuum box and the electron beam is guided through the ceiling of the box onto the target. The zero position of the focal spot, i. e. the spot position at no deflection, was adjusted manually by the operator. All experiments were carried out at 150 kV acceleration voltage, a beam current between 3 mA and 10 mA, and at 10^{-6} bar vacuum.

3. Data Acquisition

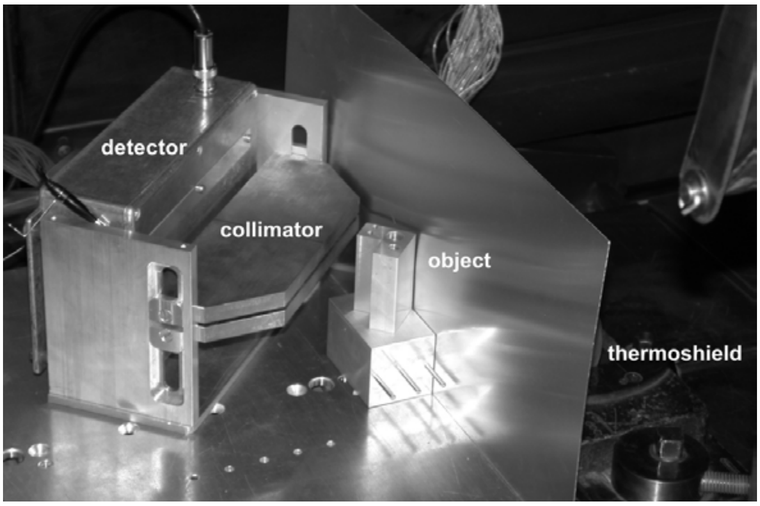

Fig. 2: Photography of the experimental measurement setup.

During a complete 1 ms movement of the focal spot 100 data samples are obtained at each of the 64 detector elements. This data matrix of one complete scan then consists of N_D x N_S measurement values, where N_D is the number of detector elements and $N_S = 100$ is the number of source positions. In order to achieve a good angular coverage with the linear detector array we placed the detector in three different positions relative to the object when we made measurements on static phantoms. In this case is $N_D = 192$. For dynamic phantoms this approach was not applicable. Here we moved the detector as close as possible to the object giving $N_D = 64$ detector values for each complete scan.

The reconstruction of the distribution of the X-ray attenuation coefficient within the measurement plane requires to compute the extinction values

$$E_{ij} = \ln \frac{I_{0,ij}}{I_{ij}} \tag{1}$$

for each pair (i, j) of detector (i) and source spot (j). Thereby I_{ij} denotes the X-ray intensity measured for an object and $I_{0,ij}$ the intensity measured at a reference, which may be a reference object with radiological properties close to the investigated object (e. g. a homogeneously filled vessel) or no object at all (zero-attenuation reference).

4. Image Reconstruction

Opposed to conventional X-ray computed tomography the linearly moving source produces data from a limited number of projection angles. This type of inverse problem is known as limited angle tomography (LAT) and has been widely studied in the past due to its importance for many practical computed tomography problems [3]. For the limited projection data set iterative image reconstruction algorithms offer some considerable advantages over modified filtered backprojection algorithms concerning artifact suppression, flexibility, and incorporation of a-priori knowledge. To perform algebraic reconstruction we consider the discrete spaces of the data, represented by the row vector **m** with $m_k = E_{ij}$ ($k=i+j\cdot N_D$), and the image to be reconstructed, represented by the row vector $\boldsymbol{\mu}$ containing the extinction values of the image pixels. Conventionally, the image is chosen as a square area between source and detector subdivided into a set of $N_P \cdot N_P$ pixels. In the particular problem we chose $N_P = 100$ and a pixel edge length of 0.5 mm giving a 50 mm x 50 mm cross-section area for reconstruction. The interrelation between data and image space is described by the weight matrix **A** that contains the contributions of each pixel to the attenuation in each ray which is easily computed as the geometrical intersection of rays and pixels.

As algorithms to solve the inverse problem to the equation $\mathbf{m} = \mathbf{A}\ \boldsymbol{\mu}$ we tested the additive algebraic reconstruction technique ART [4], the multiplicative algebraic reconstruction technique MART [5], and the simultaneous iterative reconstruction technique (SIRT) [6]. Their correction formulas are given in table 1. Thereby n denotes the iteration step, i the pixel index, j the measurement value index, and λ the relaxation parameter. The starting vector is typically $\boldsymbol{\mu}^{(0)} = \mathbf{0}$ for ART and SIRT, and $\boldsymbol{\mu}^{(0)} = \mathbf{1}$ for MART. In theoretical studies with simulated data we found, that ART and MART are superior to SIRT concerning robustness and convergence behavior for the given problem. Therefore, the results discussed have been obtained using only these two algorithms.

Table 1: Correction formulas for the three iterative image reconstruction methods.

method	**correction formula**
ART	$\boldsymbol{\mu}^{(n+1)} = \boldsymbol{\mu}^{(n)} + \lambda\left(m_k - \mathbf{A}_k\boldsymbol{\mu}^{(n)}\right)\mathbf{w}_k{}^T$
MART	$\mu_i^{(n+1)} = \mu_i^{(n)} \cdot \left(1 - \lambda \frac{a_{ij}}{a_{\max}}\left(1 - \frac{m_j}{\mathbf{A}_j \cdot \boldsymbol{\mu}}\right)\right)$
SIRT	$\boldsymbol{\mu}^{(n+1)} = \boldsymbol{\mu}^{(n)} + \lambda^{(n)} \cdot \mathbf{A}^T \cdot \left(\mathbf{m} - \mathbf{A} \cdot \boldsymbol{\mu}^{(n)}\right)$

5. Results

Fig. 3 shows the reconstruction result for a static phantom which has been made to simulate tomography of a liquid-gas two-phase flow in a small pipeline segment. The phantom consists of an aluminum ring (pipe) of 44 mm outer diameter and 2 mm thickness enclosing a PVC cylinder (fluid) with six drillings (gas bubbles) of diameters between 1 mm and 11 mm. The reconstruction shows that it is possible to resolve all gas inclusions except the 1 mm one, which is lost in the noise. As a reference we used another phantom with the same properties but without drillings (gas-free fluid). We found that MART gives better results concerning image smoothness. Also, it can be recognized that there is some deformation in the object's shape in regions close to source and detector. This is a typical artifact of limited-angle CT and may be removed by application of more dedicated image reconstruction algorithms.

Eventually we performed an experiment on the dynamic phantom that is shown in fig. 4. It consists of a DC motor driven rotating disk within an aluminum housing (cup) of 1 mm wall thickness and 40 mm outer diameter which can be filled with particles. Two steel pins of 3 mm diameter are fixed on the disk in order to force the particles to irregular movements by bouncing. Two other steel pins that descend from the cover of the cup prevent the particles from moving only along a circumferential path. As test particles we used small glass pearls from a necklace which are of 4.5 mm diameter and possess through-holes of 1 mm diameter. With the detector array this time arranged in a closer position to the object we recorded the irregular movement of the pearls during a time period of 0.8 s with a frame rate of 1000 images per second. As a reference we used the zero-attenuation reference.

Fig. 4 right shows single images of such a sequences for one, three, and ten pearls in the cup. The reconstruction algorithm in this case was MART. Reconstruction of a whole sequence took approximately 10 minutes on an Athlon 2000XP computer. Since in this scenario we have a well concentrated density distribution we achieve a good reconstruction quality even with a rather high angular limitation. It can clearly be seen, that also the through-holes in the pearls can be resolved when they appear within the imaged plane. This indicates, that we achieve an axial resolution of at least 1 mm, which is much better than with any other EBT setup. The wall of the cup and the rotating steel pins are also reconstructed whereby again the walls appear incomplete in regions with lowest angular viewing range.

6. Discussion and Conclusions

We experimentally tested a fast X-ray computed tomography technique with a scanned electron beam source that may have a high potential in imaging of transient density changes, especially in two-phase flow problems. A first experimental investigation carried out with a fast scanning high power electron beam system and a 64 element linear X-ray detector in a vacuum box showed promising results concerning a qualitative reconstruction of object details and time resolution for imaging of a multiple particle scenario. So far, however, we have not reached the limits of this technique and will proceed to improve image reconstruction with algorithms that better cope with the limited-angle problem by incorporation of problem specific a-priori knowledge, such as known radiological density ranges, geometrical properties (e. g. particle/object sizes and shapes), as well as maximum expected density change rates in time. Further, an improvement of the experimental setup with a larger detector and a separate X-ray unit may lead to the limits of reconstruction quality that can today be estimated from simulated data.

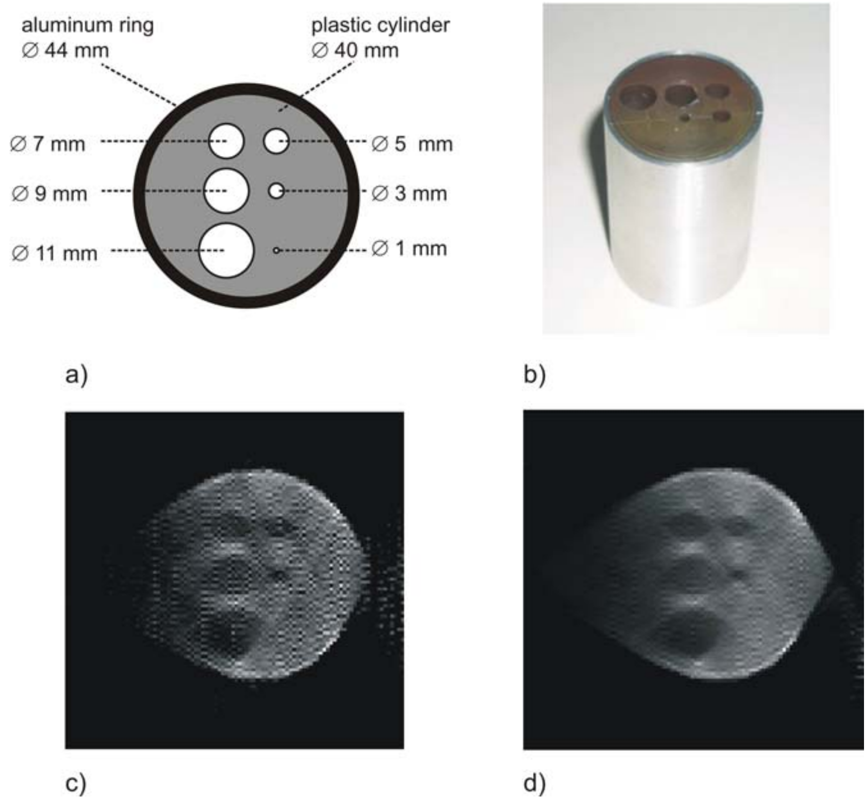

Fig. 3: Reconstruction of a static two-phase-flow phantom. a) geometry, b) photography, c) ART result, d) MART result.

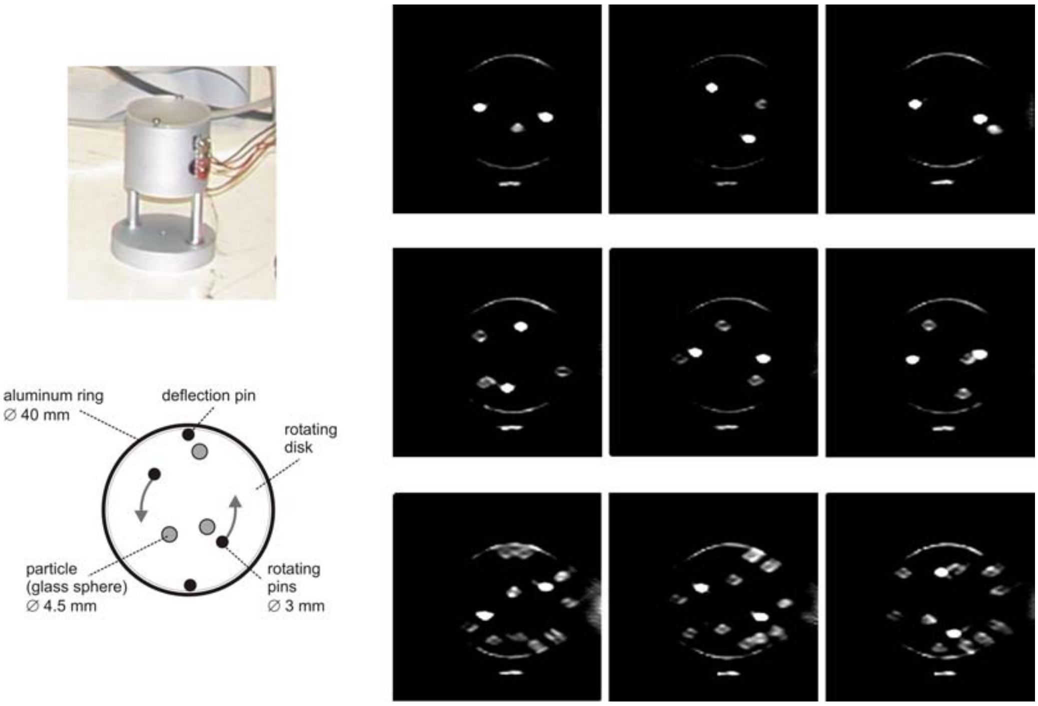

Fig. 4: Reconstruction results for a dynamic particle phanom. Left: photo and geometry of the phantom, right: images for the scenario with one (top), three (middle) and ten (bottom) particles.

References

[1] D. P. Boyd, and M. J. Lipton (1983), Cardiac computed tomography, Proc. IEEE, 71, 298

[2] M. Misawa, N. Ichikawa, M. Akai, K. Hori, K. Tamura, and G. Matsui (1998), Ultra fast X-ray CT systems for measurement of dynamic events in two-phase flow, Proceedings of the International Conference on Nuclear Engineering, (ASME/JSME/SFEN ICONE-6) (pp. 508-522), San Diego, USA

[3] D. Verhoeven (1993), Limited-data computed tomography algorithms for the physical sciences, Appl. Opt., 32, 3736

[4] R. Gordon, R. Bender, and G. T. Herman (1970), Algebraic reconstruction techniques (ART) for three-dimensional electron microscopy and X-ray photography, J. Theor. Biol., 29, 471

[5] R. de Pierro (1991), Multiplicative Iterative Methods in Computed Tomography, in G. T. Herman, A. K. Louis, and F. Natterer Ed., Mathematical Methods in Tomography (pp. 167-186), Springer Verlag

[6] P. Gilbert (1972), Iterative methods for the three-dimensional reconstruction of an object from projections, J. Theor. Biol., 36, 105.

CONTACTLESS INDUCTIVE FLOW TOMOGRAPHY: THEORY AND EXPERIMENT

Frank Stefani, Thomas Gundrum, and Gunter Gerbeth

1. Introduction

The determination of flow velocities in opaque fluids is a notorious problem in various industrial applications, including steel casting and silicon crystal growth. Obviously, the usual optical flow measurement techniques, as Laser Doppler Anemometry (LDA) or Particle Image Velocimetry (PIV), are not applicable in those cases. Actually, there are a few measurement techniques for opaque fluids, including Ultrasonic Doppler Velocimetry (UDV), mechano-optical probes, and electric potential probes [1]. However, for hot and/or chemically aggressive materials it would be most desirable to avoid any contact with the melt. The wish to reconstruct the sodium velocity in the Riga dynamo experiment [2] by an appropriate contactless method was another strong motivation for the present work.

With view on these possible applications, this report describes a *Contactless Inductive Flow Tomography* (CIFT) for electrically conducting melts, based on external magnetic field measurements. In contrast to traditional inductive flow determination based on electric potential measurements [3], the new method is restricted to fluid flows with not too small magnetic Reynolds numbers. Another shortcoming may be the fact that the method is not very accurate in the determination of local velocities. However, this point might be outweighed by the fact that the method enables online monitoring of transient flow fields in the entire fluid volume, at least with a time-resolution of a few seconds. This feature makes the method attractive for a number of technological and research applications.

2. Basic theory

When an electrically conducting medium, moving with the velocity $\mathbf{u}$, comes under the influence of an imposed steady magnetic field $\mathbf{B}_0$, an electromotive force (emf) $\mathbf{u}\times\mathbf{B}_0$ is induced that drives an electric current

$$\mathbf{j}_0 = \sigma(\mathbf{E}_0 + \mathbf{u}\times\mathbf{B}_0)\,, \tag{1}$$

where σ is the electrical conductivity of the fluid, and $\mathbf{E}_0$ is the electric field which results from the emf. The current $\mathbf{j}_0$, in turn, produces an additional magnetic field $\mathbf{b}$, so that the total current $\mathbf{j}$ becomes also dependent on the total magnetic field $\mathbf{B} = \mathbf{B}_0 + \mathbf{b}$,

$$\mathbf{j} = \sigma(\mathbf{E} + \mathbf{u}\times\mathbf{B})\,. \tag{2}$$

The ratio of the induced magnetic field $\mathbf{b}$ to the imposed magnetic field $\mathbf{B}_0$ is governed by the so-called magnetic Reynolds number

$$Rm = \mu\sigma LU\ , \tag{3}$$

where μ is the magnetic permeability of the fluid, and L and U are typical length and velocity scales of the flow, respectively. This dimensionless number is, in the most relevant technical applications, smaller than one.

We start from Eq. (2) and employ Biot-Savart's law for the magnetic field and Green's theorem for the electric potential [4,5]. In the following, we will only need the version for the steady case, in which the electric field can be expressed by the gradient of the electric potential, $\mathbf{E} = -\nabla\phi$. The generalization to the time-dependent case can be found in [6]. The integral equation system consists of one equation for the induced magnetic field in the entire volume D of the fluid,

$$\mathbf{b}(\mathbf{r}) = \frac{\sigma\mu_0}{4\pi}\int_D \frac{(\mathbf{u}(\mathbf{r}')\times\mathbf{B}(\mathbf{r}'))\times(\mathbf{r}-\mathbf{r}')}{|\mathbf{r}-\mathbf{r}'|^3}\,dV' - \frac{\sigma\mu_0}{4\pi}\oiint_S \phi(\mathbf{s}')\,d\mathbf{S}'\times\frac{\mathbf{r}-\mathbf{s}'}{|\mathbf{r}-\mathbf{s}'|^3} \quad , \tag{4}$$

and one equation for the electric potential at the fluid boundary S,

$$\phi(\mathbf{s}) = \frac{1}{2\pi}\int_D \frac{(\mathbf{u}(\mathbf{r}')\times\mathbf{B}(\mathbf{r}'))\cdot(\mathbf{s}-\mathbf{r}')}{|\mathbf{s}-\mathbf{r}'|^3}\,dV' - \frac{1}{2\pi}\oiint_S \phi(\mathbf{s}')\,d\mathbf{S}'\cdot\frac{\mathbf{s}-\mathbf{s}'}{|\mathbf{s}-\mathbf{s}'|^3} \quad . \tag{5}$$

In Eq. (4) we see that the induced magnetic field $\mathbf{b}$ depends on both the induced primary currents in the volume D and the induced electric potential ϕ at the fluid boundary S. Eqs. (4) and (5) are valid for arbitrary values of Rm, and provide a suitable mathematical set-up to handle dynamos in arbitrary domains [5]. For small Rm, however, the induced magnetic field $\mathbf{b}$ under the volume integrals on the r.h.s. of Eqs. (4) and (5) can be neglected and the total $\mathbf{B}$ can be replaced by $\mathbf{B}_0$.

In [4] we had shown that the velocity structure of the flow can be reconstructed from the external measurement of an appropriate component of the induced magnetic field (e.g., the radial component for a spherically shaped fluid volume) and the induced electric potential at the fluid boundary. There remains a non-uniqueness concerning the radial distribution of the flow [7] what can be made plausible by representing the fluid velocity by two scalars living in the whole fluid volume (e.g., the toroidal and poloidal parts). Then it is clear that two quantities measured on a two-dimensional covering of the fluid give not enough information for the reconstruction of the two desired 3D-quantities.

In [8] we had developed a general method to avoid the electric potential measurement at the fluid boundary. The main idea is to apply the external magnetic field in two different, e.g. orthogonal, directions and to measure both corresponding sets of induced magnetic fields. The main obstacle for the application of this method comes from the electric potential term at the boundary, the measurement of which we just like to circumvent. For the very special case of a spherical fluid volume, it can easily be seen, from multiplying Eq. (4) with the radial unit vector, that the radial component of $\mathbf{b}$ is unaffected by ϕ. For other than spherical fluids, however, there is always an influence of the surface term on $\mathbf{b}$. How can the influence of ϕ be taken into account without measuring it?

In the following we sketch the solution of this puzzle. Assume, for a given $\mathbf{B}_0$, all measured induced magnetic field components be collected into an NB-dimensional vector with the entries $b_i^{(B_0)}$. Assume further a certain discretization of the electric potential at the surface, denoted by an NP-dimensional vector with the entries $\phi_m^{(B_0)}$. The velocity in the domain D is discretized as an NV-dimensional vector with the entries u_k. Then, Eqs. (4) and (5) can be written in the form

$$b_i^{(B_0)} = K_{ik}^{(B_0)} u_k + L_{im} \phi_m^{(B_0)} \quad (6) \qquad \text{and} \qquad \phi_m^{(B_0)} = M_{mk}^{(B_0)} u_k + N_{mn} \phi_n^{(B_0)} \quad (7)$$

with $\mathbf{K}^{(B_0)}$ being a matrix of type (NB, NV), $\mathbf{L}$ a matrix of type (NB, NP), $\mathbf{M}^{(B_0)}$ a matrix of type (NP, NV), and $\mathbf{N}$ a matrix of type (NP, NP). Note that only the matrices $\mathbf{K}^{(B_0)}$ and $\mathbf{M}^{(B_0)}$ depend on the applied magnetic field $\mathbf{B}_0$, whereas the matrices $\mathbf{L}$ and $\mathbf{N}$ are independent of $\mathbf{B}_0$.

As it is well known from magnetoencephalography [9], the inversion of Eq. (7) is a bit tricky due to the singularity of the matrix $(\mathbf{I}-\mathbf{N})$. However, by applying the so-called deflation method [9], one ends up with a single linear relation between the desired velocity field and the measured magnetic field in the form

$$b_i^{(B_0)} = K_{ik}^{(B_0)} u_k + L_{im} (I-N)_{mn}^{-1,defl} M_{nk}^{(B_0)} u_k \quad , \tag{8}$$

where we have used the superscript '$defl$' in order to indicate the deflation method for the inversion of the matrix $(\mathbf{I}-\mathbf{N})$.

Despite the far-reaching similarity, there is one essential difference of our method compared to magnetoencephalography. While in the latter method one has to determine a single neuronal current distribution, in our case we can produce *quite different current distributions from the same flow field* just by applying various external magnetic fields $\mathbf{B}_0$ subsequently. For each applied magnetic field $\mathbf{B}_0$ we can measure the corresponding induced fields $b_i^{(B_0)}$, and utilize all of them together for the reconstruction of the flow.

For the data analysis of the experiment we will circumvent the remaining non-uniqueness problem by the use of Tikhonov regularization and the method of Tikhonov's L-curve [9]. Note that the inversion of Eq. (8) is equivalent to the minimization of the mean quadratic deviation of the measured fields $b_{i,meas}^{(B_0)}$ from the fields $b_i^{(B_0)}[\mathbf{u}]$ that are modeled according to Eq. (8). Within the regularization one adds to the functional of mean quadratic residual one or more „penalty“ functions which are chosen, for convenience, as quadratic functionals of the velocity. For our purpose we minimize the total cost functional

$$F[\mathbf{u}] = F_{B_{0x}}[\mathbf{u}] + F_{B_{0z}}[\mathbf{u}] + F_{div}[\mathbf{u}] + F_{reg}[\mathbf{u}] \tag{9}$$

with the individual parts

$$F_{B_{0x}}[\mathbf{u}] = \sum_{i=1}^{NB} \frac{1}{\sigma_{i,B_{0x}}^2} \left(b_{i,meas}^{(B_{0x})} - b_i^{(B_{0x})}[\mathbf{u}] \right)^2 \quad , \tag{10}$$

$$F_{B_{0z}}[\mathbf{u}] = \sum_{i=1}^{NB} \frac{1}{\sigma_{i,B_{0z}}^2} \left(b_{i,meas}^{(B_{0z})} - b_i^{(B_{0z})}[\mathbf{u}] \right)^2 \quad , \tag{11}$$

$$F_{div}[\mathbf{u}] = \frac{1}{\sigma_{div}^2} \sum_{k=1}^{NV} (\nabla \cdot \mathbf{u})_k^2 \Delta V_k \quad , \tag{12}$$

$$F_{reg}[\mathbf{u}] = \frac{1}{\sigma_{pen}^2} \sum_{k=1}^{NV} \mathbf{u}_k^2 \Delta V_k \quad . \tag{13}$$

The first two functionals represent, for applied transverse field $\mathbf{B}_{0x}$ and axial field $\mathbf{B}_{0z}$, respectively, the mean squared residual deviation of the measured induced magnetic fields $b_{i,meas}^{(B_0)}$ from the fields $b_i^{(B_0)}[\mathbf{u}]$ modeled according to equation (8). $F_{div}[\mathbf{u}]$ enforces the velocity field to be solenoidal, and $F_{reg}[\mathbf{u}]$ is the regularization functional which tries to minimize the kinetic energy. The parameters σ_{i,B_0} are assumed a-priori errors for the measurements of the induced fields. The parameter σ_{div} is chosen very small as it is a measure for the divergence the velocity is allowed to have. The parameter σ_{pen} determines the trade-off between minimizing the mean squared residual deviation of the observed fields and minimizing the kinetic energy of the estimated velocity field. The normal equations that follow from the minimization of the functional (9) are solved by Cholesky decomposition. By scaling the penalty parameter σ_{pen} one can derive the so-called Tikhonov's L curve, i.e., the mean squared residual in dependence on the penalty function. At the point of highest bending (the „knee") we get a good compromise between the fit of the modeled magnetic fields to the measured ones on one hand, and minimum kinetic energy on the other hand [10].

2. Experimental results

In order to demonstrate the feasibility of the contactless inductive velocity reconstruction method in real applications an experiment has been set up in which the propeller driven flow of a liquid metal has to be reconstructed solely from externally measured magnetic field data.

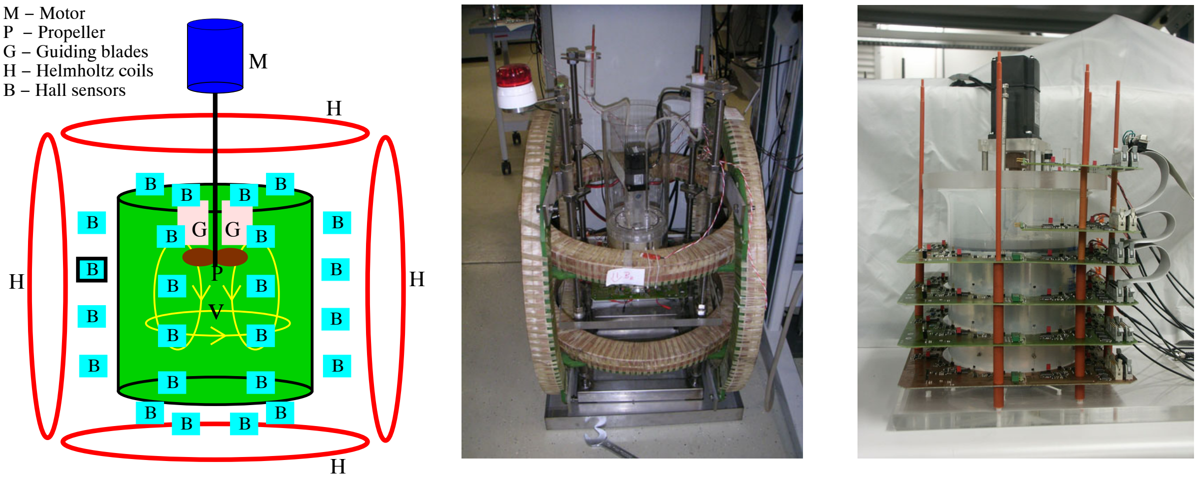

(a) (b) (c)

Fig. 1: The CIFT experiment. Schematic view (a), total view (b), and details of the vessel with the circuit boards for the Hall sensors and AD transformer.

Figure 1 shows the experimental set-up. We use 4.4 liters of the eutectic alloy $Ga^{67}In^{20.5}Sn^{12.5}$ which is liquid at room temperatures. Its density and electrical conductivity at 20°C are 6.36×10^3 kg/m^3 and 3.31×10^6 S/m, respectively. The flow is produced by a motor driven propeller with a diameter of 6 cm inside a polypropylene vessel with 18.0 cm diameter. The height of the liquid metal is 17.2 cm, giving an aspect ratio close to 1.

The propeller can rotate in both directions, resulting either in upward or downward pumping. The rotation rate can reach 2000 rpm producing a mean velocity of 1 m/s, which corresponds to an $Rm \approx 0.4$. The flow structure for the two directions is not symmetric for three reasons. At first, the propeller itself has a preferred direction. At second, it is positioned approximately at one third of the liquid height, measured from the top. At third, there are 8 guiding blades above the propeller, having two functions. For the downward pumping, they are intended to remove the upstream swirl in order not to deteriorate the pressure conditions for the propeller. For the upward pumping they remove the downstream swirl thus leaving the entire flow rather swirl-free. Hence, the downward pumping produces, in addition to the main poloidal roll, a considerable toroidal motion, too. For the upward pumping, this toroidal motion is, to a large extend, inhibited by the guiding blades. It was one of the tasks of the experiment to discriminate between those different flow structures.

Two pairs of Helmholtz coils are fed by currents of 22.5 Ampere and 32.5 Ampere, respectively, to produce alternately an axial and an tranverse field of 4 mT, which both are rather homogeneous throughout the vessel. Either field is applied for a period of 3 seconds, during which a trapezoidal signal form is used. The measurements are carried out for 0.5 seconds, 1 second after the plateau value of the trapezoidal current has been reached. Hence, we get an online monotoring with a time resolution of 6 seconds. The induced magnetic fields are measured with 49 Hall sensors, 8 of them grouped together on each of the 6 circuit boards which are located on different heights (Figs. 1a, 1c). One additional sensor is located in the center below the vessel.

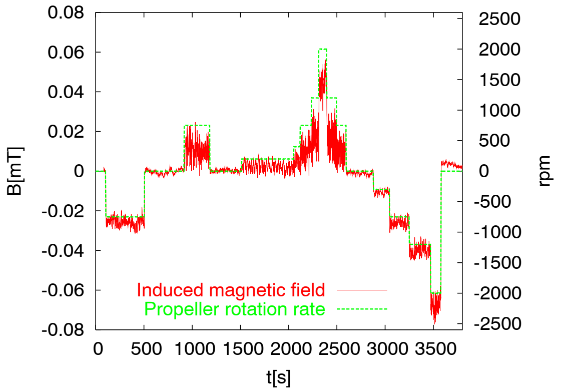

Fig. 2: Propeller rotation rate and Hall sensor signal during one run with applied axial field, as measured by the Hall sensor that is emphasized in Fig. 1a.

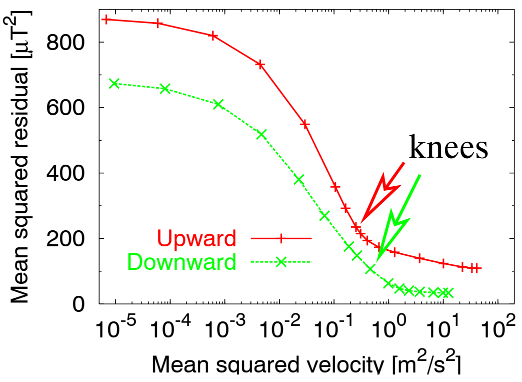

Fig. 3: Tikhonov's L curve, showing the rms in dependence of the mean energy. At the indicated "knees" one obtains a reasonable compromise between data fitting and minimum kinetic energy.

The basic problem for any practical application of the method is the reliable determination of small induced magnetic fields on the background of much larger imposed magnetic fields. For this it is indispensable to have an accurate control of the external magnetic field. In our configuration the current drift in the Helmholtz coils can be controlled with an accuracy of better than 0.1 per cent. This is sufficient since the measured induced fields are approximately 1 per cent of the applied field.

Another serious problem is the unavoidable temperature drift of the Hall sensors. This concerns their sensitivity as well as the offset. The sensitivity drift is connected with the temperature dependence of the semiconductors resistance and can be overcome by keeping the current constant. The offset problem is overcome by changing the sign of the applied magnetic field. For that purpose, we choose a trapezoidal signal form which changes its sign every 3 seconds. Figure 2 shows that by these means a stable measurement of the small induced field can be realized even over a period of one hour. After the measurement has been accomplished for the applied transversal field $\mathbf{B}_{0x}$, the same procedure is carried out for the applied axial field $\mathbf{B}_{0z}$. For both flow directions, Fig. 3 shows Tikhonov's L-curves with a clear „knee“ which is interpreted as the point with the physically most reasonable solution.

For upward and downward pumping, Figs. 4 and 5 show the induced magnetic fields measured at the 49 positions, and the inferred velocity field at 52 discretization points. In Fig. 4c we see the upward flow in the center of the cylinder and the downward flow at the rim, but nearly no rotation of the flow. In Fig. 5c we can identify the downward flow in the center and the upward flow at the rim, together with a rotation of the flow. This absence and presence of the swirl is an important feature which can evidently be discriminated by our method. It is worth to note that not only the structure of the flow, but also the range of the velocity scale is correctly reproduced by the inversion.

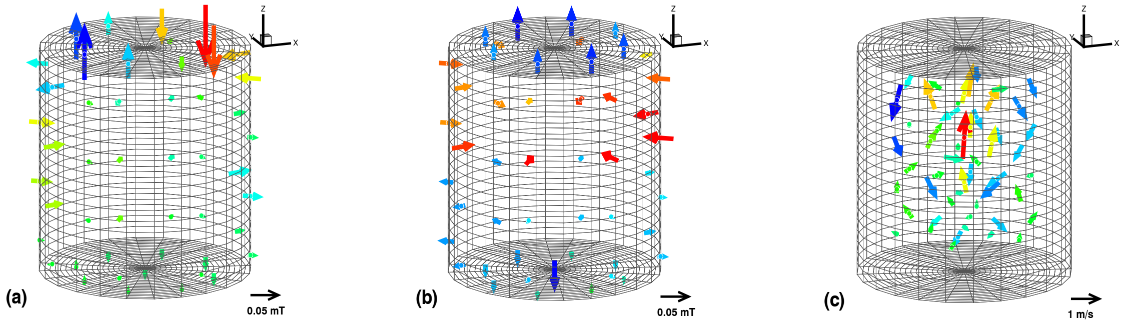

Fig. 4: The measured magnetic fields and the reconstructed velocity field for the case that the propeller pumps upward with 1200 rpm. Measured induced field for transversal applied field (a); measured induced field for applied axial field (b); and reconstructed velocity (c). For (a) and (b) the color coding discriminates between ingoing and outgoing magnetic field lines. For (c) the color coding mirrors the axial component of the velocity.

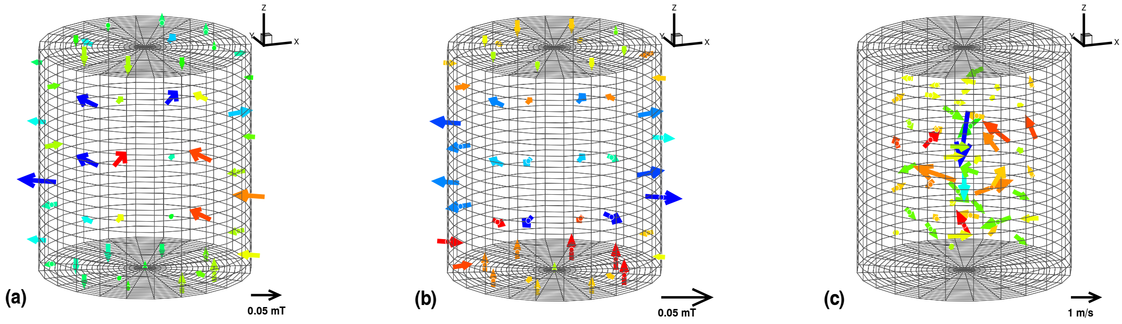

Fig. 5: The same as Figure 4, but for the propeller pumping downward with 1200 rpm.

4. Conclusions and prospects

Flow measurement based on induced electric potentials has a long tradition and a lot of practical applications [3]. The change from induced electric potentials to induced magnetic fields allows a completely contactless measuring technique for those flows whose magnetic Reynolds number is not too small. In a liquid metal experiment, we have put into practice a first version of contactless inductive flow tomography (CIFT), using two orthogonal imposed magnetic fields. A particular power of CIFT consists in a transient resolution of the full three-dimensional flow structure in steps of a few seconds. Due to its weakness, the externally applied magnetic field does not influence the flow to be measured. However, CIFT is also possible in cases where stronger magnetic fields are already present for the purpose of flow control, as, e.g., the electromagnetic brake in steel casting or the DC-field components in silicon crystal growth. The challenges for the future lay with improving the depth resolution of the method by using magnetic fields with variable frequency on one hand, and with the extension of the method to inverse dynamo problems with larger magnetic Reynolds numbers, on the other hand.

Acknowledgement

This work was supported by Deutsche Forschungsgemeinschaft under grant GE 682/10-1/2.We thank Heiko Kunadt for manufacturing the mechanical part of the experiment, and Bernd Caspar for designing the circuit boards.

References

[1] S. Eckert, G. Gerbeth, F. Stefani, and W. Witke (2003), Measuring techniques for liquid metal velocity measurements, in P.D. Lee, A. Mitchell, J.-P. Bellot, A. Jardy (Eds.), Proceedings of the 2003 International Symposium on Liquid Metal Processing and Casting (LMPC 2003) (pp. 261-271), Nancy

[2] A. Gailitis, O. Lielausis, E. Platacis, G. Gerbeth, and F. Stefani (2002), Laboratory experiments on hydromagnetic dynamos, Rev. Mod. Phys., 74, 973

[3] J. A. Shercliff (1962), The theory of electromagnetic flow-measurement, Cambridge, Cambridge University Press

[4] F. Stefani and G. Gerbeth (1999), Velocity reconstruction in conducting fluids from magnetic fields and electric potential measurements, Inverse Problems, 15, 771

[5] M. Xu, F. Stefani, and G. Gerbeth (2004), The integral equation method for a steady kinematic dynamo problem, J. Comp. Phys., 196, 102

[6] M. Xu, F. Stefani, and G. Gerbeth (2003), An integral equation approach to time-dependent kinematic dynamos in finite domains, Phys. Rev E, in press

[7] F. Stefani, G. Gerbeth (2000), On the uniqueness of velocity reconstruction in conducting fluids from measurements of induced electromagnetic fields, Inverse Problems, 16, 1

[8] F. Stefani, G. Gerbeth, A contactless method for velocity reconstruction in electrically conducting fluids (2000), Meas. Sci. Technol., 11, 758

[9] M. Hämäläinen, R. Hari, R. J. Knuutila, and O. V. Lounasmaa (1993), Rev. Mod. Phys., 65, 413

[10] P. C. Hansen (1992), Analysis of discrete ill-posed problems by means of the L-curve, SIAM Review*,* 34**,** 561

DEPRESSURIZATION OF REACTING BATCHES

Günther Hessel, Holger Kryk, Wilfried Schmitt, and Nurelegne Tefera[1]

1. Introduction

For sizing emergency relief systems of stirred tank reactors (STR) and for assessing safety relevant process states it is of vital importance to be aware of the hydrodynamics, the thermodynamics and the reaction kinetics during the reactor pressure relief. Also the accuracy of numerical calculations strongly depends on the accuracy of the sub-models to consider processes like heat and mass transfer, thermodynamics and reaction kinetics. Therefore, the aim of this work is the refinement of the modeling of the sub-processes under consideration of process conditions, which are typical for reactor pressure relief. Furthermore, experimental investigations of reaction driven pressure relief events in stirred tank reactors were carried out in order to provide a pool of process data sets for improvement and validation of computer codes like BRICK (one dimensional simulation of pressure relief events developed by the FZR [1]) and of CFD modeling.

2. Kinetics of the test reaction

As a test reaction for the investigation of the pressure relief process, the "well-known" esterification of acetic anhydride with methanol was chosen:

$$\begin{array}{ccccccc} (CH_3CO)_2O & + & CH_3OH & \rightarrow & CH_3COOCH_3 & + & CH_3COOH \\ \textit{acetic anhydride} & & \textit{methanol} & & \textit{methyl acetate} & & \textit{acetic acid} \\ \textit{AAH} & & \textit{ME} & & \textit{MA} & & \textit{AA} \end{array}$$

To separate the reaction enthalpy from the mixing enthalpy, calorimetric measurements in the reaction calorimeter RC1 were carried out along a linear temperature ramp from 17°C up to 80°C. The molar reaction enthalpy of $\Delta H_R = -66$ kJ/mol was determined.

Safety studies require a kinetic reaction model that is able to reproduce the thermal reaction course over a wide temperature range. For this purpose, up to now the kinetic models were usually developed by measurements performed in an adiabatic calorimeter where the temperature dependence is mainly fitted exactly. For improving the numerical simulation of the reactor pressure relief, a rigorous kinetic reaction model is necessary to reproduce exactly the thermal reaction course and the concentration profiles of reactants, intermediates and products both over wide temperature and concentration ranges. Moreover, this kinetic model should also describe the depressurization during different process control strategies correctly.

To check the applicability of the kinetic models, fitted by adiabatic experiments, isothermal esterification reactions at several temperatures and educt concentrations were carried out using the RC1 equipped with an in situ FTIR spectrometer. Figure 1 shows the thermal reaction course of an isothermal esterification compared to simulation results using kinetic models taken from the literature [2,3,4]. Especially, the thermal process behavior at the start phase of the reaction is not describable by the structure of the models. The acceleration of the reaction rate at the beginning of the process could be caused by autocatalytic effects (i.e. by generating acetic acid) and/or influences of side reactions (esterification of acetic acid and hydrolysis).

---

[1] Addis Ababa University, Faculty of Technology

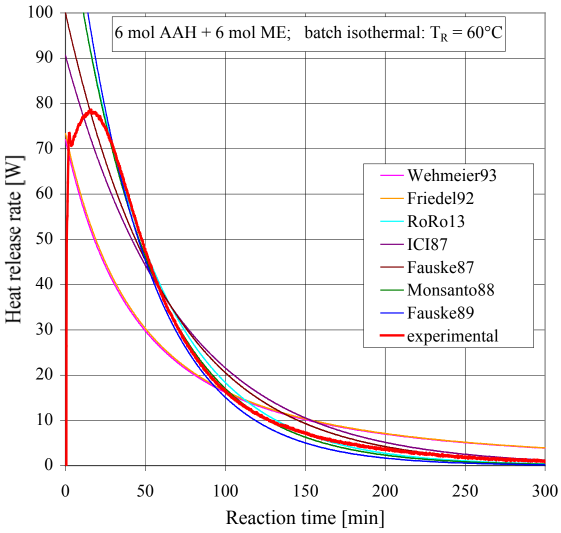

Fig.1: Thermal reaction course of the isothermal esterification

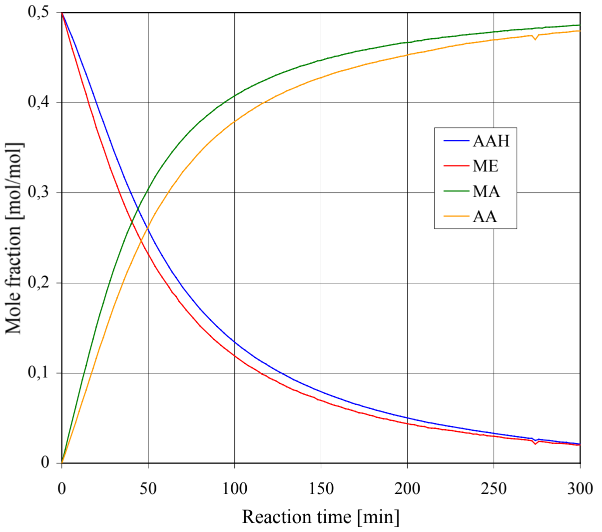

Fig.2: Concentration profiles during the esterification

For a more detailed characterization of the reaction course, additional information on the chemical composition of the reaction mixtures is necessary. By calibrating the FTIR spectrometer using samples of known concentrations, a method was found to generate concentration profiles of the educts and products on the basis of on-line FTIR measurements. Figure 2 shows the concentration profiles of the isothermal esterification. The delayed formation of AA points out the accumulation of an intermediate product during the reaction. However, preliminary simulation results indicate an additional influence of autocatalytic effects. Due to the complexity of the reaction mechanism, the following general approach was developed to fit the kinetic models, which are valid for wide temperature and concentration ranges:

- Setting up and/or choice of the model structures and estimations of the model parameters by means of isothermal experiments in the RC1/ FTIR,
- Adjustment of the model coefficients using esterification experiments in the adiabatic calorimeter PhiTecII in order to enlarge the ranges of validity,
- Verification of the models by isoperibolic experiments under process-like conditions.

On the basis of the present results, the following reaction mechanism is assumed:

- Uncatalyzed esterification of acetic anhydride,
- Esterification of acetic anhydride catalyzed by the formed acetic acid,
- Esterification of acetic acid,
- Hydrolysis of acetic anhydride.

The modeling of the reaction kinetics is still in progress.

3. Pressure relief experiments

3.1 Experimental studies under adiabatic conditions

By using the adiabatic calorimeter PhiTecII connected with a quenching unit, reactive pressure relief experiments can be performed under adiabatic conditions. They were used to:

- Predefine experiment conditions for the pressure relief experiments in the miniplant,
- Complete the data pool for improvement and validation of the computer codes for adiabatic experiments and
- Characterize chemical compositions of the reactor contents and the discharged mixtures by FTIR measurements.

For characterizing the chemical compositions of the discharged substances by FTIR measurements, a modified experimental setup was used as depicted in Figure 3.

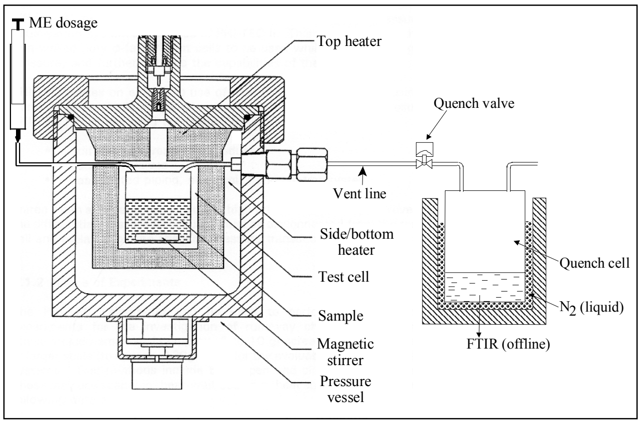

Fig.3: Experimental setup for the pressure relief in PhiTecII

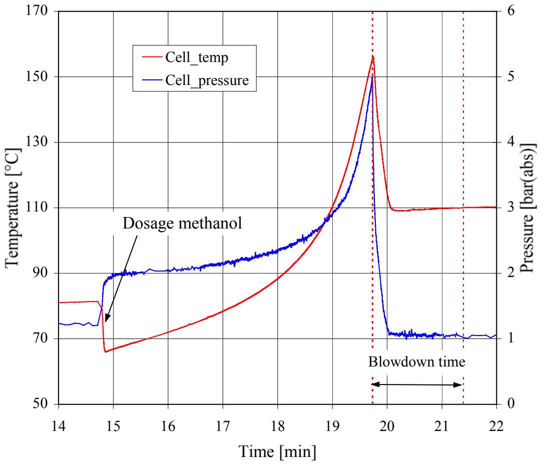

Fig.4: Temperature and pressure profiles during an adiabatic pressure relief

To stop further chemical reactions, the discharged mixture was fed into a quench cell cooled by liquid nitrogen. After disconnecting the quench cell, the discharged substances could be analyzed by FTIR spectrometry. With the help of this method, useful information on the process state during the blowdown time event was obtained. Sets of pressure relief experiments were carried out by the variation of the initial temperature (T_{start}), the temperature at the starting point of the relief (T_{relief}), the time period of the relief (Δt_{relief}) and of the initial concentrations of the educts ($n_{ME} : n_{AAH}$). To determine the masses of the discharged mixtures, the reaction cell and the quench cell were weighted after each experiment. Figure 4 shows the temperature and pressure profiles of an adiabatic pressure relief. Tables 1 and 2 summarize the results of selected experiments. The proportion of the discharged mixtures M_{dis} referring to the initial mass of the reactor content and the results of the FTIR measurements are documented versus the blowdown time period and the relief temperature. As can be seen from the results of FTIR measurements, all components of the process are present in the discharged mixtures. Therefore, subsequent reactions of the discharged components inside the vent line and in the quench cell are to be considered in the case of a pressure relief.

Tab.1: Masses and chemical compositions of discharged mixtures in dependence on blowdown time period

Δt_{relief} [s]	M_{dis} [Ma%]	concentrations [mol/mol]			
		AAH	ME	AA	MA
5	11	0.46	0.35	0.08	0.11
10	14	0.31	0.38	0.12	0.19
100	23	0.45	0.17	0.15	0.23
experimental conditions: $n_{ME} : n_{AAH}$ = 1mol : 2.5mol ; T_{start} = 65°C ; T_{relief} = 135°C					

Tab.2: Masses and chemical compositions of discharged mixtures dependence on the relief temperature

T_{relief} [°C]	M_{dis} [Ma%]	concentrations [mol/mol]			
		AAH	ME	AA	MA
115	14	0.50	0.20	0.17	0.13
135	23	0.45	0.17	0.15	0.23
155	51	0.50	0.10	0.17	0.23
experimental conditions: $n_{ME} : n_{AAH} = 1\text{mol} : 2.5\text{mol}$; $T_{start} = 65°C$; $\Delta t_{relief} = 100$ s					

The different concentrations depending on the blowdown time period according to Tab.1 indicate that the concentrations of the components vary during the pressure relief. This is caused on one hand by the different vapor pressures of the components in conjunction with the steep pressure and temperature reductions, and on the other hand by the continuation of the chemical reaction inside the reactor during the pressure relief. The variations of the concentrations depending on the relief temperature (see Tab.2) are determined by the different vapor pressure ratios of the components and by the different degrees of reaction at the time of initiating the pressure relief. By measuring the concentrations of the discharged components, useful information on the thermo-physical properties of the discharge streams can be deduced.

3.2 Pressure relief experiments under process-like conditions

Reaction driven pressure relief experiments under process-like conditions are the essential experimental studies, which are focused on the refinement of the modeling of the subprocesses in order to enhance and validate the computer codes. For this purpose, the following experimental investigations are necessary in detail:

- Pressure relief experiments at isoperibolic process control in order to generate process data sets for code validations,
- Observation of the pressure relief using high-speed video technique to detect the bubble up and foaming behaviors,
- Esterification without a pressure relief for the verification of the reaction kinetics and
- Nonreactive experiments for estimation of heat and mass transfer coefficients.

To lay the experimental foundations for the investigations, the automatic laboratory reactor (ALR/ miniplant) was modified as pictured in Fig.5.

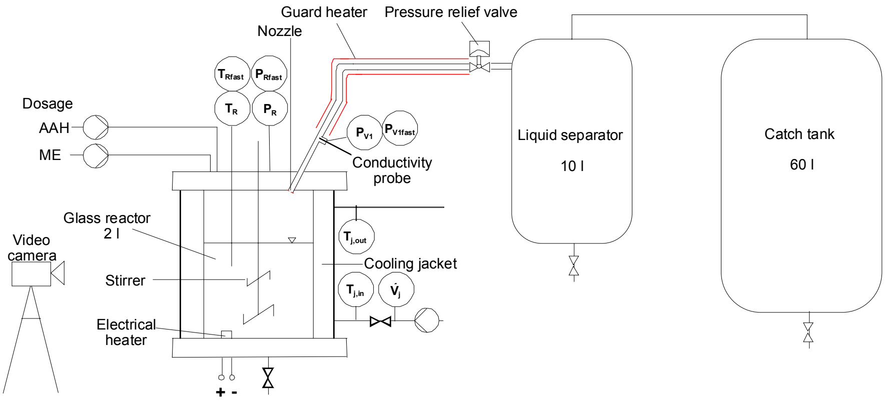

Fig.5: Experimental setup for pressure relief experiments in the miniplant

The reactions are carried out in a 2-liter STR. By positioning the discharge nozzle at the lower edge of the top cover of the reactor, the inflow behavior of the substances into the nozzle can be observed. The nozzle is replaceable to permit experiments using different critical discharge areas. The vent line is equipped with an electrical guard heater to avoid condensation processes inside the pipe. An electrical heater inside the reactor allows the experimental assessment of heat transfer coefficients and other thermodynamic plant parameters. Additional to the integrated process measurement instrumentation, the most significant signals, like the reactor pressure p_R, the reactor temperature T_R and the pressure behind the nozzle p_{v1}, can be measured by means of fast signal detection systems at measuring frequencies up to 200 Hz (fast signals). To estimate the dynamic vapor fraction of the discharged streams, a special needle-shaped conductivity sensor was developed which is placed behind the nozzle.

The experimental conditions were predefined on the basis of adiabatic experiments. To provoke a pressure relief event that is driven by the exothermal reaction, the accumulation of both reactants is necessary. This can be realized under utilization of the stratification effect by stopping the stirrer and dosing the methanol above the liquid surface of the acetic anhydride. According to real hazardous incidents, the following experimental procedure was chosen:

- Dosing the acetic anhydride,
- Heating up the reactor content to the desired temperature,
- Stopping the stirrer,
- Dosing the methanol,
- Initiating the reaction by starting the stirrer,
- Starting the pressure relief by opening the magnetic pressure relief valve.

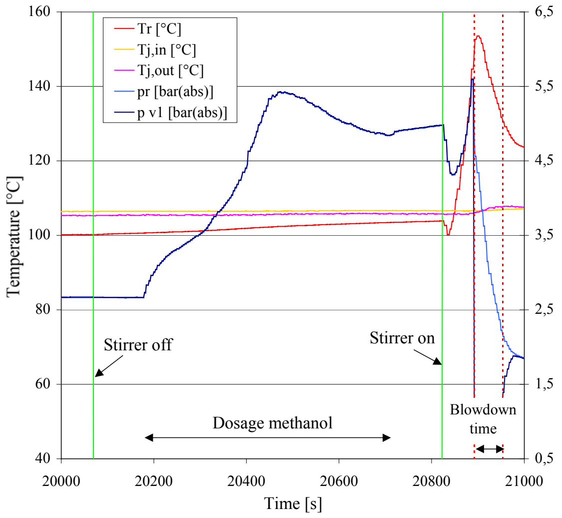

Fig.6: Test procedure of pressure relief experiments under process-like conditions

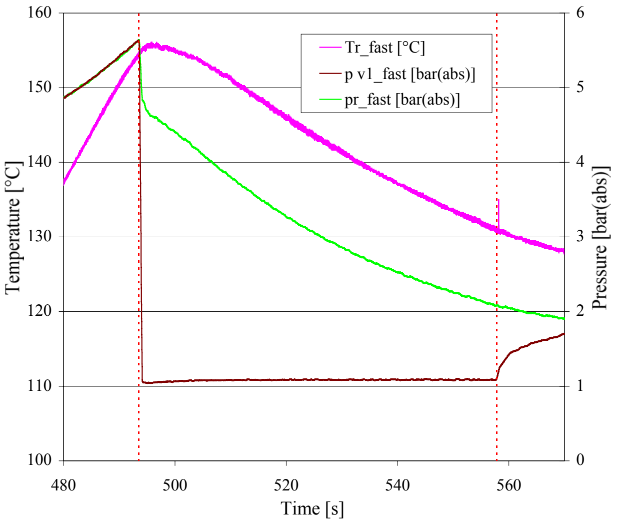

Fig.7: Temperature and pressure profiles of the fast signals during a pressure relief

Fig. 6 shows the process signals during a pressure relief in the miniplant. The increases of the reactor temperature as well as of the reactor pressure during the reaction are effected by the exothermic process. The slight decrease of the reactor temperature immediately at the beginning of the mixing process is caused by the mixing enthalpy whereas the steep decrease of the pressure is caused by the absorption of the gas into the reaction mixture. Thus, effects induced by mixing phase thermodynamics as well as mass transfer processes are to be considered by means of related model components. Temperature and pressure profiles during a pressure relief measured by the fast signal detection are shown in Fig. 7. By choosing measuring frequencies of 200 Hz for each signal, different stages of the pressure relief process could be monitored. The steep increase of the reactor pressure immediately after the opening of the pressure relief valve characterizes the discharge of the gas phase. Due to the pressure increase, the reaction mixture starts boiling and a gas-vapor mixture is discharged followed by a two-phase flow. These processes can be observed by an abrupt decreasing of the pressure gradient. The registration of these sub-processes provides important information for a better understanding of the pressure relief process in theory as well as for improvements of simulation software.

4. Summary and Outlook

Experimental methods were developed in order to refine the modeling of the sub-processes under consideration of process conditions, which are typical for pressure relief events. This was associated with upgrading and modifications of experimental facilities and techniques with the help of chemical on-line and off-line analysis.

In the case of the reaction kinetics it was found that conventional models generated as a result of adiabatic experiments are insufficient to describe the thermal and chemical reaction course over wide temperature and concentration ranges. Consequently, experimental approaches and advanced model structures were developed. Additional calorimetric experiments using improved analytical methods are necessary to evaluate the models. Furthermore, nonreactive experiments are planned for investigations of mixing phase thermodynamic behaviors.

Pressure relief experiments under adiabatic conditions were carried out to define optimal experimental conditions for experiments under process-like conditions. A method was developed to characterize the chemical composition of the discharged mixtures whereas subsequent reactions of the substances among themselves were prevented. All components contained in the mixtures may be evidenced using FTIR measurements. Moreover, the varying of the concentrations during the pressure relief event was detected. For more assured quantitative results, a further refinement of the analytical methods is in progress. The results are of vital importance for the characterization of the discharge streams and for the safety-oriented evaluation of pressure relief events in view of subsequent processes.

Primarily, the pressure relief experiments in the miniplant are used to generate process data sets to improve and validate the computer codes. By optimization of the experimental setup and the experimental conditions, a process control was realized which is similar to industrial processes. First experimental results are available. Further experiments are necessary to enlarge the data pool. New sensors and detection methods will be tested to monitor the dynamic discharge mass flow and the steam content. Additional experiments are planned in order to investigate effects of heat and mass transfer during pressure relief processes.

References

[1] D. Lucas (2000), BRICK - a one-dimensional simulation tool for multiphase flow in vessels, Chemical Engineering and Technology, 23, 845-849

[2] G. Wehmeier (1994), Theoretische und experimentelle Untersuchung der Vorgänge bei der Druckentlastung von Chemiereaktoren, Fortschr.-Ber. 3, 373, VDI Düsseldorf

[3] L. Friedel and G. Wehmeier (1991), Modelling of the vented methanol/ acetic anhydride runaway reaction using SAFIRE, J. Loss Prev. Process Ind., 4, 110-119

[4] J. C. Leung, M. J. Creed and H. G. Fisher (1989), Round-robin “Vent sizing package” results, Int. Symp. Runaway React., 264-280

MAGNETIC CONTROL OF THE FILLING PROCESS IN ALUMINUM INVESTMENT CASTING

Vladimir Galindo, Sven Eckert, Willy Witke, and Gunter Gerbeth

1. Introduction

The investment-casting process using the lost-wax method allows for a high variability of shapes and guarantees high accuracy and excellent surface quality.

The objective of this project is to control the velocity of an aluminum melt during the pouring process into the mould. The main problem is the occurrence of large velocity values at the beginning of the casting process leading to an increased generation of vortices inside the pouring channel. A high rate of turbulence in the flow means also a high risk to transport impurities, oxides or gas bubbles from the walls and the free surface, respectively, into the bulk of the casting patterns. The result is a deterioration of the mechanical properties of the casting products.

The approach we follow is the application of a transverse DC magnetic field to reduce the velocity of the melt. The task was to propose a design for a magnetic system and to find an optimal position for it at the mould.

2. Numerical Simulation

Numerical calculations were performed using the commercial, finite-element code FIDAP (FLUENT Inc.). The term for the electromagnetic Lorentz force was implemented into the code by a user defined subroutine. Moreover, an additional equation for the electric potential was solved (see equation 6). For the numerical simulations we took over the exact geometries both of the perspex model used in the model experiments with the eutectic liquid metal InGaSn (see Fig. 1 and 2) as well as the realistic configuration of the aluminum casting process.

The melt flow was simulated using the time dependent Navier-Stokes equation with the electromagnetic force density term (Lorentz-force density)

$$\vec{f_L} = \vec{j} \times \vec{B} \tag{1}$$

and taking into account the incompressibility condition $div\ \vec{v} = 0$:

$$\rho \left(\frac{\partial \vec{v}}{\partial t} + (\vec{v} \cdot \nabla)\vec{v} \right) = -\nabla p + \eta\ \nabla^2 \vec{v} + \vec{f_L} \tag{2}$$

where $\vec{v}$ is the velocity vector field, p the pressure, ρ the density, η the dynamic viscosity, $\vec{j}$ the electric current density and $\vec{B}$ is the magnetic field induction.

The flow in the melt is for the considered dimensions and velocities no more laminar. For the computation of the mean flow two turbulent models were taken into account: the 0-equation turbulence model according to the Prandtl mixing length hypothesis and the standard $k - \epsilon$ turbulence model.

With Ohm's law

$$\vec{j} = \sigma \left(-\nabla\Phi + \vec{v} \times \vec{B} \right) \tag{3}$$

and the magnetic field directing in y-direction (see Fig. 1), the following expression for the electromagnetic force density results:

$$\vec{f}_L = \sigma\, B \left\{ \left(\frac{\partial\, \Phi}{\partial\, z} - v_x\, B \right) \vec{e}_x + \left(-\frac{\partial\, \Phi}{\partial\, x} - v_z\, B \right) \vec{e}_z \right\} \tag{4}$$

The electric potential Φ is determined by the Kirchhoff's law

$$div\; \vec{j} = 0 \tag{5}$$

resulting in the following additional equation:

$$\nabla^2 \Phi + B \left\{ \frac{\partial\, v_z}{\partial\, x} - \frac{\partial\, v_x}{\partial\, z} \right\} + v_z \frac{\partial\, B}{\partial\, x} - v_x \frac{\partial\, B}{\partial\, z} = 0 \tag{6}$$

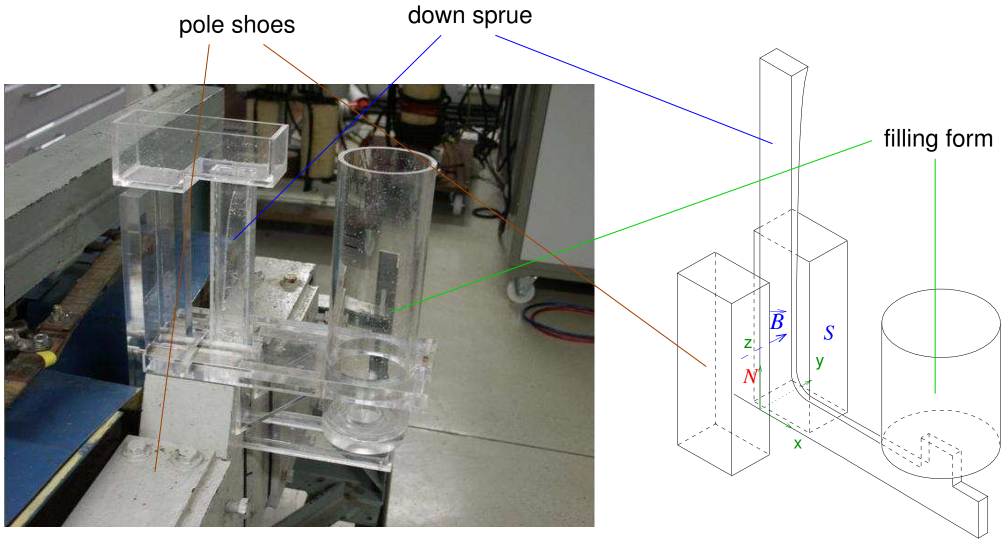

Fig. 1: Perspex model of a casting pattern positioned at the magnetic field system

For the numerical solution of eqs. (1)-(3), the following boundary conditions are used:

- The channel walls are electrically insulating.
- No-slip condition at the walls, i.e. the velocity is zero at the walls.

Numerical simulations of the time dependent filling process were carried out for the model system using InGaSn as well as the real aluminum casting unit. Different locations and field strength of the applied magnetic field have been investigated. The free melt surface in the up-comer has been treated using the volume of fluid method.

Figure 2 shows snapshots of the velocity field for the starting and intermediate periods of the process. Both figures clearly demonstrate the damping effect of the applied magnetic field and, in particular, the reduction of the velocity maxima occurring at the inner part of the bend region.

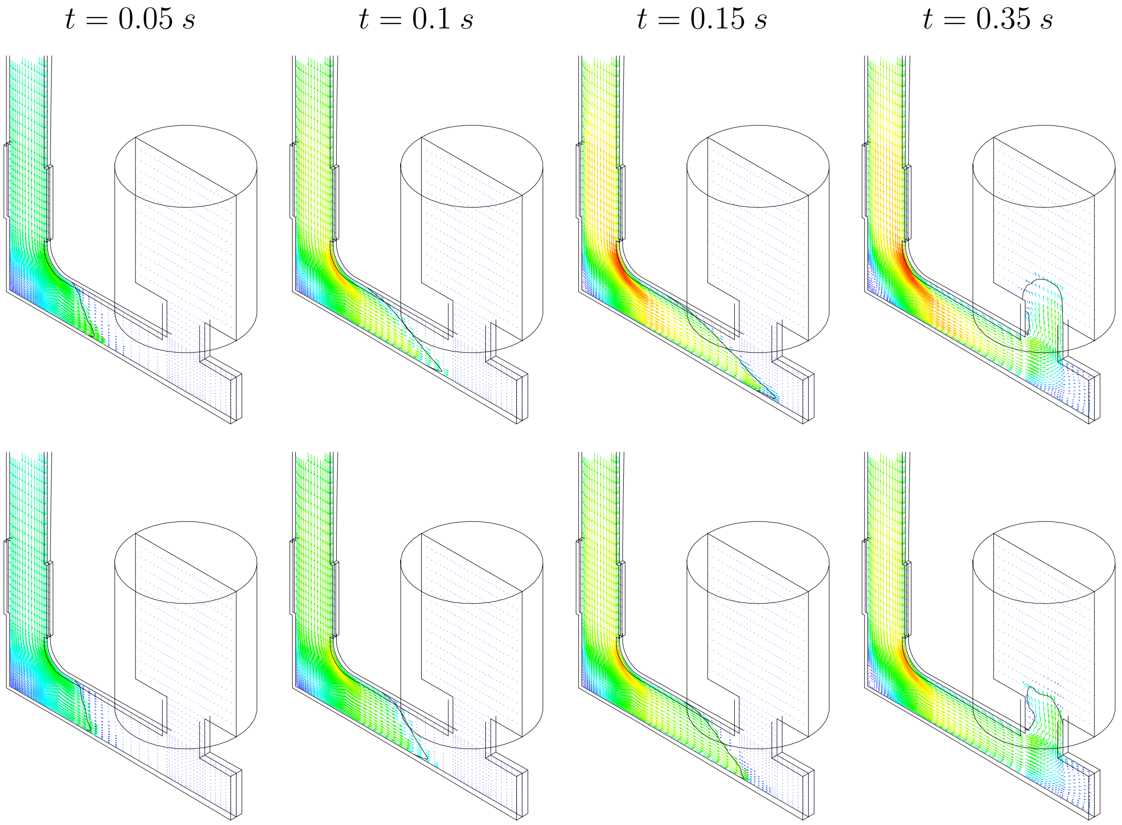

Fig. 2: Numerical simulation of the filling process starting period without (above) and with (below) an applied magnetic field of $0.5\ T$.

3. Experimental Investigations

Experiments were carried out not only using a perspex model and the eutectic melt InGaSn which is liquid at room-temperature, but also in industrial scale during the filling process of the aluminum investment casting.

During the pouring experiments with InGaSn velocity profiles were measured by means of the Ultrasound Doppler Velocimetry (UDV) [1]. The ultrasonic transducer was acoustically coupled to the channel wall. Velocity profiles were determined along the vertical pouring down sprue as well as along the horizontal channel.

In addition, the integral flow rate was measured by an inductive flow rate sensor. This flow rate measurement is of particular importance for the filling process since a more tailored flow control by the magnetic field needs a reliable flow rate measurement. Figure 3 shows a sketch of this contact-less flow meter. It consists of one emitter and two receiver coils. The emitter coil generates an alternating magnetic flux going through the fluid and the receiver coils. This flux is split into two partial fluxes by means of a ferrous flux guide. These partial fluxes are of equal magnitude if the fluid is at rest, thus causing equal voltage in each of the receiver coils. If the electrically conducting fluid is in motion, eddy currents are induced which amplify one partial flux while reducing the other. This leads to different induced voltages in the receiver coils. The voltage difference between both receiver coils is a direct measure for the integral flow rate. Note that this flow rate measuring device has been tested at the low-temperature model, and applied to the aluminum case afterwards.

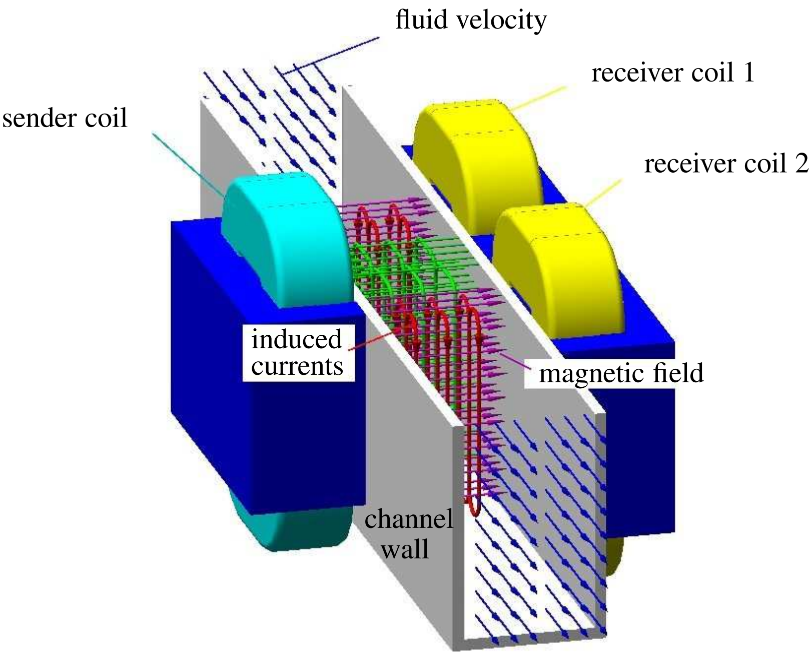

Fig. 3: Sketch of the contact-less flow rate sensor

Furthermore, the transparency of the wall material allowed for visual observations of the filling process of the perspex model. By this visual assessment and by means of UDV the occurrence of gas bubbles inside the flow channel could be detected.

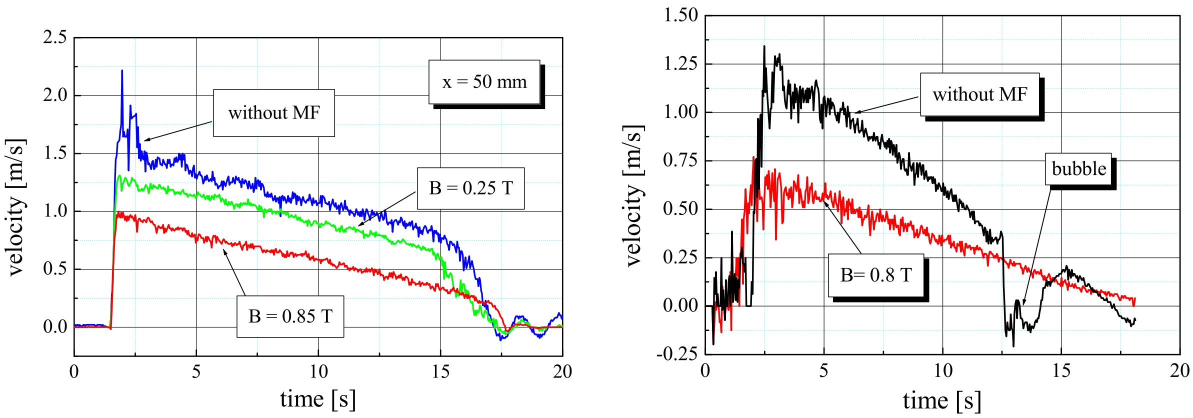

a) down sprue (5 cm distance from the bottom) b) horizontal channel

Fig. 4: Velocity measurements obtained by means of UDV for different magnetic field values

The experimental investigations demonstrated the effect of the magnetic field on the velocity of the pouring liquid metal. Figure 4 shows UDV measurements of the velocity obtained in the vertical pouring down sprue and in the horizontal channel, respectively. The application of the DC magnetic field reduces the measured velocities at any time, especially, a significant reduction of the maximum velocity peaks is observed at the beginning of the pouring process. In Figure 4b) a typical signature for a bubble passing the measuring volume can be observed, too. The UDV measurements as well as our visual observations indicate that not only the amplitude of the velocity will be decreased if the flow is exposed to the external magnetic field. In addition, the fluctuation of the velocity becomes smaller and the amount of gas inclusions in the bulk flow is reduced in a significant way.

The experimental data obtained from the model experiments were the basis for the validation of the numerical calculations. For instance, the dependence of the flow rate on the magnetic field strength was studied. Figure 5 shows a comparison of the flow rate as a function of the magnetic field related to the flow rate determined for the case without magnetic field. A qualitative agreement between numerical calculation and experiment can be noted.

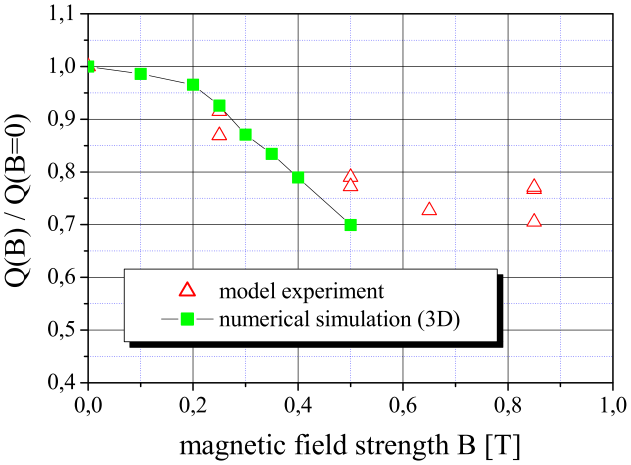

Fig. 5: Comparison of numerical and experimental results regarding the flow rate Q as a function of the magnetic field strength (related to the flow rate obtained at $B = 0$)

The validated, numerical code was an important tool to design the prototype of a magnetic system for the real aluminum investment-casting process. This magnetic system was manufactured and successfully installed at an industrial facility. First tests showed a significant prolongation of the filling time of the casting patterns. Another test was made using an open casting mould with an outflow pipe (see Figure 6). The length of the resulting flow parabola was obviously reduced with increasing magnetic field intensity. In addition, the flow meter was successfully applied to the aluminum filling process.

Fig. 6: Braking effect of the magnetic field (shorter outflow parabola)

4. Conclusions

A better understanding of the flow phenomena and filling processes of the investment casting of aluminum alloys requires better knowledge about the flow fields inside the moulds. Hence, velocity and flow rate measurements are needed. Though a first successful application of the ultrasonic Doppler velocimetry to an aluminum melt has been reported [2], its use under industrial conditions is strongly hampered because of the limited access to the melt.

To fill in this gap, the low-temperature metallic melt InGaSn has been used for model experiments. The key advantage of it consists in the fact that at this temperature a sufficient number of different measuring techniques are available. That gives the opportunity to model the filling processes in a range of characteristic transport parameters being very close to reality, with the advantage of having access to measurements as in the case of water model experiments. Validation of numerical codes at those liquid metal models provides, obviously, a profound basis for an extrapolation of the numerics to the real-scale problem.

The external magnetic field was used to damp particularly the high flow velocities of the melt at the beginning of the filling process. A significant reduction of the peak velocity at the beginning of the filling process has been shown by model experiments and numerics, and has been demonstrated in the real aluminum casting process afterwards. As an important input for the control system, a contact-less flow rate sensor has been developed and successfully applied to the aluminum casting process.

References

[1] S. Eckert, G. Gerbeth, F. Stefani, W. Witke: Measuring techniques for liquid metal velocity measurements, Proceedings LMPC, Nancy, Sept. 2003

[2] S. Eckert, G. Gerbeth, T. Gundrum, F. Stefani, W. Witke: New approaches to determine the velocity field in metallic melts. EPM 2003, 4th Int. Conference on Electromagnetic Processing of Materials, Lyon (France), Oct. 14-17,2003, Proc. PL13

VALIDATION OF COUPLED NEUTRONICS / THERMAL HYDRAULICS CODES FOR VVER REACTORS (VALCO)

Frank-Peter Weiss[1], Siegfried Mittag[1], Siegfried Langenbuch[2], Timo Vanttola[3], Anitta Hämäläinen[3], András Keresztúri[4], Jan Hádek[5], Petr Darilek[6], Petko Petkov[7], Alexander Kuchin[8], Peter Hlbocky[9], Dusan Sico[10], Serge Danilin[11], and David Powney[12]

1. Introduction

Modern safety standards require the modelling of complex transients where there is a strong interaction between the thermal-hydraulic system behaviour and space-dependent neutron kinetics. Therefore, the project is aimed at the improvement of the validation of coupled neutronics / thermal-hydraulics codes especially for VVER reactors. These coupled codes need to be validated against well-specified NPP transient scenarios.

The EU FP5 VALCO project is partially based on results earlier obtained within the EU Phare project (SRR1/95) (Ref. [1,2]). Two selected transients, one for each a VVER-440 and a VVER-1000, were analysed in this former project by different coupled-code systems. The calculated results were compared with measured transient data from original NPPs. However, in both transients, there were significant differences in the calculated reactor power, which were suspected to be due to differences in the control rod efficiencies and in the dynamic thermal physics of the fuel rod model that affects the Doppler feedback. To study neutronics effects separately, it was therefore recommended to validate the neutronics codes including the nuclear cross section data against measurements in zero-power reactors.

Furthermore, in recent years recommendations have been given for safety analyses to complement best estimate calculations by quantitative uncertainty analyses. Uncertainty analysis is needed to enable useful conclusions from best-estimate codes; otherwise single values of unknown accuracy would be used for comparison with certain limits of acceptance.

Based on these former conclusions, the primary work programme of the current project has been derived.

2. Work programme

While the transients analysed in the Phare SRR1/95 project were initiated by perturbations in the secondary circuit, transients caused by actions in the primary circuit are of special interest to the current project, e.g. transients initiated by switching-off main coolant pumps. The pur-

---

[1] Forschungszentrum Rossendorf e.V., FZR (D)
[2] Gesellschaft für Anlagen- und Reaktorsicherheit (GRS) mbH (D)
[3] Technical Research Centre of Finland, VTT (FIN)
[4] KFKI Atomic Energy Research Institute, AEKI (HU)
[5] Nuclear Research Institute Rez, plc, NRI (CZ)
[6] VUJE Trnava a.s. (SK)
[7] Institute for Nuclear Research and Nuclear Energy, INRNE (BG)
[8] State Scientific and Technical Centre on Nuclear and Radiation Safety, SSTCNRS (UA)
[9] SE, a.s.EBO, o.z., Jaslovské Bohunice (SK)
[10] SE, a.s.EBO, o.z., Mochovce (SK)
[11] Russian Research Center “Kurchatov Institute”, KI (RU)
[12] Serco Assurance, Winfrith (UK)

pose of Work Package 1, led by VTT, is therefore to extend and qualify the measurement data base for the validation of coupled codes. The analyses of new transients are to be performed with the following coupled codes: DYN3D-ATHLET, KIKO3D-ATHLET, BIPR8-ATHLET and HEXTRAN-SMABRE.

The previous transient analyses have shown that the results of calculations depend on various input parameters of the codes, model options, nodalisation etc. On the one hand, different macroscopic cross section libraries and other physical model parameters have caused deviations between the different code options. On the other hand, differences in the results of transient analyses were observed, when calculations were performed by using the same code system and input deck, but by different users. These findings initiated to adapt and apply an uncertainty analysis method to coupled codes, which is the main objective of Work Package 2, under the leadership of GRS. The first step of the uncertainty analysis is to identify and quantify all potentially important input parameters including their uncertainty bands and probability distributions. The propagation of the input uncertainties through the code runs provides the related probability distributions for the code results.

To separate the pure neutron kinetics effects from feedback effects, a specific validation of neutron kinetics (”neutronics”) models is to be performed in Work Package 3, led by FZR, by calculations of kinetics experiments, carried out in the V-1000 zero power test facility of the Kurchatov Institute Moscow. A broad spectrum of measurements is available. The V-1000 data are considered a unique material for the validation of neutron-kinetic codes for hexagonal fuel-assembly geometry. In a first validation step, measured V-1000 steady-state power distributions can be used to validate the three-dimensional two-group diffusion models, which form the ”stationary kernels” of the respective neutron-kinetics (dynamic) codes applied in the transient calculations. Results of two transient experiments carried out in the V-1000 zero power test facility have to be made available, in which different control rods were moved. These transients are to be calculated by the three-dimensional neutron kinetics codes DYN3D, HEXTRAN and KIKO3D. Libraries of two-group diffusion and kinetics parameters have to be generated, as a part of the project, by multi-group transport cell codes for the V-1000 fuel assemblies as well as for the radial and axial reflectors of the core.

3. Main achievements

3.1. Work package 1: Validation of coupled codes against measured VVER transients

Five new VVER transients were documented and added to the data base, that can be used for the validation of coupled neutronics / thermal-hydraulics codes. Coupled code validation was done with the different code combinations for the following two transients:

- Drop of a control rod at nominal power at Bohunice-3 (VVER-440),
- Coast-down of 1 from 3 MCPs at Kozloduy-6 (VVER –1000).

The Bohunice case was a real and unintended plant transient. The Kozloduy transient was part of the plant start-up tests. A short characteristic of both transients is given in Table I.

In the Bohunice measurement, the behaviour of the core during the rod drop and during the three minutes after starting control actions to reach 85 % power level is the most essential part

Table 1: Basic information of transients selected for code validation

Plant	VVER 440/213, Bohunice 3, Slovakia	VVER-1000/V-320, Kozloduy 6, Bulgaria
Initial reactor state	100 %, nominal state	65 %, three of four MCPs running
Transient type	Control rod drop and power control action (unintended event)	Coast-down of a second MCP (start up test)
Calculation aspects	Asymmetry in core	Asymmetry between loops

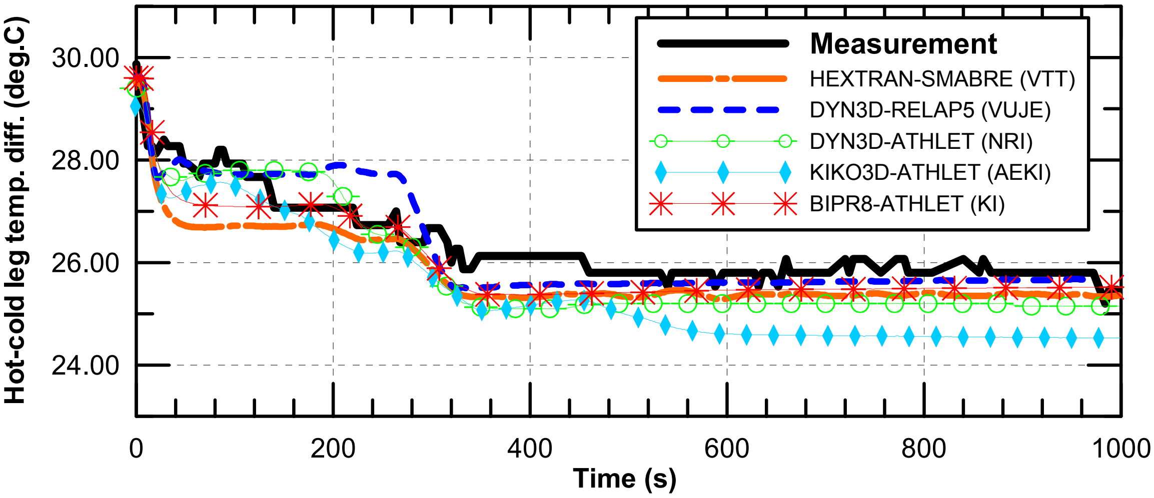

Fig. 1: Calculated and measured average coolant heat-up in the Bohunice VVER-440 core

for validation. The general behaviour during the transients was quite well calculated with all the codes: Both the power distribution changes and the fuel assembly outlet temperatures were mostly well reproduced. As an example, the coolant heat-up, which is a measure of the reactor power, is depicted in Figure 1.

All the calculated hot leg – cold leg temperature differences are within a 1.5°C band around the measurements.

Simultaneous measurements of the individual assembly outlet temperatures and the hot leg temperatures indicate that the coolant mixing in the upper plenum was weak during the transient. That was demonstrated by those codes that included a mixing model and a detailed enough core channel model. Differing results were observed in the axial power profile, in the calculated control rod worth, and in the fuel temperatures. The differences were large in the required control rod group movement to reach the same final power.

The features, that make the Kozloduy transient interesting, such as the lowered power and reverse flow in the stopped loop in the initial state, also proved to be difficult both for data collection and for modelling. The experimental data also include a record from full power nominal state, which in principle enables the definition of the initial state for the calculations. Some more specific data would, however, have been needed about the pump coast down characteristics and the control regime. Anyway, the general behaviour of the Kozloduy second pump trip was reproduced by all the codes.

3.2. Work package 2: Uncertainty analysis

In a first step, the comparison of results for the Loviisa transient "One turbo-generator load drop" [2] obtained by two coupled codes using 3D-neutronics, namely SMABRE-HEXTRAN (VTT) and ATHLET-DYN3D (FZR), and the results from ATHLET using point kinetics revealed good consistency in view of relevant sensitivities of input parameters. The final evaluation will further take into account results from ATHLET-DYN3D (NRI) and ATHLET-KIKO3D (KFKI). The sensitivities of the code results against the variations of the input parameters were evaluated using the statistical code package SUSA (Ref. [3]) of GRS.

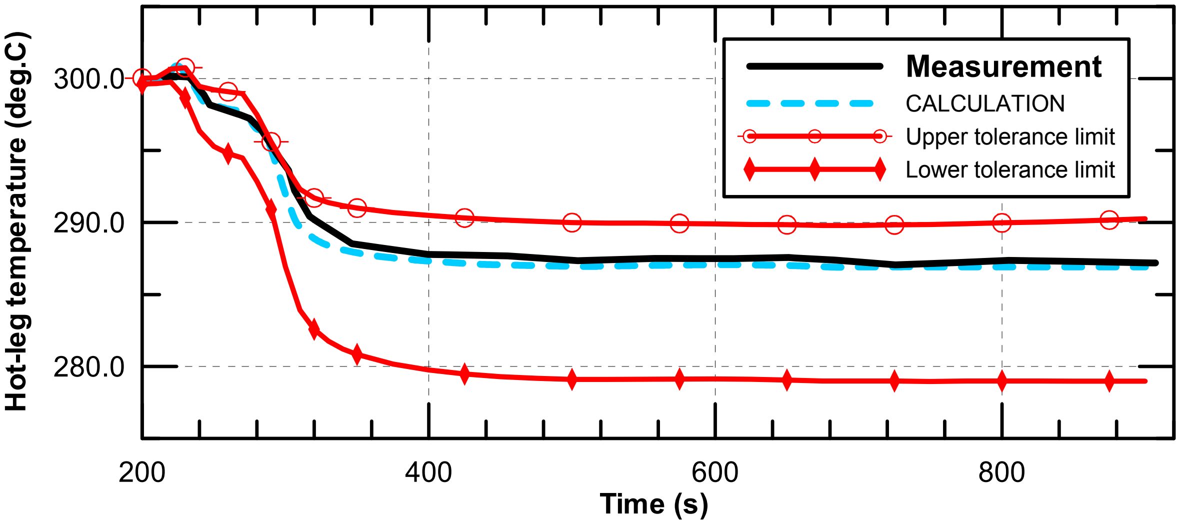

Fig. 2: Measurement and calculation for the hot-leg temperature in the SRR1/95 Loviisa VVER-440 transient. SUSA-calculated tolerance interval

Twelve input parameters have been identified in the coupled-code calculations as the main sources of uncertainty in the Loviisa (VVER-440) and Balakovo (VVER-1000) transients earlier studied in the Phare SRR1/95 project. The uncertainty analysis of the Loviisa transient, e.g., led to the conclusion that the following three parameters are mainly responsible for uncertainties in the calculations: the secondary-circuit pressure, the control-assembly position (as a function of time), and the control-assembly efficiency.

"Uncertainty bands" were derived for safety-relevant output parameters, like power, coolant heat-up in the core, primary pressure, mass flow, and pressurizer level. An example for the VVER-440 is given in Figure 2. The SUSA tolerance interval contains at least 90% of the uncertainty with a confidence level of at least 95%. The interval fully covers the measurement.

3.3. Work package 3: Validation of neutron-kinetic models

All neutron kinetic codes have well reproduced the significant radial tilt observed in both measured V-1000 steady-state power distributions. The good description is mostly due to the accuracy of the HELIOS / MARIKO model applied to calculate the asymmetric radial reflector constants. The initially observed power deviations of up to 30% between calculation and measurement had led to the re-measuring of special V-1000 geometrical parameters, such as the water-gap widths between the core and the radial reflector. The more precise geometric information then resulted in a clear reduction of the maximum power deviation down to 10%.

Inner-assembly pin-power distributions, have been calculated by two neutronic codes. The maximum deviation between measurement and both the fine-mesh diffusion code HEX2DB (INRNE) and the nodal diffusion code DYN3D, applying pin-power recovery, is below 5% in the un-rodded case. When the control rods of group X are inserted in the considered assembly, introducing strong heterogeneity, the maximum deviation is about 9%.

Systematic over-estimations of the effective multiplication factors, that were calculated by all codes for the investigated V-1000 steady states, seem to be mainly due to uncertainties in the nuclear input data of the cell codes and to the measured critical boron concentration, which was also input in the cell calculations.

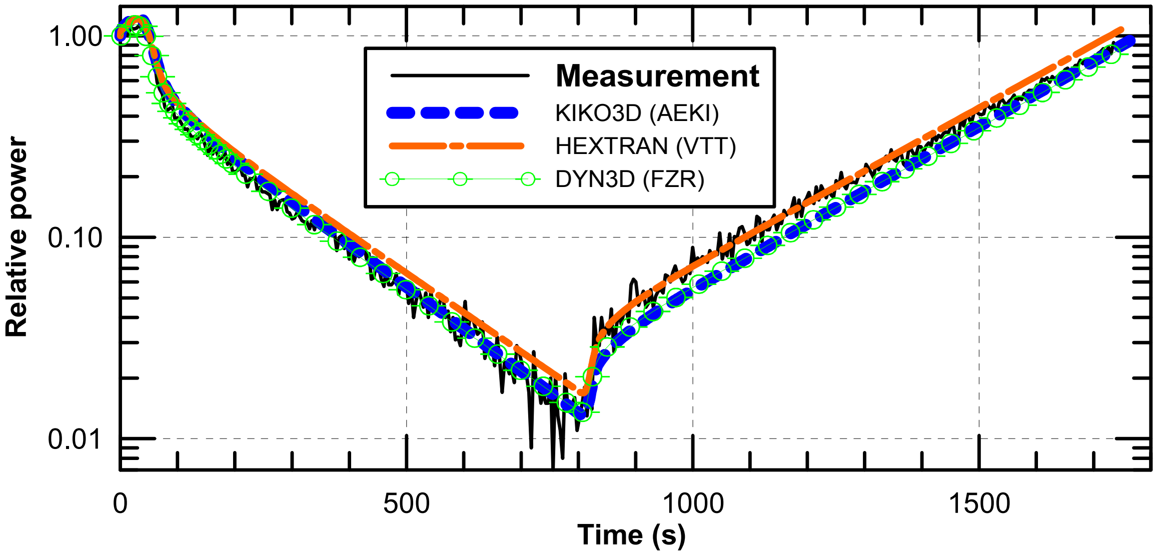

Fig. 3: V-1000 transient: Relative power versus time in FA 86 at the height of 175 cm

The two measured transients have been successfully calculated by the kinetics codes involved. A good agreement between the calculated and measured relative powers as functions of time has been reached, as Figure 3 shows for one example: Starting from a V-1000 steady state with all control rods withdrawn, a transient was initiated by inserting a single cluster of group IX and then withdrawing it again. The induced change of the local power density has been measured and calculated in some fuel assemblies by micro fission chambers in certain height positions.

4. Conclusions

The instrumentation of operating nuclear power plants is not primarily designed for measuring data suitable for coupled-code validation. Nevertheless, available information of several VVER transients has been gathered and carefully documented. In the end, the comparison between different codes and the validation against the selected NPP transients was successful. The calculations were performed without additional corrections or special “tuning”.

The SUSA uncertainty-analysis method has been successfully extended to coupled-code calculations that include 3D neutron kinetics. SUSA analyses for VVER transients have contributed to explain deviations between calculations and measurements, so far at least for the Phare SRR1/95 transients.

The Bohunice-transient calculations, as well as the uncertainty analysis for the former Loviisa transient point to the fact that results are very sensitive to the treatment of VVER-440 control assemblies. They are quite different from control rods in Western PWR and need further attention in modelling by both cell codes and nodal kinetics codes.

The validation against measurements in the V-1000 facility has demonstrated that the neutronics codes, including the applied nuclear-data input, are suitable for the calculation of power distributions and power changes caused by control-rod movements in a VVER-1000. By the same token, it would be very useful to validate VVER-440 control-assembly models, against measurements in a suitable zero-power facility. In principle, the LR0 facility of NRI Rez will fit for this purpose.

Both the VALCO project and its predecessor Phare SRR1/95 have contributed to the improved validation state of codes for VVER reactors. Transient measurements in Western NPP could enable an improvement in the coupled-code validation for these reactor types, too.

References

[1] S. Mittag, S. Kliem, F.-P. Weiß, R. Kyrki-Rajamäki, A. Hämäläinen, S. Langenbuch, S. Danilin, J. Hadek, G. Hegyi, A. Kuchin, and D. Panayotov (2001), Validation of Coupled Neutron Kinetic / Thermal-Hydraulic Codes. Part 1: Analysis of a VVER-1000 Transient (Balakovo-4), Annals of Nuclear Energy, 28, 857

[2] Hämäläinen, R. Kyrki-Rajamäki, S. Mittag, S. Kliem, F.-P. Weiß, S. Langenbuch, S. Danilin, J. Hadek, and G. Hegyi (2002), Validation of Coupled Neutron-Kinetic / Thermal-Hydraulic Codes. Part 2: Analysis of a VVER-440 Transient (Loviisa-1), Annals of Nuclear Energy, 29, 255

[3] M. Kloos and E. Hofer (2002), SUSA: User's Guide and Tutorial, GRS-report

DISCONTINUITY FACTORS FOR NON-MULTIPLYING MATERIAL IN TWO-DIMENSIONAL HEXAGONAL REACTOR GEOMETRY

Siegfried Mittag, Petko Petkov[1], and Ulrich Grundmann

1. Introduction

Two-group neutron diffusion parameters for nodal reactor core calculations are generated by using multi-group cell codes based on transport theory. The multi-group neutron reaction cross sections are condensed into two-group parameters. Spatial homogenization is applied for fuel assemblies or reflector regions. The information of the core and reflector fine structure (heterogeneity) is mostly lost in this procedure. Nevertheless, nodal diffusion codes applying homogenized two-group parameters perform nicely, despite all the approximations and the large (assembly-size) meshes used. In order to further improve the accuracy of nodal diffusion codes, applied for the prediction of assembly powers, Smith [1] introduced discontinuity factors. The basic idea is to transfer heterogeneity information from heterogeneous fine-mesh transport or diffusion calculations to the much faster nodal diffusion codes using homogenized cross sections.

For square-geometry cores in Western light water reactors, it has been demonstrated that two-group diffusion parameters, including discontinuity factors, for radial-reflector nodes are practically insensitive to the core loading [2,3]. This should also be true for hexagonal VVER cores. Tahara, Kanagawa, and Sekimoto [2] introduced a method that allows calculating discontinuity factors in two-dimensional square geometry. In the present paper, the approach has been applied for two-dimensional hexagonal geometry.

2. Method

Discontinuity factors have been defined by Smith [1] for each neutron group g at a node surface s:

$$f_g^s = \frac{\phi_g^{het,s}}{\phi_g^{\hom,s}}, \tag{1}$$

where $\phi_g^{het,s}$ is the flux calculated by a transport or diffusion code in detailed heterogeneous geometry and averaged over the node surface s. $\phi_g^{\hom,s}$ denotes the flux averaged over the same surface, after calculating the flux distribution in the node by diffusion theory, where two-group diffusion parameters are used. The latter quantities, for their part, are the result of condensing and homogenizing the multi-group cross sections that have been used in the transport calculation. The factors f_g^s are related to the "reference" heterogeneous solution, thus they are called reference discontinuity factors (RDFs).

For a transport-equivalent modeling (by a hexagonal nodal diffusion code) of a VVER-440 control absorber or reflector region, a transport solution, calculated for the detailed two-

---

[1] Institute for Nuclear Research and Nuclear Energy, Sofia (BG)

dimensional heterogeneous configuration, is needed. From the angular flux of the transport solution, side-averaged incoming and outgoing partial currents $j^{tr}_{g,in}$, $j^{tr}_{g,out}$ $(g=1,\,2)$ can be derived for the edges (sides) of the non-multiplying nodes. The "heterogeneous" fluxes on the hexagon sides s are then determined by:

$$\phi_g^{het,s} = 2(j^{tr,s}_{g,out} + j^{tr,s}_{g,in})\,. \tag{2}$$

The transport-theory net currents through side s are the differences of the partial currents:

$$J_g^{tr,s} = (j^{tr,s}_{g,out} - j^{tr,s}_{g,in})\,. \tag{3}$$

These side-averaged currents $J_g^{tr,s}$ can be used as boundary conditions for the analytical calculation of flux distributions within homogenized non-multiplying nodes (standard notation) in two-group diffusion theory:

$$\begin{aligned} -D_1\nabla^2\phi_1 + \Sigma_{t1}\phi_1 &= 0, \\ \Sigma_{t1} &= \Sigma_{a1} + \Sigma_{12}, \end{aligned} \tag{4}$$

$$-D_2\nabla^2\phi_2 + \Sigma_{a2}\phi_2 = \Sigma_{12}\phi_1\,. \tag{5}$$

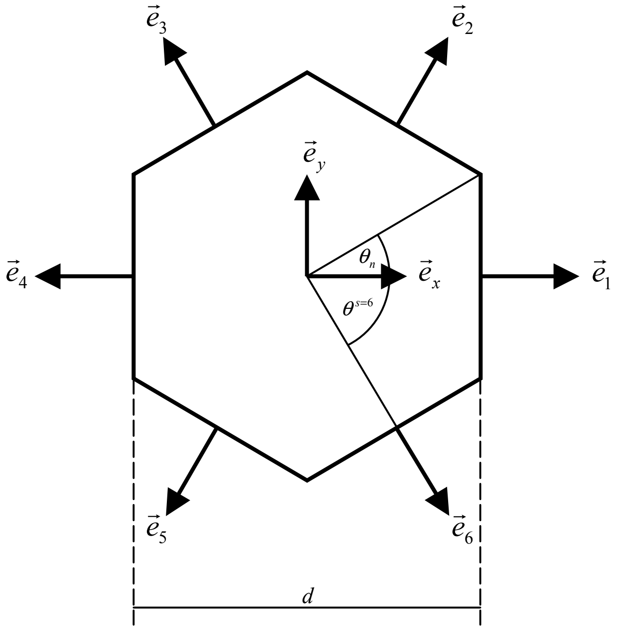

Fig. 1: Hexagon in the x-y plane showing typical angles und unit vectors.

It is easy to show that a general flux expansion in the x-y-plane

$$\begin{aligned} \phi_1(x,y) = \phi_\mu(x,y) &= \sum_{n=1}^{N}(C_n^{\mu+}e^{\mu(k_{n,x}x+k_{n,y}y)} + C_n^{\mu-}e^{-\mu(k_{n,x}x+k_{n,y}y)}), \\ \mu &= \sqrt{\Sigma_{t1}/D_1}, \\ k_{n,x} &= \cos\theta_n, \\ k_{n,y} &= \sin\theta_n, \\ \theta_n &= 2\pi(n-1)/N, \end{aligned} \tag{6}$$

satisfies the Helmholtz equation (4) for the fast flux, where $k_{n,x}$ and $k_{n,y}$ are the x- and y-components of a unit vector specifying the direction θ_n in the flux expansion (Fig. 1). The same way, the solution of the homogeneous equation of (5) can be approximated by introducing analogous functions $\phi_\nu(x,y)$, leading to

$$\phi_2 = \alpha\phi_1 + \phi_v,$$
$$\alpha = \Sigma_{12}/(\Sigma_{a2} - D_2\mu^2). \tag{7}$$

The expansion coefficients $C_n^{\mu/v+}$ and $C_n^{\mu/v-}$ can be determined by using the node boundary conditions. On the boundaries, either the flux, or its normal derivative, or a linear combination of the two must be specified [4]. For the calculation of RDFs as defined in equ. (1), the normal derivatives of the fluxes, i.e. the neutron net currents, averaged over the node faces have to be used. The currents for groups 1 and 2 are defined in diffusion theory according to Fick's law:

$$\vec{j}_1 = -D_1\nabla\phi_\mu, \tag{8}$$

$$\vec{j}_2 = -D_2(\alpha\nabla\phi_\mu + \nabla\phi_v). \tag{9}$$

Integrating the current (8) over the side s of the hexagonal node, identified by the normal vector $\vec{e}_s$ (Fig. 1), yields the average fast net current through this side:

$$J_1^s = -\frac{D_1\sqrt{3}}{d}\int_s dl^s \{\frac{\partial}{\partial x}\phi_\mu(x,y)\Big|_{along\, s}\vec{e}_s\vec{e}_x + \frac{\partial}{\partial y}\phi_\mu(x,y)\Big|_{along\, s}\vec{e}_s\vec{e}_y\}, \tag{10}$$

where d is the distance between parallel sides of the regular hexagon, $d/\sqrt{3}$ is the length of a hexagon side. The flux expansion (6) has to be introduced in (10), and solving the Neumann-Dirichlet boundary value problem by using the transport-theory currents (3) yields the six unknown coefficients C^μ. For the fast neutron group, the C^v are determined in the same manner [5].

The side-averaged "homogeneous" fluxes at the six hexagon sides can be calculated by

$$\phi_g^s = \frac{\sqrt{3}}{d}\int_s dl^s \phi_g(x,y). \tag{11}$$

The result is

$$\begin{aligned}\phi_1^{\text{hom},\ s} = \frac{\sqrt{3}}{d\mu}\sum_{n=1}^{3}\{&\frac{C_n^{\mu+}}{k_{n,y}^s}[e^{(\mu d/2)(k_{n,x}^s + k_{n,y}^s/\sqrt{3})} - e^{(\mu d/2)(k_{n,x}^s - k_{n,y}^s/\sqrt{3})}] \\ &- \frac{C_n^{\mu-}}{k_{n,y}^s}[e^{(-\mu d/2)(k_{n,x}^s + k_{n,y}^s/\sqrt{3})} - e^{(-\mu d/2)(k_{n,x}^s - k_{n,y}^s/\sqrt{3})}],\end{aligned} \tag{12}$$

$$k_{n,x}^s = \cos(\theta_n - \theta^s),$$
$$k_{n,y}^s = \sin(\theta_n - \theta^s),$$
$$\theta_n = \pi(n-1)/3;\ n = 1, 2, 3;$$
$$\theta^s = 2\pi(s-1)/6;\ s = 1, 2, \dots 6;$$

$$\begin{aligned}\phi_2^{\text{hom},\ s} = \alpha\phi_1^{\text{hom},\ s} + \frac{\sqrt{3}}{d\mu}\sum_{n=1}^{3}\{&\frac{C_n^{\nu+}}{k_{n,y}^{s}}[e^{(\nu d/2)(k_{n,x}^{s}+k_{n,y}^{s}/\sqrt{3})} - e^{(\nu d/2)(k_{n,x}^{s}-k_{n,y}^{s}/\sqrt{3})}] \\ &- \frac{C_n^{\nu-}}{k_{n,y}^{s}}[e^{(-\nu d/2)(k_{n,x}^{s}+k_{n,y}^{s}/\sqrt{3})} - e^{(-\nu d/2)(k_{n,x}^{s}-k_{n,y}^{s}/\sqrt{3})}].\end{aligned} \tag{13}$$

Inserting these “homogeneous” fluxes (12), (13) and the “heterogeneous“ fluxes (2) into equ. (1) allows calculating the reference discontinuity factors (RDFs) for both groups at the six hexagon sides.

3. Benchmark calculations

Mathematical benchmarks have been used to test the accuracy of DYN3D nodal (“coarse mesh”) diffusion calculations for VVER cores, cf. e.g. [6]. These benchmarks have been defined by fine-mesh finite-difference diffusion calculations that apply the same assembly-homogenized two-group diffusion parameters.

Other tests or benchmarks are needed, however, to quantify the additional implications of both homogenization effects and the diffusion approximation on the accuracy of calculated power distributions and effective multiplication factors. Suitable VVER-440 benchmarks have been defined by Petkov [7]. They are two-dimensional heterogeneous 23-group transport-theory solutions, calculated by the MARIKO code [8] for a VVER-440 60-degree core symmetry sector. The same transport code and the same 23-group cross sections are used to prepare the two-group diffusion parameters and assembly discontinuity factors (ADFs) for all assembly types. Conventional group-to-group albedos on the core-reflector boundary, two-group diffusion parameters for the reflector and control-absorber nodes, as well as partial currents, required for the determination of RDFs (cf. Eqs. 2 and 3), are calculated by MARIKO, too. The 23-group cross-sections (input for MARIKO) for all materials in the fuel assemblies, radial reflector and control absorber are prepared by HELIOS-1.5 using its 90-group library.

Benchmarks have been defined for the beginning and end of the first VVER-440 cycle, as well as for typical levels of depletion. For the DYN3D calculations, the reactor core has been surrounded by hexagonal reflector nodes, having the same dimensions as the fuel assemblies. The deviation of DYN3D results from the accurate reference solution clearly diminishes by the application of RDFs calculated for the radial reflector nodes according to chapter 2. In the distribution of node-averaged relative powers, the RMS error is reduced from about 6 % to below 1%. The deviation in the multiplication factor k-eff decreases from ~200 pcm to 10 pcm and lower. Using conventional group-to-group albedos instead of two-group diffusion parameters for the radial reflector provides similar good results. However, these albedos depend on the properties of the fuel environment, in which they have been calculated. It has been shown in [5] that the two-group diffusion parameters, including RDFs, for the non-multiplying hexagonal nodes practically do not depend on the neighboring fuel, which is a clear advantage over conventional albedos.

In one of the benchmarks mentioned, control group 6 is fully inserted, i.e. the fuel in the respective nodes is replaced by the non-multiplying control-assembly absorber material. Partial currents have been calculated by MARIKO for the sides of the central control absorber. Due to the symmetry, the currents and the derived RDFs are the same for all six hexagon sides. Thus, for the central control absorber, the fast and thermal RDFs are 1.002 and

Thus, for the central control absorber, the fast and thermal RDFs are 1.002 and 0.323, respectively. The small value of the thermal RDFs is due to the high thermal absorption cross section which is caused by the boron contained in the steel near to the control-absorber surface. It makes the real thermal flux on the surface clearly smaller than the thermal flux calculated by diffusion theory using control-absorber-homogenized parameters.

1	Fuel assembly number
0.000	Relative assembly power by MARIKO
0.0	Deviation (%) of DYN3D: fuel ADFs , reflector RDFs, control ass. UDFs
0.0	Deviation (%) of DYN3D: fuel ADFs , reflector RDFs, control ass. RDFs

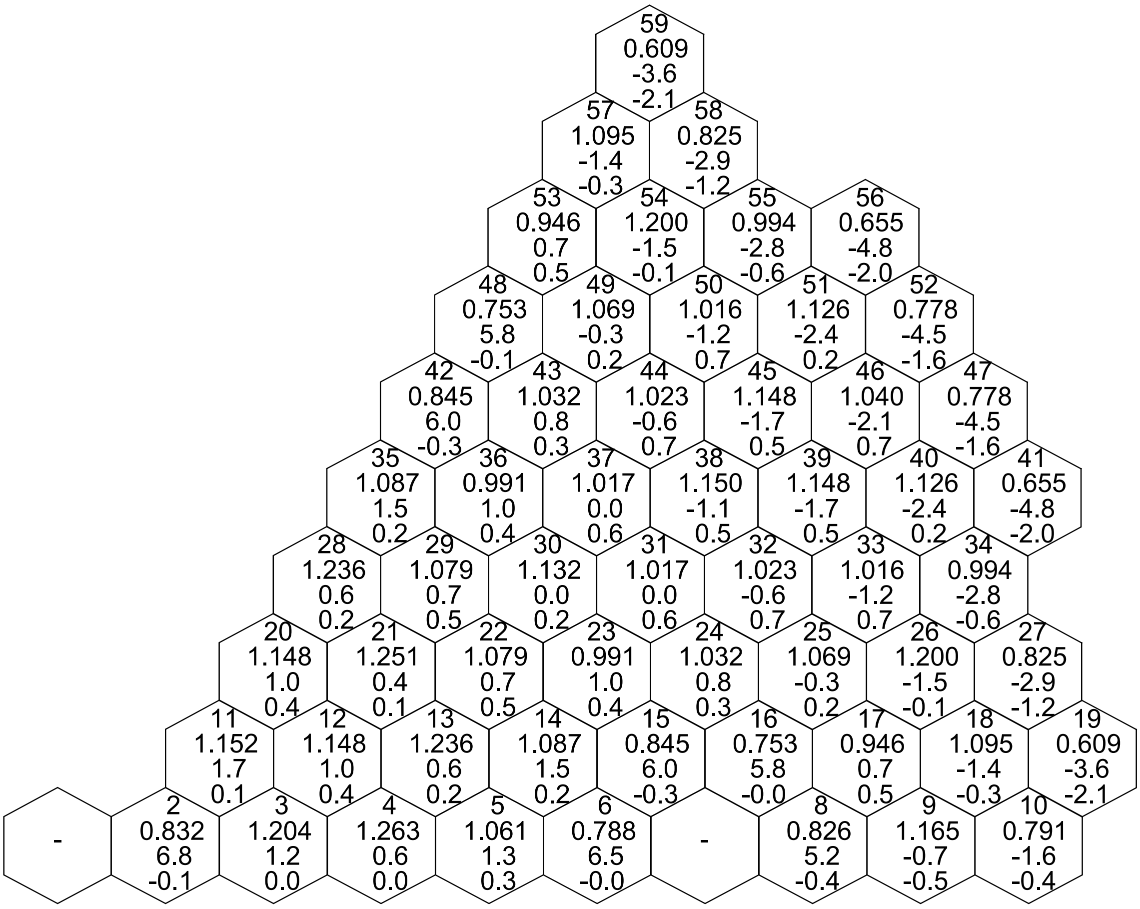

59	0.609	-3.6	-2.1
57	1.095	-1.4	-0.3
58	0.825	-2.9	-1.2
53	0.946	0.7	0.5
54	1.200	-1.5	-0.1
55	0.994	-2.8	-0.6
56	0.655	-4.8	-2.0
48	0.753	5.8	-0.1
49	1.069	-0.3	0.2
50	1.016	-1.2	0.7
51	1.126	-2.4	0.2
52	0.778	-4.5	-1.6
42	0.845	6.0	-0.3
43	1.032	0.8	0.3
44	1.023	-0.6	0.7
45	1.148	-1.7	0.5
46	1.040	-2.1	0.7
47	0.778	-4.5	-1.6
35	1.087	1.5	0.2
36	0.991	1.0	0.4
37	1.017	0.0	0.6
38	1.150	-1.1	0.5
39	1.148	-1.7	0.5
40	1.126	-2.4	0.2
41	0.655	-4.8	-2.0
28	1.236	0.6	0.2
29	1.079	0.7	0.5
30	1.132	0.0	0.2
31	1.017	0.0	0.6
32	1.023	-0.6	0.7
33	1.016	-1.2	0.7
34	0.994	-2.8	-0.6
20	1.148	1.0	0.4
21	1.251	0.4	0.1
22	1.079	0.7	0.5
23	0.991	1.0	0.4
24	1.032	0.8	0.3
25	1.069	-0.3	0.2
26	1.200	-1.5	-0.1
27	0.825	-2.9	-1.2
11	1.152	1.7	0.1
12	1.148	1.0	0.4
13	1.236	0.6	0.2
14	1.087	1.5	0.2
15	0.845	6.0	-0.3
16	0.753	5.8	-0.0
17	0.946	0.7	0.5
18	1.095	-1.4	-0.3
19	0.609	-3.6	-2.1
-			
2	0.832	6.8	-0.1
3	1.204	1.2	0.0
4	1.263	0.6	0.0
5	1.061	1.3	0.3
6	0.788	6.5	-0.0
-			
8	0.826	5.2	-0.4
9	1.165	-0.7	-0.5
10	0.791	-1.6	-0.4

Fig. 2: Benchmark - MARIKO reference solution (k-eff = 0.99351); DYN3D with UDFs (RDF=1) in CA nodes: k-eff error: +191 pcm, power RMS error: 2.82%; DYN3D with RDFs in CA nodes: k-eff error: +2 pcm, power RMS error: 0.76%.

Fig. 2 contains the benchmark results. In each node (hexagon), the second line shows the reference solution for the relative power. Assemblies No. 1 and 7 contain only control absorber (CA) material, hence power is zero there. The third and fourth lines describe DYN3D deviations from the reference for different calculation conditions. Fuel ADFs and RDFs calculated for the radial reflector are used in both cases. The results in the third line have been calculated by neglecting RDFs for the control absorbers, using unity discontinuity factors (UDF: RDF=1) instead.

The application of RDFs, calculated by the method described in the previous chapter for the control absorber, improves the accuracy of the DYN3D power prediction significantly. It should be noted that these RDFs, determined for the central control absorber (No. 1), are also used in node No. 7. Although the enrichment of half of the fuel assemblies surrounding node No. 7 is different, the RDFs perform very well here, which again underlines their independence from the properties of the neighboring fuel.

Together with the improvement of power distributions by using the RDF method, the effective multiplication factors k-eff become more accurate. Thus in the benchmark comparison, the deviation in the control-group-6 efficiency is reduced from about 200 pcm to less than 10 pcm by applying RDFs for the control absorber.

4. Conclusions

The results demonstrate that DYN3D, using homogenized two-group diffusions parameters and "two-dimensional" RDFs for reflector and control-absorber nodes, performs well in VVER-440 power predictions. The maximum deviation from the reference fine-mesh multi-group transport solution is about 2.5%, which is quite sufficient, having in mind the well-known uncertainties in the basic nuclear data.

As the VVER-440 control assemblies contain steel pellets and an intermediate boron-free zone in the region between the absorber and the so-called fuel follower, RDFs should also be calculated for these zones. Furthermore, "one-dimensional" RDFs may be derived for the bottom and top reflectors of reactor cores. The method should also be applied in the rectangular-geometry option of DYN3D.

References

[1] K. S. Smith (1986), Assembly Homogenization Techniques for Light Water Reactor Analysis, Prog. Nucl. Energy, 17, 303.

[2] Y. Tahara, T. Kanagawa, and H. Sekimoto (2000), Two-Dimensional Baffle/Reflector Constants for Nodal code in PWR Core Design, J. Nucl. Sc. Technol., 37, 986.

[3] Y. Tahara and H. Sekimoto (2000), Two-Dimensional Baffle/Reflector Constants Based on Transport Equivalent Diffusion Parameters, PHYSOR 2002 (CD), Seoul, Korea.

[4] J. R. Lamarsh (1966), Nuclear Reactor Theory, Addison-Wesley Publishing Company, Inc., Reading, Massachusetts, p. 133.

[5] S. Mittag, P. T. Petkov, and U. Grundmann (2003), Discontinuity factors for non-multiplying material in two-dimensional hexagonal reactor geometry, Annals of Nuclear Energy, 30, 1347.

[6] U. Grundmann and F. Hollstein, (1999), A Two-Dimensional Intranodal Flux Expansion Method for Hexagonal Geometry, Nucl. Science and Engineering, 133, 201.

[7] P. T. Petkov (2002), Two-Dimensional Full-Core Transport-Theory Benchmarks for WWER Reactors, Proc. XII Symposium of AER (p.191), Sunny Beach, Bulgaria.

[8] P. T. Petkov (2002), Development of a Neutron Transport Code for Many-Group Two-Dimensional Heterogeneous Calculations by the Method of Characteristics, Proc. X Symposium of AER (p. 271), Moscow, Russia.

COMPARATIVE ANALYSIS OF A PUMP COAST-DOWN TRANSIENT USING THE COUPLED CODE SYSTEMS DYN3D-ATHLET AND DYN3D-RELAP5

Sören Kliem and Yaroslav Kozmenkov

1. Introduction

Currently intense efforts are directed at the comprehensive analysis of prediction capabilities of the coupled three-dimensional neutron kinetics and one-dimensional thermal-hydraulic coupled code systems. These activities include (1) overall testing of the coupling interface, (2) verification of coupled code systems by solving international benchmark problems (conducting a code-to-code comparison) and (3) extended validation of the coupled codes against measured nuclear power plant (NPP) data. The EU FP5 VALCO project aimed at a validation of the coupled code systems for VVER reactors represents a recent example of such activities. A simulation of the real measured transient of an operating VVER-1000 power plant is considered among the tasks of the VALCO project [1]. Simulations of this transient have been performed using DYN3D-ATHLET [2] and DYN3D-RELAP5 [3] coupled code systems. The integration of the DYN3D and ATHLET codes was entirely performed at FZR, whereas the interface for coupling DYN3D and RELAP5 codes was developed in co-operation of FZR and the Russian Institute of Physics and Power Engineering (IPPE).

2. Basic features and evaluation of the coupled codes

Both coupled code systems incorporate the same code of three-dimensional neutron kinetics – DYN3D. In addition to the transient neutronic simulations, the stand-alone DYN3D code is capable to perform calculations of (1) fuel burn-up distributions in the core, (2) distributions of the equilibrium Xe and Sm concentrations, (3) spatial decay heat distribution and (4) the core thermal-hydraulic parameters. All these capabilities, except the capability of fuel burn-up calculation, are available for the considered code systems as well. The stand-alone DYN3D code should be used for the fuel burn-up calculations prior to the transient simulations.

DYN3D and ATHLET codes have been coupled in three different ways, the so-called “internal”, “external” and “parallel” coupling techniques. The applied external integration technique means that the neutron kinetics and thermal hydraulics of the core are simulated by the reactor dynamics core model DYN3D, and the system code ATHLET simulates all plant components outside the core. The thermal hydraulics of the core is simulated by the two codes DYN3D and ATHLET in the parallel coupling. In the case of the internal coupling only the neutronic model of the reactor dynamics code is integrated into the thermal-hydraulic system code. An internal coupling technique has been used to couple DYN3D with RELAP5. This type of coupling was selected primarily due to the advantages of the closed implicit solution of thermal-hydraulic equations and unrestricted application of the RELAP5 models, including modelling capabilities of the control and trip systems, to the core simulation.

Several reactor plant transients and international benchmarks aimed at the evaluation of the coupled codes have been analyzed using DYN3D-ATHLET and DYN3D-RELAP code systems. At least six transients simulated by the externally coupled DYN3D-ATHLET are related to the VVER-440 and VVER-1000 power plant units. Being developed later, the internally coupled DYN3D-RELAP5 code has been applied to a less number of exercises. So far, the VALCO project transient is the first and only real transient simulated using the DYN3D-RELAP5 code system.

3. Reference transient and reactor plant model

The reference transient chosen for the comparisons is the commissioning experiment at the 6-th unit of Kozloduy NPP (VVER-1000) documented in the framework of the EU FP5 (VALCO) project. The transient is initiated by the coast-down of the 1st loop main coolant pump (MCP) at the moment, when 3 of 4 MCPs (namely, 1st, 2nd, and 4th) are in operation. The MCP of the 3rd primary loop has been switched off about 90 minutes earlier during the first phase of conducted start-up experiments, and, according to the VALCO project specification [1], this period of unit operation is not required to be included in the simulation. The transient scenario is summarized in Table 1.

Table 1: Sequence of main events

Time, s	Event
0	MCP of the 1st primary loop is switched off (one of three operating MCPs)
0.5	10-th group of control rods starts its downward movement from 73% position to decrease reactor power
20	Set point "low level in SG1" is reached and the 2nd auxiliary feed water pump (AFWP-2) is put into operation; AWFP-1 is operating during the whole experiment
31	10-th control group reaches the lower position of 55 %
52	Switch off of the 1st pressurizer heater group
58	First opening of the pressurizer spray valve (maximum 21% at 75th second, closure at 83rd second)
88	Second opening of the pressurizer spray valve (maximum 7% at 98th second, closure at 103rd second)
380	End of transient

The computer model of the V-320 plant, which has been used in the two calculations, incorporates 4 separate primary coolant loops, steam generators and main steam lines up to their connection points to turbines. Each fuel assembly (FA) of the core model has its own thermo-hydraulic channel within a 60-degree sector of symmetry. The total number of the modeled core thermo-hydraulic channels, including 8 radial reflector channels, is 36.

The analysis and the assessment of different start-up experiments in plants with VVER-1000 reactors showed, that the coolant flow through a switched off loop into the upper plenum goes preferably to the neighboring active loop, almost not influencing the coolant flow into nozzles on the opposite side [4]. That is due to the fact, that the azimuthal angle between the two neighboring loops of one half is 55°, the angle to the next loop is 125°. Based on that experience, the upper plenum in the current calculations has been symmetrically divided into two equal volumes at the elevation level of the hot leg nozzles without direct exchange of coolant between them. The hot leg nozzles of two neighboring loops were connected to each of the introduced upper plenum volumes.

The dynamic pump models of ATHLET and RELAP5 are applied to simulate the hydraulic behavior of the MCPs. This model describes the MCP by the empirical set of homologous curves. The homologous pump characteristics employed in both validation calculations correspond to those defined in the NEA VVER-1000 Coolant Transient Benchmark. The operation of feedwater pumps is modeled as time-dependent boundary conditions, using corresponding experimental data.

There are two differences in the models of the reactor used in the DYN3D-ATHLET and DYN3D-RELAP5 calculations. The first difference concerns the axial nodalization of the core hydrodynamic channels. The core models of DYN3D-ATHLET and DYN3D-RELAP5 codes utilize 20 and 11 hydrodynamic axial nodes, respectively. Each nodalization includes two axial reflector layers - the top and the bottom reflectors of the core. The number of the fuel (neutronic) axial nodes is 18. It is the same in the two calculations.

The second difference concerns the macroscopic cross-section libraries used in compared calculations. A VVER-1000 cross-section library generated by the NESSEL code is used in the DYN3D-ATHLET simulation, whereas the library for the DYN3D-RELAP5 simulation is generated by WIMS. The generated libraries differ also in the applied cross-section approximation techniques.

4. Comparison of results

Prior to the transient simulations, the calculations of the fuel burn up distribution in the core have been performed up to 171.6 FPD using the stand-alone DYN3D code. Then, the initial state of the plant and the MCP coast down transient has been simulated by the coupled code systems.

Close predictions of the normalized radial power distributions are given by the coupled codes. The maximum discrepancy in calculated values of the normalized FA powers does not exceed 1.5% for the initial and the final state of the core.

300 seconds of the transient have been simulated using the DYN3D-ATHLET and DYN3D-RELAP5 coupled code systems. Figures 1 and 2 show a code-to-code comparison of the most representative simulation results and their validation against the plant measurements. Figure 1 shows the decreasing reactor power due to the movement of the control rod group No. 10 into the core. The calculated neutron powers demonstrate a rather good agreement with the measured data. Differences in the employed cross-section libraries, core hydrodynamic nodalizations and thermal-hydraulic models used in the simulations do not cause noticeable deviation between the neutron power predictions.

A realistic behavior of the calculated hot leg temperatures (Fig. 2) confirms the validity of the chosen simplified upper plenum nodalization. Predicted temperatures are in a close agreement with the experimental data except the hot leg temperature at the 1st reactor loop. Obtained results of calculations have not been filtered by a low-pass filter to model a real thermocouple measurement. As reported in [1], the shape of the measured hot leg 1 temperature shows either very large thermocouple time constants, or probably indicates that the measurement is disturbed by the wall temperature, which is decreasing more slowly than the fluid temperature.

The dynamic pump models of the system codes provide adequate simulation of the operating and switched off main coolant pumps, which is proofed by the close agreement of calculated and measured pump pressure differentials.

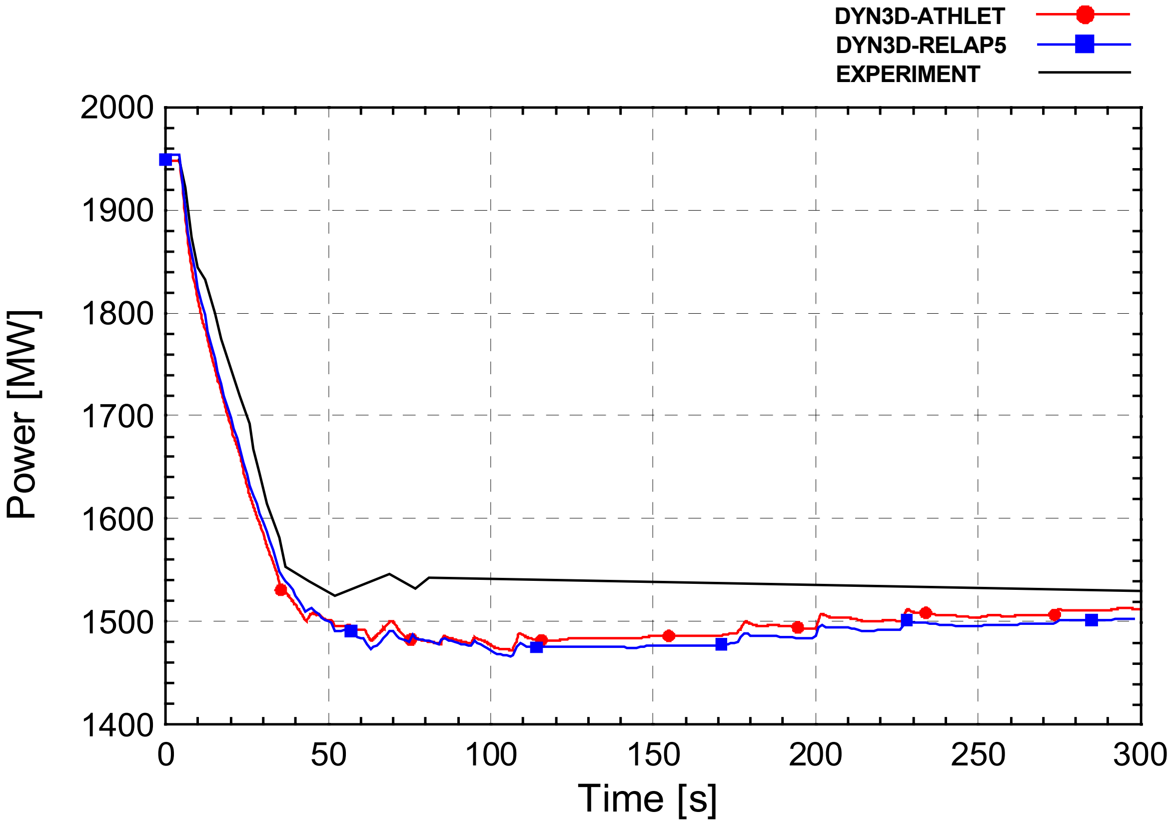

Fig. 1: Neutron power

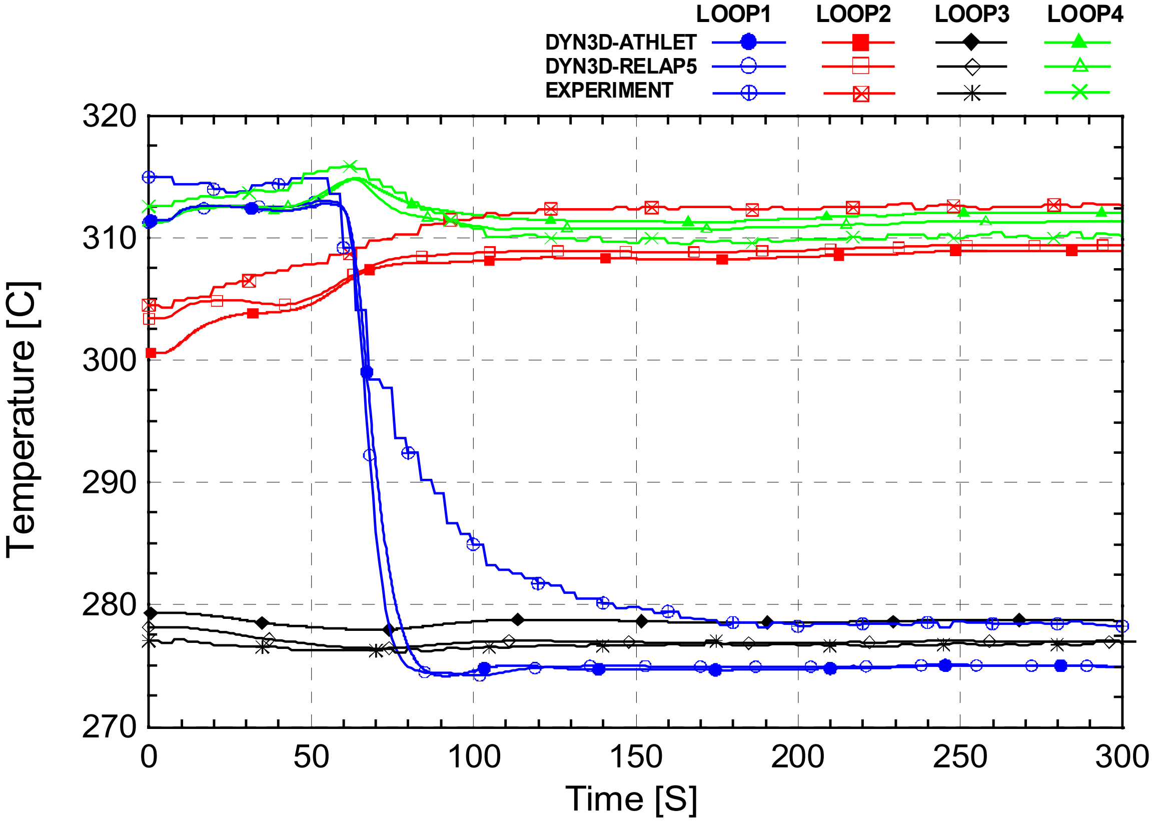

Fig.2: Hot leg temperatures

5. Conclusions

The Kozloduy-6 VVER-1000 start-up experiment was analyzed by the DYN3D-ATHLET and DYN3D-RELAP5 coupled code systems. Both the validation against experimental data and code-to-code comparison between calculated results was performed. The loop temperatures depend on the efficiency of the primary coolant mixing in the reactor upper plenum. Both code systems produced satisfactory predictions of the measured transient parameters. A close agreement of the calculated results has been demonstrated.

References

[1] A. Hämäläinen et al. (2003): Final report of VALCO WP1 extended coupled code validation, VALCO/WP1/D9

[2] U. Grundmann, D. Lucas, U. Rohde (1995): Coupling of the Thermohydraulic Code ATHLET with the Neutron Kinetic Core Model DYN3D, Proc. Int. Conf. on Mathematics and Computations, Physics and Environmental Analysis (v.1, pp.257-263), ANS, La Grange (USA)

[3] Y. Kozmenkov, Y. Orekhov, U. Grundmann, S. Kliem, U. Rohde, A. Seidel (2001): Development and Benchmarking of the DYN3D/RELAP5 Code System, Proc. Ann. Mtg. Nucl. Techn. (pp.15-18), Bonn, INFORUM GmbH

[4] U. Grundmann, S. Kliem, E. Krepper, S. Mittag et al. (1998): "Qualifizierung des Kernmodells DYN3D mit dem Störfallcode ATHLET als fortgeschrittenes Werkzeug für die Störfallanalyse von WWER-Reaktoren“, Abschlussbericht Teil 1 zum BMBF–Vorhaben 150 0925A, Rossendorf, Report FZR–216

Acknowledgement

The work was funded by Federal Ministry of Economics and Trade (BMWA) within research project 150 1260.

THERMAL ANALYSIS OF THE COOLABILITY OF SPREAD MELT BY TOP FLOODING

Eberhard Altstadt and Hans-Georg Willschuetz

1. Introduction

One possible strategy for the long term stabilization of spread corium is top-flooding. After spreading into the core catcher area the molten corium is top-flooded by a water layer to remove the decay heat. The melt consists of an oxidic and a metallic component and is assumed to be segregated with the oxide forming the upper layer. The thermodynamic processes are strongly influenced by the molten-corium-concrete interaction.

One objective of the ECOSTAR project of the 5th framework programme is to investigate the cooling potential of the top-flooding strategy. In the frame of WP2.1 a large scale spreading test was performed at the ECOKATS2 facility of the FZ-Karlsruhe (2D-demonstration test). After the immobilization of the melt the top-flooding process was started. The water was fed through a channel from one side of the spreading area.

This report describes analytical and finite element calculations related to the ECOKATS2 test. The objective is to simulate the heat removal and the crust formation. Two main phases of the process are investigated:

- the water front progression during the flooding process in order to estimate the time needed for covering the melt surface with water; this is done with the FORTRAN program FLOOD, which was developed especially for this task

- the subsequent cooling phase; the finite element code ANSYS is used to develop a thermo-fluiddynamic model of the 2 component melt

The thermal simulations are done for a melt without internal heat sources (as in the ECOKATS2 experiment). In addition to that a melt with a heat generation rate of 1 MW/m³ is considered in order to estimate the effect of the decay heat in the prototypic case.

2. Test conditions and melt properties

The melt is generated by a thermite reaction and consists of about 130 litres (895 kg) of steel and 700 litres (2305 kg) of oxide. The metal is poured first and the oxide afterwards. According to the experiences gathered so far the two melt phases will remain separated with the oxide layer being on the top. The spreading area is 2 m by 2 m. The total area including the flow channel is about 4.81 m². The estimated initial heights are 0.027 m for the iron layer and 0.147 m for the oxide layer [1]. The chemical composition of the oxide is shown in table 1:

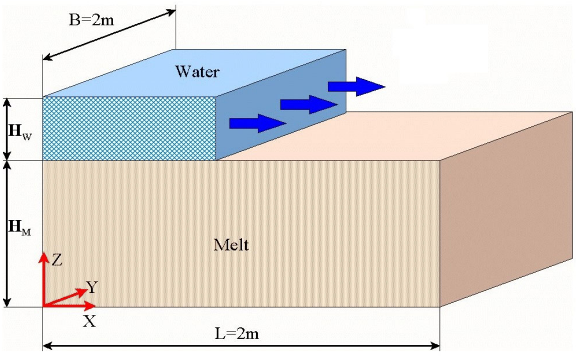

Fig. 1: Simplified scheme of the flooding process (not to scale)

Table 1: Composition of the ECOKATS2 melt (weight percent)

Al_2O_3	FeO	SiO_2	CaO
41%	24%	16%	19%

The spreading area was flooded by water along the whole width from one side of the area with a constant volume rate of 4 liters/s, see Fig. 1. The feed velocity depends on the channel height. The initial water temperature is about 20 °C. An initial melt temperature of 1830 °C was measured before the melt spreading.

3. Models for heat transfer and melt-concrete interaction

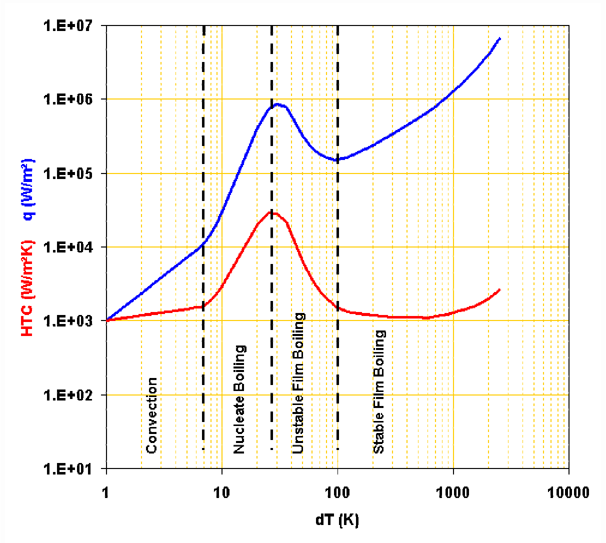

Fig. 2: Empirical correlation for heat flux (blue) and HTC (red) from an overheated surface into a boiling water layer

The heat transfer coefficient (HTC) is based on empirical correlations for a smooth horizontal surface with overlying water [5]. There are four different mechanisms for the heat transfer, depending on the temperature of the hot surface: convection boiling, nucleate boiling, unstable film boiling and stable film boiling. Fig. 2 shows the heat flux and the HTC in dependence on the temperature difference between melt surface and water layer. Due to strong melt-concrete interaction (MCI) there is an enhanced heat transport within the melt layer and into the water layer by rising gas bubbles. The enhanced heat flux into the water layer is determined by two quantities, the gas generation velocity

$$v_G = \frac{\rho_C}{\rho_G} \cdot Y_G \cdot v_{CA} = \frac{\rho_C}{\rho_G} \cdot Y_G \cdot \frac{q_C}{\rho_C \cdot \Delta h_C} \qquad (1)$$

and the rising up velocity of the gas bubbles [2]:

$$v_{up} = 1.53 \cdot \left(\frac{\sigma_S \cdot g}{\rho_M} \right)^{0.25} \qquad (2)$$

The symbols in equations (1) and (2) are: ρ_C – concrete density, ρ_G – gas density, Y_G – mass fraction of bonded gas in the concrete, v_{CA} – concrete ablation velocity, q_C – heat flux into the concrete, Δh_C – concrete dissolution enthalpy, σ_S – surface tension, ρ_M – melt density, g – gravity constant. The heat flux increase is described by a modified HTC

$$\tilde{\alpha} = \alpha \cdot \left(1 + \frac{4.5 \cdot v_G}{v_{up}} \right) \qquad (3)$$

where α is the empirical HTC according to Fig. 2. The enhanced vertical heat transfer within the melt layer due to rising gas bubbles is strongly coupled to the viscosity of the melt (especially in the mushy region). The immobilization temperature T_{imm} ($T_{sol}<T_{imm}<T_{liq}$) marks the transition from normal heat conduction to the enhanced vertical heat transfer. In the solidified

state, the porosity due to trapped gas bubbles has to be taken in consideration. For the liquid range a correlation proposed by Seiler [4] is used. Thus the following approach is made for the effective heat transfer coefficient:

$$\begin{aligned}
\lambda_{\text{eff}} &= \lambda_M(T)\cdot(1-f) = \lambda_M(T)\cdot\left[1-\left(1+\frac{v_{\text{up}}}{v_G}\right)^{-1}\right] && \text{for } T < T_{\text{imm}} \\
\lambda_{\text{eff}} &= \lambda_M(T_{\text{sol}})\cdot H_M\cdot\left[\frac{\Pr_M\cdot g}{(\eta_M/\rho_M)^2}\cdot\left(0.00274\cdot\beta_M\Delta T_M+50\cdot f^2\right)\right]^{1/3} && \text{for } T > T_{\text{imm}}
\end{aligned} \tag{4}$$

where λ_M is the value for the solidified oxide without porosity, f the volume void fraction, $\Pr_M$ the Prandtl number, η_M the viscosity, β_M the volumetric expansion coefficient, ρ_M the density and ΔT_M the vertical difference between maximum and minimum melt temperature at a certain time. It must be noted that the MCI parameters in equ. (1)-(4) are quite uncertain, since they depend on the concrete composition.

4. Water front progression during flooding

The simulation is based on a 1D cellular algorithm (Fig. 3). The melt layer and the water layer are each subdivided into 500 cells (finite volumes) along the flow direction. For the water nodes a filling level F is defined indicating whether the node is empty or completely evaporated (F = 0), partially filled with liquid water (0 < F < 1) or completely filled with liquid water (F = 1). At the beginning of each time step a transport step of the water layer is carried out. The water layer is moved one horizontal step (in flow direction), the first cell is filled with cold water.

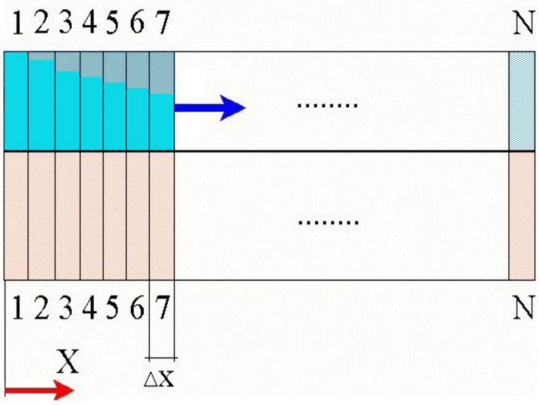

Figure 3: Cellular simulation model for estimation of water front progression during flooding

After that the temperatures of the cells are updated. For the water cells an energy balance is made considering the heat flux according to equ. (3), the temperature elevation and the evaporation. Each of the water nodes is described by one (average) temperature and one filling level (F). For the melt nodes the heat equation is solved in the vertical direction using the Galerkin method. Each of the melt cells is therefore characterized by a vertical temperature distribution. The horizontal heat conduction within a melt cell is neglected.

The feed velocity depends on a number of factors like viscosity, surface tension at the free surface, temperature and roughness of the underlying surface. An exact solution for the test condition is not possible. However, the order of magnitude can be estimated on the base of analytical solutions [3] for an ideally smooth surface with constant temperature and constant water volume flow. Assuming an inertia driven spreading regime, the feed water velocity is around 0.4 m/s [6].

The algorithm is realized in the code “FLOOD”, which has been developed using the Compaq Visual Fortran® programming tools. Because of the simplicity of the model and because of the uncertainty of the MCI parameters it is necessary to do some sensitivity studies for the uncertain parameters to get a reasonable margin for the results. The following parameter are varied:

- gas generation rate to vary the effective vertical heat transport within the melt and into the water; this variation is necessary because of the uncertainty of MCI parameters in equ. (1) - (4)
- the feed water velocity, v_{feed}, to study the hydrodynamic effects missing in the model; this is equivalent with the variation of the water layer thickness since the volume rate is constant
- Initial melt temperature at beginning of the flooding process; after thermite reaction, i.e. before melt spreading , the temperature was measured to 1830 °C; water feeding was started 40 s after completion of melt spreading, i.e. 70 s after start of melt spreading; therefore it is reasonable to assume an initial melt temperature lower than 1830 °C

The results of the sensitivity study are listed in table 2. The time for complete covering is counted from the beginning of flooding and the steam production is related to this time.

Table 2: Simulation of water front progression – parameters and results

No.	Initial melt temperature $T_{M,0}$ [°C]	gas generation rate v_G [m/s]	effective heat conduction λ_{eff} [W/m/K]	v_{feed} [m/s]	time for complete covering [s]	steam production [kg]
1	1830	0.0395	4134	0.1	125	430
2	1830	0.0395	4134	0.2	115	423
3	1830	0.0395	4134	0.4	110	420
4	1830	0.01	1763	0.4	89	306
5	1740	0.01	1763	0.4	16.9	54.3
6	1740	0.006	1266	0.4	13.2	40.5
7	1700	0.006	1266	0.4	8.6	22.1

There is only a minor influence of the feeding velocity (at constant water volume flow) on the covering time and on the steam production (calculations 1-3). Unlike this the MCI parameters and the initial melt temperature have a strong influence (calculations 4-7). In the experiment a flooding time of 12.8 s was observed [1] by infrared camera measurements, thus calculation no. 6 corresponds closest to the experimental conditions. Therefore the MCI is rather slow compared to the experiences in the literature [2,4]. This was also confirmed by post-test investigations of the concrete tub, exhibiting an erosion depth of less than 10 mm [1].

5. Cooling process after flooding

The simulation of the cooling process by an overlaying water layer is done with a finite element model. The FE-code ANSYS is used. The following effects are considered:

- vertical heat transport within three layers: oxide, metal and concrete
- heat transport into the water layer
- concrete ablation and gas generation (MCI)

Figure 4 shows the element plot. Due to the one-dimensional model all temperatures have to be considered as averaged over the spreading area for a certain height. The vertical heat transport is simulated by thermal conduction using effective heat conduction coefficients according to equ. (4). The heat transport into the water layer is modelled according to Fig. 2 and equ. (3). The concrete ablation depends on the heat flux into the concrete (equ. 1). If a concrete element reaches the liquidus temperature of the concrete, the material properties are switched to metal. The uppermost metal elements are switched to oxide. Since the main fraction of the solid concrete becomes liquid and only a minor fraction is released as gas, it is assumed that the oxide layer becomes larger during the concrete decomposition stage. In this way the thickness of metal is constant, whereas the concrete layer thickness is decreasing and the oxide layer thickness is increasing with time.

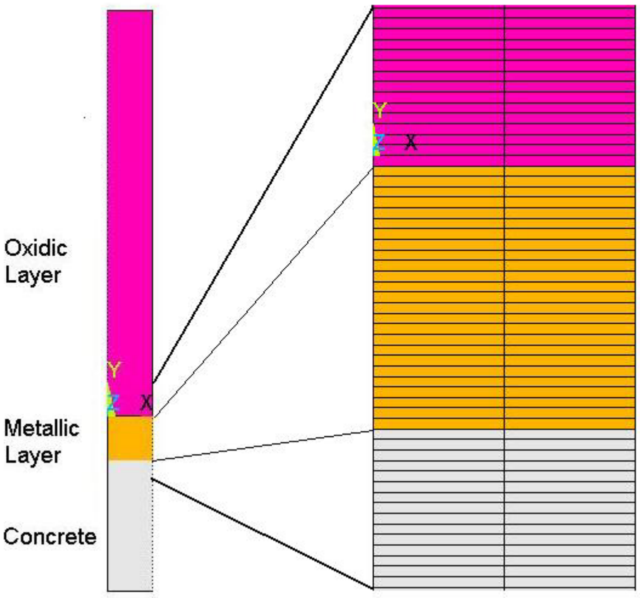

Figure 4: Melt cooling by top flooding – finite element mesh

The thermal simulation of the ECOKATS2-experiment was performed for a total time of 1800 s with time steps of 1 s. Figure 5 shows the vertical temperature profiles for different times. At the beginning (TIME 1 s) a homogeneous temperature of 2100 K is assumed for the metallic and the oxidic layer. The next curve gives the temperatures after 1 minute (TIME 60 s). Due to the strong gas release from the metal-concrete interface the effective conductivities for the metallic and the oxidic layer are very high and therefore the melt cools down homogeneously. Since there is no additional heat transfer resistance modelled between the oxidic and the metallic layer both layers appear to be unified. But the progress of the concrete erosion is clearly visible, as the lower edge of the high temperature region moves downward. This applies also for the next curves (TIME 180 s, TIME 600s).

The remaining curves show a different shape. This is due to the fact that the immobilization temperature of the oxide is reached, which means that a very high viscosity is observed even clearly above the solidus temperature. Therefore the motion of the melt is stopped and the temperature curves show a typical cool down process of a 2 layer body with different conductivities. Accordingly the concrete is heated up at a much lower rate and therefore the erosion is stopped. Figure 6 shows the heat fluxes and the concrete ablation versus time. These curves are in accordance to the observations in Fig. 5. The curve “Hflux_Bot” represents the heat flux

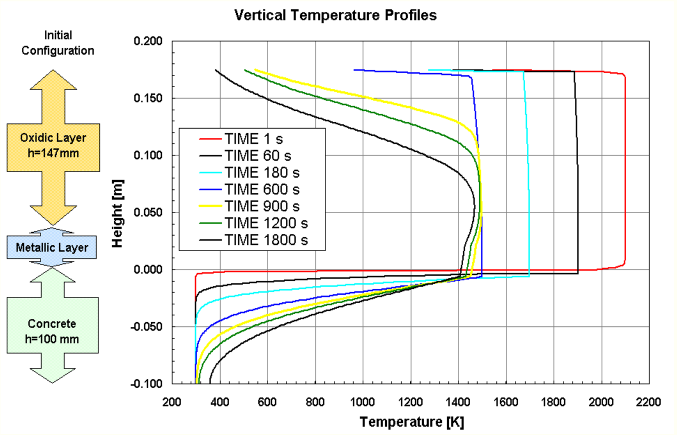

Figure 5: Temperature profiles for different times; simulation of the cooling phase of the ECOKATS2 test

from the metallic layer to the concrete and refers always to the moving interface between metal and concrete. After a peak at the beginning the heat flux reduces with some fluctuations to a level of approximately 300 kW/m² from where it reduces smoothly to a level of some 50 kW/m² at the end of the simulation. The fluctuations can be explained by the discrete modelling of the concrete erosion process. Each time an element changes its material properties from concrete to metal, the interface to which the heat flux is referred moves, too.

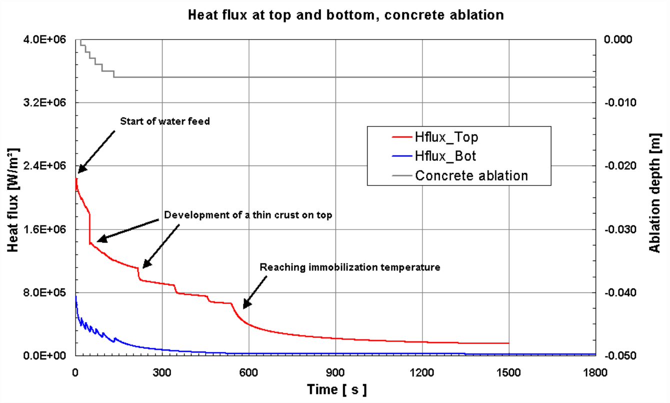

Figure 6: Heat fluxes and concrete ablation vs. time; ECOKATS2 test; red: heat flux into the water layer, blue: heat flux into the concrete; grey: concrete ablation (right axis)

The curve “Hflux_top” shows the heat flux from the top surface of the melt to the water layer. Since the gas sparging from the melt to the water enhances the normal boiling heat flux from a horizontal surface significantly, the maximum peak is reaching more than 2.3 MW/m², which is about 3 times higher than without gas sparging. Later on again fluctuations of the heat flux are observed. This is an indirect coupling effect to the bottom heat flux: since the bottom heat flux gives the concrete ablation rate, there is a proportionality to the gas sparging rate and the gas sparging rate influences the boiling heat transfer process at the top surface.

References

[1] H. Alsmeyer, T. Cron, G. Messmer, W. Haefner: Draft summary of ECOKATS2: A large scale experiment on melt spreading and subsequent cooling by top flooding, FZ Karlsruhe, October 2003
[2] J. M. Bonnet: Thermal Hydraulic Phenomena in Corium Pools for Ex-Vessel Situations: The Bali Experiment, Proceedings of the OECD Workshop on Ex-Vessel Debris Coolability, Karlsruhe 15-18 November 1999, FZKA 6475, pp 76-87, 2000.
[3] J.J. Foit: Analysis of the KATS, COMAS and CORINE Experiments; Report FZ-Karlsruhe
[4] J. M. Seiler: Phase Segregation Model and Molten Pool Thermal-Hydraulics during Molten Core-Concrete Interaction, NED vol. 166 pp 259-267, 1996.
[5] Verein Deutscher Ingenieure, VDI-Wärmeatlas, Berechnungsblätter für den Wärmeübergang, 9. Auflage, VDI-Verlag, Düsseldorf, Germany, 2002.
[6] E. Altstadt and H.-G. Willschuetz: Melt coolability by top flooding: thermal and mechanical simulations on the ECOKATS2 test; ECOSTAR-Report SAM-ECOSTAR-D41-D42-D43, February, 2004

Acknowledgements

This work was supported by the European Commission within the project ECOSTAR of the 5th frame work programme .

ANALYSIS OF THE DAMAGE OF A PRESSURE VESSEL MATERIAL IN SIMULATION EXPERIMENTS FOR LWR ACCIDENT SCENARIOS

Gudrun Mueller and Hans-Georg Willschuetz

1. Introduction

Considering the hypothetical core melt down scenario for a light water reactor the failure mode of the reactor pressure vessel (RPV) has to be investigated to assess the loadings on the containment. Experimental and numerical work is performed worldwide to get insights into possible consequences. To validate the developed computational tools numerical simulations of the Lower Head Failure experiments like OLHF or FOREVER are conducted.

An interesting question to be solved in this frame is the reason for the different shape of the failure site even under comparable loading conditions and for the same material: In some experiments like LHF-7 and EC-FOREVER-3B a rough crack surface was found at the failure site while in others like OLHF-1 a rather ductile behaviour was observed resulting in nearly blade-like edges on both sides of the vessel opening.

2. The applied RPV-steels

The vessel steel used in all tests was a manganese-molybdenum-nickel alloy. For all LHF/OLHF-tests and the EC-FOREVER-4 test the American RPV-steel A 533 Type B Class 1 was applied (cf. [1, 2]), where the OLHF and the EC4 plates were from the same heat (Dillinger Hütte, Germany), while the LHF plates were from another heat (Lukens Steel, USA). Table 1 shows the chemical composition of the steels. First the minimum and maximum values according to the ASTM-standard for A 533 Type B are given. EC3b shows values, which are in accordance with the French Standard for 16MND5, but also with the American A 533 Type B except the slight Chromium content. Comparing the Phosphorus, Sulphur and Chromium content of EC4 and OLHF it seems reasonable that they are from the same heat.

Table 1: Chemical composition according to the ASTM regulation for A 533 Type B and of the different vessels

Wt.-%	C	Si	Mn	P	S	Cr	Ni	Mo	Cu
533 min	0.000	0.130	1.070	0.000	0.000	…	0.370	0.410	…
533 max	0.250	0.450	1.620	0.035	0.035	…	0.730	0.640	…
EC3b	0.138	0.230	1.190	0.009	0.004	0.251	0.523	0.466	0.091
EC4	0.155	0.252	1.120	0.012	0.001	0.046	0.417	0.424	0.028
LHF	0.170	0.200	1.220	0.006	0.010	0.100	0.670	0.550	0.009
OLHF	0.172	0.286	1.290	0.013	0.001	0.046	0.520	0.490	0.021

The thermal treatment was done according to the appropriate regulations, but nevertheless it is assumed that the thermal treatment after forming the vessel takes a mi minor role, because the temperatures at the failure site were clearly above the austenitisation temperature in the tests and in the case of the FOREVER-experiments for a long time before failure.

3. Comparison of the FOREVER-tests with the FEM-calculations

In the frame of the FOREVER-tests pre-test calculations had been performed. These calculations were based on previous work [3, 4] and assumed the material behaviour of the 16MND5-steel for both tests.

Figure 1 shows the comparison with the experiment in case of EC3B [5]. Since the experiment did not run as scheduled, because the fuse of the heater failed two times for a few minutes (cf. Fig. 1), post test calculations had to be performed considering the transient behaviour of the heater. But even the post test calculation can be considered as conservative.

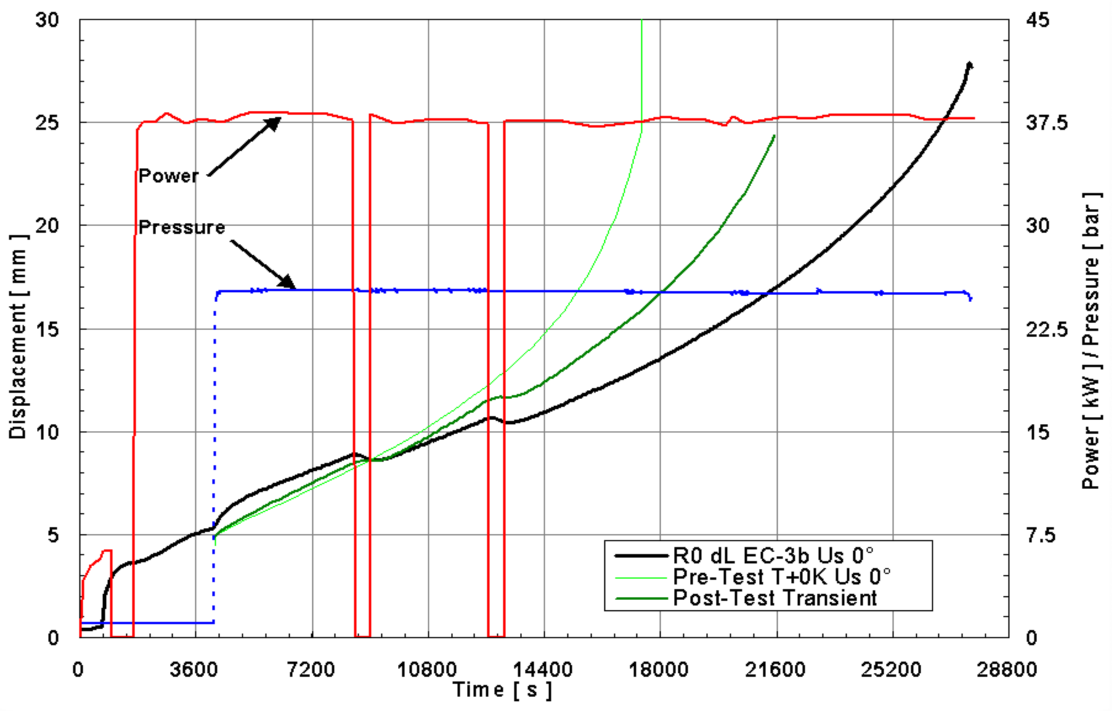

Figure 1: EC3B, displacement behaviour of bottom head, comparison of experiment and calculation, loading conditions: heating power and pressure

The behaviour in case of the EC4 test is contrary to this [6].

It was assumed that the A 533-steel might be “weaker” than the 16MND5 and therefore the temperature level in the mechanical calculation was raised by 20 K to simulate an additional “thermal weakness”. But as Figure 2 shows this calculation was not conservative: failure occurred approximately 20 minutes earlier than predicted by this calculation.

4. Structural and metallographical investigations

After their failure the FOREVER vessels were cut and it was found that the shape of the opening was remarkably different: in EC3B a rough crack surface was found at the failure site while in EC4 a rather ductile behaviour was observed resulting in nearly blade-like edges on both sides of the vessel opening. Figures 3 and 4 show this different shape (notice the different scales). It was part of the investigations to characterise the significant changes of the microstructure of the vessel wall material, which appears due to the high temperatures during the test.

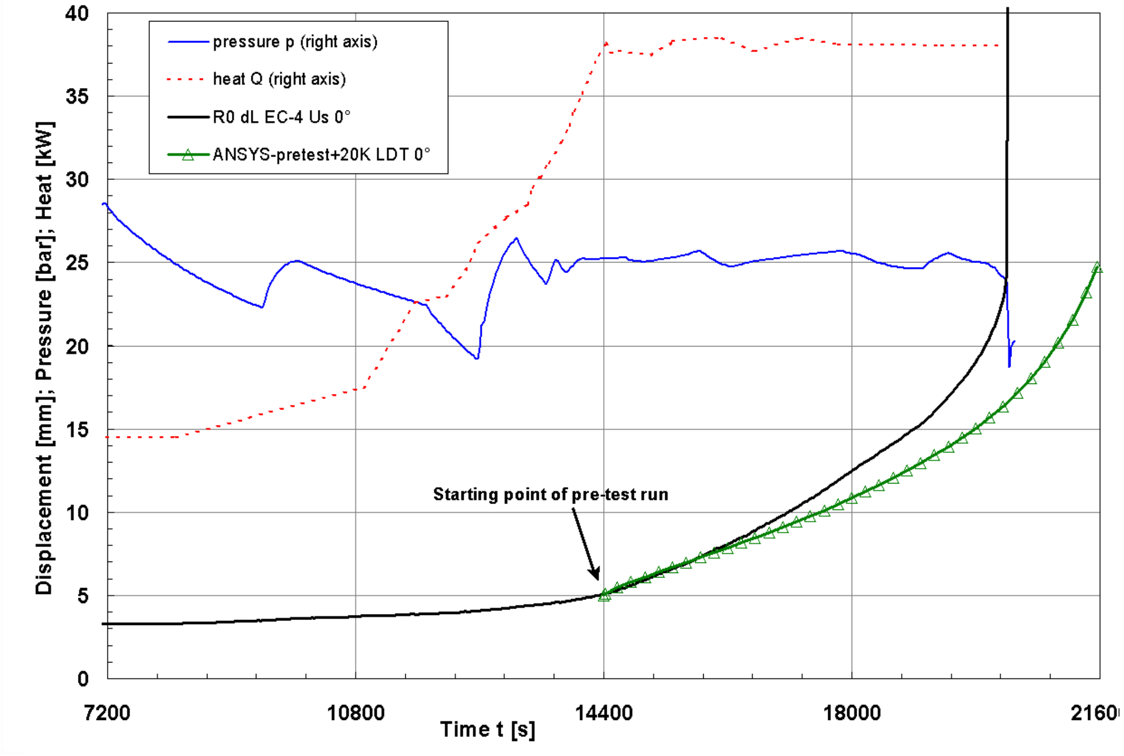

Figure 2: EC4, displacement behaviour of bottom head, comparison of experiment and calculation

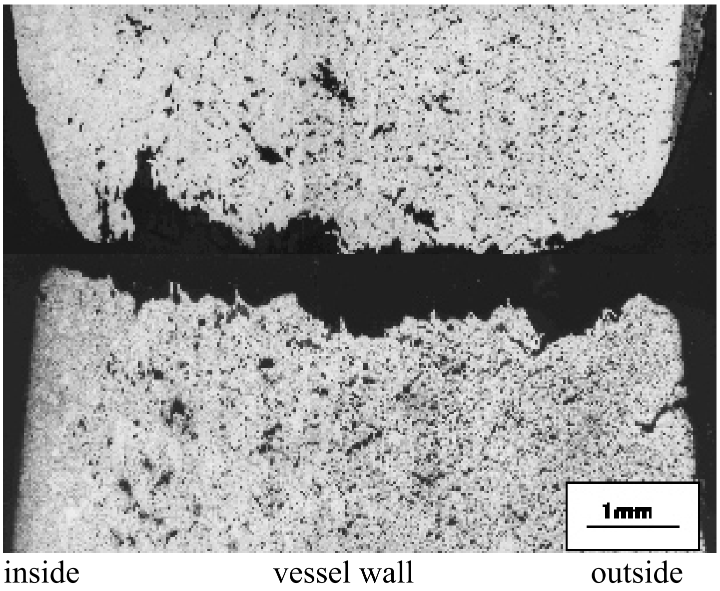

Figure 3: Macrostructure of EC3B at the crack, etched samples

These changes contain information on the thermo-mechanical loading and the failure mechanism. As mentioned before, the vessel bottoms of the FOREVER experiments EC3B and EC4 are of different material. The hemispherical bottom of EC3B was produced from a rolling plate of the French 16 MND 5 steel.

The initial microstructure of the EC3B-vessel consists of fine bainite. This is no more existing after the experiment in all examined high positions of the hemispherical bottom. Instead, a microstructure consisting of coarse bainite, coarse polygonal or banded ferrite occurs and covers almost the whole cross section. The crack, which leads to the failure of the vessel, was observed in the hemispherical part approximately 8.5 cm below the weld. It begins at the outside of the vessel wall and runs almost perpendicular through the wall to the inside. At the crack position the wall thickness decreases from 15 mm to 8.5 mm and the crack surface is rough. The formation of the crack results from the creep damage caused by the highest temperature of the experiment in this region. The appearance of creep pores depends on the temperature

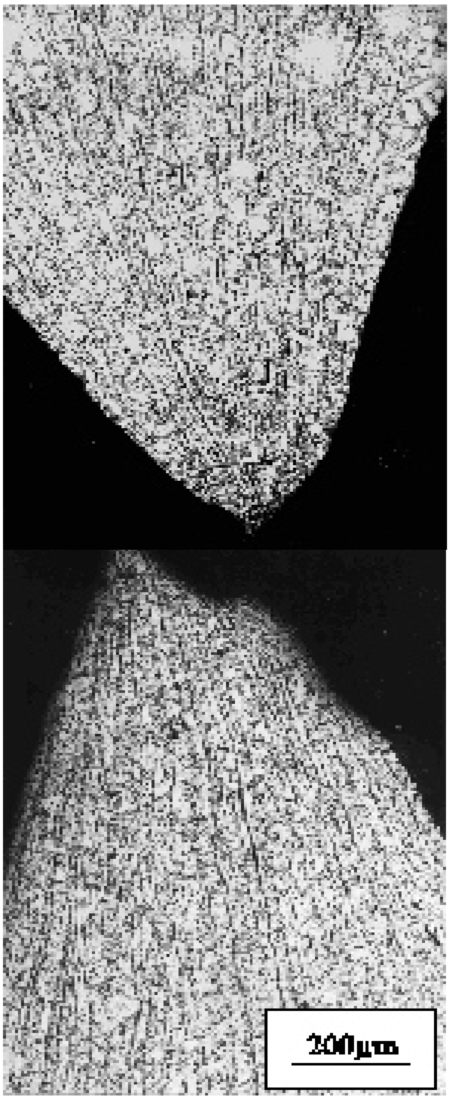

Figure 4: Microstructure of EC4 at the crack, etched samples

and loading. Most of the pores are in the vicinity of the crack (cf. Fig. 3). Their shape is partly already crack-like what proves, that the tertiary creep range is reached.

For the American A 533 steel of the EC4-vessel the initial microstructure consists of bainite, too.
Due to the temperature history during the experiment the microstructure changed mostly into coarse bainite and, depending on the temperature distribution in the vessel wall, different parts are of coarse polygonal or banded ferrite. The crack was observed in the hemispherical part approximately 7 cm below the weld. Figure 4 shows the upper and the lower end of the opening sides. At the crack position wall thickness decreases from15 mm pre-test thickness to approximately 0.2 mm and the crack surface is smooth. Near the crack there are only a few pores. The failure occurred in the region of high temperatures and high deformation.

This different damage behaviour was already observed not only between the French 16MND5 and the American A 533 B1 steel but also between two different charges of A 533 B1 in the LHF and OLHF experiments, respectively [1]. While the LHF steel shows a rough crack with little necking, the OLHF specimens failure is of the type of EC4. The creep tests at CEA SACLAY on A 533 B1 steel of LHF and OLHF confirm these results for high temperatures (cf. [1] and Figures 5 and 6). Since the chemical composition and the thermal treatment of these two A 533 B1 heats were according to the standard the following explanation was suggested in [1]: “Sulphur included in Manganese steel composition could make them fragile. This means that it is not possible to extend mechanical properties obtained from some RPV main vessel steel samples to all RPV main vessels.”

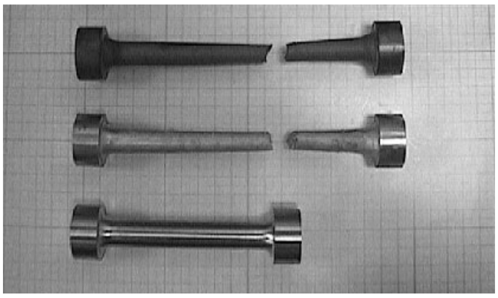

Figure 5: Fractured uniaxial creep specimen of LHF-material

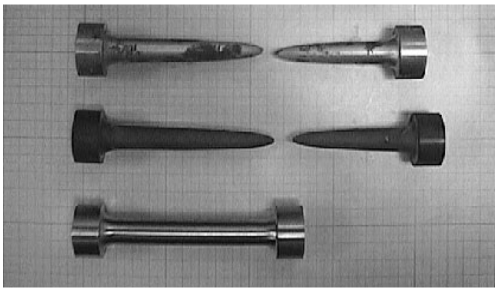

Figure 6: Fractured uniaxial creep specimen of OLHF-material

5. Conclusion

Including the latest results from the FOREVER-tests and their chemical analysis it can be seen that the sulphur content is low in all specimen, and therefore it seems not sure that the slight amount of the sulphur content is the only reason for the different crack or failure shape. This should be a topic for further investigation.

References

[1] Ph. Mongabure, Creep Tests on LHF and OLHF SA533B1 Steel, Report SEMT/LISN/RT/00-060/A, CEA, France, 2000.

[2] T.Y. Chu et al., Lower Head Failure Experiments and Analyses, Report NUREG/CR-5582, Sandia National Laboratories, USA, 1999.

[3] H.-G. Willschütz, et al., Coupled thermal structural analysis of LWR vessel creep failure experiments, Nuclear Engineering and Design, vol. 208, pp 265-282, 2001.

[4] H.-G. Willschütz, et al., Simulation of Creep Tests with French or German RPV-steel and investigation of a RPV-support against failure, Annals of Nuclear Energy, vol. 30, pp 1033-1063, 2003.

[5] A. Giri, et al., EC-FOREVER Experiments on Thermal and Mechanical Behaviour of a Reactor Pressure Vessel during a Severe Accident. Technical Report. EC-FOREVER-3(B) test.. Stockholm, Sweden, 2002

[6] B.R. Sehgal, et al., EC-FOREVER Experiments on Thermal and Mechanical Behaviour of a Reactor Pressure Vessel during a Severe Accident. Technical Report. EC-FOREVER-4 test. Stockholm, Sweden, 2002

Acknowledgement

This work has been funded by the German Ministry of Economics and Labour BMWA under Contract No. 150 12 54. The authors are responsible for the scientific contents.
The authors are grateful to Mrs. M. Roßner for her metallographic investigations.

CHARACTERIZATION OF RADIATION EFFECTS IN REACTOR PRESSURE VESSEL STEELS BY MEANS OF SMALL-ANGLE NEUTRON SCATTERING

Andreas Ulbricht and Jürgen Böhmert

1. Introduction

The range of the reactor pressure vessel (RPV) surrounding the core is subjected to significant neutron dose during the lifetime of a nuclear power plant. Neutron irradiation influences the mechanical properties of the RPV steels by increasing the strength (neutron hardening) and decreasing the toughness (neutron embrittlement). This is relevant for the safety and, thus, has been an object of manifold research activities for long time. Whereas the work has preferentially addressed the mechanical properties, the microstructural changes due to neutron radiation have been hardly investigated. One of the main reasons for that is, not at least, that the microstructural radiation effects are hardly detectable by the established microstructural analysis methods. In the consequence, the mechanism of the phenomenon has not yet completely understood up to now.

The microstructure that arises in RPV steels, primarily as a consequence of radiation-enhanced diffusion and defect clustering, is extremely fine-scaled, i.e. has a magnitude of a few nanometres. Small-angle neutron scattering (SANS) measurements are able to detect such small clusters and can provide qualitative and quantitative information for evolution of physical understanding of the irradiation-induced structure and of the changes of the mechanical properties resulting from that.

The radiation susceptibility changes with the type of steel. Therefore the role of particular material parameters in defect evolution should be worked out.

2. Experimental conditions

Table 1 gives the composition of the investigated materials. In addition to the prototype material 15Kh2MFA (code KAB) of the VVER-440/230 construction type, six ASTM steels, i.e. 1 weld and 5 base metals, with modification in the Cu and P content were selected from the IAEA-Coordinated Research Program "Optimizing Surveillance Programs and Their Analysis". The irradiations were carried out in distinct radiation channels of the prototype reactor VVER-2 in Rheinsberg (Germany) with different exposure levels up to neutron fluences of 10^{20} cm^{-2} ($E_n > 1$ MeV, equivalent to 0.14 dpa) at 528 K.

The measurements were conducted at SANS spectrometers of HMI Berlin [1] and ILL Grenoble [2] using $10 \times 10 \times 0.8$ mm^3 discs cut from the halves of broken Charpy specimens. The samples were placed in a saturating magnetic field of 1.4 T perpendicular to the neutron beam direction (wavelength 0.5 nm) in order to separate nuclear and magnetic scattering. A possible composition of the irradiation-induced clusters can be derived from the ratio of these two different scattering intensities.

Table 1: Chemical composition of the RPV steels (values in wt.-%, rest Fe).

Material (code)	C	Si	P	V	Cr	Mn	Ni	Cu	Mo
A508 cl.3 (JWQ)$^{1)\,2)}$	0.09	0.30	0.026	0.002	0.04	1.29	1.10	0.26	0.48
A508 cl.3 (JFL)$^{2)}$	0.17	0.25	0.004	0.004	0.16	1.42	0.75	0.01	0.52
A533B cl.1 (JRQ)$^{2)\,3)}$	0.20	0.23	0.020	0.008	0.13	1.42	0.80	0.15	0.52
A533B cl.1 (JPA)$^{2)}$	0.18	0.27	0.018	0.01	0.15	1.47	0.82	0.33	0.54
A533B cl.1 (JPB)$^{2)}$	0.18	0.26	0.017	0.01	0.15	1.42	0.83	0.01	0.54
A533B cl.1 (JPC)$^{2)}$	0.18	0.27	0.007	0.01	0.15	1.45	0.81	0.01	0.54
15Kh2MFA (KAB)$^{4)}$	0.14	0.24	0.011	0.27	2.60	0.55	0.24	0.22	0.62

$^{1)}$ weld metal, all the others are base metals; $^{2)}$ IAEA-CRP-program; $^{3)}$ IAEA reference material; $^{4)}$ prototype material of the VVER-440/230 construction type.

3. Results

SANS is an indirect structural analysis method. It does not provide a real space image but only the Fourier transform of the averaged spatial scattering density distribution. As an example, Fig. 1 shows the measured volume-fraction related size distribution functions calculated by Fourier analysis [3] for the material 15Kh2MFA (KAB) after different exposure levels.

The qualitative course of the size distribution is similar for all materials investigated. The distributions are bimodal with a steep peak near 1 nm and a broad plateau caused by structure inhomogeneities of different size. The first peak appears in the irradiated conditions and is partly or almost completely reduced by annealing. Material composition and irradiation conditions do not change the position and the shape but clearly affect the heigth of the peak. The plateau part of the size distribution is hardly influenced by irradiation.

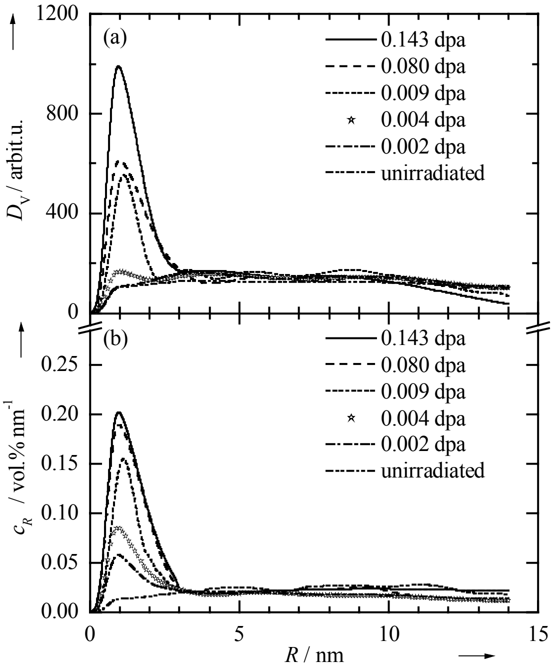

Fig. 1: Volume distribution functions, c_R, of scattering defects in 15Kh2MFA RPV steel after different irradiation levels weighted with the scattering contrast $\Delta\eta^2$; (a) $D_V = c_R\Delta\eta^2_{\mathrm{nuc}}$; (b) $c_R\Delta\eta^2_{\mathrm{mag}}$, absolute values for non-ferromagnetic defects.

The results emphasize that the first peak characterizes the radiation induced defects. The difference of the integral under the peak for the irradiated condition and unirradiated initial state, Δc, is considered to be the volume fraction of the radiation defects.

The size distribution functions in Fig. 1 are calculated from the measured courses of (a) the nuclear and (b) the magnetic scattering cross sections.

Both size distribution functions are weigthed with the scattering contrast, $\Delta\eta^2_{\mathrm{nuc}}$ and

$\Delta\eta^2_{\mathrm{mag}}$, respectively. The position of the peak maximum and the half width is unchanged but the relative height is changed for the different exposure levels in Fig. 1 (a) and (b). SANS detects the same radiation-induced features from the nuclear and magnetic scattering behaviour of the sample but the intensities are different. That means that the composition averaged over all irradiation induced clusters is modified in the case of the 15Kh2MFA steel presented by increasing irradiation.

The volume fraction of radiation defects can be determined under the assumption that the scatterers are non-ferromagnetic inhomogeneities embedded in a ferromagnetic matrix. The results calculated in this way are given in Table 2 for all investigated materials after a radiation damage of 0.08 dpa.

The dependence of the volume content of radiation defects from the exposure level is depicted in Fig 2 (a) for the materials A533B cl.1 (JRQ), A508 cl.3 (JFL) and 15Kh2MFA (KAB).

4. Discussion and conclusion

Fast neutron irradiation produces defects of radii up to 3 nm. The mean radius of the defects is approximately constant and equal to about 1 nm in all cases. The evolution of the defect content for a particular steel is not linear in response to the irradiation damage values given as displacements per atom. The defect type is not uniform. The average composition of defects can be changed with increasing neutron fluence. So, the clusters formed at first must be Cu rich in the 15Kh2MFA steel as indicated by the high ratio between magnetic und nuclear scattering intensity. This ratio decreases with increasing irradiation. With decreasing Cu content of the matrix, as well the formation rate as the Cu content are reduced indicated by the decreasing A-ratio. Such a behaviour was not observed for the materials A533B cl.1 (JRQ) and A503 cl.3 (JFL). The ratio is different for both materials but approximately constant over the different exposure levels. Generally, the ratio between magnetic and nuclar scattering is lower in all ASTM steels in comparison to 15Kh2MFA. This can be explained by a mixed cluster composition of Ni, Mn and vacancies. The material A508 cl. 3 (JFL) has the lowest ratio. It corresponds to vacancy rich clusters, i.e. voids.

The content of copper is the most essential parameter controlling the radiation susceptibility. Nickel rich steels (for instance the materials with code JPA, JRQ) and especially welds (code JWQ) have a higher radiation susceptibility related to the volume content of the radiation

Table 2: Irradiation induced volume content ($\Delta c = c_{irr} - c_{unirr}$; $c = \int c_R dR$) of non-ferromagnetic defects and changes of Vickers hardness, ΔHV10, after a radiation damage of 0.08 dpa (1 displacement per atom corresponds to a neutron fluence of 10^{21} cm^{-2} with $E_n > 0.5$ MeV), A-ratio = 1 + $\Delta\eta^2_{\mathrm{mag}}/\Delta\eta^2_{\mathrm{nuc}}$.

Material (code)	Characteristic features	Δ*c* / vol.-%	ΔHV10	A-ratio
A508 cl.3 (JWQ)	high P and Cu, medium Ni	0.86 ± 0.03	118 ± 6	2.4
A508 cl.3 (JFL)	low P and Cu, medium Ni	0.02 ± 0.01	19 ± 6	1.4
A533B cl.1 (JRQ)	high P, medium Cu and Ni	0.34 ± 0.02	83 ± 6	2.4
A533B cl.1 (JPA)	high P and Cu, medium Ni	0.75 ± 0.03	113 ± 4	2.5
A533B cl.1 (JPB)	high P, low Cu, medium Ni	0.04 ± 0.01	39 ± 9	1.7
A533B cl.1 (JPC)	low P and Cu, medium Ni	0.02 ± 0.01	36 ± 6	1.6
15Kh2MFA (KAB)	Medium P, high Cu, low Ni	0.26 ± 0.02	67 ± 5	3.1

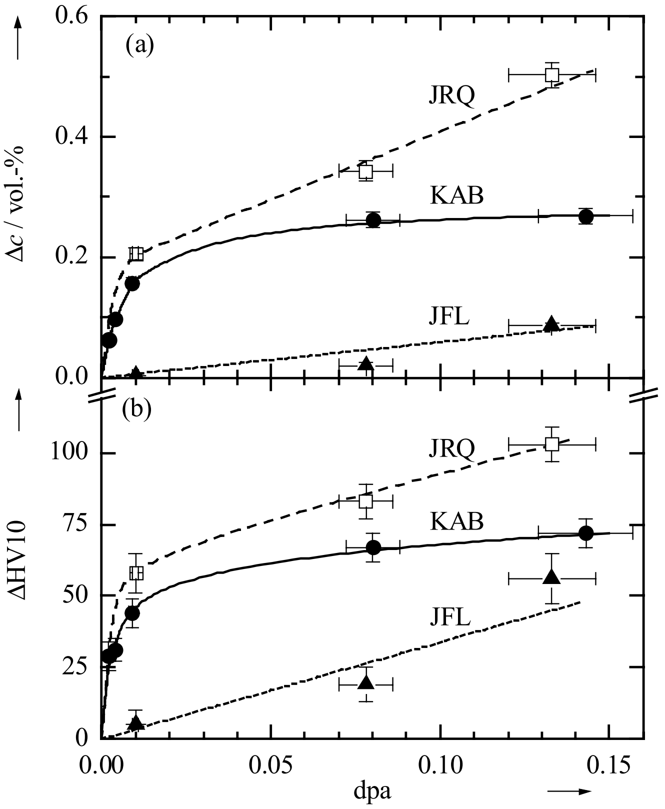

Fig. 2: (a) Volume fraction of radiation-induced defects, Δc, and (b) changes of Vickers hardness, ΔHV10, in 15Kh2MFA (KAB), A503 cl.3 (JFL) and A533B cl.1 (JRQ) after different irradiation levels.

defects, Δ*c*, as nickel poor steels (code KAB) with the same content of deleterious elements as copper. The content of phosphorous in the material does not play an important role for the cluster evolution under irradiation.

The comparison of the changes of the Vickers hardness, ΔHV10, in Fig. 2 (b) with the radiation induced defect content, Δ*c*, in Fig. 2 (a) shows the same dependence on the dpa values. Furthermore for a certain exposure level the values in Table 2 show that higher changes of hardness correspond to higher contents of defects. This can be taken as evidence that the assumption of non-ferromagnetic radiation defects is correct. However, the relation between ΔHV10 and Δ*c* is also influenced by the defect composition.

References

[1] U. Keiderling and A. Wiedenmann (1995), New SANS instrument at the BER II reactor in Berlin, Germany, *Physica B* **213&214**, 895-897.
[2] P. Lindner, R. P. May and P. A. Timmins (1992), Upgrading of the SANS instrument D11 at ILL, *Physica B* **180&181**, 967-972.
[3] O. Glatter (1980), Determination of particle-size distribution functions from small angle scattering data by means of the indirect transformation method, *J. Appl. Cryst.* **13**, 7-11.

POST SERVICE INVESTIGATIONS OF VVER-440 RPV STEEL FROM NPP GREIFSWALD

Bertram Boehmer, Juergen Boehmert, and Udo Rindelhardt

1. Introduction

Pressure vessel integrity assessment after long-term service irradiation is commonly based on surveillance program results. Radiation loading, metallurgical and environmental histories, however, can differ between surveillance and RPV materials. Therefore, the investigation of RPV material from decommissioned NPPs offers the unique opportunity to evaluate the real toughness response. This has been done several times, but only at prototype reactors. A chance is given now through the investigation of material from the decommissioned VVER-type Greifswald NPP to evaluate the state of a standard RPV design and to assess the quality of prediction rules and assessment tools.

2. Characteristics of the Greifswald NPP and dismantling procedure

Between 1973 and 1979, four units (unit power 440 MW_{el}) of the Russian Pressurized Water Reactor line VVER-440/230 were put into operation in Greifswald (East Germany). Design, material production and operation conditions are identical or almost identical for more than 30 similar units in Russia and Eastern Europe. The Greifswald RPV material is very suitable for investigating embrittlement phenomena: The neutron flux is very high (small water gap: 16 cm), the operation temperature is low (270 °C) and the material is sensitive to neutron embrittlement (Cu content > 0.12 %, high P content in weld). Therefore the accepted embrittlement limits were already reached after about 12 cycles, and the RPVs had to be annealed in the range of the most critical weld 4 (see Fig.3) to continue their operation. In 1990, after the German reunification all units were shut down.

The operation time, radiation characteristics and annealing states of the four Greifswald units are given in Table 1.

Table 1: Operation/annealing conditions of the Greifswald units

unit	cycles	Effective days	Annealed in
1	15	4215.02	1988
1(after annealing)	2	627.4	-
2	14	4067.4	1990
3	12	3581.8	1990
4	11	3207.9	not

The chemical composition and the initial mechanical properties of the RPV material in the core-near region are presented in Tables 2 and 3.

The dismantling of the unit 1 RPV will start in 2004. The RPV will be moved to a special cutting place, where it will be horizontally cut in rings (approx. 1 m high). Then the rings will be cut by a vertical saw into pieces (approx. 40 cm). For the material investigation program pieces of 125 x 125 mm with a thickness of 140 mm will be cut with the same system. It must be guaranteed that the material temperature increase due to the cutting process is well below the reactor service temperature. This was checked by control measurements and FEM simulation [1].

Table 2: Chemical composition in the core region (in weight %, Fe balance)

unit /material	C	Si	Mn	Cr	Ni	Mo	V	P	S	Cu
1 base	0,16	0,30	0,40	2,78	0,18	0,63	0,27	0,010	0,013	0,13
weld	0,09	0,29	0,50	1,78	0,29	0,40	0,19	0,015^1 (0,036)^2	0,012	0,12
2 base	0,16	0,28	0,46	2,60	0,18	0,66	0,28	0,013	0,012	
weld	0,08	0,17	0,63	1,50	0,19	0,46	0,17	0,011 (0,032)^2	0,013	0,18
3 base	0,13	0,26	0,39	2,85	0,15	0,68	0,19	0,012	0,012	
weld	0,09	0,21	0,59	1,69	0,18	0,47	0,27	0,014^1 (0,035)^2	0,013	0,12
4 base	0,17	0,27	0,47	3,00	0,15	0,63	0,29	0,016	0,014	
weld	0,08	0,19	0,56	1,73	-	0,52	0,21	0,012^1 (0,035)^2	0,014	0,16

1) P content in welding wire

2) P content in weld seam

Table 3: Mechanical properties in the core region

unit	R_{pm}/MPa	$R_{p0.2}$/MPa	A/%	Z/%
1	650	580	23,0	74,6
2	624	525	26,6	76,0
3	650	537	21,0	75,5
4	644	515	24,2	78,7

During cutting under typical operational conditions the temperature was measured by thermocouples positioned at three midwall thickness positions in different distances from the saw kerf and by a high-resolving thermal imager system (VARISCAN VS 3011PC, Jenoptik AG) depicting a surface of 45 mm x 45 mm. The results of the measurements were used as the calibration data for the thermal FEM simulation with the FEM code ANSYS. The maximum temperature calculated reaches 159° C and is clearly higher than the maximum value of 35 °C measured by the thermocouple or of 112 °C measured by thermal imager respectively. This proves that the simulation is conservative and the heating during sawing is insignificant in regard to annealing.

3. Investigation program and results

3.1 Fluence calculations

Knowledge of neutron fluence integrals $\phi_{E>0.5MeV}$, $\phi_{E>1MeV}$ and dpa-values at the inner and outer pressure vessel walls are prerequisites for planning the material investigations. They were obtained with the help of a Green's functions method. The Green's functions $G_{jk}(\vec{r},i)$ were calculated earlier by the Monte Carlo code TRAMO [2]. The fluence for energy group i at point $\vec{r}$ and time t is calculated as following sum over all assemblies j and height intervals k:

$$\Phi(\vec{r},i,t) = \sum_{\mathrm{jk}} \mathrm{q}_{\mathrm{jk}}(t) G_{jk}(\vec{r},i) \,, \tag{1}$$

where $G_{jk}(\vec{r},i)$ is defined as fluence at point $\vec{r}$ originating from 1 fission neutron emerging in source element *jk*, covering the *k*-th height interval of fuel assembly *j*.

$\mathrm{q}_{\mathrm{jk}}(t)$ is the number of source neutrons emitted in element *jk* during the time interval *[0,t]*.

$$\mathrm{q}_{\mathrm{jk}}(t) = \int_0^t \mathrm{Q}_{\mathrm{jk}}(t')\, dt' \tag{2}$$

where $\mathrm{Q}_{\mathrm{jk}}(t')$ is the source rate in neutrons per second from source element *jk.*

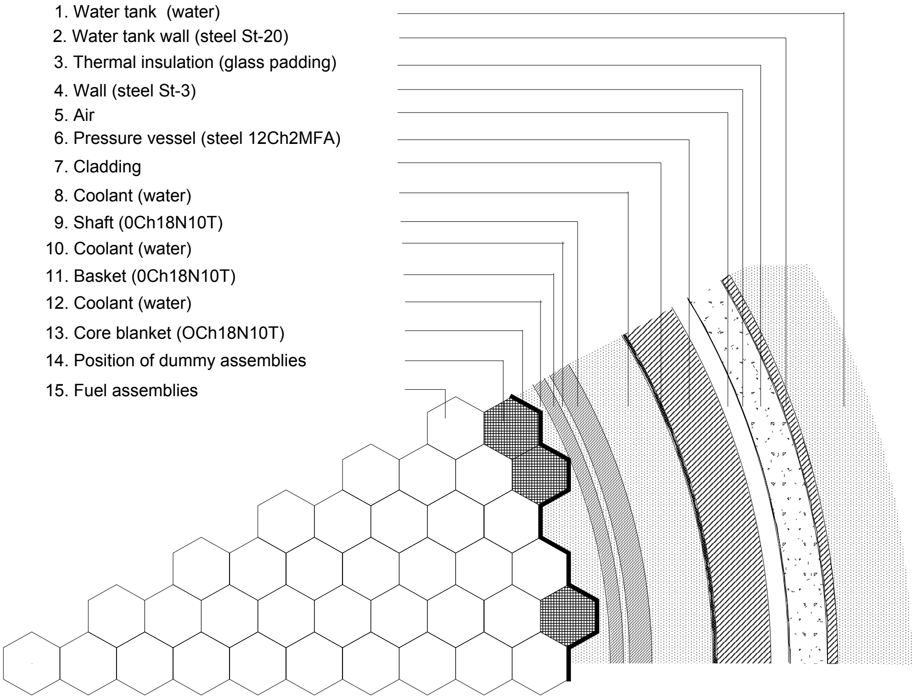

The geometrical model used in the calculations is illustrated in Fig. 1. As the geometrical and transport characteristics had a 30° mirror symmetry in the 60° sector and the neutron sources a 60° rotational symmetry, the Greens functions were calculated for the shown 30° symmetry sector of the reactor and the fluences for a 60° sector. The fluence for any other azimuthal angle θ is equal to the fluence in the 60° sector at the angle

$$\theta_{60} = \theta - 60 \ \mathrm{int}(\theta / 60) \tag{3}$$

where int means the integer part of the expression in brackets.

The fluence integrals $\Phi_{E>0.5MeV}$ and $\Phi_{E>1.0MeV}$ and dpa were calculated

- for the outer and inner wall of the pressure vessel
- for 10 height intervals of 25 cm each and

- 20 azimuthal angular intervals of 3° each.
- for the total operation period of the units 1, 2, 3 and 4
- for unit 1 additionally for the last two cycles (after the annealing).

Some of these results characterizing the irradiation state of the Greifswald units are shown in Fig. 2 and Table 4. They are completely given in [3].

Table 4: Azimuthal maximum of $\phi_{E>1MeV}$ *(in units of* 10^{19} *n/cm*^{2}*)*

unit	inner wall axial maximum	inner wall weld 4	outer wall axial maximum	outer wall weld 4
1	4.4	3.3	0.69	0.49
1 (after annealing)	0.40	0.29	0.058	0.042
2	5.3	4.1	0.83	0.60
3	4.4	3.4	0.68	0.50
4	4.0	3.1	0.62	0.45

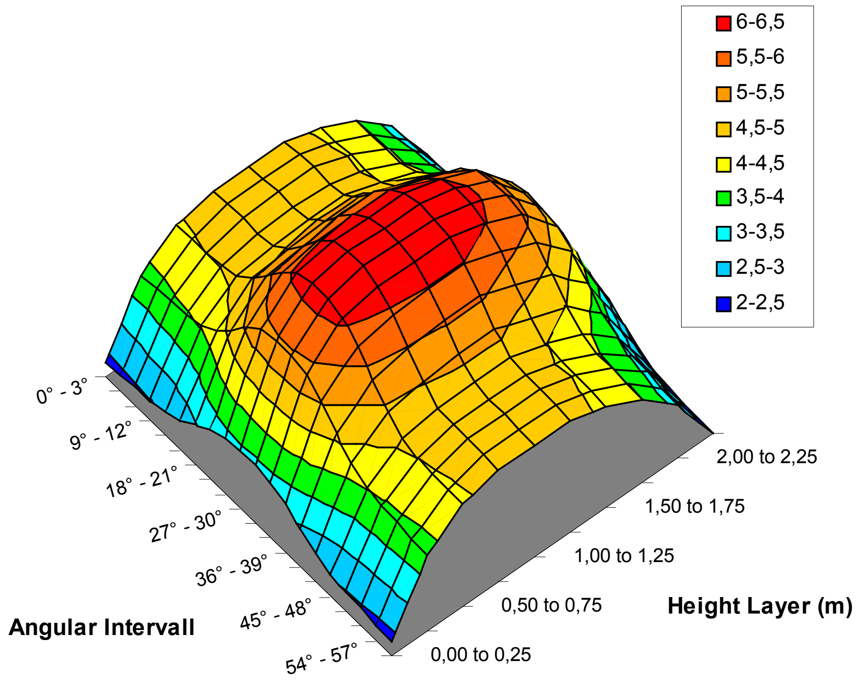

Fig. 2: Fluence $\phi_{E>0.5MeV}$ *in units of* 10^{19} *n/cm*^{2} *for unit 4 inner wall from 11 Cycles*

Further calculations will include studies of the influence of gamma irradiation, of the radiation spectra and of flux rate effects. Time dependent neutron and gamma flux spectra will be needed. Fortunately, a very detailed documentation exists of all necessary reactor data over the whole time of operation of each unit. Based on new calculations of pin-wise time-dependent neutron sources and an updated nuclear data base, Monte Carlo calculations are being prepared of time-dependent neutron and gamma fluence spectra at all positions throughout the RPV wall, where the material pieces will be taken.

3.2 Material Investigations

The working program is focused on the characterization of the material state. It comprises chemical analysis, microstructure investigations (by means of metallography, electron microscopy and SANS) and mechanical testing (hardness measurements, tensile tests, Charpy tests, fracture mechanics tests). The material investigation will be carried out based on pieces from the following 4 height positions (in mm relative to the core midplane, core height 2500 mm, see Fig. 3):

- 1 - Reference material position (weld 3) at -2825 mm (below core)
- 2 - Critical weld position (weld 4) at -915 mm
- 3 - Maximum neutron load position (base metal) at 0 mm
- 4 - Reference material position (weld 5) for the estimation of thermal ageing and gamma effects at +1715 mm.

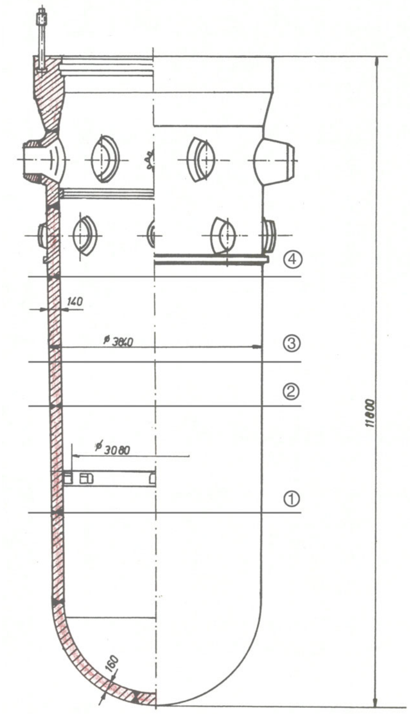

Fig. 3: Four cutting levels (marked 1 to 4) at the RPV

The following results of the program can be expected [3]:

- Determination of fracture toughness parameters (T_0,K_{IC}) at irradiated states
- Characterization of the real vessel wall and weld properties in radial and azimuthal direction
- Verification of toughness parameters correlations
- Validation of code approaches and embrittlement predictions
- Validation of plant annealing as industrial process
- Evaluation of the re-embrittlement behavior
- Identification of the most critical safety-related issues
- Enlargement of the data base.

Simultaneously, material stocks for further research programs including benchmark experiments to verify NDT embrittlement characterization methods will be obtained.

References

1. Th. Moessner, E. Altstadt, J. Boehmert, R. Weiß: Erwaermung des Reaktordruckbehaelters des Blockes 8 des KKW Greifswald bei der Zerlegung mittels Saegetechnik, FZR-Report 310, Rossendorf, Januar 2001
2. U. Barz, J. Konheiser: Monte-Carlo-Programm TRAMO – Moeglichkeiten und Anleitung zur Nutzung, FZR-Report 245, Rossendorf, Dezember1998
3. TACIS-Project NUCRUS 96601, Final Report, Brussels 2000

GAMMA AND NEUTRON SPECTRA INVESTIGATIONS IN IRON-WATER BENCHMARK CONFIGURATIONS FOR THE VERIFICATION OF MONTE CARLO CALCULATIONS IN REACTOR MATERIAL DOSIMETRY

Bertram Boehmer, Martin Grantz[1], Wolfgang Hansen[2] , Dietmar Hinke[3], Jörg Konheiser, Hans-Christoph Mehner[1], Klaus Noack, Ralf Schneider[2], Ingrid Stephan and Siegfried Unholzer[3]

1. Introduction

Recent findings indicate that gamma radiation can contribute to the embrittlement of reactor materials. Material tests of components of the High Flux Isotope Reactor (HFIR) in the Oak Ridge National Laboratory have shown that the level of the measured radiation embrittlement exceeds the expectations resulting from fast neutron fluence. Only, if additionally material damaging effects of gamma rays were included into the consideration, the observed rate of displacements per atom (DPA) comes in conformity with the theory [1]. The higher efficiency of γ-rays in producing freely-migrating defects [2] can further influence the embrittlement of reactor materials. These new findings may affect future safety assessments of reactor pressure vessels.

Some existing transport codes, e.g. the widely applied Monte Carlo code MCNP [3], are capable of calculating coupled neutron/gamma problems, but a systematic validation for gamma spectrum calculations for reactor dosimetry purposes is not yet done. Furthermore, the Monte Carlo code TRAMO [4] developed for neutron transport calculations in reactor dosimetry has been extended for calculations of coupled neutron/gamma processes with a necessity of the validation of the new features. Therefore, an experimental benchmark programme at two low power training and research reactors was started to measure both, neutron and gamma flux spectra behind and inside of transmission modules consisting of variable iron and water slabs. The comparison of the first series of experiments with MCNP calculations is presented.

2. Description of the Experiment

In order to verify neutron/gamma calculations, transmission experiments under defined benchmark conditions have been carried out with various water/iron configurations. Plates of iron, stainless steel (SS) and water slabs were combined to variable transmission modules in a range of thicknesses being relevant for reactor pressure vessels. The transmission modules were irradiated in the neutron and gamma beam of horizontal experimental reactor channels facing the reactor cores. Two reactor facilities with completely different core designs were used for the investigations - the AKR of the Technical University Dresden and the ZLFR of the University of Applied Sciences Zittau/Görlitz (Fig. 1).

For the first measurements, transmission modules were arranged inside the irradiation channel of the AKR (so-called inner position in Fig. 1, distance of the modules from the channel exit -18 cm) with detector positions behind the modules (detector distances from the module

---

[1] Hochschule Zittau/Görlitz, Fachbereich Maschinenwesen
[2] Technische Universität Dresden, Institut für Energietechnik
[3] Technische Universität Dresden, Institut für Kern- und Teilchenphysik

surface d = 0.5 cm and 72.5 cm). For further experiments transmission modules were placed at both reactors outside the reactor because of the more favourable background conditions at a distance of +10 cm from the channel exit (outer position) with alternative detector positions behind and in some cases inside the modules.

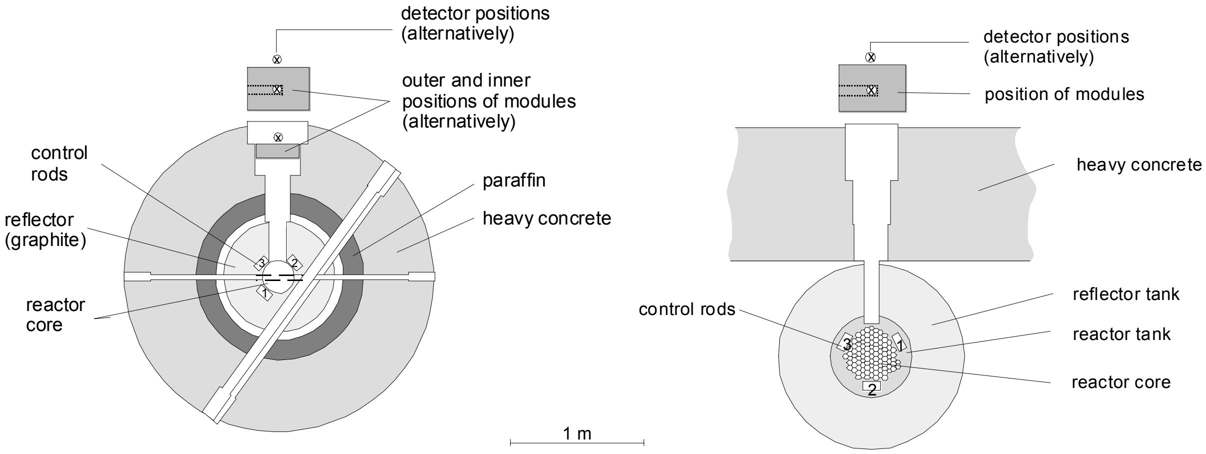

Fig. 1: Horizontal cross sections of the AKR (left) and ZLFR (right) reactor facilities with the positions of the transmission modules

The transmission modules at the inner position of AKR had a diameter of 37 cm and those in the outer position were rectangular (65 cm high and 50 cm wide) and composed by 1 cm thick Fe or stainless steel (X5CrNi18.10) plates and water tanks of various thicknesses. In order to enable spectrum measurements inside the modules some of the Fe and SS slabs were prepared with quadratic horizontal channels (5 cm x 5 cm) for the insertion of the detector. These channels were closed by corresponding plugs if not in use. The combinations and thicknesses of the materials investigated in the experimental programme are summarized in Table 1.

Table 1: Transmission modules investigated

combinations and thicknesses	combinations and thicknesses
10 cm SS	18 cm SS
10 cm SS + 5 cm H_2O	4 cm Fe + 3.4 cm H_2O
3.4 cm H_2O	8 cm Fe + 8 cm H_2O
9.6 cm H_2O	3.4 cm H_2O + 4 cm Fe
20 cm H_2O	8 cm H_2O + 8 cm Fe
5 cm Fe	3.4 cm H_2O + 10 cm SS + 12 cm H_2O + 15 cm Fe
10 cm Fe	22 cm SS + 17.6 cm H_2O + 18 cm Fe
18 cm Fe	

All measurements and calculations are compared on an absolute scale without any normalisation. In order to determine the reactor power absolute reaction rates measured near the core centre by means of a calibrated fission chamber and a set of activation foils were compared with corresponding MCNP calculations and related to the power monitor of the reactor [5,6].

A NE213 scintillation spectrometer, well described by absolutely determined response matrices for both neutrons and photons was used as proton recoil and Compton spectrometer for the simultaneous measurement of neutron flux spectra in the energy range between about 1 and 9 MeV as well as flux spectra of gammas with energies > 0.3 MeV[7]. The liquid scintillator had a cylindrical shape with diameter and length of 3.8 cm. To enable measurements inside the transmission modules the NE213 scintillator was coupled to the photomultiplier in all measurements by means of a 500 mm long light guide. In this way, only scintillator and light guide had to be inserted into the prepared channel of the module whereas the photomultiplier was outside.

3. Results

The experimental results were compared with neutron and gamma energy spectra calculated with MCNP (nuclear data from ENDF/B-VI), both on absolute scale for a given reactor power. As a typical result, neutron spectra per lethargy interval for modules in the inner position of AKR are shown in Fig. 2 for transmission modules consisting of 10 cm SS and 10 cm SS + 5 cm H_2O with detector positions behind the module in 0.5 cm distance. Additionally, the corresponding gamma energy spectra are presented in Fig. 3 for a detector position in 72.5 cm distance from the transmission module.

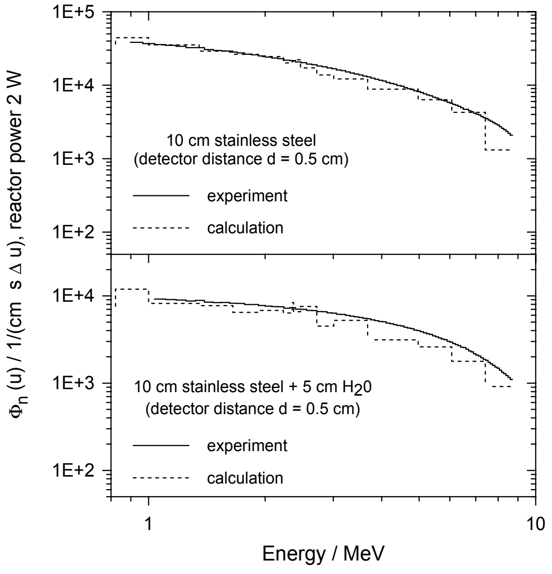

Fig. 2: Measured and calculated neutron spectra per lethargy interval for two transmission modules in the inner position of AKR

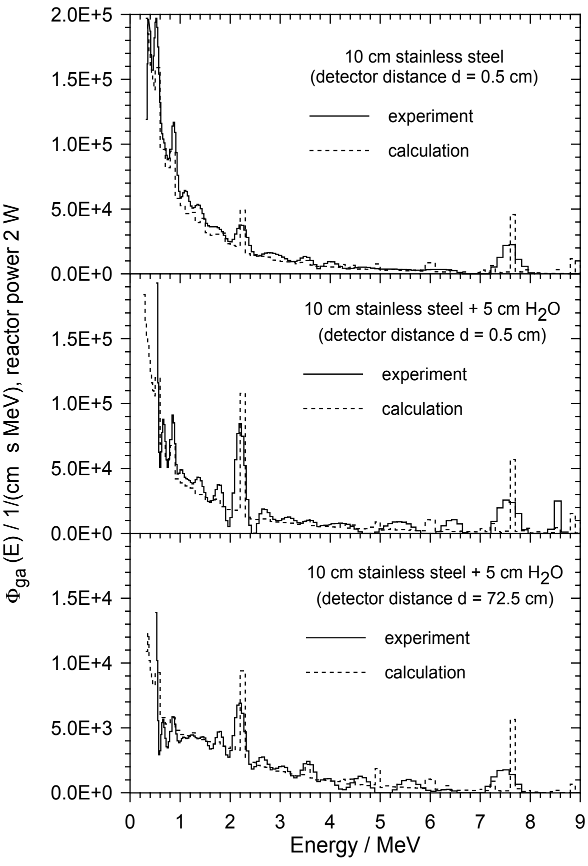

Fig. 3: Measured and calculated gamma energy spectra for two transmission modules for two transmission modules in the inner position of AKR

Quantitative comparisons in different energy intervals are given in Table 2. In all cases, the background at the detector position from neutrons scattered in the reactor shielding and from gammas produced by neutron capture in the material outside the transmission modules has been included in the MCNP calculations so that the calculated spectra can be compared directly with the experiment.

The investigations show that the experimentally determined neutron and gamma fluxes for the described iron-water benchmark agree with MCNP calculations also on an absolute scale within the expected range of discrepancies given mainly by uncertainties in nuclear data and the experimental methods. Hence, the experimental results analysed in more detail can be used in the next step for the validation of nuclear data and of the extended version of the three-dimensional Monte Carlo code TRAMO.

Table 2: C/E comparison of flux integrals in different energy ranges for transmission modules in inner position of AKR

module and detector distance from module (d)	energy interval [MeV]	calculation $[1/cm^2/s]$	experiment $[1/cm^2/s]$	C/E
		gamma flux		
10 cm SS	0.35-8.0	1.55E+05	1.80E+05	0.859
d = 0.5 cm	1.0-8.0	8.16E+04	9.65E+04	0.845
	3.0-8.0	2.55E+04	3.04E+04	0.838
10 cm SS+5 cm H_2O	0.4-8.75	1.24E+05	1.59E+05	0.780
d = 0.5 cm	1.0-8.75	7.73E+04	9.68E+04	0.798
	3.0-8.75	2.70E+04	3.74E+04	0.720
10 cm SS+5 cm H_2O	0.4-8.75	1.49E+04	1.49E+04	1.004
d = 72.5 cm	1.0-8.75	1.10E+04	1.10E+04	0.996
	3.0-8.75	3.88E+03	3.69E+03	1.052
		neutron flux		
10 cm SS	1.0-8.7	3.67E+04	3.89E+04	0.944
d = 0.5 cm	3.0-8.7	7.49E+03	8.97E+03	0.835
10 cm SS+5 cm H_2O	1.0-8.7	1.08E+04	1.28E+04	0.847
d = 0.5 cm	3.0-8.7	3.02E+03	4.03E+03	0.750

References

[1] R.D. Cheverton *et al.* (1988), Evaluation of HFIR pressure-vessel integrity considering radiation embrittlement, ORNL/TM-10444

[2] D.E. Alexander, L.E. Rehn (1998), The role of gamma rays and freely-migrating defects in reactor pressure vessel embrittlement, in H. Aït Abderrahim, P. D'hondt and B. Ošmera (Ed.) World Scientific, Proceedings 9th Intern. Symp. on Reactor Dosimetry (Sept. 2-6 1996) (pp.508-515), Prague

[3] J.F. Briesmeister (1993), MCNP - A general Monte Carlo n-particle transport code (Version 4A), Manual, LA-12625-M

[4] H.-U. Barz, J. Konheiser (1990), TRAMO - A flexible multigroup neutron transport code on the basis of the Monte Carlo method for flux calculations, Rossendorf, ZfK-705

[5] R. Schneider et al. (2001), Absolute Neutron Flux Monitoring in Neutron and Gamma Transmission Experiments at the Dresden Training Reactor AKR, in Inforum, Proceedings of the Jahrestagung Kerntechnik 2001 (p 637), 15.-17.Mai 2001,Dresden

[6] I. Stephan (1989), Entwicklung einer Mehrkomponentensonde zur Bestimmung spektraler Reaktorparameter, Dissertation TU Dresden

[7] S. Unholzer et al. (2000), The measurement of neutron and neutron induced photon spectra in fusion reactor related assemblies, in Nucl. Instr. Meth. A, Proceedings Intern. Workshop on Neutron Field Spectrometry in Science, Technology and Radiation Protection, June 4-8 2000 Pisa (Italy)

Acknowledgement

The work was supported by the Deutsche Forschungsgemeinschaft (DGF).

Summaries of research activities

Accident analysis of nuclear reactors

U. Grundmann,
S. Kliem,
J. Krepel,
S. Mittag,
U. Rohde,
F. Schäfer

Development, Validation and Application of the Code Complex DYN3D – ATHLET

The method of so called "Reference Discontinuity Factors "(RDF) known from the literature has been extended to hexagonal fuel element geometry and implemented into the code DYN3D. The RDF method is based on the equivalence of the neutron currents on the boundary between multiplying and non-multiplying materials (absorbers, reflectors), determined with neutron transport methods to those calculated by diffusion theory. By applying RDFs, a significant improvement of the accuracy of neutron flux calculations has been achieved. The method was validated by calculating various benchmark tasks.

The Rossendorf reactor dynamics code DYN3D coupled with various thermo-hydraulic system codes (ATHLET, RELAP5) has firstly been provided to users from German expert organizations (TÜV) and industries (FANP) on their request as a comprehensively validated tool for transient analyses. The validation of the code complex has e.g. been performed by simulating real transients in NPP within the European project VALCO. Within this project, a statistical method for quantitative uncertainty assessment, developed by GRS for thermo-hydraulic analyses, has firstly been applied to coupled codes including neutron kinetics.

The development of a 1D version of DYN3D for molten salt reactors (MSR) has been completed. The code DYN1D-MSR has been validated against benchmark experiments performed at the MSRE test reactor at the Oak Ridge National Laboratory. The development of a 3D code version was started.

supported by BMWA, EU, TÜV and industries

G. Grunwald,
T. Höhne,
M. Kliem,
S. Kliem,
H.-M. Prasser,
U. Rohde

Coolant mixing in pressurised water reactors

Within the European project FLOMIX-R, a comprehensive data base from coolant mixing experiments performed at the Rossendorf ROCOM test facility has been elaborated and provided to the project partners for CFD code validation. During an invited guest stay at CEA Grenoble, one of the ROCOM experiments has been calculated with the French CFD code TRIO_U using the so called Large Eddy Simulation for advanced turbulence modeling. The unique value of the Rossendorf coolant mixing data for code validation purposes is based on detailed data from wire mesh sensors with high resolution in space and time. On request of industry, special experiments on the mixing of fluid with lower density (lower borated water with higher temperature) simulating so called natural circulation scenarios after loss-of-coolant accidents, have been performed. The results are to be used in nuclear regulatory procedures. In further experiments charged by nuclear utilities, the thermal loads due to the impingement of an ECC-water jet on the reactor pressure vessel inner wall of a BWR and on boron mixing in the emergency core coolant (ECC) accumulator of a PWR have been *funded by BMWA, EU and industries*

investigated. For the boron mixing experiments, a special sensor lance was developed for the measurement of the axial boron concentration distribution in a 1:5 scaled model of the ECC accumulator.

H.-G. Willschütz, E. Altstadt

Component behaviour during severe accidents

A coupled thermo-mechanic finite element model was developed for the evaluation of the convection of the corium melt and the viscoplastic deformation of the reactor pressure vessel (RPV) wall. Pre- and post-test calculations have been performed for the Swedish EC-FOREVER-5 and 6 experiments, which were targeted to the phenomenon of the gap formation between melt crust and RPV wall. Neither in the experiment nor in the calculation a gap formation could be observed.

Within the EU project ECOSTAR, a model was developed for the ex-vessel cooling of a spread corium melt (metal and oxide layer), which is top-flooded by water. This model describes the flooding process, the heat transport into the water layer and into the substratum, the crust formation and the concrete erosion. It was applied to the ECOKATS2-experiments performed at FZ Karlsruhe. A good agreement of calculated and measured vertical temperature distribution, cooling rate and concrete erosion could be stated.

supported by EU

Materials and components safety

H.-W. Viehrig,
J. Dzugan,
M. Werner,
E. Altstadt

Development and application of methods for fracture mechanical characterisation of RPV steel

The second part of the radio nuclide laboratory has been approved by the Saxonian authority after successful inactive pilot run. In February 2004 the permission for handling of radioactive material will be given. In this way the preconditions for the investigation of pressure vessel material of the dismantled Greifswald NPP are fulfilled.

The unirradiated VVER-440 RPV steel of the Greifswald NPP (unit 8) exhibits a large scattering of the fracture toughness and inter-granular cleavage fracture. It is therefore a suitable material for testing the applicability of the master curve concept to inter-granular cleavage fracture and to inhomogeneous microstructure.

In the frame of the Co-ordinated Research Programme “Surveillance Programmes Results Application to Reactor Pressure Vessel Integrity Assessment” the institute contributed to the “IAEA Guide-lines for Application of the Master Curve Approach to Reactor Pressure Vessel Integrity”.

In the FP6 of the EU the FZR substantially contributed to the elaboration of the Integrated Project PERFECT (Prediction of Irradiation Damage Effects in Reactor Components), the contract was signed in December 2003.

A new correction function was developed for the measurement of fracture resistance curves of ductile steels using the unloading compliance technique with Charpy specimens. This correction function leads to an improvement of the accuracy in case of large deflections. The interpretation of experiments was supported by FEM calculations. The plasticity model of Gurson, Tvergaard and Needleman was implemented into the FE code ANSYS. This enables the simulation of crack growth.

At double notched Charpy specimens the development of a primary and a secondary crack was experimentally investigated. FE calculations confirm the interpretation of a sigmoid primary crack as combined mode I and mode II crack.

J. Böhmert,
A. Ulbricht,
A. Gokhman,
G. Müller,
K. van Ouytsel

Analysis of the irradiation induced damage of the microstructure of materials

Microstructural changes of different RPV steels were investigated after irradiation and thermal annealing, as well as after a repeated irradiation and subsequent thermal annealing. By SANS analyses, it could be shown that the radiation induced damage was less after the second irradiation compared to the first irradiation. This could be a hint that the embrittlement disposition decreases after a thermal treatment.

The vicinity of a crack tip in steel and aluminium specimens was investigated by SAXS. Damage structures could be mapped and damage parameters could be determined. Additionally FEM calculations were performed to verify the damage region in M(T) specimens.

The influence of hydrogen on the toughness reduction of irradiated RPV steels was investigated. At operating temperatures the deformation behaviour is not significantly changed by H deposition even at high neutron doses. In accordance with that result also the SANS measurements give no indication for an interaction between microstructural irradiation defects and H atoms. However, a significant additional embrittlement by hydrogen is observed at low irradiation temperatures.

supported by EU

E. Altstadt

Modelling of components behaviour under accident conditions

In the frame of an industry cooperation an integrity analysis was done for a supporting component of the steam separator of the NPP KKI-1. An upwards directed cold water jet was taken as load. The material stresses and strains were calculated by a FE model.

supported by E.ON Nuclear Power

J. Konheiser, B. Boehmer, A. Rogov

Computational evaluation of radiation exposure of RPV steels by means of the Monte Carlo code TRAMO

Two sub-projects are processed within the framework of the scientific and technical cooperation between Germany and Russia in the field of safety research for nuclear power reactors. One sub-project aims at the assessment of the radiation exposure of certain material samples which are planned to be taken from the pressure vessels of the decommissioned VVER-440 reactors of the former Greifswald NPP. The reactor data that are necessary for the calculations were provided by NIS Rheinsberg. On the base of these data the TRAMO calculation models have been established for four sample positions in the pressure vessel of unit 1. The required nuclear data were produced from the nuclear data library ENDF/B-VI by means of the NJOY code.

supported by BMWA

Particle and radiation transport

J. Konheiser,
K. Noack,
B. Boehmer,
A. Rogov

Calculation of neutron and gamma fields

The extension of the FZR Monte-Carlo-Codes system TRAMO from a pure neutron transport code to coupled neutron and gamma transport could be finished. Now, the current work is focused on the verification of TRAMO by comparison both with results of the American MCNP code and with measurements made in suitable experiments. In the framework of a DFG project together with the TU Dresden and the University of Applied Sciences Zittau/Görlitz, neutron/gamma transmission experiments are carried out which are of importance regarding reactor dosimetry applications. The results of these measurements are used for the verification of MCNP and TRAMO. The verification of TRAMO is also the objective of the work which is carried out in the framework of the EU research project REDOS. The countries participating in this project calculate neutron and gamma fluences by means of different codes and nuclear data libraries and the results are compared with data that were measured at Mock-ups of Russian VVER type reactors in the UJV Rez.

supported by DFG, EU

R. Koch

Transmutation

In 2003, the numerical analysis of theoretical concepts was continued concerning the transmutation of actinides and the reduction of long-lived radioactive fission products, accumulated during the operation of light water reactors. The work was focused on a model of a molten salt reactor. With a code system based on the Monte Carlo transport code MCNP-4C and the nuclide generation and depletion code ORIGEN 2.1 calculations with different model parameters and varying recycling strategies were carried out, in particular concerning the tasks of the EU-project MOST. Comparing the results with other groups it was found that the results of calculations with the evaluated nuclear reaction data libraries ENDF/B-VI and JEF 2.2 can be notably different in the case of the thorium-uranium-233 fuel cycle, e. g. regarding the inventory of transuranic nuclides in the equilibrium and in the incinerated nuclides at equal and constant power-level.

C. Beckert

Pulsed photo-neutron source at ELBE

Neutron flux and background for time-of-flight (TOF) measurements were calculated using the Monte Carlo Code MCNP/4C2. From that, conclusions were drawn related to the construction and material selection for neutron radiator, vacuum steel shell, beam dump and collimator. Further on, the neutron pulse width at the radiator was calculated which together with the time resolution of the detectors determines the attainable neutron energy resolution. The calculations also showed, that the neutron intensity at the measuring place could be significantly increased by increasing the cross section of the radiator to (11 mm)^2 without significantly deteriorating the energy resolution of the neutron cross section measurements. In addition, the calculations demonstrated, that the brilliant pulse structure of the electron beam of

ELBE allows to reach energy resolutions better than 1% for measurements with neutrons up to 10 MeV using a flight path of only 3.6 m. The current beam parameters enable a usable neutron energy range for the measurements from 660 keV up to about 7 MeV.

supported by DFG

R. Kuechler,
K. Noack

Radio-nuclide migration

Suitable batch and column experiments were carried out to study the dissolution (weathering) of the minerals calcite and pyrite in a chemical environment, which is determined by the solution products of both minerals. Both solution processes were modeled by means of the program system POLLUTRANS. The calculation results were compared with the results of measurements. The analysis showed that the effective, chemically reactive surface of the mineral grains is significantly smaller than their geometrical surface. The same effect was already observed in investigations of gypsum weathering. Similar investigations for the mineral composition uraninite/pyrite are in preparation. A first column experiment aiming at the study of mineral dissolution under the influence of bacteria (thiobacillus ferrooxidans) showed that the bacteria activity leads to an accelerated dissolution of pyrite. Also, the oxygen which is solved in the seepage water, significantly affects the process of pyrite weathering. Therefore, the oxygen consumption by the pyrite dissolution is to be measured by means of an optical spectrometer. The oxygen measurements were started.

Safety and effectiveness of chemical processes

G. Hessel,
H. Kryk,
H.-M. Prasser
W. Schmitt,
N. Tefera,
M. Gad

Depressurization of multicomponent systems

Pressure relief experiments with reactive and foamily non-reactive mixtures were carried out in an automatic laboratory- (scale) reactor ALR. The experimental results, obtained for process-like conditions, were used for validation of numerical predictions performed with the SAFIRE/VENT software package. Furthermore, the results provide a pool of process data for the improvement and validation of the code BRICK.

Purpose-built needle probes and a high-speed video camera were applied to trace the two-phase flow initiation in the reactor vessel and vent line after pressure relief. Studies were focussed on the improved modelling of the reaction kinetics and of the mass and heat transfer as a function of the two-phase flow behaviour. An infrared spectrometer was applied to measure the reactant and products concentrations. Experimental tests in reaction calorimeters (RC1 and "adiabatic" PhiTecII) were performed in advance to make available a detailed reaction kinetic model.

supported by industry

G. Hessel,
H. Kryk,
H.-M. Prasser,
W. Schmitt

Clarification and simulation of strongly exothermic chemical reactions

To use the heat balance for calorimetric measurements, the reaction calorimeter RC1 was equipped with additional temperature sensors in the jacket coolant. Results showed that it is possible to trace the thermal reaction course even if the physical properties are strongly changing (e.g. during polymerisation). However, temperature gradients across the pipe cross section at the exit of the cooling jacket raise a problem for accurate power measurements. These gradients must be reduced by appropriate internals. The manufacturer of RC1 (Mettler-Toledo AG) was interested in this development.

Furthermore, the process behaviour of Grignard reactions was investigated under isoperibolic and adiabatic conditions in RC1 and PhiTecII, respectively, because the different process control leads to inconsistent results classified as relevant to safety. Significant differences in the process behaviour could be proven by corresponding experiments. It was found that the thermal process control is not responsible but the various hydrodynamic conditions in both calorimeters cause the safety-relevant differences.

H.-M.Prasser,
A. Zaruba,
A. Böttger
W. Zimmermann

Electrochemistry

Flow profiles without reaction were initially optimised at the mock-up of an electrolytic cell for electrochemical treatment of acid mine water. In particular, appropriate spacers were chosen, which fix the anion exchange membrane between the cathode and anode compartment. In a test case, the cell was operated in electrolysis mode, simultaneously applying optical methods for characterising the forming gas phase. The electrolysis operation under process-like conditions is planned.

T. Weier,
J.Hüller,

Magnetic control of electrochemical processes

The application of an external magnetic field to a copper electrolysis cell

G. Gerbeth

showed a significant effect on the limiting cell current. The magnetic field changes the flow structure and, thus, the material transport. PIV measurements of the flow and shadowgraph technique concentration measurements showed that the electromagnetic forces are capable of changing or even reversing the natural buoyant flow in the cell.

Liquid metal magnetohydrodynamics

I. Grants,
A. Cramer,
S. Eckert,
Ch. Zhang,
G. Gerbeth

Basics of MHD flows

The linear and non-linear stability of metal flows in rotating and superimposed steady magnetic fields has been studied. For the first time in fluid mechanics, the occurrence of non-normal nonlinear subcritical instabilities has been first predicted by numerical simulations and afterwards verified experimentally. The flow of a liquid metal driven by a rotating magnetic field shows such instabilities against small but finite disturbances, thus reducing the value of the critical control parameter by a factor of four compared to the linear instability threshold. These results have direct consequences in crystal growth applications of magnetic fields for such cases where the flow should be kept laminar.

Velocity measurements in rotating and traveling magnetic fields showed the new phenomenon of low-frequency spatio-temporal variations of the mean velocity profile for which no adequate theoretical description exists up to now. For the flow of gas bubbles in liquid metals, ultrasonic velocity measurements allowed to resolve even the flow oscillations in the wake of rising bubbles.

supported by
DFG

J. Priede,
G. Gerbeth

Crystal growth

A novel two-phase stirrer has been designed and installed for the growth of single crystals at the float-zone facility of IFW Dresden. This stirrer works with a second coil placed above the primary HF-coil and provides a fluid motion in the molten zone which leads to a beneficial change of the solid-liquid phase boundary. The latter is modified from concave to convex over most of the zone radius, thus providing better conditions for the growth of single crystals.

supported by
DFG

V. Galindo,
W. Witke,
S. Eckert,
B. Willers,
G. Gerbeth

Metallurgy

Based on numerical simulations and low-temperature model experiments, a steady magnetic field has been designed and built for the investment casting process of aluminum alloys. The magnet brakes the melt flow and, particularly, reduces the velocity peaks at the beginning of the filling process. This results in a significant reduction of oxid entrapment thus improving the quality of the casted aluminum alloys. Systematic tests with the industry partner TITAL Bestwig resulted in the clear tendency that the application of the magnet leads to an improved quality of the cast units.

In order to influence the microstructure of solidified metals, basic studies on the role of convection during the solidification process have been performed. Various compositions of a Pb-Sn-alloy have been solidified under the influence of a rotating magnetic field. The microstructure changed, from a columnar dendritic one without magnetic field to an equiaxed one in case of an additional stirring of the liquid phase due to the magnetic field action.

supported by
BMBF, DFG

F. Stefani,
Th. Gundrum,
U. Günther,

Dynamo effect

In further campaigns at the Riga dynamo, the frequency spectra of magnetic field fluctuations have been resolved, showing an –11/3 decay

M. Xu,
G. Gerbeth

as predicted by theory. Use of the Ultrasonic Doppler velocimetry allowed to measure the velocity field in the outer part of the dynamo module. A double torus structure of that flow field was found in good agreement with numerical simulations. The integral equation approach for dynamos has been developed and applied to steady as well as unsteady dynamos in various geometries. The approach allows to limit the calculational domain to the fluid volume, thus allowing kinematic dynamo simulations for any fluid volume.

supported by
EU, DFG

T. Weier,
G. Mutschke,
V. Shatrov,
G. Gerbeth

Boundary layer control in electrolytes

A significant control of lift- and drag-coefficients is possible by application of electromagnetic forces. Surprisingly, oscillatory Lorentz forces with a zero integral momentum input are capable of resulting in an integral lift increase in the same order as steady Lorentz forces. However, the energetic effort reduces in case of oscillatory forces by two to three orders of magnitude compared to the steady case. Systematic studies have been performed in order to extract the relevant scaling laws between lift increase and momentum coefficient as well as frequency of the electromagnetic excitation.

supported by
DFG

S. Eckert,
A. Cramer,
Th. Gundrum,
F. Stefani,
G. Gerbeth

Measuring techniques

The ultrasonic Doppler velocimetry (UDV) has been successfully applied to velocity measurements in high-temperature liquid melts like PbBi or aluminum. First tests in molten copper and steel have not yet been successful due to the complicated problem of acoustic contact between the wave-guide material and the melt. A fully contact-less tomography of the three-dimensional velocity field in a liquid metal has been demonstrated experimentally. The method turned out to be robust and stable. Even the transient change of the velocity field could be correctly monitored.

supported by
DFG

Thermo-fluiddynamics

D. Lucas,
J.-M. Shi

Qualification of CFD models

Models for the lift force , the wall force and the turbulent dispersion force were implemented into the code CFX-5. As result of a comparison between measured and calculated radial gas fraction profiles, the "Favre averaged drag model" was found to be the best performing correlation for the turbulent dispersion force. Next step is the implementation of a multi-bubble-class model in co-operation with ANSYS-CFX (developer of CFX). The derivation of model equations is first done using an own 1D model which allows the fast testing of correlations for bubble forces against TOPFLOW data, before they are implemented into the 3D code. In some regions of the flow map, a scaling capability of the equations were achieved that allows to transfer results from one pipe diameter to another. Further activities are directed at the modelling of bubble coalescence and break-up along the flow path.

supported by
BMWA

E. Krepper,
A. Grahn

Simulation of the transport of insulation material

A study was started on the transport of insulation material released from the thermal insulation of pipes and components during loss-of-coolant accidents in NPP with the coolant flow towards the building sump. The work is performed in co-operation with the University Zittau/Görlitz (FH). The subject is of high safety relevance, since the particles and fibres can lead to a blockage of the sieves in front of the suck-in nozzles of the ECC circulation lines in the sump of the reactor building. Rossendorf is responsible for the part of the CFD modelling , while the necessary experiments are carried out in Zittau. In first calculations it was shown that an Euler-Euler continuum model is able to predict the behaviour of the particle suspension as well as the sedimentation and the agglomeration on top of the sieves.

supported by
BMWA

H.-M. Prasser,
A. Böttger,
J. Zschau,
U. Hampel,
H. Pietruske,
D. Hoppe,
C. Zippe
E. Schleicher,
A. Bieberle,
M. Speck,
St. Boden,
T. Sühnel

Measuring technology

The design work on a wire-mesh sensor with 64x64 measuring points for an application at a saturation pressure of 7 MPa was completed. The manufacturing was started. A completely new design allows to maintain the lateral resolution of 3 mm also for experiments at high pressure and temperature.

In the EU project WAHALoads, the dynamics of the gas-liquid interface during spontaneous, condensation-induced water hammers was visualised for the first time using needle probes and a mesh sensor of FZR. A novel combination of conductivity probes with micro-thermocouples allowed a detailed observation of heat exchange processes at the interfacial area.

The qualification of a diversified level measuring system developed by FZR was completed by FANP according to KTA regulations. The device is now ready for application at BWRs.

At the electron beam test assembly built in co-operation with IKE Stuttgart an X-ray tomogramme of a dynamic object was recorded with a framing rate of 1 kHz. The achieved imaging quality is comparable to the world-wide leading devices in Japan (Mitsubishi), while the costs are much lower. A particular challenge is the development of image reconstruction methods for small-angle tomography, which are necessary in the given geometry of the developed scanned electron-beam tomography set-up. The method is subject of a patent application.

The work on rotation-angle synchronised gamma-tomography was continued. Main goals were the increase of resolution and an improvement of the spectroscopic properties of the radiation detectors. The latter allowed to reduce the influence of scattered gamma-quanta. The tomography system was successfully used to visualise the phase distribution inside a hydraulic coupling of Voith Turbo in Crailsheim.

Furthermore, image processing methods were developed, that allow to measure velocities, gas fractions and bubble sizes in a bubbly flow. A special trajectory tracking for single bubbles was programmed and used to quantify the turbulent dispersion coefficient in a bubble column. The data is used for CFD code validation.

By order of the industry, an optical micro-bubble sensor was developed, which is based on a pulsed short exposure illumination combined with a CCD sensor. Bubble sizes are measured using the Hough transform technique.

TOPFLOW – thermohydraulic test facility

H.-M. Prasser,
H. Carl,
P. Schütz,
H. Pietruske,
M. Beyer,
K. Lindner,
M. Tamme,
St. Weichelt,
H. Rußig
Ch. Vallee

Evolution of flow structure in vertical pipes

Up to now, air-water tests were performed in the test sections DN50 and DN200. The parameters covered wide parts of the flow map. The structure of the interfacial area was recorded using wire-mesh sensors developed by FZR. For the measurement of the gas velocity, two sensors were placed in a small distance behind each other.

The data was evaluated with respect to scaling effects. New conclusions were drawn concerning the influence of the pipe diameter on the flow structure and especially on the shape of large bubbles. Furthermore, the influence of the pipe diameter on the transition from wall to central void fraction peak in a bubbly flow was studied. The data evaluation is performed in the frame of the R&D project "thermal fluid dynamics of multi-phase systems".

For the experiments on the evolution of the two-phase flow structure along the flow path, a special test section DN200 with variable gas injection was developed and constructed. The set-up was certified by TÜV and is ready for use. It can be used both for air-water and steam-water experiments.

Flow structure in the hot leg of the primary circuit of a PWR

The work on the design of the new hot leg test section of TOPFLOW could be finished. The construction has been started. The experiment is mostly financed by project funds of BMWA.

Monographs

Weiß, F.-P.; Kliem, S.
Boron dilution Transients in PWRs
Unterrichtsmaterial für die Frederic Joliot/Otto Hahn Summer School, Karlsruhe,August 20-29, 2003

Publications in journals

Böhmer, B.; Grantz, M.; Hansen, W.; Hinke, D.; Konheiser, J.; Noack, K.; Mehner, H.-C.; Stephan, I.; Unholzer, S.
Measurements of gamma and neutron flux spectra in iron-water configurations
Kerntechnik 68 (2003) 5-6

Cumblidge, S. E.; Motta, A. T.; Catchen, G. L.; Brauer, G.; Böhmert, J.
Evidence for irradiation-induced metallic precipitates in neutron-irradiated model alloys and pressure vessel weld steel, using Doppler-broadening positron spectroscopy
Journal of Nuclear Materials, Volume 320, No. 3, August, 2003, p. 245-257

Eckert, S.; Gerbeth, G.; Melnikov, Vladimir I.
Velocity measurements at high temperatures by ultrasound Doppler velocimetry using an acoustic wave guide
Experiments in Fluids, Vol.35/5 (2003), 381-388

Gailitis, A.; Lielausis, O.; Platacis, E.; Gerbeth, G.; Stefani, F.
The Riga dynamo experiment
Surveys in Geophysics 24 (2003) 247-267

Gocht, T.; Traichel, A.; Hampel, R.; Prasser, H.-M.
Innovative transient-proof hydrostatic level measuring method
Kerntechnik 68 (2003) 3, pp. 97-101.

Gokhman, A.; Böhmert, J.; Ulbricht, A.
A kinetic study of copper precipitates under VVER-type reactor condition
Radiation Effects and Defects in Solids, Vol. 158 (2003) pp. 783-792

Gokhmann, A.; Böhmert, J.
A Kinetics Study of Vacancy Cluster Evolution Under VVER-Type Reactor Condition
Radiation Effects and Defects in Solids, July 2003, Vol. 158, No . 7, pp. 499-511

Grants, I.; Gerbeth, G.
Experimental study of non-normal non-linear transition to turbulence in a rotating magnetic field driven flow
Physics of Fluids, USA, Vol. 15, No 10 (2003) 2803-2809

Grundmann, U.; Kliem, S.
Analyses of the OECD Main Steam Line Break Benchmark with the Codes DYN3D and ATHLET
Nuclear Technology 142(2003) 146-153

Günther, U.; Stefani, F.
Isospectrality of spherical MHD dynamo operators: Pseudo-Hermiticity and a no-go theorem
Journal of Mathematical Physics 44 (2003) 3097-3111

Hertlein, R.; Umminger, K.; Kliem, S.; Prasser, H.-M.; Höhne, T.; Weiß, F.-P.
Experimental and Numerical Investigation of Boron Dilution Transients in Pressurized Water Reactors
Nuclear Technology, vol. 141,January 2003, pp. 88-107

Hessel, G.; Kryk, H.; Schmitt, W.; Seiler, T.; Weiß, F.-P.; Hilpert, R.; Roth, M.
Modellbasiertes Online-Zustandserkennungssystem für exotherme chemische Prozesse
Technische Überwachung Bd. 44, Nr. 5 (2003) 43-47

Hüller, J.; Pham, M. T.; Howitz, S.
Thin layer copper ISE for fluidic microsystem
Sensors & Actuators B. 91(2003) 17-20

Ivanov, A. A.; Anikeev, A. V.; Bagryansky, P. A.; Deichuli, P. P.; Korepanov, S. A.; Lizunov, A. A.; Maximov, V. V.; Murakhtin, S. V.; Savkin, V. Ya.; Den Hertog, D. J.; Fiksel, G.; Noack, K.
Experimental Evidence of High-Beta Plasma Confinement in an Axially Symmetric Gas Dynamic Trap
Physical Review Letters, 90 (2003) 105002

Krepper, E.; Prasser, H.-M.
Experimental and numerical investigation of one and two phase natural convection
Scientific Papers of the Kielce University of Technology, Series Mechanics,Vol. 77, 2003, pp. 33-39

Lucas, D.; Krepper, E.; Prasser, H.-M.
Evolution of flow patterns, gas fraction profiles and bubble size distributions in gas-liquid flows in vertical tubes
Transactions of the Institute of Fluid-Flow Machinery 112(2003)37-46

Lucas, D.; Krepper, E.; Prasser, H.-M.
Experimental investigation and modeling of air/water flows in vertical pipes
In: M. Sommerfeld (Ed.), Bubbly Flows - Analysis, Modelling and Calculation, Heat and Mass Transfer Series, Springer-Verlag,Berlin, Heidelberg, 2004, pp. 101-115

Lucas, D.; Prasser, H.-M.
Pulsations of the Mass Flow Rate during Pressure Relief
International Journal of Thermal Sciences 42(2003)5-14

Misawa, M.; Tiseanu, I.; Prasser, H.-M.; Ichikawa, N.; Akai, M.
Ultra-fast x-ray tomography for multi-phase flow interface dynamic studies
Kerntechnik 68 (2003) 3, pp. 85-90.

Mittag, S.; Petkov, P.; Grundmann, U.
Discontinuity factors for non-multiplying material in two-dimensional hexagonal reactor geometry
Annals of Nuclear Energy 30/13 (2003) pp. 1347-1364

Neumann, H.; Plevachuk, Y.; Allenstein, F.
Investigation of Marangoni convection in monotectic melts by resistance measurements
Materials Science & Engineering A361 (2003) 155-164

Nikrityuk, P. A.; Eckert, K.; Grundmann, R.; Willers, B.; Eckert, S.
Modeling and measurements of two-phase Pb-Sn alloy solidification in an external magnetic field
Journal of Thermal Science, Vol. 12, 2003, pp. 357-362

Ouytsel, K. van; Batist, R. de; Schaller, R.
An internal friction working model to advance the understanding of effects of radiation and thermal ageing on reactor pressure-vessel steel
International Journal of Pressure Vessels and Piping 80 (2003) 275-284

Prasser, H.-M.; Baldauf, D.; Fietz, J.; Hampel, U.; Hoppe, D.; Zippe, C.; Zschau, J.; Christen, M.; Will, G.
Time Resolving Gamma-Tomography for Periodically Changing Gas Fraction Fields
Flow Measurement and Instrumentation 14 (2003)3 pp. 119-125

Prasser, H.-M.; Böttger, A.; Zschau, J.; Gocht, T.
Needle shaped conductivity probes with integrated micro-thermocouple and their application in rapid condensation experiments with non-condensable gases
Kerntechnik 68 (2003) 3, pp. 114-120.

Prasser, H.-M.; Grunwald, G.; Höhne, T.; Kliem, S.; Rohde, U.; Weiss, F.-P.
Coolant mixing in a PWR - deboration transients, steam line breaks and emergency core cooling injection - experiments and analyses
Nuclear Technology 143 (2003) 37-56

Rindelhardt, U.; Böhmer, B.; Böhmert, J.
RPV Integrity Assessment by Operational Feedback: Post Service Investigations of VVER-type NPPs
Transactions of ANS, Vol. 88,(2003)p. 547

Rindelhardt, U.; Grzelak, K.
Kleinwasserkraftnutzung am Grenzfluss Lausitzer Neiße
Elektrizitätswirtschaft Heft 22 (2003), S. 58

Schaffrath, A.; Walter, D.; Delmastro, D.; Giménez, M.; Zanocco, P.
Berechnung des Notkondensators des argentinischen Integralreaktors CAREM
atw Internationale Zeitschrift für Kernenergie 48 (2003), Nr. 2, S. 111-115

Sehgal, B. R.; Theerthan, A.; Giri, A.; Karbojian, A.; Willschütz, H.-G.; Kymäläinen, O.; Vandroux, S.; Bonnet, J. M.; Seiler, J. M.; Ikkonen, K.; Sairanen, R.; Bhandari, S.; Bürger, M.; Buck, M.; Widmann, W.; Dienstbier, J.; Techy, Z.; Taubner, R.; Theofanous, T.; Dinh, T. N.
Assessment of reactor vessel integrity (ARVI)
Nuclear Engineering and Design, vol 221, pp 23-53

Shatrov, V.; Mutschke, G.; Gerbeth, G.
Three-dimensional linear stability analysis of lid-driven MHD cavity flow
Physics of Fluids (August 2003) Vol. 15, No. 8 , pp 2141-2151

Shatrov, V.; Priede, J.; Gerbeth, G.
Three-dimensional linear stability analysis of the flow in a liquid spherical droplet driven by an alternating magnetic field
Physics of Fluids, March 2003, Vol. 15, Number 3, pp 668-678

Shi, J.-M.; Breuer, M.; Durst, F.; Schaefer, M.
An improved numerical study of the wall effect on hot-wire measurements
ASME, J. Heat Transfer, 125:595-603, 2003

Shi, J.-M.; Gerlach, D.; Breuer, M.; Durst, F.; Lange, C. F.
Analysis of heat transfer from single wires close to walls
Phys. Fluids, 15 (2003) 908-921

Stefani, F.; Gerbeth, G.
Oscillatory mean-field dynamos with a spherically symmetric, isotropic helical turbulence parameter alpha
Physical Review E 67 (2003), 027302

Steinwarz, W.; Koller, W.; Dyllong, N.; Häfner, W.; Journeau, C.; Seiler, J. M.; Froment, K.; Cognet, G.; Goldstein, S.; Fischer, M.; Hellmann, S.; Nie, M.; Eddi, M.; Alsmeyer, H.; Allelein, H.-J.; Spengler, C.; Bürger, M.; Sehgal, B. R.; Koch, M. K.; Büscher, T.; Alkan, Z.; Petrov, J. B.; Gaune-Escard, M.; Weiss, F.-P.; Altstadt, E.; Bandini, G.
Ex-vessel core melt stabilization research (ECOSTAR)
Nuclear Engineering and Design, 221 (2003) 77-94

Viehrig, H.-W.; Boehmert, J.
Application of the Master Curve Approach for the Irradiation Embrittlement Evaluation of Pressure Vessels Steels
International Steel Research 74 (2003), No. 9, September, pp. 577-583

Weier, T.; Gerbeth, G.; Mutschke, G.; Lielausis, O.; Lammers, G.
Control of flow separation using electromagnetic forces
Flow, Turbulence and Combustion, Vol. 71, No. 1-4, pp. 5-17

Willschütz, H.-G.; Altstadt, E.; Sehgal, B. R.; Weiss, F.-P.
Simulation of creep tests with French or German RPV-steel and investigation of a RPV-support against failure
Annals of Nuclear Energy, vol 30, 10, pp 1033-1063

Conference contributions (including poster contributions)

Altstadt, E.; Fischer, E.; Kumpf, H.; Nagel, G.; Sgarz, G.; Weiß, F.-P.
Analysis of irradiation induced creep of bolts of a PWR core baffle
Tagungsband der Jahrestagung Kerntechnik 2003, Berlin 20. -22. Mai 2003, S. 591-594

Altstadt, E.; Fischer, E.; Kumpf, H.; Nagel, G.; Sgarz, G.; Weiß, F.-P.
Mechanical analysis of a PWR core baffle with consideration of irradiation induced creep of bolts
2003 International Congress on Advanced Nuclear Power Plants (ICAPP'03), May 4-7, 2003, Cordoba, Spain

Altstadt, E.; Willschütz, H.-G.
Arbeiten zur Simulation prototypischer In-Vessel-Retention-Szenarien auf Basis von Vergleichsrechnungen mit mittelskaligen Experimenten
3. Workshop KOMPETENZVERBUND KERNTECHNIK am 8.10.2003, MPA, Stuttgart, Proceedings-CD

Ballesteros, A.; Garcia, G.; Böhmer, B.; Ošmera, B.; Keresztúri, A.; Ilieva, K.; Acosta, B.; Smutný, V.; Polke, E.; Zaritsky, S.; Ortego, P.
Reactor Dosimetry: Accurate Determination and Benchmarking of Radiation Field Parameters, relevant for Pressure Vessel Monitoring (REDOS)
FISA-2003 - Symposium on EU Research in Reactor Safety, 10-13 November 2003, Luxembourg

Beckert, C.; Freiesleben, H.; Grosse, E.; Naumann, B.; Weiß, F.-P.
Particle Flux Calculations for a Pulsed Photoneutron Source at the Radiation Source ELBE
Jahrestagung Kerntechnik 2003, Berlin, 20.-22. Mai 2003, Tagungsbericht S. 47-51

Böhmer, B.; Böhmert, J.; Rindelhardt, U.
Post Service Investigations of VVER-440 RPV Steel from NPP Greifswald
Structural Integrity and Life of NPP Equipment "SIL 2003" Kyiv, Ukraine, May 20-22,2003

Böhmer, B.; Borodkin, G.; Brodkin, E.; Egorov, A.; Konheiser, J.; Kozhevnikov, S.; Manturov, G.; Voloschenko, A.; Zaritsky, S.
ANISN-DORT-ROZ-MCNP-TRAMO Neutron-Gamma Flux Intercomparison Exercise for a Simple Testing Model
11th International Symposium on Reactor Dosimetry, 18 -23 August 2002 in Brussels, Belgium, Proceedings by World Scientific Publ., ISBN 981-238-448-0, p. 572-579

Böhmer, B.; Borodkin, G.; Konheiser, J.; Noack, K.; Polke, E.; Rogov, A.; Vladimirov, P.
Neutron and Gamma Fluence and Radiation Damage Parameters of Ex-core Components of Russian and German Light Water Reactors
11th International Symposium on Reactor Dosimetry, 18 -23 August 2002 in Brussels, Belgium, Proceedings by World Scientific Publ., ISBN 981-238-448-0, p. 286-294

Böhmert, J.; Viehrig, H.-W.; Ulbricht, A.
Bewertung der Neutronenversprödung von WWER-Druckbehälterstählen anhand der Ergebnisse der Bestrahlungsexperimente Rheinsberg
Jahrestagung Kerntechnik 2003, Tagungsbericht, 20. - 22. 05. 2003, Berlin, S. 595-598

Borodin, V. A.; Böhmert, J.
Embrittlement of Reactor Pressure Vessel Steel A508: A Look on Mesoscopic Levels
13. International Conference on Strength of Material, 25.-30.08.2003, Budapest, Hungary, Book of Abstracts, p. 113

Borodkin, G.; Böhmer, B.; Konheiser, J.; Manturov, G.; Polke, E.; Brodkin, E.; Jegorov, A.; Zaritsky, S.
Balakovo-3 Ex-vessel Exercise: Analysis of Calculation Results Intercomparison and Comparison with Reference Data
11th International Symposium on Reactor Dosimetry, August 18-23, 2002 in Brussels, Belgium, Proceedings by World Scientific Publ., ISBN 981-238-448-0, p. 665-673

Cramer, A.; Eckert, S.; Heinzelmann, C.; Lampe, D.; Gerbeth, G.
Efficient melt mixing due to the combined action of a rotating and a travelling magnetic field
EPM 2003, 4th Int. Conference on Electromagnetic Processing of Materials, Lyon (Frankreich), 14-17.10.2003, CD-ROM, C3-10.5 (2003)

Cramer, A.; Gerbeth, G.; Terhoeven, P.; Krätzschmar, A.
Fluid Flow Measurements in Electrically Driven Vortical Flows
Modelling for Electromagnetic Processing, Hannover, March 24 - 26, 2003. Proceedings pp 241-246, 2003

Cramer, A.; Gerbeth, G.; Terhoeven, P.; Krätzschmar, A.
Fluid Velocity Measurements in Electro-Vortical Flows
132nd Annual Meeting & Exhibition (TMS), San Diego, California, March 2-6, 2003

Dzugan, J.; Viehrig, H.-W.
Application of the Normalization Method to Various Fracture Toughness Specimens
13. International Conference on the Strength of Materials, 25.-30.08.2003, Budapest, Hungary

Eckert, S.; Gerbeth, G.
Control of gas bubble injection into liquid metals by electromagnetic forces
In: J. Banhart, N. Fleck, A. Mortensen (Eds.), Cellular Metals: Manufacture, Properties, Applications, pp. 83-88 International Conference MetFoam 2003, Berlin, 23.06-25.06.2003

Eckert, S.; Gerbeth, G.; Cramer, A.; Willers, B.; Witke, W.; Galindo, V.
Liquid metal model experiments on casting and solidification processes
Int. Symposium on liquid metal processing and casting and solidification processes, Nancy (France), Sept. 21-24, 2003. Proceedings, Eds.: P.D.Lee, A.Mitchell, J.-P.Bellot, A.Jardy, 333-343, 2003.

Eckert, S.; Gerbeth, G.; Gundrum, T.; Stefani, F.; Witke, W.
New approaches to determine the velocity field in metallic melts
EPM 2003, 4th Int. Conference on Electromagnetic Processing of Materials, Lyon (Frankreich), October 14-17, 2003, Lyon, France, CD-ROM, PL13

Eckert, S.; Gerbeth, G.; Stefani, F.; Witke, W.
Measuring techniques for liquid metal velocity measurements
Int. Symposium on liquid metal processing and casting, Nancy (France), Sept. 21-24, 2003. Proceedings, Eds.: P.D.Lee, A.Mitchell, J.-P.Bellot, A.Jardy, 261-271, 2003.

Filip, O.; Hermann, R.; Gerbeth, G.; Priede, J.; Shatrov, V.
Effect of hydrodynamics on microstructure evolution of Nd-Fe-B alloys
"EUROMAT 2003", Lausanne (Schweiz), 01.-05.09.2003

Gailitis, A.; Lielausis, O.; Platacis, E.; Gerbeth, G.; Stefani, F.
New Results in the Riga Dynamo Experiment
Jahrestagung der Astronomischen Gesellschaft, 15-20 September 2003 in Freiburg im Breisgau

Galindo, V.; Cramer, A.; Eckert, S.; Gerbeth, G.
Velocity measuring techniques at FZR and status of MULTIMAG
Use of magnetic fields in crystal growth, Workshop, Riga (Lettland), 5.-6.12.2003

Gerbeth, G.; Priede, J.; Shatrov, V.; Hermann, R.; Filip, O.
Motion of a Nd-Fe-B melt in levitated or float-zone operated samples and its control
DPG-Tagung Dresden, 24.-28.03.2003, Symposium "Phasenumwandlungen in Schmelzen"

Gokhman, A.; Böhmert, J.; Ulbricht, A.
Calculation of the Scattering Factor from the Shell Model of Nanoscale Defects
XV International Conference on X-ray Diffraction & Crystal Chemistry of Minerals, St. Petersburg, 15.-19.09.2003

Grundmann, U.; Mittag, S.
DYN3D Calculations for the V-1000 Test Facility and Comparisons with the Measurements
Proceedings of 13. Symposium of AER,p. 521-539, Dresden, 22-26. September, 2003

Grundmann, U.; Rohde, U. (Editors)
Different Simulations of the Phase 2 of the OECD/NRC BWR Turbine Trip Benchmark with the Code DYN3D
Annual Meeting on Nuclear Technology, Berlin, May 20 - 22, 2003

Grunwald, G.; Höhne, T.; Kliem, S.; Prasser, H.-M.; Rohde, U.; Weiß, F.-P.
Coolant Mixing Studies for the Analysis of Hypothetical Boron Dilution Transients in a PWR
11. International Conference on Nuclear Engineering ICONE-11, Tokyo, Japan, April 20-23, 2003, Proceedings CD-ROM paper 36325

Günther, U.; Stefani, F.; Gerbeth, G.
A no-go theorem for isospectral alpha^2-dynamos
Mathematical Aspects of Natural Dynamos, Caramulo, Portugal, August 31 - September 6, 2003.

Hämäläinen, A.; Vanttola, T.; Weiss, F.-P.; Mittag, S.; Kliem, S.; Kozmenkov, Y.; Keresztúri, A.; Hádek, J.; Strmensky, C.; Stefanova, S.; Kuchin, A.; Hlbocky, P.; Siko, D.; Danilin, S.
Validation of coupled codes in VALCO WP1 using measured VVER data
13. Symposium of AER, Dresden, 22-26 September, 2003, pp. 555-576

Hermann, R.; Behr, G.; Gerbeth, G.; Priede, J.; Schultz, L.
Control of floating-zone single crystal growth by magnetic fields
2nd French German Crystal Growth Meeting, 10th-13th March 2003, Nancy, FRANCE

Hermann, R.; Filip, O.; Gerbeth, G.; Priede, J.
Microstructure of Nd-Fe-B alloys influenced by the melt hydrodynamics
DPG-Tagung Dresden, 24.-28.03.2003, Symposium "Phasenumwandlungen in Schmelzen"

Hessel, G.; Kryk, H.; Schmitt, W.; Seiler, T.; Weiß, F.-P.; Hilpert, R.; Roth, M.; Deerberg, G.
Monitoring System for Multiphase Hydrogenation in Chemical Plants
Proceedings of the 5th IFAC Symposium on Fault Detection, Supervision and Safety for Technical Processes SAFEPROCESS'2003, Washington, D.C., USA, June 9-11, 2003, pp. 969-974

Höhne, T.; Kliem, S.; Prasser, H.-M.; Rohde, U.
Experimental and Numerical Mixing Studies inside a Reactor Pressure Vessel
4th ASME/JSME Joint Fluids Engineering Conference, July 2003, Hawaii, USA, CD-ROM

Kliem, M.
Experimental validation of the porous media approach for rod bundle geometry under crossflow conditions.
11th International Conference on Nuclear Engineering, Tokyo, Japan, April 20-23, 2003 ICONE11-36502

Kliem, S.
Comparison of the updated solutions of the 6th dynamic AER benchmark - main steam line break in a NPP with VVER-440
XIII. AER-Symposium on VVER Physics and Reactor Safety, Dresden, Germany, September 23-26, 2003, Proceedings pp. 413-444

Kliem, S.; Mittag, S.
Analysis of a hypothetical boron dilution event by means of the neutron kinetic core model DYN3D using different cross section libraries
Fachtag der KTG-Fachgruppen "Betrieb" und "Reaktorphysik und Berechnungsmethoden" 13.-14.02.2003, Rossendorf, Proceedings CD-ROM

Kliem, S.; Prasser, H.-M.; Grunwald, G.; Höhne, T.; Rohde, U.; Weiß, F.-P.
ROCOM experiments on the coolant mixing in the upper plenum of a PWR
Jahrestagung Kerntechnik, Berlin,20.-22.Mai 2003, Proceedings pp. 73-76

Kliem, S.; Rohde, U.; Weiß, F.-P.
Analysis of PWR core behaviour after the entrance of underborated water
Fachsitzung "Experimentelle und theoretische Untersuchungen zu Borverdünnungstransienten in DWR" auf der Jahrestagung Kerntechnik 2003, Berlin, 20.-22. Mai 2003, Berichtsheft S.85-96

Krepel, J.; Grundmann, U.; Rohde, U.
Development and Verification of a Reactor Dynamics Code for Molten Salt Reactors with Flowing Fuel
Annual Meeting on Nuclear Technology 2003, Berlin, 15. - 17. May 2003

Krepper, E.
CFD modelling of subcooled boiling
The 10th International Topic Meeting on Nuclear Reactor Thermal Hydraulics (NURETH-10), Seoul, Korea, October 5 - 9, 2003

Krepper, E.
CFD Modelling of subcooled boiling
XIII. AER-Symposium on VVER Physics and Reactor Safety, Dresden, Germany, September 23-26, 2003, Proceedings pp. 819-833

Krepper, E.; Lucas, D.; Shi, J.
Modelling of bubble flow in vertical pipes
Multiphase Flows in Industrial Applications CFX-Germany, FZ-Rossendorf 28.-30.04.03

Kryk, H.; Hessel, G.; Schmitt, W.; Seiler, T.; Weiß, F.-P.; Hilpert, R.; Roth, M.
On-line concentration estimation during chemical reactions using adaptive heat/ mass balances
4th European Congress of Chemical Engineering, 21-25 September 2003 Granada, Spain, Topic 10 Abstracts, O-10.2-001

Lucas, D.; Krepper, E.; Prasser, H.-M.
Experimental investigations and modelling on the transition from bubble to slug flow in vertical pipes
Proceedings of the German-Japanese Workshop on Multiphase Flow, Karlsruhe, August 25-27, 2002, FZKA 6759(http://www.emsi.fzk.de/gjwmf2002/pdf/Proceedings_FZKA6759.pdf), pp. C-1 - C-12

Lucas, D.; Krepper, E.; Prasser, H.-M.
Modelling of bubble flow in vertical pipes
The 10 th International Topical Meeting on Nuclear Reactor Thermal Hydraulics (NURETH-10), Seoul, Korea, October 5-9, 2003, Paper A00301

Lucas, D.; Krepper, E.; Prasser, H.-M.; Rohde, U.; Weiß, F.-P.
Constitutive laws for interaction of gas bubbles within the liquid flow field – modelling and experimental basis
Use of computational fluid dynamics codes for safety analysis of reactor systems, Joint IAEA/NEA technical meeting, Pisa, Italy, November 11-13, 2002, IAEA-TECDOC-1379, IAEA, Vienna, 2003

Lucas, D.; Prasser, H.-M.
First experimental results of measurements on air/water flow in a vertical pipe with an inner diameter of 194 mm
41st European Two-Phase Flow Group meeting, Norway, May 12-13, 2003

Manera, A.; Prasser, H.-M.; Hagen, T. H. J. J. van der
Suitability of Drift-flux models, void-fraction evolution and 3D flow pattern visualization during stationary and transient flashing flow in a vertical pipe
The 10th International Topical Meeting on Nuclear Reactor Thermal Hydraulics (NURETH-10), Seoul, Korea, October 5-9, 2003; conference-CD: A00108

Manera, A.; Rohde, U.; Prasser, H.-M.; Hagen, T. H. J. J. van der
Modeling of flashing-induced instabilities in the start-up phase of natural-circulation BWRs using the code FLOCAL
The 10th International Topical Meeting on Nuclear Reactor Thermal Hydraulics (NURETH-10), Seoul, Korea, October 5-9, 2003; conference-CD: A00506

Manera, A.; Schäfer, F.
Experimental and theoretical investigations of flashing induced instabilities at the CIRCUS test facility
Annual Meeting on Nuclear Technology, May 20-22, 2003, Berlin, Germany, Proceedings, P. 89-92

Mercurio, G.; Eckert, S.
CFD simulation of a bubbly flow experiment with liquid PbBi eutectic alloy and Nitrogen
Computational Methods in Multiphase Flow II, A.A.Mammoli, C.A.Brebbia (Eds.), WIT Press 2004, Southampton pp.395-404, (Proc. of the Second International Conference on Computational Methods in Multiphase Flow, Santa Fe, New Mexico, USA, 2003)

Mittag, S.; Petkov, P. T.; Grundmann, U.
Discontinuity factors for non-multiplying hexagonal nodes in VVER reactors
13. Symposium of AER, Dresden, 22-26 September, 2003, pp. 89-108

Petkov, P. T.; Mittag, S.
Two-dimensional heterogeneous transport theory hot zero-power benchmarks for the WWER-1000 reactors
13. Symposium of AER, Dresden, 22-26 September, 2003, pp. 77-88

Petkov, P. T.; Mittag, S.; Christoskov, I.; Kamenov, K.; Antov, A.; Bakalov, I.; Wehner, H.
A new DYN3D library for the WWER-1000 reactors
13. Symposium of AER, Dresden, 22-26 September, 2003, pp. 109-122

Prasser, H.-M.
Measurement Techniques for Multiphase Flows
Multiphase Flows in Industrial Applications CFX-Germany, ANSYS-CFX / FZR workshop, FZ-Rossendorf 28.-30.04.03, Lecture on Short Course on Multiphase Flows

Prasser, H.-M.
Wire-Mesh Sensors - a Useful Tool for Two-phase Flow Model Development
Multiphase Flows in Industrial Applications CFX-Germany, ANSYS-CFX / FZR workshop, FZ-Rossendorf 28.-30.04.03.

Prasser, H.-M.; Beyer, M.; Böttger, A.; Carl, H.; Lucas, D.; Schaffrath, A.; Schütz, P.; Weiß, F.-P.; Zschau, J.
Influence of the pipe diameter on the structure of the gas-liquid interface in a vertical two-phase pipe flow
10th International Topical Meeting on Nuclear Reactor Thermal Hydraulics (NURETH-10), Seoul, Korea, October 5-9, 2003; conference-CD: A00308

Prasser, H.-M.; Böttger, A.; Zschau, J.; Baranyai, G.; Ezsöl, Gy.
Thermal effects during condensation induced water hammer behind fast acting valves in pipelines
11th International Conference on Nuclear Engineering Tokyo, JAPAN, April 20-23,2003, Proceedings ICONE11-36310

Prasser, H.-M.; Höhne, T.; Kliem, S.; Rohde, U.; Weiß, F.-P.
Untersuchung der Kühlmittelvermischung an der Versuchsanlage ROCOM - Experimente und Modellierung
Fachsitzung "Experimentelle und theoretische Untersuchungen zu Borverdünnungstransienten in DWR" auf der Jahrestagung Kerntechnik 2003, Berlin, 20.-22. Mai 2003, Berichtsheft S.57-83

Priede, J.; Gerbeth, G.; Hermann, R.; Filip, O.; Behr, G.
Two-phase induction melting with tailored flow control
EPM 2003, 4th Int. Conference on Electromagnetic Processing of Materials, Lyon (Frankreich), 14-17.10.2003, CD-ROM, P213 (2003)

Reddy, Vanga B. N.; Krepper, E.; Prasser, H.-M.; Zaruba, A.; Lopez de Bertodano, M. A.
Experimental and Numerical Studies of Flow in Rectangular Bubble Columns
The 10th International Topical Meeting on Nuclear Reactor Thermal Hydraulics (NURETH-10), Seoul, Korea, October 5-9, 2003
Multiphase Flows in Industrial Applications CFX-Germany, FZ-Rossendorf 28.-30.04.03

Rindelhardt, U.; Böhmer, B.; Böhmert, J.
RPV Integrity Assessment by Operational Feedback: Post Service Investigations of VVER-type NPPs
ANS 2003 Annual Meeting, San Diego, June 2003

Rohde, U.; Weiss, F.-P.; Karlsson, R.; Hemström, B.; Lillington, J.; Scheuerer, M.; Tuomisto, H.; Toppila, T.; Dury, T.; Cvan, M.; Muehlbauer;, P.; Toth, I.; Elter, J.; Bezrukov, Y.
Fluid mixing and flow distribution in the reactor circuit (FLOMIX-R)
Symposium FISA-2003 - EU research in reactor safety, Luxembourg, November 10-13, 2003; Pre-proceedings pp. 198-204

Schäfer, F.; Manera, A.
Investigation of flashing-induced instabilities at the CIRCUS test facility using the code ATHLET
The 10 th International Topical Meeting on Nuclear Reactor Thermal Hydraulics (NURETH-10), Seoul, Korea, October 5-9, 2003

Stefani, F.; Gerbeth, G.
A contactless inductive velocity reconstruction method for metallic and semiconducting melts
132nd Annual Meeting and Exhibition (TMS), San Diego, California, March 2-6,2003

Stefani, F.; Xu, M.; Gerbeth, G.
A Biot-Savart method to handle time-dependent dynamos in arbitrary domains
Jahrestagung der Astronomischen Gesellschaft, 15-20 September 2003 in Freiburg im Breisgau

Uhlemann, M.; Müller, G.; Böhmert, J.
Hydrogen Embrittlement of Reactor Pressure Vessel Steels
EDEM 2003 - International Conference on Environmental Degradation of Engineering Materials, Bordeaux, 29.06-02.07.2003, Vollversion auf CD

Viehrig, H.-W.; Boehmert, J.
Maßnahmen zur Sicherung der Betriebsdauer des Reaktordruckbehälters
Vertiefungskurs der Schweizerischen Vereinigung für Atomenergie, Betriebsdauermanagement der Kernkraftwerke, 27. und 28. November 2003, Winterthur, Schweiz.

Viehrig, H.-W.; Böhmert, J.
Anwendung des Master-Curve-Konzeptes zur Zähigkeitscharakterisierung von Druckbehälterstählen
Tagungsband der 35. Tagung des DVM-Arbeitskreises Bruchvorgänge, Fortschritte in der Bruch- und Schädigungsmechanik, 18. und 19. Februar 2003, Freiburg, S. 81 - 90

Weiss, F.-P.; Mittag, S.; Langenbuch, S.; Vanttola, T.; Hämäläinen, A.; Keresztúri, A.; Hádek, J.; Darilek, P.; Petkov, P. T.; Kuchin, A.; Hlbocky, P.; Sico, D.; Danilin, S.; Powney, D.
Validation of Coupled Neutronics / Thermal Hydraulics Codes for VVER Reactors (VALCO)
Symposium FISA-2003 - EU research in reactor safety, European Commission, Luxembourg, 10-13 November 2003, Pre-proceedings pp. 490-495

Weiß, F.-P.; Kliem, S.
Boron dilution Transients in PWRs
Lecture at Frederic Joliot/Otto Hahn Summer School, Karlsruhe,August 20-29, 2003

Willers, B.; Eckert, S.; Michel, U.; Zouhar, G.
Effect of the fluid convection driven by a rotating magnetic field on the solidification of a PbSn alloy
EUROMAT 2003, Lausanne, 1.-5. September 2003

Willers, B.; Eckert, S.; Michel, U.; Zouhar, G.; Nikrityuk, P.; Eckert, K.
Experimental and numerical study about the solidification of a PbSn alloy exposed to a rotating magnetic field
EPM 2003, 4th Int. Conference on Electromagnetic Processing of Materials, Lyon (Frankreich), 14-17.10.2003, CD-ROM, A2-3.7 (2003)

Willschütz, H.-G.
Erkenntnisse aus den Experimenten der FOREVER-Reihe und den begleitenden Finite Elemente-Rechnungen
Jahrestagung Kerntechnik 2003, 20.-22. Mai 2003, Berlin

Willschütz, H.-G.; Altstadt, E.
Post Test Calculation of Tube Creep Failure Experiments
Jahrestagung Kerntechnik 2003, Berlin, 20.-22. Mai 2003, Tagungsband S. 141-146

Willschütz, H.-G.; Altstadt, E.; Sehgal, B. R.; Weiß, F.-P.
FEM-Calculation of Different Creep-Tests with French and German RPV-Steels
17th International Conference on Structural Mechanics in Reactor Technology, SMiRT 17, Prague, Czech Republic, August 17-22, 2003

Willschütz, H.-G.; Altstadt, E.; Sehgal, B. R.; Weiß, F.-P.
Validation of a creep and plasticity model for French and German RPV-steels
OLHF Seminar 2002, Madrid, Spain, June 2002; OECD Nuclear Energy Agency Proceedings February 2003, NEA/CSNI/R(2003)1, pp 117-136

Willschütz, H.-G.; Altstadt, E.; Weiss, F.-P.; Sehgal, B. R.
Post-Test Calculations of Medium Scaled Pressure Vessel Creep Failure Experiments
2003 International Congress on Advances in Nuclear Power Plants ICAPP '03 May 4-7, 2003; Congress Palais, Córdoba, SPAIN, Proceedings on CD

Xu, M.; Stefani, F.; Gerbeth, G.
An integral equation approach to unsteady kinematic dynamos
Mathematical Aspects of Natural Dynamos, Caramulo, Portugal, August 31 - September 6 , 2003.

Contributions to proceedings and other collected editions

Altstadt, E.; Fischer, E.; Kumpf, H.; Nagel, G.; Sgarz, G.; Weiß, F.-P.
Analysis of irradiation induced creep of bolts of a PWR core baffle
Tagungsband der Jahrestagung Kerntechnik 2003, Berlin 20. -22. Mai 2003, S. 591-594

Altstadt, E.; Fischer, E.; Kumpf, H.; Nagel, G.; Sgarz, G.; Weiß, F.-P.
Mechanical analysis of a PWR core baffle with consideration of irradiation induced creep of bolts
2003 International Congress on Advanced Nuclear Power Plants (ICAPP'03), May 4-7, 2003, Cordoba, Spain

Altstadt, E.; Willschütz, H.-G.
Arbeiten zur Simulation prototypischer In-Vessel-Retention-Szenarien auf Basis von Vergleichsrechnungen mit mittelskaligen Experimenten
3. Workshop KOMPETENZVERBUND KERNTECHNIK am 8.10.2003, MPA, Stuttgart, Proceedings-CD

Ballesteros, A.; Garcia, G.; Böhmer, B.; Ošmera, B.; Keresztúri, A.; Ilieva, K.; Acosta, B.; Smutný, V.; Polke, E.; Zaritsky, S.; Ortego, P.
Reactor Dosimetry: Accurate Determination and Benchmarking of Radiation Field Parameters, relevant for Pressure Vessel Monitoring (REDOS)
FISA-2003 - Symposium on EU Research in Reactor Safety, 10-13 November 2003, Luxembourg

Beckert, C.; Freiesleben, H.; Grosse, E.; Naumann, B.; Weiß, F.-P.
Particle Flux Calculations for a Pulsed Photoneutron Source at the Radiation Source ELBE
Jahrestagung Kerntechnik 2003, Berlin, 20.-22. Mai 2003, Tagungsbericht S. 47-51

Böhmer, B.; Böhmert, J.; Rindelhardt, U.
Post Service Investigations of VVER-440 RPV Steel from NPP Greifswald
Structural Integrity and Life of NPP Equipment "SIL 2003" Kyiv, Ukraine, May 20-22,2003

Böhmer, B.; Borodkin, G.; Brodkin, E.; Egorov, A.; Konheiser, J.; Kozhevnikov, S.; Manturov, G.; Voloschenko, A.; Zaritsky, S.
ANISN-DORT-ROZ-MCNP-TRAMO Neutron-Gamma Flux Intercomparison Exercise for a Simple Testing Model
11th International Symposium on Reactor Dosimetry, 18 -23 August 2002 in Brussels, Belgium, Proceedings by World Scientific Publ., ISBN 981-238-448-0, p. 572-579

Böhmer, B.; Borodkin, G.; Konheiser, J.; Noack, K.; Polke, E.; Rogov, A.; Vladimirov, P.
Neutron and Gamma Fluence and Radiation Damage Parameters of Ex-core Components of Russian and German Light Water Reactors
11th International Symposium on Reactor Dosimetry, 18 -23 August 2002 in Brussels, Belgium, Proceedings by World Scientific Publ., ISBN 981-238-448-0, p. 286-294

Böhmert, J.; Viehrig, H.-W.; Ulbricht, A.
Bewertung der Neutronenversprödung von WWER-Druckbehälterstählen anhand der Ergebnisse der Bestrahlungsexperimente Rheinsberg
Jahrestagung Kerntechnik 2003, Tagungsbericht, 20. - 22. 05. 2003, Berlin, S. 595-598

Borodin, V. A.; Böhmert, J.
Embrittlement of Reactor Pressure Vessel Steel A508: A Look on Mesoscopic Levels
13. International Conference on Strength of Material, 25.-30.08.2003, Budapest, Hungary, Book of Abstracts, p. 113

Borodkin, G.; Böhmer, B.; Konheiser, J.; Manturov, G.; Polke, E.; Brodkin, E.; Jegorov, A.; Zaritsky, S.
Balakovo-3 Ex-vessel Exercise: Analysis of Calculation Results Intercomparison and Comparison with Reference Data
11th International Symposium on Reactor Dosimetry, August 18-23, 2002 in Brussels, Belgium, Proceedings by World Scientific Publ., ISBN 981-238-448-0, p. 665-673

Cramer, A.; Eckert, S.; Heinzelmann, C.; Lampe, D.; Gerbeth, G.
Efficient melt mixing due to the combined action of a rotating and a travelling magnetic field
EPM 2003, 4th Int. Conference on Electromagnetic Processing of Materials, Lyon (Frankreich), 14-17.10.2003, CD-ROM, C3-10.5 (2003)

Cramer, A.; Gerbeth, G.; Terhoeven, P.; Krätzschmar, A.
Fluid Flow Measurements in Electrically Driven Vortical Flows
Modelling for Electromagnetic Processing, Hannover, March 24 - 26, 2003. Proceedings pp 241-246, 2003

Delpech, M.; Dulla, S.; Garzenne, C.; Kophazi, J.; Krepel, J.; Lebrun, C.; Lecarpentier, D.; Mattioda, F.; Ravetto, P.; Rineiski, A.; Schikorr, M.; Szieberth, M.
Benchmark of Dynamics Simulation Tool for Molten Salt Reactors
Proceedings of the international conference GLOBAL 2003, 2182-2187, New Orleans, LA, November 2003

Eckert, S.; Galindo, V.; Witke, W.; Gerbeth, G.; Gerke-Cantow, R.; Nicolai, H.; Steinrücken, U.
Application of a DC magnetic field to the filling process of aluminium investment casting
EPM 2003, 4th Int. Conference on Electromagnetic Processing of Materials, Lyon (Frankreich), 14-17.10.2003, CD-ROM, P205 (2003)

Eckert, S.; Gerbeth, G.
Control of gas bubble injection into liquid metals by electromagnetic forces
In: J. Banhart, N. Fleck, A. Mortensen (Eds.), Cellular Metals: Manufacture, Properties, Applications, pp. 83-88 International Conference MetFoam 2003, Berlin, 23.06-25.06.2003

Eckert, S.; Gerbeth, G.
Local velocity measurements in lead-bismuth and sodium flows using the Ultrasound Doppler Velocimetry
NURETH-10 in Seoul (Korea), 05.-09.10.2003, Paper K00201

Eckert, S.; Gerbeth, G.; Cramer, A.; Willers, B.; Witke, W.; Galindo, V.
Liquid metal model experiments on casting and solidification processes
Int. Symposium on liquid metal processing and casting and solidification processes, Nancy (France), Sept. 21-24, 2003. Proceedings, Eds.: P.D.Lee, A.Mitchell, J.-P.Bellot, A.Jardy, 333-343, 2003.

Eckert, S.; Gerbeth, G.; Gundrum, T.; Stefani, F.; Witke, W.
New approaches to determine the velocity field in metallic melts
EPM 2003, 4th Int. Conference on Electromagnetic Processing of Materials, Lyon (Frankreich), October 14-17, 2003, Lyon, France, CD-ROM, PL13

Eckert, S.; Gerbeth, G.; Stefani, F.; Witke, W.
Measuring techniques for liquid metal velocity measurements
Int. Symposium on liquid metal processing and casting, Nancy (France), Sept. 21-24, 2003. Proceedings, Eds.: P.D.Lee, A.Mitchell, J.-P.Bellot, A.Jardy, 261-271, 2003.

Gokhman, A.; Böhmert, J.; Ulbricht, A.
Calculation of the Scattering Factor from the Shell Model of Nanoscale Defects
XV International Conference on X-ray Diffraction & Crystal Chemistry of Minerals, St. Petersburg, 15.-19.09.2003

Grundmann, U.; Mittag, S.
DYN3D Calculations for the V-1000 Test Facility and Comparisons with the Measurements
Proceedings of 13. Symposium of AER,p. 521-539, Dresden, 22-26. September, 2003

Grundmann, U.; Rohde, U. (Editors)
Different Simulations of the Phase 2 of the OECD/NRC BWR Turbine Trip Benchmark with the Code DYN3D
Annual Meeting on Nuclear Technology, Berlin, May 20 - 22, 2003

Grunwald, G.; Höhne, T.; Kliem, S.; Prasser, H.-M.; Rohde, U.; Weiß, F.-P.
Coolant Mixing Studies for the Analysis of Hypothetical Boron Dilution Transients in a PWR
11. International Conference on Nuclear Engineering ICONE-11, Tokyo, Japan, April 20-23, 2003, Proceedings CD-ROM paper 36325

Hämäläinen, A.; Vanttola, T.; Weiss, F.-P.; Mittag, S.; Kliem, S.; Kozmenkov, Y.; Keresztúri, A.; Hádek, J.; Strmensky, C.; Stefanova, S.; Kuchin, A.; Hlbocky, P.; Siko, D.; Danilin, S.
Validation of coupled codes in VALCO WP1 using measured VVER data
13. Symposium of AER, Dresden, 22-26 September, 2003, pp. 555-576

Hampel, U.; Zschau, J.; Prasser, H.-M.
Diagnostik von Ein- und Mehrphasenströmungen mit Leitfähigkeits-Gittersensoren
Proceedings 6. Dresdner Sensor-Symposium - Sensoren für zukünftige Hochtechnologien und Neuentwicklungen für die Verfahrenstechnik, Band 20, G. Gerlach Hrsg., pp. 33-36, w.e.b. Universitätsverlag, 2003

Hessel, G.; Kryk, H.; Schmitt, W.; Seiler, T.; Weiß, F.-P.; Hilpert, R.; Roth, M.; Deerberg, G.
Monitoring System for Multiphase Hydrogenation in Chemical Plants
Proceedings of the 5th IFAC Symposium on Fault Detection, Supervision and Safety for Technical Processes SAFEPROCESS'2003, Washington, D.C., USA, June 9-11, 2003, pp. 969-974

Höhne, T.; Kliem, S.; Prasser, H.-M.; Rohde, U.
Experimental and Numerical Mixing Studies inside a Reactor Pressure Vessel
4th ASME/JSME Joint Fluids Engineering Conference, July 2003, Hawaii, USA, CD-ROM

Kliem, M.
Experimental validation of the porous media approach for rod bundle geometry under crossflow conditions.
11th International Conference on Nuclear Engineering, Tokyo, Japan, April 20-23, 2003 ICONE11-36502

Kliem, S.
Comparison of the updated solutions of the 6th dynamic AER benchmark - main steam line break in a NPP with VVER-440
XIII. AER-Symposium on VVER Physics and Reactor Safety, Dresden, Germany, September 23-26, 2003, Proceedings pp. 413-444

Kliem, S.; Mittag, S.
Analysis of a hypothetical boron dilution event by means of the neutron kinetic core model DYN3D using different cross section libraries
Fachtag der KTG-Fachgruppen "Betrieb" und "Reaktorphysik und Berechnungsmethoden" 13.-14.02.2003, Rossendorf, Proceedings CD-ROM

Kliem, S.; Prasser, H.-M.; Grunwald, G.; Höhne, T.; Rohde, U.; Weiß, F.-P.
ROCOM experiments on the coolant mixing in the upper plenum of a PWR
Jahrestagung Kerntechnik, Berlin,20.-22.Mai 2003, Proceedings pp. 73-76

Kliem, S.; Rohde, U.; Weiß, F.-P.
Analysis of PWR core behaviour after the entrance of underborated water
Fachsitzung "Experimentelle und theoretische Untersuchungen zu Borverdünnungstransienten in DWR" auf der Jahrestagung Kerntechnik 2003, Berlin, 20.-22. Mai 2003, Berichtsheft S.85-96

Krepel, J.; Grundmann, U.; Rohde, U.
Development and Verification of a Reactor Dynamics Code for Molten Salt Reactors with Flowing Fuel
Annual Meeting on Nuclear Technology 2003, Berlin, 15. - 17. May 2003

Krepper, E.
CFD modelling of subcooled boiling
The 10th International Topic Meeting on Nuclear Reactor Thermal Hydraulics (NURETH-10), Seoul, Korea, October 5 - 9, 2003

Krepper, E.
CFD Modelling of subcooled boiling
XIII. AER-Symposium on VVER Physics and Reactor Safety, Dresden, Germany, September 23-26, 2003, Proceedings pp. 819-833

Kryk, H.; Hessel, G.; Schmitt, W.; Seiler, T.; Weiß, F.-P.; Hilpert, R.; Roth, M.
On-line concentration estimation during chemical reactions using adaptive heat/ mass balances
4th European Congress of Chemical Engineering, 21-25 September 2003 Granada, Spain, Topic 10 Abstracts, O-10.2-001

Lucas, D.; Krepper, E.; Prasser, H.-M.
Experimental investigations and modelling on the transition from bubble to slug flow in vertical pipes
Proceedings of the German-Japanese Workshop on Multiphase Flow, Karlsruhe, August 25-27, 2002, FZKA 6759(http://www.emsi.fzk.de/gjwmf2002/pdf/Proceedings_FZKA6759.pdf), pp. C-1 - C-12

Lucas, D.; Krepper, E.; Prasser, H.-M.
Modelling of bubble flow in vertical pipes
The 10 th International Topical Meeting on Nuclear Reactor Thermal Hydraulics (NURETH-10), Seoul, Korea, October 5-9, 2003, Paper A00301

Lucas, D.; Krepper, E.; Prasser, H.-M.; Rohde, U.; Weiß, F.-P.
Constitutive laws for interaction of gas bubbles within the liquid flow field – modelling and experimental basis
Use of computational fluid dynamics codes for safety analysis of reactor systems, Joint IAEA/NEA technical meeting, Pisa, Italy, November 11-13, 2002, IAEA-TECDOC-1379, IAEA, Vienna, 2003

Lucas, D.; Prasser, H.-M.
First experimental results of measurements on air/water flow in a vertical pipe with an inner diameter of 194 mm
41st European Two-Phase Flow Group meeting, Norway, May 12-13, 2003

Manera, A.; Prasser, H.-M.; Hagen, T. H. J. J. van der
Suitability of Drift-flux models, void-fraction evolution and 3D flow pattern visualization during stationary and transient flashing flow in a vertical pipe
The 10th International Topical Meeting on Nuclear Reactor Thermal Hydraulics (NURETH-10), Seoul, Korea, October 5-9, 2003; conference-CD: A00108

Manera, A.; Rohde, U.; Prasser, H.-M.; Hagen, T. H. J. J. van der
Modeling of flashing-induced instabilities in the start-up phase of natural-circulation BWRs using the code FLOCAL
The 10th International Topical Meeting on Nuclear Reactor Thermal Hydraulics (NURETH-10), Seoul, Korea, October 5-9, 2003; conference-CD: A00506

Manera, A.; Schäfer, F.
Experimental and theoretical investigations of flashing induced instabilities at the CIRCUS test facility
Annual Meeting on Nuclear Technology, May 20-22, 2003, Berlin, Germany, Proceedings, P. 89-92

Mercurio, G.; Eckert, S.
CFD simulation of a bubbly flow experiment with liquid PbBi eutectic alloy and Nitrogen
Computational Methods in Multiphase Flow II, A.A.Mammoli, C.A.Brebbia (Eds.), WIT Press 2004, Southampton pp.395-404, (Proc. of the Second International Conference on Computational Methods in Multiphase Flow, Santa Fe, New Mexico, USA, 2003)

Mittag, S.; Petkov, P. T.; Grundmann, U.
Discontinuity factors for non-multiplying hexagonal nodes in VVER reactors
13. Symposium of AER, Dresden, 22-26 September, 2003, pp. 89-108

Müller, G.; Ulbricht, A.; Böhmert, J.; Uhlemann, M.
Einfluss von Wasserstoff auf die Zähigkeit von bestrahlten Reaktordruckbehälterstählen
Proceedings CD, Vortrag, 3. Workshop Kompetenzverbund Kerntechnik 8. Oktober 2003

Petkov, P. T.; Mittag, S.
Two-dimensional heterogeneous transport theory hot zero-power benchmarks for the WWER-1000 reactors
13. Symposium of AER, Dresden, 22-26 September, 2003, pp. 77-88

Petkov, P. T.; Mittag, S.; Christoskov, I.; Kamenov, K.; Antov, A.; Bakalov, I.; Wehner, H.
A new DYN3D library for the WWER-1000 reactors
13. Symposium of AER, Dresden, 22-26 September, 2003, pp. 109-122

Prasser, H.-M.; Beyer, M.; Böttger, A.; Carl, H.; Lucas, D.; Schaffrath, A.; Schütz, P.; Weiß, F.-P.; Zschau, J.
Influence of the pipe diameter on the structure of the gas-liquid interface in a vertical two-phase pipe flow
10th International Topical Meeting on Nuclear Reactor Thermal Hydraulics (NURETH-10), Seoul, Korea, October 5-9, 2003; conference-CD: A00308

Prasser, H.-M.; Böttger, A.; Zschau, J.; Baranyai, G.; Ezsöl, Gy.
Thermal effects during condensation induced water hammer behind fast acting valves in pipelines
11th International Conference on Nuclear Engineering Tokyo, JAPAN, April 20-23,2003, Proceedings ICONE11-36310

Prasser, H.-M.; Höhne, T.; Kliem, S.; Rohde, U.; Weiß, F.-P.
Untersuchung der Kühlmittelvermischung an der Versuchsanlage ROCOM - Experimente und Modellierung
Fachsitzung "Experimentelle und theoretische Untersuchungen zu Borverdünnungstransienten in DWR" auf der Jahrestagung Kerntechnik 2003, Berlin, 20.-22. Mai 2003, Berichtsheft S.57-83

Priede, J.; Gerbeth, G.; Hermann, R.; Filip, O.; Behr, G.
Two-phase induction melting with tailored flow control
EPM 2003, 4th Int. Conference on Electromagnetic Processing of Materials, Lyon (Frankreich), 14-17.10.2003, CD-ROM, P213 (2003)

Reddy, Vanga B. N.; Krepper, E.; Prasser, H.-M.; Zaruba, A.; Lopez de Bertodano, M. A.
Experimental and Numerical Studies of Flow in Rectangular Bubble Columns
The 10th International Topical Meeting on Nuclear Reactor Thermal Hydraulics (NURETH-10), Seoul, Korea, October 5-9, 2003
Multiphase Flows in Industrial Applications CFX-Germany, FZ-Rossendorf 28.-30.04.03

Rohde, U.; Weiss, F.-P.; Karlsson, R.; Hemström, B.; Lillington, J.; Scheuerer, M.; Tuomisto, H.; Toppila, T.; Dury, T.; Cvan, M.; Muehlbauer;, P.; Toth, I.; Elter, J.; Bezrukov, Y.
Fluid mixing and flow distribution in the reactor circuit (FLOMIX-R)
Symposium FISA-2003 - EU research in reactor safety, Luxembourg, November 10-13, 2003; Pre-proceedings pp. 198-204

Schäfer, F.; Manera, A.
Investigation of flashing-induced instabilities at the CIRCUS test facility using the code ATHLET
The 10 th International Topical Meeting on Nuclear Reactor Thermal Hydraulics (NURETH-10), Seoul, Korea, October 5-9, 2003

Uhlemann, M.; Müller, G.; Böhmert, J.
Hydrogen Embrittlement of Reactor Pressure Vessel Steels
EDEM 2003 - International Conference on Environmental Degradation of Engineering Materials, Bordeaux, 29.06-02.07.2003, Vollversion auf CD

Ulbricht, A.; Heinemann, A.
Synergism effects of hydrogen and radiation defects in steel
BENSC Experimental Reports 2002 (eds. Y. Kirschbaum, M. Tovar, D. Bischoff, R. Michaelsen), HMI-B 590, p. 220, Hahn-Meitner Institut Berlin, April 2003.

Viehrig, H.-W.; Boehmert, J.
Maßnahmen zur Sicherung der Betriebsdauer des Reaktordruckbehälters
Vertiefungskurs der Schweizerischen Vereinigung für Atomenergie, Betriebsdauermanagement der Kernkraftwerke, 27. und 28. November 2003, Winterthur, Schweiz.

Viehrig, H.-W.; Böhmert, J.
Anwendung des Master-Curve-Konzeptes zur Zähigkeitscharakterisierung von Druckbehälterstählen
Tagungsband der 35. Tagung des DVM-Arbeitskreises Bruchvorgänge, Fortschritte in der Bruch- und Schädigungsmechanik, 18. und 19. Februar 2003, Freiburg, S. 81 - 90

Weiss, F.-P.; Mittag, S.; Langenbuch, S.; Vanttola, T.; Hämäläinen, A.; Keresztúri, A.; Hádek, J.; Darilek, P.; Petkov, P. T.; Kuchin, A.; Hlbocky, P.; Sico, D.; Danilin, S.; Powney, D.
Validation of Coupled Neutronics / Thermal Hydraulics Codes for VVER Reactors (VALCO)
Symposium FISA-2003 - EU research in reactor safety, European Commission, Luxembourg, 10-13 November 2003, Pre-proceedings pp. 490-495

Willers, B.; Eckert, S.; Michel, U.; Zouhar, G.
Effect of the fluid convection driven by a rotating magnetic field on the solidification of a PbSn alloy
EUROMAT 2003, Lausanne, 1.-5. September 2003

Willers, B.; Eckert, S.; Michel, U.; Zouhar, G.; Nikrityuk, P.; Eckert, K.
Experimental and numerical study about the solidification of a PbSn alloy exposed to a rotating magnetic field
EPM 2003, 4th Int. Conference on Electromagnetic Processing of Materials, Lyon (Frankreich), 14-17.10.2003, CD-ROM, A2-3.7 (2003)

Willschütz, H.-G.; Altstadt, E.
Post Test Calculation of Tube Creep Failure Experiments
Jahrestagung Kerntechnik 2003, Berlin, 20.-22. Mai 2003, Tagungsband S. 141-146

Willschütz, H.-G.; Altstadt, E.; Sehgal, B. R.; Weiß, F.-P.
FEM-Calculation of Different Creep-Tests with French and German RPV-Steels
17th International Conference on Structural Mechanics in Reactor Technology, SMiRT 17, Prague, Czech Republic, August 17-22, 2003

Willschütz, H.-G.; Altstadt, E.; Sehgal, B. R.; Weiß, F.-P.
Validation of a creep and plasticity model for French and German RPV-steels
OLHF Seminar 2002, Madrid, Spain, June 2002; OECD Nuclear Energy Agency Proceedings February 2003, NEA/CSNI/R(2003)1, pp 117-136

Willschütz, H.-G.; Altstadt, E.; Weiss, F.-P.; Sehgal, B. R.
Post-Test Calculations of Medium Scaled Pressure Vessel Creep Failure Experiments
2003 International Congress on Advances in Nuclear Power Plants ICAPP '03 May 4-7, 2003; Congress Palais, Córdoba, SPAIN, Proceedings on CD

FZR-Reports

Altstadt, E.; Beckert, C.; Eckert, S.; Freiesleben, H.; Galindo, V.; Grosse, E.; Naumann, B.; Weiß, F.-P.
Energiedispersive Untersuchung der Wechselwirkung schneller Neutronen mit Materie; Teilbericht : Auslegung des Neutronen-Produktionstargets
Wissenschaftlich-Technische Berichte / Forschungszentrum Rossendorf; FZR-369 Maerz 2003

Altstadt, E.; Carl, H.; Weiß, R.
Fluid-Structure Interaction Investigations for Pipelines
Wissenschaftlich-Technische Berichte / Forschungszentrum Rossendorf, FZR-393, Dezember 2003

Altstadt, E.; Willschütz, H.-G.
Schmelzerückhaltung im RDB nach Verlagerung von Corium in das untere Plenum Zusammenfassung der bisherigen Ergebnisse des Projekts Nr.: 150 1254
Wissenschaftlich-Technische Berichte / Forschungszentrum Rossendorf; FZR-370 März 2003

Böhmert, J.; Gokhman, A.; Große, M.; Ulbricht, A.
Nachweis, Interpretation und Bewertung bestrahlungsbedingter Gefügeänderungen in WWER-Reaktor-Druckbehälterstählen
Wissenschaftlich-Technische Berichte / Forschungszentrum Rossendorf, FZR-381, Juni 2003

Böttger, A.; Gocht, T.; Prasser, H.-M.; Zschau, J.
Transiente Kondensationsversuche an einem Notkondensator - Einzelrohr
Wissenschaftlich-Technische Berichte / Forschungszentrum Rossendorf; FZR-383, Juli 2003

Dzugan, J.
Crack initiation determination for Charpy size specimens
Wissenschaftlich-Technische Berichte / Forschungszentrum Rossendorf; FZR-366, Februar 2003

Dzugan, J.
Crack lengths calculation by unloading compliance technique for Charpy size specimens
Wissenschaftlich-Technische Berichte / Forschungszentrum Rossendorf; FZR-385, Juli 2003

Grundmann, U.; Kliem, S.
Validierung des gekoppelten neutronenkinetischen-thermohydraulischen Codes ATHLET/DYN3D mit Hilfe von Messdaten des OECD Turbine Trip Benchmarks
Wissenschaftlich-Technische Berichte / Forschungszentrum Rossendorf; FZR-384 Dezember 2003

Grunwald, G.; Höhne, T.; Kliem, S.; Prasser, H.-M.; Richter, K.-H.; Rohde, U.; Weiß, F.-P.
Kühlmittelvermischung in Druckwasserreaktoren - Teil 2, Experimentelle Ausrüstung und Simulation der Vermischung
Wissenschaftlich-Technische Berichte / Forschungszentrum Rossendorf; FZR-367 Februar 2003

Höhne, T.
CFD-Post Test Analysen der dichtegetriebenen Vermischungsexperimente an der

ROCOM Versuchsanlage
Wissenschaftlich-Technische Berichte / Forschungszentrum Rossendorf; FZR-386, Juli 2003

Höhne, T.
Modellierung der Kühlmittelvermischung in Druckwasserreaktoren
Wissenschaftlich-Technische Berichte / Forschungszentrum Rossendorf; FZR-382, Juni 2003

Hoppe, D.
Untersuchungen zur strukturellen Modellverbesserung durch Symbiosen zwischen Modellen
Wissenschaftlich-Technische Berichte / Forschungszentrum Rossendorf; FZR-374 April 2003

Ouytsel, K. van; Böhmert, J.; Müller, G.
A Small Angle X-ray Scattering Method to Investigate the Crack Tip in Metals
Wissenschaftlich-Technische Berichte / Forschungszentrum Rossendorf; FZR-388, August 2003

Prasser, H.-M.; Lucas, D.; Krepper, E.; Baldauf, D.; Böttger, A.; Rohde, U.; Schütz, P.; Weiß, F.-P.; Zippe, C.; Zippe, W.; Zschau, J.
Strömungskarten und Modelle für transiente Zweiphasenströmungen
Wissenschaftlich-Technische Berichte / Forschungszentrum Rossendorf; FZR-379 Juni 2003

Stephan, I.; Prokert, F.; Scholz, A.; Böhmert, J.
Bestimmung der Bestrahlungstemperatur im Bestrahlungsprogramm Rheinsberg II
Wissenschaftlich-Technische Berichte / Forschungszentrum Rossendorf, FZR-376, April 2003

Weiß, F.-P.; Rindelhardt, U. (Editors)
Institute of Safety Research; Annual Report 2002
Wissenschaftlich-Technische Berichte (FZR-Report); FZR-380, Juni 2003

Zippe, C.; Hoppe, D.; Fietz, J.; Hampel, U.; Hensel, F.; Mäding, P.; Prasser, H.-M.; Zippe, W.
Berührungslose Messung von Phasen- und Konzentrationsverteilungen in Blasensäulen mit positronenemittierenden Radionukliden
Wissenschaftlich-Technische Berichte / Forschungszentrum Rossendorf; FZR-289, September 2003

Patents

Zschau, J.
Anordnung zur Bestimmung der Phasenverteilung in strömenden Mehrphasenmedien und Verfahren zur Auswertung der mit der Anordnung gewonnenen Messsignale
DE 103 18 548.8

Eckert, S.; Galindo, V.; Gerbeth, G.; Lampe, D.; Witke, W.
Verfahren und Anordnung zur Messung des Durchflusses elektrisch leitfähiger Medien
DE 103 25 973.2

Prasser, H.-M.; Hampel, U.
Anordnung zur Röntgentomographie mit einem elektronisch abgelenkten Elektronenstrahl
DE 103 56 601.5

Priede, J.; Gerbeth, G.
IFW – Hermann, R.; Behr, G.; Schultz, L.; Uhlemann, H.-J.
Verfahren und Vorrichtung zum Ziehen von Einkristallen durch Zonenziehen
DE 103 28 859.7

Priede, J.; Gerbeth, G.
IFW – Hermann, G.; Schultz, L.; Filip, O.
Verfahren und Vorrichtung zur schmelzmetallurgischen Herstellung von Magnetlegierungen auf Nd-Fe-B-Basis
DE 103 28 861.7

Priede, J.; Gerbeth, G.
IFW – Hermann, G.; Filip, O.
Verfahren und Vorrichtung zur schmelzmetallurgischen Herstellung von Magnetlegierungen auf Nd-Fe-B-Basis
DE 103 31 152.1

Awards

Hans-Georg Willschütz

Siempelkamp Kompetenzpreis 2003

for the contribution

„Erkenntnisse aus den Experimenten der FOREVER-Reihe und den begleitenden Finite-Elemente-Rechnungen“

presented at the Annual Meeting on Nuclear Technology 2003, Berlin

Guests

Reddy Vanga, Brahma Nanda
01.01.2003 - 11.01.2003
31.01.2003 - 01.03.2003
29.04.2003 - 29.05.2003
30.06.2003 - 31.0820.03
Purdue University West Lafayette/USA

Puttaert, Isabelle
24.01.2003 - 27.01.2003
Luxembourg

Melnikov, Vladimir Prof.
27.01.2003 - 06.02.2003
Novgorod Technical University/Russland

Khokhlov, Valeri
28.01.2003 – 06.02.2002
Novgorod Technical University/Russland

Davidson, Peter Prof.
02.02.2003 – 04.02.2003
Universität Cambridge/Großbritannien

Bezrukov, Yuri Dr.
22.02.2203 – 26.02.2003
20.09.2003 – 26.09.2003
GIDROPRESS Podolsk/Russland

Bykov, Mikhail Dr.
22.02.2003 – 26.02.2003
GIDROPRESS Podolsk/Russland

Kozmenkov, Yaroslav
03.03.2003 – 31.12.2003
RRC IPPE Obninsk/Russland

Kuchin, Oleksandr
08.03.2003 – 15.03.2003
27.09.2003 – 02.10.2003
Scientific-Technical Centre for Nuclear and Radiation Safety of the Ukraine, Kiew/Ukraine

Khalimonchuk, Volodomyr
08.03.2003 – 15.03.2003
27.09.2003 – 02.10.2003
Scientific-Technical Centre for Nuclear and Radiation Safety of the Ukraine, Kiew/Ukraine

Grants, Ilmars Dr.
22.03.2003 – 14.04.2003
Institute of Physics Riga/Lettland

Gelfgat, Yuri Prof.
26.03.2003 – 11.04.2003
Institute of Physics Riga/Lettland

Bakalov, Ivan
05.04.2003 – 19.04.2003
ENPRO-Consult Ltd. Sofia/Bulgarien

Lizorkin, Mikhail Dr.
14.04.2003 – 18.04.2003
Kurchatov Institut Moskau/Russland

Nikonov, Sergej
14.04.2003 – 18.04.2003
Kurchatov Institut Moskau/Russland

Plevachuk, Yuri Dr.
23.04.2003 – 07.05.2003
17.11.2003 – 29.11.2003
Staatliche Universität Lviv/Ukraine

Glück, Markus
27.04.2003 – 30.04.2003
Universität Erlangen

Priede, Janis Dr.
13.05.2003 – 31.05.2003
03.11.2003 – 15.11.2003
Institute of Physics Riga/Lettland

Filzwieser, Iris
30.05.2003 – 30.05.2003
Universität Loeben/Österreich

Kozlov, Dmitry Dr.
31.05.2003 –20.07.2003
RIAR Dimitriovgrad/Russland

Tefera, Nurelegne Dr.
17.06.2003 - 11.09.2003
Addis Ababa University, Äthiopien

Gad-el-Hal, Mohamed Prof.
27.06.2003 – 27.06.2003
Virginia Commonwealth University Richmond/USA

Gokhman, Oleksandr Prof.
25.07.2003 – 04.09.2003
SUP Universität Odessa/Ukraine

Ivanov, Alexandre Prof.
28.07.2003 – 24.08.2003
Budker Institute Novosibirsk/Russland

Bagrianski, Petr Dr.
28.07.2003 – 24.08.2003
Budker Institute Novosibirsk/Russland

Gailitis, Agris Prof.
25.08.2003 – 28.08.2003
Institute of Physics Riga/Lettland

Borodin, Vladimir Dr.
31.08.2003 – 30.09.2003
Kurchatov Institut Moskau/Russland

Sydiachenko, Viacheslav Dr.
22.09.2003 – 22.11.2003
Ukrainische Akademie der Wissenschaften/Ukraine

Kotsarev, Alexander
20.09.2003 – 27.09.2003
Kurchatov Institut Moskau/Russland

Kovbasenko, Yurj Dr.
27.09.2003 – 30.09.2003
Scientific-Technical Centre for Nuclear and Radiation Safety of the Ukraine, Kiew/Ukraine

Kolesnichenko, Ilya
03.10.2003 – 30.11.2003
Akademie der Wissenschaften Russland/Russland

Voskoboinikov, Roman Dr.
04.11.2003 – 01.12.2003
Kurchatov Institut Moskau/Russland

Ganchenkova, Maria Dr.
07.11.2003 – 07.12.2003
Kurchatov Institut Moskau/Russland

Borodkin, Gennady
16.11.2003 – 07.12.2003
Gasatomnadzor Moskau/Russland

Gad, Moustafa
24.11.2003 – 28.11.2003
TU Hamburg/Harburg

Junk, Markus
24.11.2003 – 28.11.2003
TÜV Nord, Hamburg

Stefanova, Svetla
24.11.2003 – 14.12.2003
Bulgarian Academy of Sciences Sofia/Bulgarien

Jakubsky, Vit
01.12.2003 – 04.12.2003
Nuclear Physics Institute Rez/Tschechien

Murasov, Michael
01.10.2003 – 31.04.2004
University of Kiev /Ukraine

Meetings und Workshops

KTG-Fachtagung “Reaktorbetrieb und Kernüberwachung”
Rossendorf, 13. – 14. 02.2003

Multiphase Flows in Industrial Applications, ANSYS-CFX/FZR CFX short course and CFD workshop
Rossendorf, 28. – 30. 04. 2003

1st NURESIM-PTS meeting
Rossendorf, 11.06.2003

13th Symposium of “Atomic Energy Research” Association on Reactor Physics and Reactor Safety of VVER
Dresden, 22. – 26.09.2003

Klausurtagung des SFB 609 „Elektromagnetische Strömungsbeeinflussung für Metallurgie, Kristallzüchtung und Elektrochemie“
Rossendorf, 06. – 07.11.2003

Seminars of the Institute

Dr. R. Koch
Einführung in den Salzschmelzenreaktor
21. 01. 2003

Dr. K. Noack
Einfluss der Gammastrahlung auf die Schädigung von Druckbehältermaterialien und auf reaktordosimetrische Messungen
30. 01. 2003

Prof. P. Davidson, Universität Cambridge
The role of angular momentum in MHD turbulence
04. 02. 2003

Dr. W. Baehr, Bundesanstalt für Materialprüfung
Werkstoff- und bruchmechanische F/E-Arbeiten an der Bundesanstalt für Materialforschung und –prüfung
06. 03. 2003

Dr. E. Krepper
CFD-Modellierung von unterkühltem Sieden
13. 03. 2003

Prof. S. Asai, Nagoya University
Recent Activities on Electromagnetic Processing of Materials in Nagoya University
20. 03. 2003

Dr. D. Lucas, Dr. H.-M. Prasser
Experimentelle Untersuchungen zur Struktur von Blasenströmungen von vertikalen Rohren
28. 03. 2003

Dr. E. Altstadt
Thermische und mechanische Analyse einer DWR-Kernumfassung unter dem Einfluss von Neutronen- und Gammastrahlung
17. 04. 2003

Dr. G. Gerbeth, Dr. J. Priede, R. Hermann, G. Behr (IFW Dresden)
Magnetfeldkontrolle der Floating-Zone Kristallzüchtung
30. 04. 2003

Dr. S. Mittag, Dr. U. Grundmann, P.T. Petkov (INRE Sofia)
Erhöhung der Genauigkeit von Neutronenflussberechnungen durch Anwendung von Diskontinuitäts-Faktoren
08. 05. 2003

S. Kliem, Dr. H.-M. Prasser
ROCOM-Experimente zur Vermischung des Kühlmittels im oberen Plenum
27.05.2003

Dr. K. van Ouytsel
Kleinwinkelstreuung – eine Nachweismethode für Strukturschädigung durch Verformung?
19. 06. 2003

W. Queitsch (Verbundnetz Gas HG Leipzig)
Gewährleistung der Sicherheit von Hochdruck-Fernleitungen für Erdgas
16. 09. 2003

J. Krepel
Simulation von Transienten in Salzschmelzereaktoren mit dem Code DYN1D-MSR
09. 10. 2003

A. Ulbricht
Vergleichende Bewertung der Bestrahlungssuszeptibilität von RDB-Stählen aus der Sicht der SANS-Strukturanalyse
16. 10. 2003

Dr. U. Hampel, Dr. D. Hoppe
Röntgen- und Gamma-Tomografie – Beispiele und Perspektiven
13. 11. 2003

Dr. Y. Plevachuk (Ivan Frank National University, Liv, Ukraine)
Electrophysical measurements for strongly aggressive liquid metals and semiconductors
25. 11. 2003

Dr. J.-M. Shi
Implementierung und Validierung von Modellansätzen für Kraftwirkung auf Blasen im Code CFX-5
27. 11. 2003

Lecture courses

Prof. Dr. Frank-Peter Weiß
Zuverlässigkeit und Sicherheit technischer Systeme
TU Dresden, Fakultät Maschinenwesen
SS 2003 und WS 2003

Prof. Dr. Udo Rindelhardt
Erneuerbare Energien I und II
Universität Leipzig, Fakultät für Physik und Geowissenschaften
SS 2003 und WS 2003

Departments of the Institute

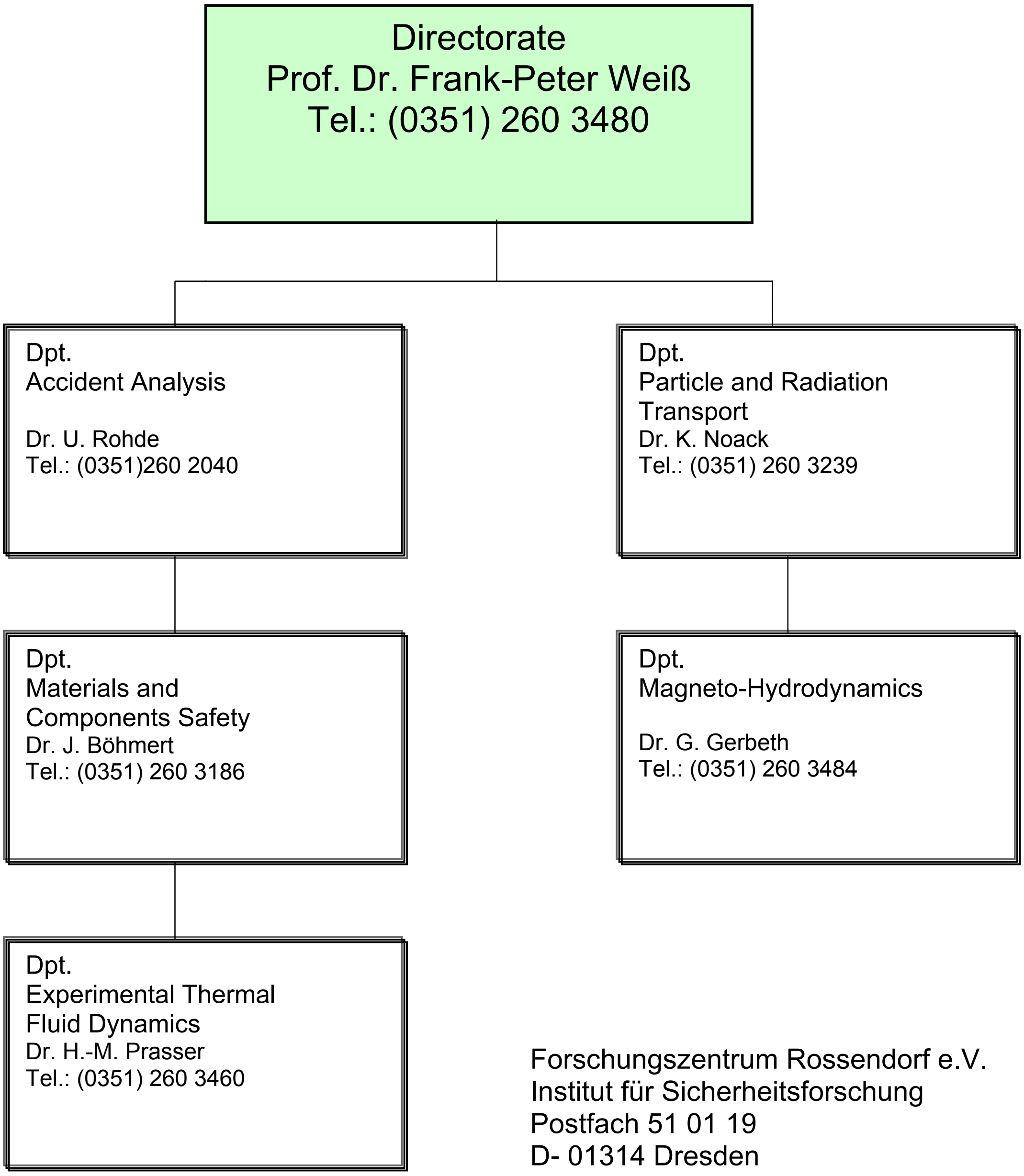

Forschungszentrum Rossendorf e.V.
Institut für Sicherheitsforschung
Postfach 51 01 19
D- 01314 Dresden

Personnel

Director: Prof. Dr. Frank-Peter Weiß

Scientific Staff

Altstadt, Eberhard
Beckert, Carsten
Beyer, Matthias
Böhmer, Bertram
Böhmert, Jürgen Dr.
Böttger, Arndt
Budnik, Sergey
Carl, Helmar Dr.
Chatrov, Viktor Dr.
Cramer, Andreas
Dzugan, Jan
Eckert, Sven Dr.
Erlebach, Stephan
Fietz, Jürgen Dr.
Galindo, Vladimir Dr.
Gerbeth, Gunter Dr.
Gommlich, Andre
Grahn, Alexander
Grants, Ilmars Dr.
Grundmann, Ulrich Dr.
Gundrum, Thomas
Günther, Uwe Dr.
Heinzelmann, Christian
Hessel, Günther
Hoppe, Dietrich Dr.
Höhne, Thomas Dr.
Hüller, Jürgen Dr.
Kliem, Margarita
Kliem, Sören
Koch, Reinhard Dr.
Konheiser, Jörg
Kozmenkov, Yaroslav
Krepper, Eckhard Dr.
Kryk, Holger Dr.
Küchler, Roland Dr.
Lucas, Dirk Dr.
Mittag, Siegfried Dr.
Müller, Gudrun Dr.
Mutschke, Gerd Dr.
Neumann, Hartmut Dr.
Noack, Klaus Dr.
Prasser, Horst-Michael Dr.
Rindelhardt, Udo Prof. Dr.
Rohde, Ulrich Dr.
Schäfer, Frank Dr.
Schleicher, Eckhard
Schmitt, Wilfried Dr.
Schütz, Peter
Shi, Jun-Mei Dr.
Stefani, Frank Dr.
Stephan, Ingrid Dr.
Van Ouytsel, Kristel Dr.
Weier, Tom
Werner, Matthias Dr.
Willers, Bernd
Willschütz, Hans-Georg
Witke, Willy
Xu, Mingtian Dr.
Zippe, Cornelius Dr.
Zschau, Jochen Dr.

PhD Students

Buchenau, Dominique
Krepel, Jiri
Vallee, Christophe
Varshney, Kapil
Zaruba, Aliaksandr
Zhang, Chaojie

Technical Staff

Behrens, Sieglinde
Berger, Torsten
Bombis, Doris
Borchardt, Steffen
Döring, Frederik
Forker, Klaus
Futterschneider, Hein
Henke, Steffen
Kunadt, Heiko
Leonhardt, Wolf-Dietrich
Leuner, Bernd
Lindner, Klaus
Losinski, Claudia
Nowak, Bernd
Pietzsch, Jens
Pietruske, Heiko
Richter, Annett
Richter, Henry
Richter, Joachim
Richter, Petra
Roßner, Michaela
Rott, Sonja
Rußig, Heiko
Schleßiger, Heike
Schneider, Gisela
Skorupa, Ulrich
Sühnel, Tobias
Tamme, Marko
Tamme, Günter
Walter, Denis
Webersinke, Wolfgang
Weichelt, Steffen
Weiß, Rainer
Zimmermann, Wilfried